University of Stuttgart
Germany

Daniel
Kienle

Phase-Field Modeling of Multi-Field Problems with Applications to Hydraulic-Elastic-Plastic Fracturing

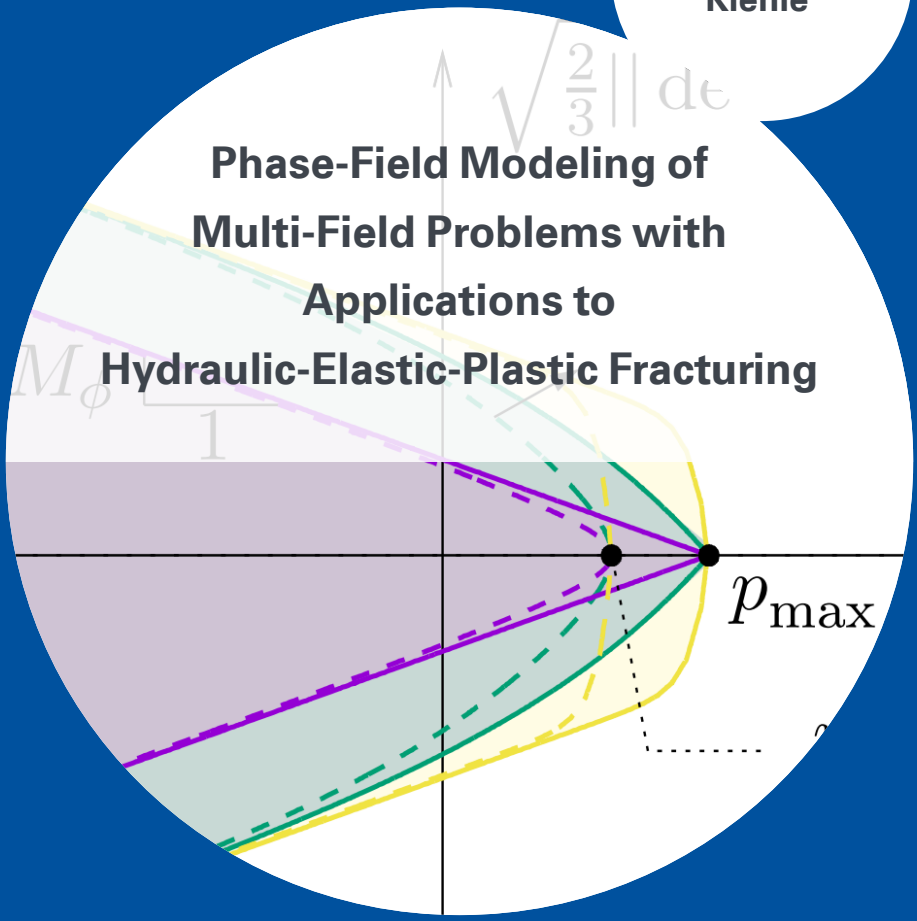

11

Publication series of the
Institute of Applied Mechanics (IAM)

Phase-Field Modeling of Multi-Field Problems with Applications to Hydraulic-Elastic-Plastic Fracturing

Von der Fakultät Bau- und Umweltingenieurwissenschaften der Universität Stuttgart
und dem Stuttgart Center for Simulation Science
zur Erlangung der Würde eines Doktor-Ingenieurs (Dr.-Ing.)
genehmigte Abhandlung

von

Daniel Kienle

aus Heidenheim an der Brenz

Hauptbericht:	Prof. Dr.-Ing. Marc-André Keip
1. Mitbericht:	Prof. Dr. rer. nat. Oliver Sander
2. Mitbericht:	Prof. Dr.-Ing. Laura De Lorenzis

Tag der mündlichen Prüfung: 29.08.2022

Institut für Mechanik (Bauwesen) der Universität Stuttgart
2022

Publication series of the Institute of Applied Mechanics (IAM), Volume 11
Institute of Applied Mechanics
University of Stuttgart, Germany, 2022

Organisation und Verwaltung:

Institut für Mechanik (Bauwesen)
Lehrstuhl fur Materialtheorie
Universität Stuttgart
Pfaffenwaldring 7
70569 Stuttgart
Tel.: +49 (0)711 685-66378
Fax: +49 (0)711 685-66347

ISBN 978-3-937399-59-1 (D 93 Stuttgart)

für Annika, Leonor und Ava

Danksagung

Die wissenschaftliche Arbeit an meiner Promotion habe ich im Dezember 2015 am Institut für Mechanik bei Prof. Dr.-Ing. Christian Miehe begonnen. Seine fachliche Begeisterung sowie Kompetenzen habe mich dazu bewogen, diesen Schritt zu gehen. Dafür möchte ich ihm herzlich danken.

Während meiner Zeit und Arbeit am Institut für Mechanik, gab es regen Austausch mit meinen Kollegen, fachlicher sowie auch privater Natur. Für diese schöne und interessante Zeit möchte ich allen Beteiligten danken. Hervorzuheben hierbei ist Steffen Mauthe, der mich schon bei der Bachelor- und Masterarbeit unterstützt hat. Des Weiteren möchte ich mich bei Stephan Teichtmeister und Matthias Rambausek für die tollen fachlichen und linux-bezogen Diskussionen bedanken. Mit meinem Studien- sowie Bürokollegen Felix Göküzüm habe ich die Zeit im Studium sowie am Institut sehr genossen, dafür danke ich ihm. Das angenehm Büro- und Arbeitsumfeld wurde auch durch die Kollegen Aref Nathegi, Elten Poluhkov, Fadi Aldakheel, Daniel Vallicotti, Lukas Böger, Omkar Nadgir, Ashish Sridhar, David Krach, Matthias Ruf, Alixa Sonntag geprägt. Dies möchte ich nicht missen. Für das Gelingen der Arbeit sind außerdem mitverantwortlich Samuel Burbulla, Alexander Müller, Prof. Dr. rer. nat. Oliver Sander und Jun.-Prof. Dr. rer. nat. Carsten Gräser. Für den Austausch und Input danke ich ihnen sehr.

Weiterer Dank gilt der finanziellen Unterstützung durch den SFB1313 sowie dem BMBF-Projekt Paraphase. In beiden Forschungsprojekten gab es natürlich auch regen privaten und fachlichen Austausch, was ich sehr genossen habe. Für die tolle Unterstützung, v.a. organisationaler Natur, möchte ich mich bei den Sekretärinnen Nadine Steinecke und Leonie Fischer bedanken. Nicht zu vergessen ist natürlich Prof. Dr.-Ing. Marc-André Keip, welcher den Lehrstuhl durch eine schwierige Zeit geführt hat und dabei stets unterstützend zur Seite stand. Vielen Dank an dieser Stelle.

Besonderen Dank möchte ich abschließend meiner Familie widmen. Meinen Eltern und meiner Schwester, die mich immer in meinen Entscheidungen und meinem Weg unterstützt und bestärkt haben. Der allerhöchste Dank gilt meiner Frau Annika, die mir in allen Lebenslagen und Entscheidungen eine Hilfe ist und schon lange war. Sie hat mich mental bei der Erstellung der Arbeit am meisten unterstützt.

Daniel Kienle

Table of Contents

Abstract

Over the last decades the initiation and growth of fracture in materials was subject of intensive research in the field of continuum mechanics. Thereby the focus was to understand the ongoing processes and predict the initiation as well as the growth of fracture. To do so mathematical formulations in form of partial differential equations have been proposed. The research started with the investigation of fracture in linear elastic materials. Here the material behaviour before the fracture initiation is well known and does not need any special treatment when it comes to modeling. One of the reasons for the difficulty in modeling of fracture stems from the non–smooth nature of the cracked areas, since the mathematical description of a continuum is based on smooth functions. In literature several techniques are applied to overcome this issue, such as extended finite element method (XFEM), discrete fracture model or phase-field approach.

The know-how gained from the modeling of fracture in elastic materials was soon applied to multi-field problems such as in elastic-plastic, electro-mechanical, magneto-mechanical, chemo-mechanical or hydro-mechanical solids. In these materials a coupling between the deformation and the additionally introduced physical aspect takes place. This causes the initiation and propagation of fracture. The multi-field problems demand an efficient numerical analysis due to the increase of unknowns which have to be determined.

The overall goal of the described research is the reduction or replacement of physical experiments in the production or development process of new parts, materials or techniques. For example modeling of chemo-electro-mechanical fracturing might be used to make electric cars more crash resistant and even cheaper. Another example could be the application of a hydro-mechanical fracture model in the development of hydraulic fracturing techniques. Thereby it could help to weigh the risks and the potential of this new method.

In order to propose and design new model formulations which incorporate the desired phenomena the basic concepts of continuum mechanics and thermodynamics are used as a methodical basis. These concepts incorporate the mathematical description of motion and deformation of a body, as well as the definition of mechanical stress and thermal flux and the derivation of physical balance laws. Although this general framework is sketched in this work for pure thermo-mechanical two-component systems it can be extended towards additional physical effects in a straightforward manner. The behaviour of a specific material type is then specified by constitutive functions which are constructed in such a way that they obey certain modeling principles. In a second step the designed mathematical description of the problem can be transferred into a variational formulation which then can be used for the derivation of a numerical treatment. Thereby the geometry of the desired domain together with the fields of the unknowns (displacement, etc.) are discretized by the means of the finite-element method. This finally yields to a range of systems of linear equations which then can be solved by an appropriate solution scheme.

In the presented work the above mentioned process of model conception and numerical treatment is used for ductile fracture in porous metals, fracturing in frictional ductile materials and frictional ductile materials at hydraulic fracture. The obtained research results are given in terms of three attached scientific articles. In the first article the phase-field modeling of fracture in isotropic porous solids is formulated in a variational framework. The porous solid can thereby undergo large elastic-plastic deformations. The

crack is described by the phase-field approach to fracture which regularizes sharp crack surfaces in a pure continuum setting. It originates both from *gradient damage modeling* and fracture mechanics. The plastic deformations are characterized by a model for porous plasticity which incorporates the evolution of the void fraction by means of a simple growth law. It is linked to a *gradient plasticity formulation*. The fracture phase field is driven by the local elastic-plastic work density on which the failure criterion is based on.

With this formulation it is possible to model classical ductile failure problems such as *cup-cone failure surfaces*. Therefor two material parameters are sufficient to describe the failure behaviour. These parameters are the *critical work density* and the *shape parameter*. While the first one specifies the onset of damage the second one controls the growth of the postcritical damage until the final rupture. In order to model damage zones to be inside of plastic zones or vice versa, two length scales are introduced. One controls the regularization of the plastic response and the other the regularization of the damage zone.

The second article presents a model for ductile fracture in frictional materials. It is based on the already mentioned phase-field approach to fracture. Combining a *non-associative* Drucker-Prager-type elastic-plastic constitutive formulation with the evolution equation for the crack phase-field yields a failure criterion in terms of an elastic-plastic energy density. Due to the non-associative formulation of the Drucker-Prager-type yield function for frictional materials, the model is not formulated within the variational framework. However it still follows similar concepts. The model accounts for large elastic-plastic deformations of the material. The hardening behaviour of the frictional material such as soil is characterized by an isotropic hardening mechanism. It is capable to capture both *friction* and *cohesion hardening*. A *modified* enhanced element formulation is used for the numerical treatment. Hereby it guarantees a locking- and hourglass-free response.

In the last scientific article a model for hydraulically induced fracturing of elastic-plastic solids is proposed. It is formulated within a variational framework yielding a global minimization structure. Again the phase-field approach to fracture is deployed here. It is combined with an associative Drucker–Prager-type yield-criterion function. Thereby this yield-criterion function characterizes the plastic deformations of the full fluid-solid mixture. The elastic fluid storage and the fluid transport within the porous medium are governed by a Darcy–Biot–type material description. The flow within the fractures is characterized by an increase of the permeability in crack direction yielding a Poiseuille–type flow. Similarly to the mechanical strain the fluid storage decomposes into an elastic and plastic part. The elasto-plastic deformations are limited to the infinitesimal strain regime. Due to the global minimization structure a $H(\mathrm{div})$-conforming finite-element formulation is chosen. Locking phenomena originating from the plastic evolution are eliminated by using a enhanced-assumed-strain formulation additionally.

Zusammenfassung

In den letzten Jahrzehnten war die Entstehung und das Wachstum von Brüchen in Materialien Gegenstand intensiver Forschung in der Kontinuumsmechanik. Der Schwerpunkt lag dabei auf dem Verständnis der zugrundeliegenden Prozesse und der Vorhersage des Bruchanfangs sowie des Bruchwachstums. Zu diesem Zweck wurden mathematische Formulierungen in Form von partiellen Differentialgleichungen entwickelt. Es wurden zunächst Brüche in linear elastischen Materialien untersucht. Bei diesen Materialien ist das Materialverhalten vor der Bruchinitiierung bekannt und bedarf keiner besonderen Behandlung bei der Modellierung. Einer der Gründe für die Schwierigkeiten bei der Modellierung des Bruchs liegt in der nicht glatten Beschaffenheit der gerissenen Bereiche, da die mathematische Beschreibung eines Kontinuums auf glatten Funktionen beruht. In der Literatur werden verschiedene Techniken angewandt, um dieses Problem zu lösen, wie z.B. die erweiterte Finite-Elemente-Methode (XFEM), das diskrete Bruchmodell oder der Phasenfeldansatz.

Das aus der Modellierung des Bruchs in elastischen Materialien gewonnene Know-how wurde bald auf Mehrfeldprobleme wie z.B. in elastisch-plastischen, elektro-mechanischen, magneto-mechanischen, chemo-mechanischen oder hydro-mechanischen Festkörpern angewandt. In diesen Materialien findet eine Kopplung zwischen der Verformung und dem zusätzlich eingebrachten physikalischen Aspekt statt. Dies bewirkt die Initiierung und Ausbreitung des Bruchs. Die Mehrfeldprobleme erfordern aufgrund der Zunahme der zu bestimmenden Unbekannten eine effiziente numerische Analyse.

Das Ziel der beschriebenen Forschung ist die Reduzierung oder der Ersatz von physikalischen Experimenten im Produktions- oder Entwicklungsprozess von neuen Komponenten, Materialien oder Techniken. Beispielsweise könnte die Modellierung von chemo-elektro-mechanischen Rissen genutzt werden, um Elektroautos unfallsicherer und sogar günstiger zu machen. Ein weiteres Beispiel könnte die Anwendung eines hydro-mechanischen Bruchmodells bei der Entwicklung hydraulischer Bruchtechniken (Hydraulic Fracturing) sein. Dabei könnte das hydro-mechanischen Bruchmodell helfen, die Risiken und das Potenzial dieser neuen hydraulischen Bruchtechniken abzuwägen.

Um neue Modellformulierungen zu entwerfen, welche die gewünschten Phänomene einbeziehen, werden die Grundkonzepte der Kontinuumsmechanik und Thermodynamik als methodische Grundlage verwendet. Diese Konzepte beinhalten die mathematische Beschreibung von Bewegung und Verformung eines Körpers sowie die Definition von mechanischer Spannung und Wärmefluss und die Herleitung von physikalischen Gesetzen für das mechanische Gleichgewicht. Obwohl dieser allgemeine Rahmen in dieser Arbeit für rein thermo-mechanische Zweikomponentensysteme skizziert wird, kann er auf einfache Weise auf zusätzliche physikalische Effekte erweitert werden. Das Verhalten eines bestimmten Materialtyps wird dann durch konstitutive Funktionen spezifiziert, die so konstruiert sind, dass sie bestimmten Modellierungsprinzipien gehorchen. In einem zweiten Schritt kann die entworfene mathematische Beschreibung des Problems in eine Variationsformulierung überführt werden, die dann zur Ableitung einer numerischen Implementierung verwendet werden kann. Dabei wird die Geometrie der gewünschten Probe zusammen mit den Feldern der Unbekannten (Verschiebung, etc.) mit Hilfe der Finite-Elemente-Methode diskretisiert. Daraus ergibt sich schließlich eine Reihe von linearen Gleichungssystemen, die dann durch ein geeignetes numerisches Lösungsverfahren gelöst werden können.

In der vorliegenden Arbeit wird der oben erwähnte Prozess der Modellkonzeption und numerischen Implementierung für duktilen Bruch in porösen Metallen, Duktilbruch in granularen Materialien und granulare Materialien mit hydraulischem Duktilbruch verwendet. Die erzielten Forschungsergebnisse werden in Form von drei beigefügten wissenschaftlichen Artikeln dargestellt. Im ersten Artikel wird die Phasenfeldmodellierung des Bruchs in isotropen porösen Festkörpern im variationellen Kontext formuliert. Der poröse Festkörper kann dabei große elastisch-plastische Verformungen erfahren. Der Riss wird durch den Phasenfeldansatz für Bruch beschrieben, wobei scharfe Rissflächen für eine Kontiuumsdarstellung regularisiert werden. Die Phasenfeldformulierung hat ihre Wurzeln sowohl bei der *Gradientenschädigungsmodellierung* als auch in der *Bruchmechanik*. Die plastischen Verformungen werden durch ein Modell für poröse Plastizität charakterisiert, das die Entwicklung des Hohlraumanteils mittels eines einfachen Wachstumsgesetzes einbezieht. Es ist mit einer *Gradientenplastizitätsformulierung* verknüpft. Das Bruchphasenfeld wird durch die lokale elastisch-plastische Arbeitsdichte getrieben, auf welcher das Versagenskriterium beruht.

Mit dieser Formulierung ist es möglich, klassische duktile Versagensprobleme zu modellieren, wie z.B. sogennate *Cup-Cone*-Brüche. Hierfür werde zwei Materialparameter eingeführt, welche das Versagensverhalten beschreiben. Diese Parameter sind die *kritische Arbeitsdichte* und der *Formparameter*. Während der erste den Schädigungsbeginn spezifiziert, steuert der zweite das Wachstum der postkritischen Schädigung bis zum endgültigen Bruch. Um Schadenszonen so zu modellieren, dass sie innerhalb von plastischen Zonen liegen und umgekehrt, werden zwei Längenskalen eingeführt. Eine steuert die Regularisierung der plastischen Verformung und die andere die Regularisierung der Schädigungszone.

Der zweite Artikel stellt ein Modell für duktilen Bruch in granularen Materialien vor. Es basiert auf dem bereits erwähnten Phasenfeldansatz für den Bruch. Die Kombination einer *nicht-assoziativen* elastisch-plastischen konstitutiven Formulierung basierend auf dem Drucker-Prager-Modell mit der Evolutionsgleichung für das Riss-Phasenfeld ergibt ein Versagenskriterium in Form einer elastisch-plastischen Energiedichte. Aufgrund der nicht-assoziativen Formulierung der Fließfunktion vom Typ Drucker-Prager für granulare Materialien wird das Modell nicht im variationellen Rahmen formuliert. Es folgt jedoch ähnlichen Konzepten. Das Modell berücksichtigt große elastisch-plastische Verformungen des Materials. Das Verfestigungsverhalten des granularen Materials, wie z.B. Boden, ist durch einen isotropen Verfestigungsmechanismus gekennzeichnet. Er ist in der Lage, sowohl *Reibungs-* als auch *Kohäsionsverfestigung* zu erfassen. Für die numerische Behandlung wird eine *modifizierte* verbesserte Elementformulierung (enhanced element) verwendet. Dies garantiert ein „locking“- und „hourglass“-freies Verhalten.

Im letzten wissenschaftlichen Artikel wird ein Modell für die hydraulisch induzierte Rissbildung von elastisch-plastischen Festkörpern entwickelt. Es wird im variationellen Rahmen formuliert, wodurch sich eine globale Minimierungsstruktur ergibt. Auch hier wird wieder der Phasenfeldansatz für Risse eingesetzt. Er wird mit einer assoziativen Fließkriteriumsfunktion vom Typ Drucker-Prager kombiniert. Dabei charakterisiert diese Fließkriteriumsfunktion die plastischen Verformungen des vollständigen Fluid-Feststoff-Gemisches. Die elastische Flüssigkeitsspeicherung und der Flüssigkeitstransport innerhalb des porösen Mediums werden durch eine Darcy–Biot-artige Materialbeschreibung bestimmt. Die Strömung innerhalb der Risse ist durch eine Erhöhung der Permeabilität in Rissrichtung gekennzeichnet, wodurch eine Poiseuille-artige Strömung entsteht.

Ähnlich wie bei der mechanischen Verzerrung zerfällt die Flüssigkeitsspeicherung in einen elastischen und plastischen Teil. Die elasto-plastischen Verformungen sind auf das infinitesimale Dehnungsregime begrenzt. Aufgrund der globalen Minimierungsstruktur wird eine $H(\mathrm{div})$-konforme Finite-Elemente-Formulierung gewählt. „Locking“-phänomene, die von der plastischen Evolution herrühren, werden durch die zusätzliche Verwendung einer „enhanced-assumed-strain“-Formulierung eliminiert.

Chapter 1

Introduction

The main objective of computational mechanics is to reduce physical experiments in the production and development process of new parts, materials and techniques. The basic idea is to apply the principles of continuum mechanics and thermodynamics to describe physical phenomena of interest. The mathematical description developed then enables numerical implementations. Knowledge of mechanics, applied mathematics, and computer science is required to achieve a robust implementation of the desired model that provides physically sound simulation results.

This reduction in physical experiments results from the desire to save time and money in the development process. In order to validate the models underlying the numerical simulation, benchmark tests are performed on the basis of the experimentally obtained data. But there is another reason for the growing interest in simulations. This interest in simulations is fueled by today's dramatic increase in computing power, which enables very fast and efficient simulations. As a result, interest in simulations has long ceased to be just a part of academic research. This is also reflected in the visions of Industry 4.0 and digital twins, which require robust and physically sound simulation models.

Examples of these models, which are part of intensive research, are multi-field problems characterized by elastic-plastic deformation, fracture mechanics and poro-hydro-elasticity. Models describing such applications can be used for the simulation of, for example, tension tests, deformations appearing within crash tests or deep drawing. Another usage can be found in the simulation of the initiation and growth of fracture patterns. A real world example for a model of poro-hydro-plasticity can be found in footsteps in the sand. An illustration of the mentioned examples is given in Figure 1.1.

From a technical point of view, the models in the framework of computational mechanics are derived from physical equilibrium laws that yield partial differential equations. This mathematical description of the problem is solved by a suitable numerical solution procedure. Here, a distinction can be made between numerical solution methods, finite

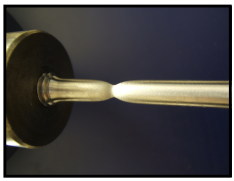
[1]

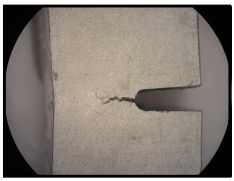
[2]


[3]

Figure 1.1: Visualization of real world examples for models in the field of continuum mechanics. On the left a tension test of a metal rod is shown. In the middle an example of fracture growth is depicted. The right most picture shows footsteps in sand as a real world example of poro-hydro-plasticity.

element solvers (in context of the finite element method) or finite element design.

This work is embedded in the field of continuum mechanics. Its central theme is the modeling of fracture initiation and growth in different types of materials such as elastic-plastic material and elastic-plastic porous media. Fracture itself is described based on a phase field approach. This is one of the modeling techniques used in fracture mechanics. It has gained great popularity in the last decade due to its robustness and the possibility of extending it to other physical phenomena, e.g. elastic-plastic material or hydraulic coupling. A general overview of the underlying theory of damage and fracture mechanics can be found in Section 1.1.1.

Furthermore the main focus of this work is the extension of phase-field fracture towards multiphysics problems. Thereby following multiphysics problems are considered: i) fracture driven by elastic-plastic deformations and ii) hydraulically induced fracture in porous-elastic-plastic materials.

An overview about the underlying theory of these problems is given in Section 1.1.2 and Section 1.1.3. In the next section the research results presented in this work are embedded into the state of the art.

1.1. Motivation and State of the Art

The occurrence and growth of fractures happens in everyday life. Often people don't take much notice of it, but in some situations it really is a matter of life and death (e.g. in the failure of large structures, buildings, ships, or airplanes). At first glance, the fracture process does not seem particularly complicated - a object simply breaks into two or more pieces. However, if one describes the fracture initiation and even the fracture growth mathematically, things get more complicated. In the context of the finite element method, the complication arises from the desire to describe a discontinuous process with a continuous formulation.

[1] g2mtlabs.com/metallurgical-consulting/mechanical-testing-mechanical-properties-assessment
[2] metallurgyfordummies.com/fracture-mechanics-concepts.html
[3] comsol.com/blogs/poroelasticity-in-sand

Modeling of fracture in continuum mechanics is driven by the aim to know under which loading a mechanical part or construction will fail. The field of fracture mechanics was established by Griffith 1920. This work was published during World War I and the goal was to understand the failure of metallic machine parts.[4] In the beginning the fracturing of brittle materials was investigated. Due to various modifications and extensions the field of fracture mechanics has grown considering the size of the scientific community working on that field.

In the last decades the modeling of fracture was applied on coupled problems such as elastic-plastic deformations yielding a ductile fracture propagation or the extension towards hydraulically induced fractures. But not only the constitutive material modeling of fracture was further improved but also the numerical treatment of the differential equations describing the deformation and fracturing process have been investigated.

There are various fracture modeling techniques and formulations, such as stress intensity factor, J-integral, extended finite element method, discrete fracture model and phase-field approach. As already mentioned before, this work considers the modeling of fracture based on a phase-field approach with the focus on the extension towards multiphysics problems. In what follows an overview about fracture mechanics, elastic-plastic deformations coupled with fracture mechanics and hydraulically induced fractures is given.

1.1.1. Damage and Fracture Mechanics

At the beginning of the 20th century people experienced failure of large structures such as ships or aircrafts. These failures often arose by cracks in the metallic structure. This observation fueled the interest in the research of damage and fracture mechanics. Figure 1.2 shows three different historical disasters initiated by cracks.

In the context of continuum mechanics the modeling of failure can be achieved by different approaches. Two approaches are shortly discussed here. While in damage mechanics a strain softening behavior arising from damage processes on the micro level of the material is considered, the geometric discontinuity on the macro level originating from the fracture development is taken into account in fracture mechanics.

[5]

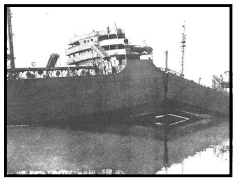

[6]

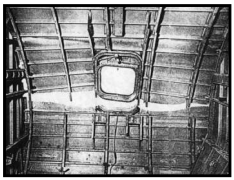

[7]

Figure 1.2: Three different historical disasters initiated by cracks. On the left the Boston Molasses Disaster from 1919 where a large tank burst is shown. In the middle a picture of the hull fracture of the SS Schenectady from 1943 is given. On the right a crack in the hull of a de Havilland Comet aircraft is shown. This failure led to several plane crashes in the 1950s.

[4] doi.org/10.1093/oso/9780198851875.003.0012

For fundamental works on damage mechanics see for example Chaboche 1981, 1988, Lemaitre 1984, Kachanov 1986, Belytschko et al. 1988, and Simo and Ju 1987a,b. Hereby a variable defined as the fraction of the broken and the total surface in the body is used to describe the damage process. This yields a local theory with problems with respect to the numerical implementation. By additionally using also the gradient of the damage variable one arrives at the gradient damage models as for example done by Peerlings et al. 1996, Frémond and Nedjar 1996 and Comi 1999. The additionally introduced gradient of the damage variable comes along with a *damage length scale*. This supplementary material parameter controls the size of the localization zone of the damage area and can be obtained from macroscopic experiments.

On the other hand fracture mechanics considers the macroscopic crack with its geometrical discontinuity. The field of fracture mechanics was initiated by Griffith 1920, 1924. It was extended towards ductile materials based on the introduction of a plastic dissipation due to crack growth by Irwin 1957, 1958. Furthermore the latter contributions introduced the *stress intensity factor*. A variational formulation of brittle fracture was introduced by Francfort and Marigo 1998. This formulation is based on Griffith's energetic approach and introduces the crack surface itself as unknown. Hereby the solution of the problem can be found based on operations adapted from image segmentation by Mumford and Shah 1989.

The above-mentioned variational formulation was further made feasible in terms of the numerical treatment by Bourdin et al. 2008, where a regularization of the crack surface was introduced. This is based on a so-called phase-field variable which also can be considered as a damage variable. Similar considerations of the regularization can be also found in Ambrosio and Tortorelli 1990. An approach of a viscous regularization of the Ginzburg-Landau evolution equation leads to a similar formulation. It can be found in Hakim and Karma 2009 and Kuhn and Müller 2010. Furthermore, the works Miehe et al. 2010 and Pham et al. 2011 use gradient damage models to regularize the description of Griffith-type brittle fracture.

Such models that use a phase-field variable to regularize the sharp crack discontinuity are considered as phase-field approach to fracture. The underlying mathematical structure of these formulations is similar to the structure of gradient damage models. However the starting point of the derivation of the phase-field approach to fracture is on the macroscopic level. Therefore its physical interpretation differs from the gradient damage models, see de Borst and Verhoosel 2016.

1.1.2. Elastic-Plastic Deformations and Ductile Fracture

The field of plasticity, or elastic-plastic deformations of metals, goes back to Tresca 1864 who conducted experiments on metals and introduced the yield criterion named after him.[8] The main idea of plastic or non-recoverable deformations is to limit the mechanical

[5] en.wikipedia.org/wiki/Great_Molasses_Flood

[6] en.wikipedia.org/wiki/SS_Schenectady

[7] extremetech.com/extreme/129764-tech-wrecks-lessons-from-some-of-the-biggest-hardware-screw-ups/3

[8] doi.org/10.1007/978-3-662-53605-6_281-1

stress in the body by an elastic domain. This domain is characterized by a yield criterion function. Various yield criteria have been introduced. A smooth version of Tresca's yield criterion was introduced by von Mises 1913. The Tresca and von-Mises yield criterion are the classical yield criteria used in metal plasticity. The plastic deformations of frictional materials, e.g. soil, can be described by the yield criterion of Coulomb 1776, where the model introduced by Drucker and Prager 1952 is a smooth approximation of it. A general framework combing the many fundamental considerations of the theory of plasticity can be found in Hill 1950.

More advanced plasticity models for metals incorporate micro-mechanical mechanisms based on micro voids. They are derived by analytical homogenization techniques yielding a macroscopic constitutive formulation, see for example Rice and Tracey 1969 and Gurson 1975. A further enhancement of these models can be found in Needleman and Tvergaard 1984 and Rousselier 1987. Other models for porous plasticity in metals including the effect of micro voids can be found for example in Suquet 1992, Ponte Castañeda and Zaidman 1994 and Leblond et al. 1994.

Another group of formulations for plastic deformations is related to frictional or granular materials. Some examples of these types of material are sand, soil, coal, grains, cereal, pharmaceutical powders, etc. Here the mechanical properties of the conglomeration are governed by the friction between the particles which is strongly effected by the moisture. Models for plastic deformations of such frictional materials can be found in Drucker and Prager 1952, Zienkiewicz et al. 1975, Vermeer and de Borst 1984, de Boer 1988, Simo and Meschke 1993 and Ehlers 1995. The numerical robustness of formulations based on the model of Drucker and Prager 1952 is not always guaranteed. This arises from a singularity of the formulation under tensile stress conditions. One way to overcome this issue is to smooth out this singularity based on a constant perturbation-type parameter, see Abbo and Sloan 1995 or Lambrecht and Miehe 1999, 2001.

Combining the *plastic deformations* and the process of *damage* or fracture yields to the phenomenon of *ductile fracture*. Hereby the macroscopic fracturing process is driven by extensive plastic deformations. The elastic-plastic deformation mechanism yields to a growth of micro-cracks, which ends up as macro-cracks. These finally degrade the global stiffness of the structure. The fracturing process goes on until the critical state where rupture occurs.

Pure phenomenological models for ductile fracture based on a micro-mechanical approach can be found for example in Johnson and Cook 1985, Lemaitre 1985, Lemaitre and Chaboche 1990, Besson 2010 and Li et al. 2011. The latter works combine models for local plasticity and local damage. Regarding the numerical implementation using the finite element method, this yields a strongly mesh dependent formulation both in the plastic response in case of softening as well as in the damage response.

A first step towards a mesh independent formulation is the coupling of *local* plasticity with gradient-damage models, see for example de Borst et al. 1999, Nedjar 2001 and Reusch et al. 2003. Other works combine gradient-damage-type *phase-field models* of fracture with a local plasticity model, such as Duda et al. 2015, who proposed a model where the initiation and propagation of fracture is formulated in the sense of brittle fracture in elastic-plastic materials. In addition Alessi et al. 2015 and Miehe et al. 2015a use the sum of the elastic and plastic energy in the fracture driving force and therefore account for a transition from brittle to ductile fracture. Furthermore the latter two models

are based on variational principles. By incorporating a characteristic degradation function in terms of the amount of plastic deformation ductile fracture is modeled by Ambati et al. 2015. An experimental verification can found in Ambati et al. 2016.

In order to have mesh independent formulation in both the plastic as well as in the damage response, a non-local concept has to be used also for the plasticity model. The non-local concept can be found in a gradient-plasticity formulation, see for example Aslan et al. 2011, Dimitrijevic and Hackl 2011, Saanouni and Hamed 2013 and Miehe et al. 2015a. Despite the mesh independence the introduction of a length scale for both the plastic as well as the damage zone has another advantage. It can be ensured that the fracture zone is inside the plastic zone yielding a physically more sound overall behavior.

[9]

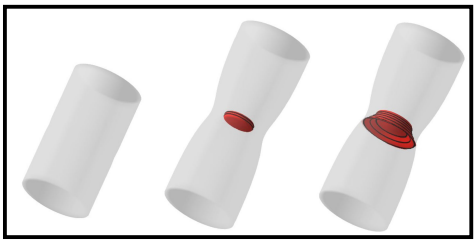

[10]

Figure 1.3: The so-called cup-cone failure occurs in ductile metals under uniaxial loading. The failure mode is named after the shape of the fracture surface. It originates from growth of micro voids in the metal. On the left a cup-cone failure from a tension test is shown. The right shows the numerical simulation results of such a tension test, see Chapter 4 or Miehe et al. 2016. Here the red color indicates the fracture surface.

Within the above-mentioned context two publications are attached in this work. They are directly related to the modeling of ductile fracture based on the phase-field approach. In Chapter 4 a scientific article about *porous plasticity at fracture* is given. It considers:

- A plasticity formulation in the context of the finite strain theory. Here a multiplicative decomposition of the deformation into an elastic and a plastic part is used.
- A micromorphic regularization of gradient plasticity using an additional material parameter as an internal length scale. It controls the size of the plastic zone.
- A Gurson-type yield function for porous plasticity in metals considering the growth of micro voids. The growth law is formulated in terms of the total volume change.
- A global variational minimization principle combined with a general return mapping scheme for plasticity. The latter is formulated in the spectral space.

With this formulation at hand it is possible to simulate the formation of a so-called cup-cone failure. This failure is characterized by the shape of the fracture surface. It

[9] usna.edu/NAOE/_files/documents/Courses/EN380/Course_Notes/Ch11_Fracture.pdf
[10] doi.org/10.1016/j.cma.2016.09.028

typically appears during uniaxial loading of metal rods. An experimental as well as a numerical result of such a test can be found in Figure 1.3. The detailed discussion of the underlying model and the simulation is given in Chapter 4.

The publication given in Chapter 5 combines a plasticity formulation for frictional materials with the phase-field approach to fracture. Thereby it considers *frictional ductile materials at fracture* with the focus on:

- A plasticity formulation in the context of the finite strain theory. Here a multiplicative decomposition of the deformation into an elastic and a plastic part is used.
- A *non-associative* Drucker–Prager-type yield criterion describing frictional materials with a regularization to overcome the singularity under tensile stress conditions.
- An incorporation of an isotropic hardening mechanism. This mechanism can distinguish between *cohesive* dominated hardening and *frictional* dominated hardening.
- A suitable and robust finite element formulation. The formulation is proven to guarantee a locking- as well as an hourglass-free response.

Scenarios such as compression of a clay column leading to a shear band formation can be simulated by such a model. The experimental as well as the numerical result of such a scenario is shown in Figure 1.4. The underlying model, the numerical simulation and other scenarios are discussed in Chapter 5.

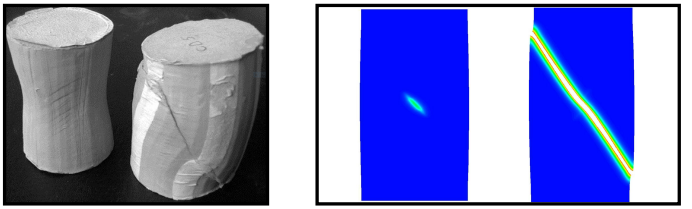

[11] [12]

Figure 1.4: Not only metals undergo elastic-plastic deformations, but also the deformation of frictional or granular materials such as soil or clay can be considered to be elastic-plastic. The left picture shows a compression test of a clay column. On the right the simulation results corresponding to such a test can be seen. The model for the simulation is discussed in Chapter 5 or in Kienle et al. 2019. Here the colors indicate the level of the fracture phase-field variable. Areas where the fracture occurs are colored in white.

1.1.3. Fracture with Hydro–Mechanical Coupling

In order to model hydraulic fracturing in elastic or plastic media it is necessary to describe the mechanical deformation of the underlying porous medium. Furthermore the

[11] doi.org/10.1016/S0020-7683(02)00177-4
[12] doi.org/10.1016/j.ijsolstr.2019.02.006

interaction between the fluid and the solid matrix has to be characterized. There are two main approaches to do so. On the one hand there is the so-called *Theory of Porous Media* (TPM) with individual balance laws for each phase within the porous medium, see for example Bluhm and de Boer 1997, de Boer 2000 and Ehlers 2002. On the other hand there is the framework considered as *Biot's theory of consolidation*, see Terzaghi 1925, Biot 1941, Bear 1972 and Detournay and Cheng 1993. Within the latter framework combined balance laws characterizing the fluid-solid mixture of the porous medium are considered.

Next to the mechanical deformations the fluid flow has to be described. The fluid flow within a porous medium can be modeled by the law of Darcy 1856. It was derived based on experimental observations but can also be obtained via homogenization of the Navier–Stokes equations, see Whitaker 1986. Darcy's law gives the relation of the fluid flux and the pressure differences in terms of the permeability of the porous medium.

The modeling of fracturing in porous media can be achieved by the coupling of the mechanical description of the porous medium and the phase-field approach to fracture. In Ehlers and Luo 2017, Heider and Markert 2017 and Ehlers and Luo 2018 the phase-field approach to fracture is embedded in the TPM. On the other hand in Mikelić et al. 2015a, Mikelić et al. 2015b, Mikelić et al. 2015c, Miehe et al. 2015b, Wilson and Landis 2016, Wu and Lorenzis 2016, Mauthe and Miehe 2017 and Cajuhi et al. 2018, Biot's theory of consolidation is combined with the phase-field approach to fracture. A comparison of the phase-field models for hydraulic fracturing with analytical solutions obtained by Sneddon and Lowengrub 1969 can be found in Bourdin et al. 2012, Wilson and Landis 2016, Mauthe 2017, Santillán et al. 2017 and Chukwudozie et al. 2019 .

Besides the description of hydraulic fracturing based on the phase-field approach to fracture there exists a number of alternative formulations. In Adachi et al. 2007 a review of so-called planar hydraulic fracturing models is given. These reviewed models are rooted in linear elastic fracture mechanics. A treatment based on the formulation of the boundary element method is considered in Castonguay et al. 2013. Furthermore, the model in Damjanac et al. 2010 is based on the discrete element method. Additionally, the extended or generalized finite element method is another established method for the description of cracks. For applications to porous media, see Dahi-Taleghani and Olson 2011, Gupta and Duarte 2014, Gordeliy and Peirce 2013a,b and Shauer and Duarte 2019.

Special care has to be taken for the fluid flow in porous media at fracture, since the flow in the fractured areas is higher than in the surrounding porous medium. This can be achieved by introducing terms in the governing equations for the fluid phase which depend on the phase-field variable. It allows then an interpolation between the flow described by Darcy's law within the porous medium and the flow characterized by the Navier–Stokes equations within fractures, see for example Ehlers and Luo 2017; Ehlers and Luo 2018. Another approach to model the flow is an interpolation of the permeability in Darcy's law between the intact porous medium and the fracture. Hereby the permeability in the fracture is obtained by averaging the fluid volume flux described by the Navier–Stokes equations over the fracture width. This procedure is often referred to as parallel plate concept or cubic law and yields a Poiseuille–type flow within the cracks. The resulting permeability inside the fracture is then a function of the fracture width, see for example Miehe et al. 2015b.

Furthermore, special treatment is related to the numerical treatment of pours media

characterized by a porous-elastic constitutive material law. A common approach is to introduce the displacement field and the fluid pressure as unknown fields. This leads to a global saddle-point problem. In a finite-element context the so called Babuška-Brezzi-Ladyzhenskaya condition (BBL or inf-sup condition) has to be fulfilled, see Babuška 1973; Brezzi 1974. In Miehe et al. 2015b a formulation in terms of the displacement field and the fluid flux as unknown fields is proposed. This yields a global minimization problem which is a priori stable and not related by the BBL condition. However a conforming finite element formulation demands a special finite element design such as $H(\mathrm{div})$-conforming Raviart-Thomas elements, see Raviart and Thomas 1977. A general overview of the numerical treatment of poro-elasticity in the finite-element context is given by Teichtmeister et al. 2019.

The above-mentioned works on fracturing in porous media are all considering a solid matrix undergoing pure elastic deformations. Johnson and Cleary 1991 concluded from experimental observations that a formulation only accounting for elastic deformations is not sufficient to describe the associated processes. In order to overcome this insufficiency a coupled model of elastic and plastic deformations combined with the phase-field approach to fracture can be considered. Such models have been suggested by Pise et al. 2019 and Aldakheel et al. 2020, while the latter one is based on Biot's theory and the former one on TPM. However both miss an underlying variational structure. They incorporate a Drucker–Prager-type yield criterion function, see Drucker and Prager 1952, formulated in terms of the effective stress acting on the solid matrix in contrast to a formulation in terms of the total stress.

Embedded in this aforementioned context the scientific article in Chapter 6 combines a description of an elastic-plastic porous medium with the phase-field approach to fracture. Thus it describes *frictional ductile materials at hydraulically induced fracture* and considers:

- A variational framework for porous-elastic-plastic solids at fracture yielding a global minimization structure with a general return mapping scheme for plasticity.
- A Darcy–Biot-type formulation describing the solid deformation and the fluid transport in the porous medium. Hereby a Poiseuille–type flow within the cracks is used.
- A decomposition of the fluid content into a contribution due to elastic as well as plastic deformations. Here the change of plastic fluid content is irreversible.
- A Drucker–Prager-type yield criterion function for the full fluid-solid mixture in terms of the fluid pressure and the total stress acting on the mixture.

The model discussed in Chapter 6 is capable of describing fracking processes in a solid matrix undergoing elastic and plastic deformations. Thereby a formulation of poro-hydro-elasticity is combined with a model for plasticity in frictional materials. A graphical visualization of these effects as well as of a fracking process can be found in Figure 1.5

[13] motherearthnews.com/nature-and-environment/environmental-policy/fracking-hydraulic-fracturing-zmgz12fmzrog

[14] irmca.org/image/23/400

[15] doi.org/10.1016/S0020-7683(02)00177-4

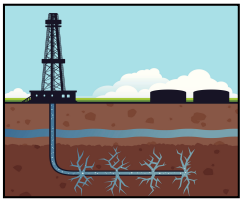

[13]

fracking process

[14]

poro-hydro-elasticity

[15]

plasticity

Figure 1.5: The model in Chapter 6 describes fracking processes by combing different descriptions of the deformation of a porous medium. The left shows a graphical visualization of such a fracking process. In the middle an illustration of poro-hydro-elasticity is given. On the right a plastic deformation in frictional material is shown.

1.2. Objectives and Overview

In Part I, the underlying methodology of this work is described briefly. The methodology is thereby thematically decomposed into two chapters. Chapter 2 discusses the basic concepts of continuum thermo-mechanics in combination with mass transport. In here the mathematical description of the motion and the deformation is introduced. It is followed by the definition of the mechanical stress, thermal flux and mass flow. In the end of Chapter 2 physical balance laws that characterize the deformation and mass flow of a multicomponent system in context of the large strain theory are postulated.

These physical balance laws are the starting point of Chapter 3 where a general modeling framework for continuum mechanics is outlined. In here the initial boundary value problem is defined leading to the conclusion that constitutive functions have to be introduced. The constitutive functions close the system of equations. Their construction underlies certain principles and they define the specific material behavior.

After the discussion of the principles, the general mathematical description of the deformation and the flow within a two-component system is transferred to a variational framework. This serves as a basis for the numerical treatment in the last part of Chapter 2. The discussion of the numerical treatment in the context of the finite element formulation closes Part I.

The introduced framework is the basis of the corresponding publications for this cumulative dissertation. The three developed publications are given in Part II. At the beginning of this part all authors, the title, the publishing journal as well as the current status of the particular article are listed. It is structured as follows:

- Chapter 4 includes a publication about porous plasticity at fracture entitled

"**Phase Field Modeling of Fracture in Porous Plasticity: A Variational Gradient-Extended Eulerian Framework**".

Miehe, C. , D. Kienle, F. Aldakheel and S. Teichtmeister (2016). In: *Computer Methods in Applied Mechanics and Engineering* 312, pp. 3–50.

- Chapter 5 gives a scientific article related to frictional ductile materials at fracture entitled

"**A Finite-Strain Phase-Field Approach to Ductile Failure of Frictional Materials**".

Kienle, D., F. Aldakheel and M.-A. Keip (2019). In: *International Journal of Solids and Structures* 172, pp. 147–162.

- Chapter 6 provides a paper on frictional ductile materials at hydraulic fracture entitled

"**A Variational Minimization Formulation for Hydraulically induced Fracturing in Elastic-Plastic Solids**".

Kienle, D. and M.-A. Keip (2021). In: *International Journal of Fracture*, pp. 1–25.

— Part I —

Continuum Mechanics and Modeling Framework

Chapter 2

Concepts of Continuum Thermo-Mechanics

The present work is embedded in the field of continuum mechanics and thermodynamics. The basic concepts of this field are presented in this chapter. The framework is motivated within the finite strain theory and follows the notation of the lectures Miehe 2005, 2006 on advanced mechanics from the Institute of Applied Mechanics at the University of Stuttgart. In what follows a brief introduction will be given.

Hereby the description of the motion of a body is introduced in Section 2.1. Based on this description further mappings for geometric quantities can be specified. These mappings describe how the quantities change under deformation and are considered as kinematic mappings. With the kinematic mappings at hand deformation tensors can be defined. After the basic mathematical description of the motion and deformation, stress measures, thermal flux and mass transport are discussed in Section 2.2. This is then the basis for the formulation of the physical balance equations in Section 2.3 and 2.4. They characterize the deformation and flux in a multicomponent system in a mechanical and thermodynamical way. For more details, see the classical textbooks of Truesdell and Noll 1965, Biot 1965a, Malvern 1969, Bear 1972, Marsden and Hughes 1983, Bear and Bachmat 1991, Holzapfel 2000, Coussy 2004 or Gurtin et al. 2010.

2.1. Motion and Kinematics

The starting point of the mechanical and thermodynamical description of the deformation of a body in a multicomponent system is the definition of the motion and the kinematic quantities. This is done in the setting of the finite strain theory. The corresponding considerations for the infinitesimal strain theory can be obtained by a linearization of the general finite strain theory.

2.1.1. Description of motion

Mathematically, the motion is described on the basis of a *material body* B as a set of material points $P \in B$ in a region $\mathcal{B}_t \subset \mathcal{R}^3$ in the Euclidean space $\mathcal{R}^3$ at the time $t \in \mathcal{R}_+$.

The configuration $\mathcal{B}_t$ of the body B is described by the mapping $\boldsymbol{\chi}_t$

$$\boldsymbol{\chi}_t(P) = \begin{cases} B & \to \mathcal{B}_t \subset \mathcal{R}^3 \\ P & \mapsto \boldsymbol{x} = \boldsymbol{\chi}_t(P), \end{cases} \tag{2.1}$$

which assigns each point $P \subset B$ to a place $\boldsymbol{x} \subset \mathcal{B}_t$ in the Euclidean space $\mathcal{R}^3$. For large strain deformations the motion of the body is described by a set of configurations which are characterized by the time, see Figure 2.1.

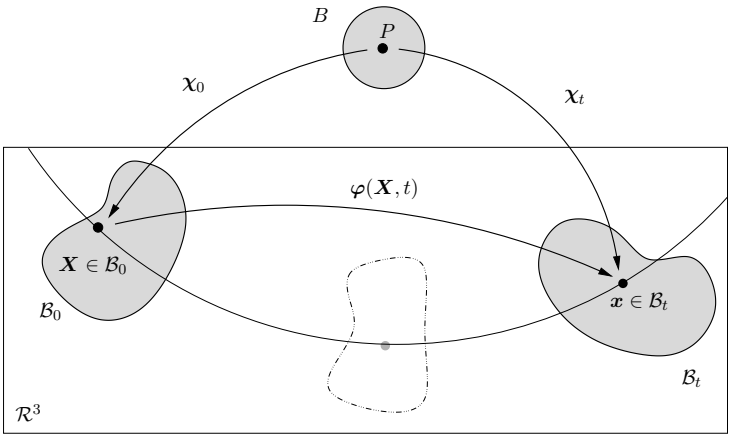

Figure 2.1: The motion of a material body B in Euclidean space $\mathcal{R}^3$ described by the mappings $\boldsymbol{\chi}_t$. The reference configuration $\mathcal{B}_0 \in \mathcal{R}^3$ and the current configuration $\mathcal{B}_t \in \mathcal{R}^3$ are considered as differentiable manifolds. The spatial (Eulerian) coordinates $\boldsymbol{x}$ are linked to the material (Lagrangian) coordinates $\boldsymbol{X}$ by the deformation map $\boldsymbol{\varphi}(\boldsymbol{X}, t)$. The interested reader is referred to Marsden and Hughes 1983.

2.1.2. Description of deformations

The non–linear deformations are described by the deformation map $\boldsymbol{\varphi}(\boldsymbol{X}, t)$. It is defined as

$$\boldsymbol{\varphi} = \begin{cases} \mathcal{B}_0 \times \mathcal{T} & \to \mathcal{R}^3 \\ (\boldsymbol{X}, t) & \mapsto \boldsymbol{x} = \boldsymbol{\varphi}(\boldsymbol{X}, t) = \boldsymbol{\chi}_t \circ \boldsymbol{\chi}_0^{-1}. \end{cases} \tag{2.2}$$

The deformation map is a mapping between the Lagrangian $\mathcal{B}_0$ and the Eulerian $\mathcal{B}_t$ configuration. The deformation map is visualized in Figure 2.1. The Lagrangian configuration is also considered as reference or material configuration while the Eulerian configuration is also considered as current or spatial configuration.

2.1.3. Velocity and acceleration

Based on the definition of deformation map $\boldsymbol{\varphi}(\boldsymbol{X}, t)$ in (2.2), the *material velocity* $\boldsymbol{V}$ is obtained as its first time derivative

$$\boldsymbol{V}(\boldsymbol{X}, t) := \frac{\mathrm{d}}{\mathrm{d}t}\boldsymbol{\varphi}(\boldsymbol{X}, t) = \frac{\partial}{\partial t}\boldsymbol{\varphi}(\boldsymbol{X}, t), \tag{2.3}$$

and the *acceleration* $\boldsymbol{A}$ is obtained as its second time derivative

$$\boldsymbol{A}(\boldsymbol{X},t) := \frac{\mathrm{d}}{\mathrm{d}t}\boldsymbol{V}(\boldsymbol{X},t) = \frac{\partial^2}{\partial t^2}\boldsymbol{\varphi}(\boldsymbol{X},t) \ . \tag{2.4}$$

Note that the material velocity and acceleration are expressed here in terms of the material coordinates $\boldsymbol{X}$. Despite this dependence, they are vector fields of the spatial configuration, hence $\boldsymbol{V} \in \mathcal{B}_t$ and $\boldsymbol{A} \in \mathcal{B}_t$. By inserting the inverse of the deformation map $\boldsymbol{\varphi}$ into (2.3) the *spatial velocity* is obtained as

$$\boldsymbol{v}(\boldsymbol{x},t) := \boldsymbol{V}(\boldsymbol{\varphi}^{-1}(\boldsymbol{x},t),t) = \boldsymbol{V} \circ \boldsymbol{\varphi}^{-1}(\boldsymbol{x}) = \frac{\partial}{\partial t}\boldsymbol{x}(t) \ . \tag{2.5}$$

The *spatial acceleration* is gained by the time-derivative and the application of the chain rule. This yields

$$\begin{aligned} \boldsymbol{a}(\boldsymbol{x},t) := \frac{\mathrm{d}}{\mathrm{d}t}\boldsymbol{v}(\boldsymbol{x},t) &= \frac{\partial}{\partial t}\boldsymbol{v}(\boldsymbol{x},t) + \frac{\partial}{\partial \boldsymbol{x}}\boldsymbol{v}(\boldsymbol{x},t) \cdot \frac{\partial}{\partial t}\boldsymbol{x}(t) \\ &= \frac{\partial}{\partial t}\boldsymbol{v}(\boldsymbol{x},t) + \nabla_{\boldsymbol{x}}\boldsymbol{v}(\boldsymbol{x},t) \cdot \boldsymbol{v}(\boldsymbol{x},t) \ . \end{aligned} \tag{2.6}$$

Here the spatial gradient operator $\nabla_{\boldsymbol{x}}(\cdot) := \partial_{\boldsymbol{x}}(\cdot)$ was introduced. The spatial acceleration is the sum of a local part and a convective part due to the time dependency of $\boldsymbol{x}$.

2.1.4. Kinematic mappings

Based on the geometric quantities given by tangent, area and volume, three different kinematic mappings can be derived. Therefore a curve that is parameterized in the Lagrangian and Eulerian space is considered.

Deformation gradient. In order to describe the local deformation at a material point in a body, the most fundamental kinematic quantity, the *deformation gradient* is introduced. It is given as the gradient of the deformation map with respect to the Lagrangian coordinate $\boldsymbol{X}$

$$\boldsymbol{F}(\boldsymbol{X},t) := \nabla\boldsymbol{\varphi}(\boldsymbol{X},t) \ . \tag{2.7}$$

To avoid interpenetration of matter, the following condition must hold

$$J := \det[\boldsymbol{F}] > 0 \ . \tag{2.8}$$

Under a geometrical view point the deformation gradient can be interpreted as a mapping for tangent vectors. Consider a curve that is parameterized in the Lagrangian and Eulerian configuration. The Lagrangian representation of this curve is given by $\boldsymbol{C}(\theta) \in \mathcal{B}_0$ and the Eulerian representation by $\boldsymbol{c}(\theta) = \boldsymbol{\varphi}(\boldsymbol{C}(\theta),t) \in \mathcal{B}_t$. The argument of that curve is the variable $\theta \in \mathcal{R}$. The material and spatial tangents to the curve are $\boldsymbol{T} = \partial_\theta \boldsymbol{C} \in T_{\boldsymbol{X}}\mathcal{B}_0$ and $\boldsymbol{t} = \partial_\theta \boldsymbol{c} \in T_{\boldsymbol{x}}\mathcal{B}_t$. Here $T_{\boldsymbol{X}}\mathcal{B}_0$ is the Lagrangian covariant space and $T_{\boldsymbol{x}}\mathcal{B}_t$ is the Eulerian covariant space. Deriving the deformation map now with respect to the variable θ yields a relation between the material and spatial tangent vectors

$$\boldsymbol{t} = \frac{\mathrm{d}\boldsymbol{c}(\theta)}{\mathrm{d}\theta} = \frac{\mathrm{d}\boldsymbol{\varphi}(\boldsymbol{C}(\theta))}{\mathrm{d}\theta} = \nabla\boldsymbol{\varphi} \cdot \frac{\mathrm{d}\boldsymbol{C}(\theta)}{\mathrm{d}\theta} = \boldsymbol{F}\boldsymbol{T} \ . \tag{2.9}$$

Here the deformation gradient can be identified as mapping of a tangent vector between the Lagrangian and Eulerian configuration. It can be written as

$$\boldsymbol{F} : \begin{cases} T_{\boldsymbol{X}}\mathcal{B}_0 \to T_{\boldsymbol{x}}\mathcal{B}_t, \\ \boldsymbol{T} \mapsto \boldsymbol{t} = \boldsymbol{F}\boldsymbol{T}. \end{cases} \tag{2.10}$$

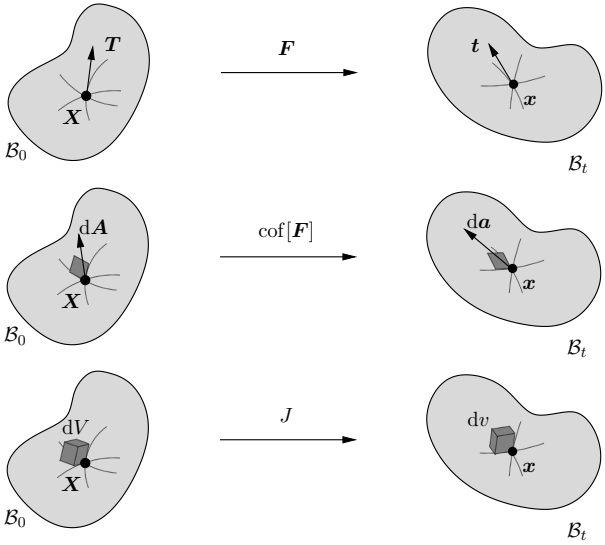

Figure 2.2: The kinematic mappings of continuum mechanics map geometric quantities from the reference $\mathcal{B}_0$ into the current configuration $\mathcal{B}_t$. The deformation gradient $\boldsymbol{F}$ is used as tangent map $\boldsymbol{t} = \boldsymbol{F}\boldsymbol{T}$. Areas are mapped by the Jacobian and the deformation gradient $\mathrm{d}\boldsymbol{a} = J\boldsymbol{F}^{-T}\mathrm{d}\boldsymbol{A} = \mathrm{cof}[\boldsymbol{F}]\mathrm{d}\boldsymbol{A}$. Volumes are mapped by the Jacobian $\mathrm{d}v = J\mathrm{d}V$.

Normal and area map. To define a normal map and area map, two curves ($\boldsymbol{C}_1$, $\boldsymbol{C}_2$ and $\boldsymbol{c}_1$, $\boldsymbol{c}_2$) are introduced in the Lagrangian and Eulerian configuration. An area element ($\mathrm{d}\boldsymbol{A}$ and $\mathrm{d}\boldsymbol{a}$) in the Lagrangian and Eulerian configuration can now be expressed in terms of the tangents onto the two introduced curves. This yields

$$\mathrm{d}\boldsymbol{a} = \boldsymbol{t}_1 \times \boldsymbol{t}_2 = \boldsymbol{F}\boldsymbol{T}_1 \times \boldsymbol{F}\boldsymbol{T}_2 = J\boldsymbol{F}^{-T}(\boldsymbol{T}_1 \times \boldsymbol{T}_2) = \mathrm{cof}[\boldsymbol{F}]\mathrm{d}\boldsymbol{A}\ , \tag{2.11}$$

where the cofactor of the deformation gradient is identified as area map. Note that the areas in here are expressed as vectors. The scalar areas are defined as $\mathrm{d}\boldsymbol{A} = \boldsymbol{N}\mathrm{d}A$ and $\mathrm{d}\boldsymbol{a} = \boldsymbol{n}\mathrm{d}a$, where the Lagrangian and Eulerian normals $\boldsymbol{N} \in T^*_{\boldsymbol{X}}\mathcal{B}_0$ and $\boldsymbol{n} \in T^*_{\boldsymbol{x}}\mathcal{B}_t$ onto the areas are considered. For mapping the normal vectors the determinant of the deformation map in (2.11) can be neglected since its only preserves the change of the deforming area. The normal map is given by:

$$\boldsymbol{F}^{-T} : \begin{cases} T^*_{\boldsymbol{X}}\mathcal{B}_0 \to T^*_{\boldsymbol{x}}\mathcal{B}_t, \\ \boldsymbol{N} \mapsto \boldsymbol{n} = \boldsymbol{F}^{-T}\boldsymbol{N}\ . \end{cases} \tag{2.12}$$

Volume map. The volume map is derived by considering three curves and three tangents in the Lagrangian and Eulerian configuration. Defining a volume element ($\mathrm{d}V$, $\mathrm{d}v$) based on these tangents yields

$$dv = \boldsymbol{t}_1 \cdot (\boldsymbol{t}_2 \times \boldsymbol{t}_3) = \boldsymbol{F}\boldsymbol{T}_1 \cdot (\boldsymbol{F}\boldsymbol{T}_2 \times \boldsymbol{F}\boldsymbol{T}_3) = J\mathrm{d}V \ . \tag{2.13}$$

Here the determinant of the deformation gradient serves as volume map and is defined by

$$J : \begin{cases} \mathcal{R}_+ \to \mathcal{R}_+, \\ \mathrm{d}V \mapsto \mathrm{d}v = \det \boldsymbol{F} \ \mathrm{d}V = J\mathrm{d}V \ , \end{cases} \tag{2.14}$$

where $\mathrm{d}V$ is a Lagrangian volume element and $\mathrm{d}v$ is its Eulerian counterpart. The above introduced kinematic mappings are illustrated in Figure 2.2.

2.1.5. Deformation and metric tensors

In order to measure the deformation of a body a quantity without any physical units is used. The starting point for the derivation of such a quantity in the finite strain theory is the length of a vector $\boldsymbol{T}$ in the Lagrangian covariant space and its Eulerian counterpart $\boldsymbol{t} = \boldsymbol{F}\boldsymbol{T}$. The length is considered as the distance of two points.

To determine the length, metric tensors have to be defined. The metric tensors $\boldsymbol{G}$ and $\boldsymbol{g}$ represent the mapping from the covariant to contravariant space in the Lagrangian and Eulerian configuration respectively. They are defined as

$$\boldsymbol{G} : \begin{cases} T_{\boldsymbol{X}}\mathcal{B}_0 \to T^*_{\boldsymbol{X}}\mathcal{B}_0, \\ \boldsymbol{T} \mapsto \boldsymbol{N} = \boldsymbol{G}\boldsymbol{T} \end{cases} \quad \text{and} \quad \boldsymbol{g} : \begin{cases} T_{\boldsymbol{x}}\mathcal{B}_t \to T^*_{\boldsymbol{x}}\mathcal{B}_t, \\ \boldsymbol{t} \mapsto \boldsymbol{n} = \boldsymbol{g}\boldsymbol{t}. \end{cases} \tag{2.15}$$

A visualization of these mappings can be found in Figure 2.3.

The length of the covariant vectors $\boldsymbol{T}$ and $\boldsymbol{t}$ is now expressed in terms of the norm with respect to the corresponding metric tensor:

$$|\boldsymbol{T}|_{\boldsymbol{G}} = \sqrt{\boldsymbol{T} \cdot (\boldsymbol{G}\boldsymbol{T})} \quad \text{and} \quad |\boldsymbol{t}|_{\boldsymbol{g}} = \sqrt{\boldsymbol{t} \cdot (\boldsymbol{g}\boldsymbol{t})}. \tag{2.16}$$

With the definition of the length of the covariant vectors at hand two different measures of the deformation can be derived. Setting the length of the Lagrangian covariant vector to unit length $|\boldsymbol{T}|_{\boldsymbol{G}} = 1$ the stretch in the direction of $\boldsymbol{T}$ is then obtained as

$$\lambda := |\boldsymbol{t}|_{\boldsymbol{g}} = \sqrt{\boldsymbol{t} \cdot (\boldsymbol{g}\boldsymbol{t})} = \sqrt{(\boldsymbol{F}\boldsymbol{T}) \cdot \boldsymbol{g}(\boldsymbol{F}\boldsymbol{T})} = \sqrt{\boldsymbol{T}\boldsymbol{C}\boldsymbol{T}} = |\boldsymbol{T}|_{\boldsymbol{C}} \ , \tag{2.17}$$

where the definition (2.12) was used. Here the *right Cauchy-Green deformation tensor* $\boldsymbol{C}$ was introduced as

$$\boldsymbol{C} := \boldsymbol{F}^T\boldsymbol{g}\boldsymbol{F}. \tag{2.18}$$

It is a rotation-independent deformation tensor which excludes rigid-body rotations and translations. The procedure of measuring the stretch can be done vice versa by setting the length of the Eulerian covariant vector to unit length $|\boldsymbol{t}|_{\boldsymbol{g}} = 1$. Now the inverse stretch in the direction of $\boldsymbol{t}$ is obtained as

$$\frac{1}{\lambda} := |\boldsymbol{T}|_{\boldsymbol{G}} = \sqrt{\boldsymbol{T} \cdot (\boldsymbol{G}\boldsymbol{T})} = \sqrt{(\boldsymbol{F}^{-1}\boldsymbol{t}) \cdot \boldsymbol{G}(\boldsymbol{F}^{-1}\boldsymbol{t})} = \sqrt{\boldsymbol{t}\boldsymbol{c}\boldsymbol{t}} = |\boldsymbol{t}|_{\boldsymbol{c}} \ , \tag{2.19}$$

where $\boldsymbol{c}$ is the *left Cauchy-Green deformation tensor*. It is defined as

$$\boldsymbol{c} := \boldsymbol{F}^{-T}\boldsymbol{G}\boldsymbol{F}^{-1} =: \boldsymbol{b}^{-1}. \tag{2.20}$$

The inverse of the left Cauchy-Green deformation tensor $\boldsymbol{b}$ is considered as *Finger tensor*. The left Cauchy-Green deformation is also a rotation-independent deformation tensor which excludes rigid-body rotations and translations. The right and left Cauchy-Green deformation tensor represent the Lagrangian and Eulerian counterpart of the Eulerian and Lagrangian metric. A visualized of this representation is given in Figure 2.3.

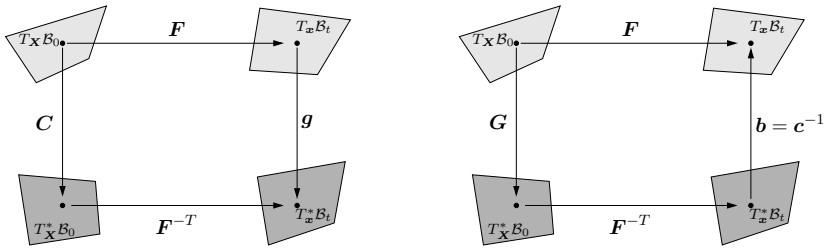

Figure 2.3: Visualization of right Cauchy-Green tensor $\boldsymbol{C}$, the Eulerian metric $\boldsymbol{g}$, the Lagrangian metric $\boldsymbol{G}$, the Finger tensor $\boldsymbol{b}$. Given are the covariant spaces for the Lagrangian ($T_{\boldsymbol{X}}\mathcal{B}_0$) and Eulerian ($T_{\boldsymbol{x}}\mathcal{B}_t$) configuration and the contravariant spaces for the Lagrangian ($T^*_{\boldsymbol{X}}\mathcal{B}_0$) and Eulerian ($T^*_{\boldsymbol{x}}\mathcal{B}_t$) configuration. This representation is adapted from the lecture note Miehe 2006.

2.2. Fundamental Stress Measures, Thermal Flux and Mass transport

Up to this point, the definition of the motion and the kinematic quantities of a body in a multicomponent system have been discussed. In order to describe a multicomponent system in a thermodynamic way one has to introduce the absolute temperature $\theta(\boldsymbol{x}, t)$, its gradient $\nabla_{\boldsymbol{x}}\theta(\boldsymbol{x}, t)$ and the chemical potential $\mu(\boldsymbol{X}, t)$ of a component. Note that the temperature and its gradient are parameterized by the Eulerian coordinates $\boldsymbol{x}$. They can be reparameterized by inserting $\boldsymbol{x} = \boldsymbol{\varphi}(\boldsymbol{X})$.

For a thermodynamic description of a body the energy which is stored within the body has to be considered. This stored energy is described by conjugated variables. These conjugated variables are the deformation and the mechanical stress, the temperature and the entropy, the temperature gradient and the thermal flux vector, as well as the mass flow and the chemical potential. In this chapter the definition of the mechanical stress, the thermal flux vector and the mass flow vector are discussed briefly. Chapter 2.3 then combines the conjugated variables by formulating physical balance equations.

Applying the *method of sections* developed by EULER yields the mechanical surface traction $\boldsymbol{t}(\boldsymbol{x}, t)$, the thermal flux $q(\boldsymbol{x}, t)$ and the mass flux $h(\boldsymbol{x}, t)$. They act on the surface

of a part $\mathcal{P}_{\mathcal{B}_t} \subset \mathcal{B}_t$ and represent the mechanical, the thermal and the mass transport effects acting from the part $\mathcal{B}_t \setminus \mathcal{P}_{\mathcal{B}_t}$ onto it. The material representation of the part $\mathcal{P}_{\mathcal{B}_t}$ is given by $\mathcal{P}_{\mathcal{B}_0} = \boldsymbol{\varphi}^{-1}(\mathcal{P}_{\mathcal{B}_t}) \subset \mathcal{B}_0$. The method of sections and the corresponding quantities are visualized in Figure 2.4. In what follows a relation between the mechanical traction and mechanical stress, between the thermal flux and thermal flux vector as well as between the mass flux and the mass flow vector is given.

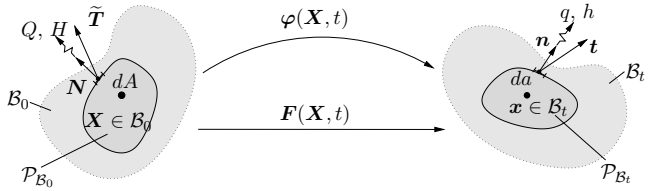

Figure 2.4: The method of sections applied in the Lagrangian and the Eulerian configuration. The mechanical and thermal interactions from the individual parts are represented by the traction vectors ($\widetilde{\boldsymbol{T}}$, $\boldsymbol{t}$), the heat flux (Q, q) and the mass flux (H, h). They act on the boundary of parts $\mathcal{P}_{\mathcal{B}_0}$ and $\mathcal{P}_{\mathcal{B}_t}$.

2.2.1. Cauchy's stress theorem

The mechanical surface traction $\boldsymbol{t}(\boldsymbol{x},t)$ is given as a linear function of the spatial surface normal $\boldsymbol{n}$. This relation is expressed in terms of a second-order tensor field $\boldsymbol{\sigma}(\boldsymbol{x},t)$. The existence of such a tensor field, namely the *Cauchy stress*, is given by *Cauchy's stress theorem*

$$\boldsymbol{t}(\boldsymbol{x},t;\boldsymbol{n}) := \boldsymbol{\sigma}(\boldsymbol{x},t)\boldsymbol{n} \ . \tag{2.21}$$

The ratio of current force and the current (deformed) area is the physical interpretation of the Cauchy stress. Since in most numerical applications integrals over the volume and the area are expressed in the reference configuration, it is convenient to introduce a more suitable stress measure. Therefore the stress $\boldsymbol{\sigma}$ is multiplied with the volume map J

$$\boldsymbol{\tau}(\boldsymbol{x},t) := J\boldsymbol{\sigma}(\boldsymbol{x},t) \ , \tag{2.22}$$

where $\boldsymbol{\tau}$ is the *Kirchhoff stress*. Note that $\boldsymbol{\sigma}$ and $\boldsymbol{\tau}$ are symmetric tensors expressed in the Eulerian configuration giving the following mappings

$$\boldsymbol{\sigma} : \begin{cases} T^*_{\boldsymbol{x}}\mathcal{B}_t \to T_{\boldsymbol{x}}\mathcal{B}_t, \\ \boldsymbol{n} \mapsto \boldsymbol{t} = \boldsymbol{\sigma}\boldsymbol{n} \end{cases} \quad \text{and} \quad \boldsymbol{\tau} : \begin{cases} T^*_{\boldsymbol{x}}\mathcal{B}_t \to T_{\boldsymbol{x}}\mathcal{B}_t, \\ \boldsymbol{n} \mapsto J\boldsymbol{t} = \boldsymbol{\tau}\boldsymbol{n} \ . \end{cases} \tag{2.23}$$

The stress measure which is used in experimental analyses is often given by the *1st Piola-Kirchhoff stress* $\widetilde{\boldsymbol{P}}$. It relates the current force to the reference area. Hence a Cauchy-like relation reads

$$\boldsymbol{T}(\boldsymbol{X},t;\boldsymbol{N}) := \widetilde{\boldsymbol{P}}(\boldsymbol{X},t)\boldsymbol{N} \ . \tag{2.24}$$

Here $\boldsymbol{N}$ is a material normal and $\boldsymbol{T}$ is a traction vector defined as current force over reference area. Using the area map and the relation $\boldsymbol{t}\mathrm{d}a = \boldsymbol{T}\mathrm{d}A$ yields the 1st Piola-Kirchhoff stress in terms of the Cauchy stress

$$\widetilde{\boldsymbol{P}} = J\boldsymbol{\sigma}\boldsymbol{F}^{-T} \ . \tag{2.25}$$

An often used modification of the 1st Piola-Kirchhoff stress is obtained by multiplying it with the Eulerian metric tensor $\boldsymbol{g}$, e.g. $\boldsymbol{P} = \boldsymbol{g}\widetilde{\boldsymbol{P}}$. Note that in a Cartesian setting $\boldsymbol{g} = \boldsymbol{1}$ and therefore $\boldsymbol{P} = \widetilde{\boldsymbol{P}}$. These two stress measures are non-symmetric and map from the reference to the current configuration

$$\widetilde{\boldsymbol{P}} : \begin{cases} T^*_{\boldsymbol{X}}\mathcal{B}_0 \to T_{\boldsymbol{x}}\mathcal{B}_t, \\ \boldsymbol{N} \mapsto \boldsymbol{T} = \widetilde{\boldsymbol{P}}\boldsymbol{N} \end{cases} \quad \text{and} \quad \boldsymbol{P} : \begin{cases} T^*_{\boldsymbol{X}}\mathcal{B}_0 \to T^*_{\boldsymbol{x}}\mathcal{B}_t, \\ \boldsymbol{N} \mapsto \widetilde{\boldsymbol{t}} = \boldsymbol{P}\boldsymbol{N} \ . \end{cases} \tag{2.26}$$

The last stress measure, namely the *2nd Piola-Kirchhoff stress*, relates the reference force to the reference area

$$\boldsymbol{S} : \begin{cases} T^*_{\boldsymbol{X}}\mathcal{B}_0 \to T_{\boldsymbol{x}}\mathcal{B}_0, \\ \boldsymbol{N} \mapsto \widetilde{\boldsymbol{T}} = \boldsymbol{S}\boldsymbol{N} \ . \end{cases} \tag{2.27}$$

The 2nd Piola-Kirchhoff stress can be related to the 1st Piola-Kirchhoff stress by

$$\boldsymbol{S} = \boldsymbol{F}^{-1}\boldsymbol{P}. \tag{2.28}$$

A Cauchy-like relation for the 2nd Piola-Kirchhoff stress is obtained as

$$\widetilde{\boldsymbol{T}}(\boldsymbol{X}, t; \boldsymbol{N}) = \boldsymbol{S}(\boldsymbol{X}, t)\boldsymbol{N}. \tag{2.29}$$

The 2nd Piola-Kirchhoff stress is again symmetric. A commutative visualization of the stress tensors is given in Figure 2.5.

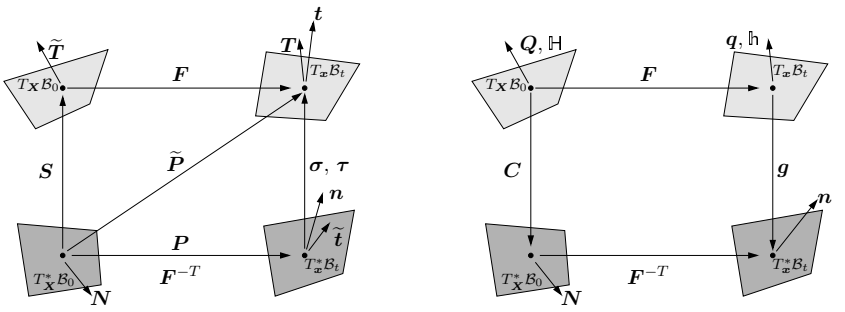

Figure 2.5: Commutative visualization of different stress measures, heat flux vectors and mass flow vectors. Given are the covariant spaces for the Lagrangian ($T_{\boldsymbol{X}}\mathcal{B}_0$) and Eulerian ($T_{\boldsymbol{x}}\mathcal{B}_t$) configuration and the contravariant spaces for the Lagrangian ($T^*_{\boldsymbol{X}}\mathcal{B}_0$) and Eulerian ($T^*_{\boldsymbol{x}}\mathcal{B}_t$) configuration. This representation is adapted from the lecture note Miehe 2006.

2.2.2. Heat flux

Similar to Cauchy's stress theorem its thermal counterpart gives the heat flux q as a the linear function of the spatial normal $\boldsymbol{n}$. Furthermore it is expressed in terms of the spatial heat flux vector $\boldsymbol{q}(\boldsymbol{x}, t)$

$$q(\boldsymbol{x}, t; \boldsymbol{n}) := \boldsymbol{q}(\boldsymbol{x}, t) \cdot \boldsymbol{n} \ . \tag{2.30}$$

Like the Cauchy stress the spatial heat flux vector $\boldsymbol{q}$ is expressed in the Eulerian configuration. Following the ideas of different stress measures a Lagrangian heat flux vector $\boldsymbol{Q}$ can be introduced as

$$\boldsymbol{Q} := J\boldsymbol{F}^{-1}\boldsymbol{q} \ . \tag{2.31}$$

The relation for the Lagrangian heat flux vector is given by

$$Q(\boldsymbol{X}, t; \boldsymbol{N}) := \boldsymbol{Q}(\boldsymbol{X}, t) \cdot \boldsymbol{N} \ , \tag{2.32}$$

where the relationship $QdA = qda$ was used. A commutative visualization of the heat flux vector is given in Figure 2.5.

2.2.3. Mass transport

Applying the above used procedure to mass transport in a multicomponent system (e.g. fluid-saturated porous medium) yields a linear relation of the spatial normal $\boldsymbol{n}$ and the Eulerian relative mass flux h

$$h(\boldsymbol{x}, t; \boldsymbol{n}) := \mathbb{h}(\boldsymbol{x}, t) \cdot \boldsymbol{n} \ . \tag{2.33}$$

Here $\mathbb{h}$ is the Eulerian mass flow vector. In analogy to different stress measures a Lagrangian mass flow vector $\mathbb{H}$ can be expressed as

$$\mathbb{H} := J\boldsymbol{F}^{-1}\mathbb{h} \quad \text{and} \quad H(\boldsymbol{X}, t; \boldsymbol{N}) := \mathbb{H}(\boldsymbol{X}, t) \cdot \boldsymbol{N} \tag{2.34}$$

with H as the Lagrangian relative mass flux.

2.3. Physical Balance Laws

With the deformation, the stress, the heat flux and the mass flow at hand almost all quantities are introduced which are needed for the formulation of the physical balance laws. The missing quantities are the temperature, the entropy, the temperature gradient and the chemical potential as already mentioned. Before formulating the balance laws for the specific quantities, a general form of the balance law for a global and local statement is introduced. The general global and local statements can be formulated in the Lagrangian as well in the Eulerian configuration. Since the actual physics happen in the Eulerian configuration this setting will be the starting point. After the introduction of the general forms the specific local forms in Eulerian configuration as well as in the Lagrangian form are given for a pure thermo-mechanical framework without considerations of the mass transport. In the last subsection the specific local forms in the Lagrangian form are given for a multicomponent system taking account for the mass transport.

2.3.1. General global form

To balance global quantities like mass, linear momentum, angular momentum, energy and entropy, we make use of the general form of a balance law of a global quantity $\mathcal{X}_{\mathcal{B}_t}$ in $\mathcal{B}_t$

$$\dot{\mathcal{X}}_{\mathcal{B}_t} = \frac{\mathrm{d}}{\mathrm{d}t}\mathcal{X}_{\mathcal{B}_t} = \frac{\mathrm{d}}{\mathrm{d}t}\int_{\mathcal{B}_t} \xi_t^{\mathcal{X}} \mathrm{d}v = \int_{\mathcal{B}_t} s_t^{\mathcal{X}} \mathrm{d}v + \int_{\mathcal{B}_t} p_t^{\mathcal{X}} \mathrm{d}v + \int_{\partial\mathcal{B}_t} \boldsymbol{f}_a^{\mathcal{X}} \cdot \boldsymbol{n} \mathrm{d}a. \tag{2.35}$$

This represents the general global form in the Eulerian configuration. It is expressed in terms of the field density $\xi_t^{\mathcal{X}}$ of the global quantity $\mathcal{X}_{\mathcal{B}_t}$ with respect to the current unit volume, its supply $s_t^{\mathcal{X}}$, its production $p_t^{\mathcal{X}}$ and its flux over the boundary $\boldsymbol{f}_a^{\mathcal{X}} \cdot \boldsymbol{n}$. Note that the Eulerian form of the general balance law (2.35) can be recast in the Lagrangian form by using the corresponding mapping of volume and area. Hereby a Lagrangian volume and surface quantity $\boldsymbol{a}$ is obtain by $\boldsymbol{a}_0 = J\boldsymbol{a}_t$ and $\boldsymbol{a}_A = J\boldsymbol{a}_a\boldsymbol{F}^{-T}$. This yields

$$\dot{\mathcal{X}}_{\mathcal{B}_t} = \int_{\mathcal{B}_0} s_0^{\mathcal{X}} \mathrm{d}V + \int_{\mathcal{B}_0} p_0^{\mathcal{X}} \mathrm{d}V + \int_{\partial\mathcal{B}_0} \boldsymbol{f}_A^{\mathcal{X}} \cdot \boldsymbol{N} \mathrm{d}A \; . \tag{2.36}$$

2.3.2. General local form

Recasting and using the *divergence theorem* as well as *localization theorem*, the global forms of the balance law (2.35) and (2.36) yield the *local forms* of the balance law

$$\dot{\xi}_0^{\mathcal{X}} = s_0^{\mathcal{X}} + p_0^{\mathcal{X}} + \mathrm{Div}(\boldsymbol{f}_A^{\mathcal{X}}) \quad \text{and} \quad \dot{\xi}_t^{\mathcal{X}*} = s_t^{\mathcal{X}} + p_t^{\mathcal{X}} + \mathrm{div}(\boldsymbol{f}_a^{\mathcal{X}}) \; . \tag{2.37}$$

Here $(2.37)_1$ is the Lagrangian and $(2.37)_2$ is the Eulerian form.

Note that the Eulerian rate of a field density a is obtained by $\dot{a}_t^* = \dot{a}_o J^{-1} = \dot{a}_t + a_t \dot{J} J^{-1}$. Using the Eulerian velocity $\boldsymbol{v}(\boldsymbol{x}, t) = \frac{\mathrm{d}}{\mathrm{d}t}\boldsymbol{\varphi}[\boldsymbol{\varphi}(\boldsymbol{x}, t)^{-1}, t]$, the Eulerian rate of a field density can be written as $\dot{a}_t^* = \dot{a}_t + a_t \,\mathrm{div}\, \boldsymbol{v}$.

2.3.3. Specific local forms in a one-component system

The balances of interest are the balance of mass, linear momentum, angular momentum, energy and entropy. The general form of a local balance law (2.37) yields the Eulerian local forms of the balance of:

mass:	$\dot{\rho}_t^* = \dot{\rho}_t + \rho_t \,\mathrm{div}\, \boldsymbol{v} = 0$	(2.38)
linear momentum:	$\mathrm{div}(\boldsymbol{\sigma}) + \rho_t \boldsymbol{b} = \rho_t \dot{\boldsymbol{v}}$	(2.39)
angular momentum:	$\boldsymbol{\sigma}^T = \boldsymbol{\sigma}$	(2.40)
energy:	$\boldsymbol{\sigma} : \boldsymbol{d} + \rho_t r - \mathrm{div}(\boldsymbol{q}) = \dot{e}_t^*$	(2.41)
entropy:	$\rho_t r + \delta_t - \mathrm{div}(\boldsymbol{q}) + \boldsymbol{q}\dfrac{\nabla_{\boldsymbol{x}}\theta}{\theta} = \theta \dot{\eta}_t^*$	(2.42)

Here ρ_t is the current *density of mass*, $\boldsymbol{b}$ is the *body force*, r is the *specific heat source*, e_t is the current *internal energy density*, δ_t is the *dissipation density* with respect to the current volume, θ is the *absolute temperature* and η_t is the *entropy density* with respect to the current volume. Furthermore the rate of deformation tensor is given as $\boldsymbol{d} := \frac{1}{2}\boldsymbol{F}^T\dot{\boldsymbol{C}}\boldsymbol{F}^{-1} = \frac{1}{2}\boldsymbol{\pounds}_{\boldsymbol{v}}\boldsymbol{g} = \mathrm{sym}(\boldsymbol{g}\nabla_{\boldsymbol{x}}\boldsymbol{v})$.

Note that from (2.41) and (2.42) one can see that the energy which is stored in the body is described by the conjugated variables $\{\boldsymbol{\sigma}, \boldsymbol{d}\}$, $\{\theta, \eta_t\}$, and $\{\boldsymbol{q}, \nabla_{\boldsymbol{x}}\theta\}$.

Similar to Eulerian local forms the Lagrangian local forms are obtained as the balance

of:

$$\text{mass:} \qquad \rho_0 = J\rho_t \tag{2.43}$$

$$\text{linear momentum:} \qquad \mathrm{Div}(\boldsymbol{P}) + \rho_0 \boldsymbol{b} = \rho_0 \dot{\boldsymbol{V}} \tag{2.44}$$

$$\text{angular momentum:} \qquad (\boldsymbol{F}\boldsymbol{P}^T)^T = \boldsymbol{F}\boldsymbol{P}^T \tag{2.45}$$

$$\text{energy:} \qquad \boldsymbol{P} : \dot{\boldsymbol{F}} + \rho_0 r - \mathrm{Div}(\boldsymbol{Q}) = \dot{e}_0 \tag{2.46}$$

$$\text{entropy:} \qquad \rho_0 r + \delta_0 - \mathrm{Div}(\boldsymbol{Q}) + \boldsymbol{Q}\frac{\nabla\theta}{\theta} = \theta\dot{\eta}_0. \tag{2.47}$$

Where the density of mass per unit reference volume is given as ρ_0. The internal energy density per unit reference volume is depicted as e_0. The reference dissipation density has the symbol δ_0 while η_0 is the entropy density per unit reference volume. The material velocity is given as $\boldsymbol{V}(\boldsymbol{X}, t) := \frac{\mathrm{d}}{\mathrm{d}t}\boldsymbol{\varphi}(\boldsymbol{X}, t)$. The conjugated variables for the description of the energy in the Lagrangian setting are $\{\boldsymbol{P}, \boldsymbol{F}\}$, $\{\theta, \eta_0\}$ and $\{\boldsymbol{Q}, \nabla\theta\}$.

2.3.4. Specific local forms in a multicomponent system

In analogy to a pure thermo-mechanical setting the Lagrangian local forms of a multicomponent system can be derived. Thereby the mass balance is formulated for each component. Under the assumption of a two-component system with the components solid and fluid, the local forms are obtained as the balance of:

$$\text{mass of solid:} \qquad \varrho_0^s = J\varrho_t^s \tag{2.48}$$

$$\text{mass of fluid:} \qquad -\mathrm{Div}(\mathbb{H}) = \dot{\varrho}^f \tag{2.49}$$

$$\text{linear momentum:} \qquad \mathrm{Div}(\boldsymbol{P}) + \varrho_0 \boldsymbol{b} - \mathrm{Div}(\mathcal{H}) = \tfrac{\mathrm{d}}{\mathrm{d}t}\mathcal{V} \tag{2.50}$$

$$\text{angular momentum:} \qquad (\boldsymbol{F}\boldsymbol{P}^T)^T = \boldsymbol{F}\boldsymbol{P}^T \tag{2.51}$$

$$\text{energy:} \qquad \boldsymbol{P} : \dot{\boldsymbol{F}} + \varrho_0 r - \mathrm{Div}(\boldsymbol{Q}) + (\boldsymbol{b} - \boldsymbol{a}^f) \cdot \boldsymbol{F}\mathbb{H} - \mathrm{Div}(h^f \mathbb{H}) = \dot{e}_0 \tag{2.52}$$

$$\text{entropy:} \qquad \varrho_0 r + \delta_0 - \mathrm{Div}(\boldsymbol{Q}) + \boldsymbol{Q}\frac{\nabla\theta}{\theta} - \theta\,\mathrm{Div}(\eta^f \mathbb{H}) = \theta\dot{\eta}_0. \tag{2.53}$$

Here $\mathcal{V} = (\varrho_0 + \varrho^f)\boldsymbol{V} + \boldsymbol{F}\mathbb{H}$ is the momentum per unit reference volume. The term $\mathrm{Div}(\mathcal{H})$ with $\mathcal{H} = [\boldsymbol{V} + \boldsymbol{F}\mathbb{H}/(\varrho_0^f + \varrho^f)] \otimes \mathbb{H}$ represents the rate of momentum due to convection of the fluid. The reference density is given by $\varrho_0 = \varrho_0^s + \varrho_0^f$, where ϱ_0^s is reference partial density of the solid and ϱ_0^f the reference partial density of the fluid. Furthermore the relative change of fluid mass is given as ρ^f. For the derivation, in particular, of the balance of linear momentum for a multicomponent system, the interested reader is referred to Biot 1977, Coussy 2004 or Gajo and Denzer 2011.

The quantities $\boldsymbol{a}^f$, η^f, h^f represent the acceleration, the entropy and the enthalpy of the fluid. In the next section the the entropy and the enthalpy of the fluid yield a definition of the chemical potential of the fluid. The conjugated variables for this setting are given as $\{\boldsymbol{P}, \boldsymbol{F}\}$, $\{\theta, \eta_0\}$, $\{\boldsymbol{Q}, \nabla\theta\}$ and $\{h^f, \eta^f; \mathbb{H}\}$.

2.4. Dissipation Postulate

In this section the *second law of thermodynamics* is introduced and the evaluated. Similar to the above section, this section is split into one-component systems and two-components systems. The latter systems take mass transport into account.

2.4.1. Dissipation Postulate for one-component systems

According to the second law of thermodynamics, the entropy production should always be positive, hence

$$\delta_0 \geq 0 \quad \text{and} \quad \delta_t \geq 0. \tag{2.54}$$

To derive now the *Clausius-Planck inequality* three steps are performed. First the equations in the Eulerian configuration (2.41), (2.42), $(2.54)_2$ are combined. This is also done for their Lagrangian counterpart (2.46), (2.47), $(2.54)_1$. Then the obtained equations are rearranged under the assumption of isothermal conditions ($\dot{\theta} = 0$, $\nabla\theta = \boldsymbol{0}$). As a third step the *Helmholtz free energy* density $\psi_0 := e_0 - \theta\eta_0$ per unit reference volume and per unit current volume $\psi_t := e_t - \theta\eta_t$ are inserted which yields the Clausius-Planck inequality for the Eulerian configuration

$$\delta_t = \boldsymbol{\sigma} : \boldsymbol{d} - \dot{\psi}_t^* = \boldsymbol{\sigma} : \boldsymbol{d} - \dot{\psi}_0 J^{-1} \geq 0, \tag{2.55}$$

as well as for the Lagrangian configuration

$$\delta_0 = \boldsymbol{P} : \dot{\boldsymbol{F}} - \dot{\psi}_0 \geq 0. \tag{2.56}$$

The global entropy production D, i.e. the global dissipation, is obtained by transferring the statement $(2.54)_1$ into a global form by integrating over the reference volume $\mathcal{B}_0$

$$D = \int_{\mathcal{B}_0} \delta_0 \, \mathrm{d}V = \int_{\mathcal{B}_0} \boldsymbol{P} : \dot{\boldsymbol{F}} - \dot{\psi}_0 \, \mathrm{d}V \geq 0 \, . \tag{2.57}$$

It can also be obtained by integrating over the current volume $\mathcal{B}_t$

$$D = \int_{\mathcal{B}_t} \delta_t \, \mathrm{d}v = \int_{\mathcal{B}_t} \boldsymbol{\sigma} : \boldsymbol{d} - \dot{\psi}_0 J^{-1} \, \mathrm{d}v \geq 0 \tag{2.58}$$

By using the definition of the Kirchhoff stress in (2.22) this can be formulated in terms of an integral over the reference volume

$$D = \int_{\mathcal{B}_0} \boldsymbol{\tau} : \boldsymbol{d} - \dot{\psi}_0 \, \mathrm{d}V \geq 0 \tag{2.59}$$

Comparing (2.57) and (2.59) the identity of stress powers can be identified

$$\mathcal{P} = \boldsymbol{P} : \dot{\boldsymbol{F}} = \boldsymbol{\tau} : \boldsymbol{d} \, . \tag{2.60}$$

In the subsequent treatment only integrals over the reference volume will be used. Therefore only the Helmholtz free energy density ψ_0 per unit reference volume has to be formulated. For convenience the index $(\cdot)_0$ will be dropped in what follows, hence $\psi = \psi_0$.

2.4.2. Dissipation Postulate for two-component systems

In the same manner as for one-component systems the second law of thermodynamics is evaluated for a two-component system. The equations (2.52), (2.53), $(2.54)_1$ are combined and the Helmholtz free energy density ψ_0 is used. This yields

$$\delta_0 = \boldsymbol{P} : \dot{\boldsymbol{F}} - \dot{\psi}_0 + \mu \dot{\varrho}^f + \big[-\nabla \mu + \boldsymbol{F}^T (\boldsymbol{b} - \boldsymbol{a}^f) \big] \cdot \mathbb{H} \geq 0. \tag{2.61}$$

Here $\mu := h^f - \theta \eta^f$ is the *Gibbs free energy* density of the fluid. For a two-component system (solid and fluid) this is equal to *chemical potential* of the fluid.

The entropy production can be split into a local and convective part $\delta_0 = \delta_0^{\text{loc}} + \delta_0^{\text{con}}$. The corresponding parts are given as

$$\delta_0^{\text{loc}} = \boldsymbol{P} : \dot{\boldsymbol{F}} - \dot{\psi}_0 + \mu \dot{\varrho}^f \geq 0 \quad \text{and} \quad \delta_0^{\text{con}} = \mathbb{B} \cdot \mathbb{H} \geq 0. \tag{2.62}$$

Here $\mathbb{B} = -\nabla \mu + \boldsymbol{F}^T (\boldsymbol{b} - \boldsymbol{a}^f)$ is the thermodynamic driving force for the fluid flow and therefore its conjugated variable. Finally the global dissipation in the Lagrangian configuration can be given as

$$D = \int_{\mathcal{B}_0} \delta_0 \, \mathrm{d}V = \int_{\mathcal{B}_0} \boldsymbol{P} : \dot{\boldsymbol{F}} - \dot{\psi}_0 + \mu \dot{\varrho}^f + \mathbb{B} \cdot \mathbb{H} \, \mathrm{d}V \geq 0. \tag{2.63}$$

Chapter 3

Modeling Framework

Up to now the kinematics and physical balance laws which are needed for the description of a two-component system in a continuum mechanical and thermodynamical way have been introduced. In this chapter the initial boundary value problem of continuum mechanics is recalled. In order to close the system of equations additional constitutive relations have to be introduced. This is achieved by the construction of a (Helmholtz) free energy density ψ on the one hand. Thereby it has to satisfied the basic principles for constitutive functions in continuum mechanics. These principles will be discussed shortly in the following. On the other hand a dissipation potential destiny ϕ is introduced in order to describe the constitutive response of the body. In this chapter only the reference configuration is considered and isothermal conditions are assumed.

3.1. Initial Boundary Value Problem

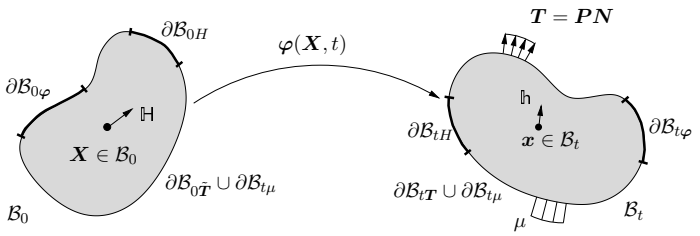

Figure 3.1: The physical balance laws, the inital values as well as the boundary conditions form the intial boundary value problem. The boundary of the domain is decomposed into a Dirchlet $(\mathcal{B}_{0\boldsymbol{\varphi}}, \mathcal{B}_{0H}, \mathcal{B}_{t\boldsymbol{\varphi}}, \mathcal{B}_{tH})$ and Neumann boundary $(\mathcal{B}_{0\tilde{\boldsymbol{T}}}, \mathcal{B}_{0\mu}, \mathcal{B}_{t\boldsymbol{T}}, \mathcal{B}_{t\mu})$ in the reference as well as in the current configuration.

The goal of initial boundary value problem in continuum mechanics is the determination of the unknown fields for given initial values and given boundary values. In basic continuum mechanics the unknown field is the deformation map $\boldsymbol{\varphi}(\boldsymbol{X},t)$, for coupled

problems additional unknowns can be introduced in a straightforward manner. For a two-component system the unknown fields are the deformation map $\boldsymbol{\varphi}(\boldsymbol{X},t)$ and the fluid mass flow $\mathbb{H}(\boldsymbol{X},t)$. Considering the domain $\mathcal{B}_0$ with the given initial conditions

$$\boldsymbol{\varphi}(\boldsymbol{X},t_0) = \boldsymbol{\varphi}_0(\boldsymbol{X}) \quad \text{in} \quad \mathcal{B}_0, \tag{3.1}$$
$$\boldsymbol{V}(\boldsymbol{X},t_0) = \boldsymbol{V}_0(\boldsymbol{X}) \quad \text{in} \quad \mathcal{B}_0, \tag{3.2}$$
$$\varrho^f(\boldsymbol{X},t_0) = 0 \quad \text{in} \quad \mathcal{B}_0, \tag{3.3}$$
$$\mathbb{H}(\boldsymbol{X},t_0) = \mathbb{H}_0(\boldsymbol{X}) \quad \text{in} \quad \mathcal{B}_0, \tag{3.4}$$

where the initial values of the deformation map, the material velocity, the relative change of fluid mass and the fluid mass flow vector are given at time t_0 as $\boldsymbol{\varphi}_0$, $\boldsymbol{V}_0$, 0 and $\mathbb{H}_0$.

Next, the boundary $\partial\mathcal{B}_0$ of the body $\mathcal{B}_0$ is decomposed into the Dirichlet boundaries $\partial\mathcal{B}_{0\boldsymbol{\varphi}} = \partial\mathcal{B}_0 \setminus \mathcal{B}_{0\boldsymbol{T}}$ and $\partial\mathcal{B}_{0H} = \partial\mathcal{B}_0 \setminus \mathcal{B}_{0\mu}$, as well as the Neumann boundaries $\partial\mathcal{B}_{0\boldsymbol{t}} = \partial\mathcal{B}_0 \setminus \mathcal{B}_{0\boldsymbol{\varphi}}$ and $\partial\mathcal{B}_{0\mu} = \partial\mathcal{B}_0 \setminus \mathcal{B}_{0H}$. At the Dirichlet boundaries the given deformation map $\bar{\boldsymbol{\varphi}}(\boldsymbol{X},t)$ and the given fluid mass flow vector $\bar{\mathbb{H}}(\boldsymbol{X},t)$ are prescribed while at the Neumann boundaries the given mechanical traction $\bar{\boldsymbol{T}}(\boldsymbol{X},t)$ and the given chemical potential $\bar{\mu}(\boldsymbol{X},t)$ are prescribed,

$$\boldsymbol{\varphi}(\boldsymbol{X},t) = \bar{\boldsymbol{\varphi}}(\boldsymbol{X},t) \quad \text{on} \quad \partial\mathcal{B}_{0\boldsymbol{\varphi}}, \tag{3.5}$$
$$\boldsymbol{T}(\boldsymbol{X},t) = \bar{\boldsymbol{T}}(\boldsymbol{X},t) \quad \text{on} \quad \partial\mathcal{B}_{0\boldsymbol{T}}, \tag{3.6}$$
$$\mathbb{H}(\boldsymbol{X},t) = \bar{\mathbb{H}}(\boldsymbol{X},t) \quad \text{on} \quad \partial\mathcal{B}_{0H}, \tag{3.7}$$
$$\mu(\boldsymbol{X},t) = \bar{\mu}(\boldsymbol{X},t) \quad \text{on} \quad \partial\mathcal{B}_{0\mu}. \tag{3.8}$$

The goal is now to determine the deformation map $\boldsymbol{\varphi}(\boldsymbol{X},t)$ and the fluid mass flow vector $\mathbb{H}(\boldsymbol{X},t)$ such that they satisfy the physical balance laws in (2.48) - (2.51), the Clausius-Planck inequality with fluid flow in (2.61), the initial conditions in (3.1) - (3.4) as well as the boundary conditions in (3.5) - (3.8). Up to this point no specific material behavior is taken into account yet. In order to account for the specific material behavior constitutive functions will be constructed. This is discussed in what follows.

3.2. Closure Problem of the System of Equations

In order to determine the deformation map and the mass flow vector a system of equations is solved. In the sense of its solutions, the behavior of such a system is governed by the ratio of the number of equations and the number of unknowns. A closer look at this ratio is now taken. The system of equations is given as

$$\text{(2.48):} \qquad \varrho_0^s = J\varrho_t^s \tag{3.9}$$
$$\text{(2.49):} \qquad -\operatorname{Div}(\mathbb{H}) = \dot{\varrho}^f \tag{3.10}$$
$$\text{(2.50):} \qquad \operatorname{Div}(\boldsymbol{P}) + \varrho_0\boldsymbol{b} - \operatorname{Div}(\mathcal{H}) = \tfrac{\mathrm{d}}{\mathrm{d}t}\mathcal{V} \tag{3.11}$$
$$\text{(2.51):} \qquad (\boldsymbol{F}\boldsymbol{P}^T)^T = \boldsymbol{F}\boldsymbol{P}^T \tag{3.12}$$
$$\text{(2.61):} \qquad \boldsymbol{P} : \dot{\boldsymbol{F}} - \dot{\psi}_0 + \mu\dot{\varrho}^f + \mathbb{B}\cdot\mathbb{H} \geq 0. \tag{3.13}$$

It sums up to $1+1+3+3+1=9$ scalar equations. On the other hand there are the unknowns

- mass density of solid ϱ_t^s, (3.14)
- relative change of fluid mass ϱ^f, (3.15)
- 1st Piola-Kirchhoff stress $\boldsymbol{P}$, (3.16)
- deformation map $\boldsymbol{\varphi}$, (3.17)
- fluid mass flow vector $\mathbb{H}$, (3.18)
- free energy density ψ, (3.19)
- chemical potential μ, (3.20)

which sum up to $1+1+9+3+3+1+1=19$ scalar unknowns. This yields the conclusion that $19-9=10$ additional equations are needed in order to close the system of equations.

These additional equations are given in terms of constitutive functions and specify the material behavior. Clearly, they give a relationship between the deformation and the stress tensor, the relative change of fluid mass and the chemical potential as well as between the fluid mass flow vector and the chemical potential.

3.3. Constitutive Relations

In this section the formulation of constitutive relations is discussed in a general way. Thereby certain principles and concepts have to be taken into account. These principles are exemplified for the construction of the free energy density ψ. At the end of this subchapter the constitutive relations which close the system of equations will be obtained.

3.3.1. Principle of Determinism

This principle states that the energy density $\psi(\boldsymbol{X},t)$ at the material point $\boldsymbol{X}$ for the current time t is determined by the full history of the deformation and flux process of all material points. This yields the energy density as a function of the deformation map $\boldsymbol{\varphi}(\boldsymbol{Y},\tau)$ and the relative change of fluid mass $\varrho^f(\boldsymbol{Y},\tau)$ at all material points $\boldsymbol{Y}\in\mathcal{B}_0$ at any previous time $\tau\in[0,t)$

$$\psi(\boldsymbol{X},t)=f\big(\boldsymbol{\varphi}(\boldsymbol{Y},\tau),\varrho^f(\boldsymbol{Y},\tau)\big)\qquad\forall\boldsymbol{Y}\in\mathcal{B}_0\quad\text{and}\quad\forall\tau\in[0,t). \tag{3.21}$$

This principle rules out any stochastic or random behavior in the material modeling.

3.3.2. Concept of Internal Variables

Since it is not practicable to account for the full history, the statement (3.21) is reduced by introducing the field of the *internal variables* $\mathfrak{I}(\boldsymbol{x},t)$, which stores the necessary history

parameters of the deformation and flux process. With this the energy density does not depend on any previous time τ but only on the current time

$$\psi(\boldsymbol{X},t) = f\big(\boldsymbol{\varphi}(\boldsymbol{Y},t), \varrho^f(\boldsymbol{Y},t), \mathfrak{I}(\boldsymbol{Y},t)\big) \qquad \forall \boldsymbol{Y} \in \mathcal{B}_0. \tag{3.22}$$

As the internal variables appear as additional unknowns their initial conditions have to be given

$$\mathfrak{I}(\boldsymbol{X},t_0) = \mathfrak{I}_0(\boldsymbol{X}) \quad \text{in} \quad \mathcal{B}_0. \tag{3.23}$$

Furthermore the evolution of the internal variables is governed by an additional constitutive function $\dot{\mathfrak{I}}(\boldsymbol{X},t)$

$$\dot{\mathfrak{I}}(\boldsymbol{X},t) = g\big(\boldsymbol{\varphi}(\boldsymbol{Y},t), \varrho^f(\boldsymbol{Y},t), \mathfrak{I}(\boldsymbol{Y},t)\big) \qquad \forall \boldsymbol{Y} \in \mathcal{B}_0. \tag{3.24}$$

3.3.3. Principle of Local Actions

The dependence of the constitutive response on $\boldsymbol{Y} \in \mathcal{B}_0$ is now relaxed by the assumption that the constitutive response at a material point $\boldsymbol{X} \in \mathcal{B}_0$ is only governed by the material points $\boldsymbol{Y} \in \mathcal{N}_{\boldsymbol{X}}$. Here $\mathcal{N}_{\boldsymbol{X}}$ is a neighborhood of the point $\boldsymbol{X}$. Using a first-order Taylor polynomial of the deformation map, the internal variables and the relative change of fluid mass yields the a *theory of grade one*. As a result the free energy density is expressed in term of the deformation map, the internal variables and their gradients

$$\psi(\boldsymbol{X},t) = f\big(\boldsymbol{\varphi}(\boldsymbol{X},t), \boldsymbol{F}(\boldsymbol{X},t), \varrho^f(\boldsymbol{X},t), \nabla\varrho^f(\boldsymbol{X},t), \mathfrak{I}(\boldsymbol{X},t), \nabla\mathfrak{I}(\boldsymbol{X},t)\big). \tag{3.25}$$

The same argument also holds for the evolution of the internal variables

$$\dot{\mathfrak{I}}(\boldsymbol{X},t) = g\big(\boldsymbol{\varphi}(\boldsymbol{X},t), \boldsymbol{F}(\boldsymbol{X},t), \varrho^f(\boldsymbol{X},t), \nabla\varrho^f(\boldsymbol{X},t), \mathfrak{I}(\boldsymbol{X},t), \nabla\mathfrak{I}(\boldsymbol{X},t)\big). \tag{3.26}$$

For better readability the arguments $\boldsymbol{X}$ and t will be dropped in the following.

3.3.4. Principle of Material Objectivity

This principle (PMO) has to be fulfilled at all times. It is fundamental in terms of geometrically nonlinear continuum mechanics. It was introduced in the work of Truesdell and Noll 1965. It states two invariances of the constitutive response: (i) frame invariance and (ii) invariance with respect to rigid body motions. The first statement is considered as passive version of PMO and requires the material equations to be independent of the observer. The second statement is referred to as active version.[16] It demands the constitutive response to be independent of a rigid-body motion superimposed onto the current configuration. Mathematically speaking, both yield the following transformation

$$\boldsymbol{x}^+(t) = \boldsymbol{Q}\boldsymbol{x}(t) + \boldsymbol{s}(t) \quad \overset{\boldsymbol{x}(t)=\boldsymbol{\varphi}(\boldsymbol{X},t)}{\Rightarrow} \quad \boldsymbol{\varphi}^+(\boldsymbol{X},t) = \boldsymbol{Q}\boldsymbol{\varphi}(\boldsymbol{X},t) + \boldsymbol{s}(t), \tag{3.27}$$

where $\boldsymbol{Q} \in SO(3)$ is an arbitrary rotation tensor. $SO(3)$ is the 3D rotation group including all rotations in $\mathbb{R}^3$ and $\boldsymbol{s}(t)$ is an arbitrary translation vector. A scalar function is

[16] doi.org/10.1007/978-3-662-04109-3

considered as invariant with respect to the transformation (3.27) if it satisfies $(\cdot)^+ = (\cdot)$. This yields the condition for the constitutive energy response

$$\psi^+\big(\boldsymbol{\varphi}^+, \boldsymbol{F}^+, \mathfrak{I}, \varrho^f, \nabla\varrho^f, \mathfrak{J}, \nabla\mathfrak{J}\big) \stackrel{!}{=} \psi\big(\boldsymbol{\varphi}, \boldsymbol{F}, \varrho^f, \nabla\varrho^f, \mathfrak{J}, \nabla\mathfrak{J}\big), \tag{3.28}$$

and the condition for the constitutive evolution of the internal variables

$$\dot{\mathfrak{J}}^+\big(\boldsymbol{\varphi}^+, \boldsymbol{F}^+, \mathfrak{I}, \varrho^f, \nabla\varrho^f, \mathfrak{J}, \nabla\mathfrak{J}\big) \stackrel{!}{=} \dot{\mathfrak{J}}\big(\boldsymbol{\varphi}, \boldsymbol{F}, \varrho^f, \nabla\varrho^f, \mathfrak{J}, \nabla\mathfrak{J}\big). \tag{3.29}$$

In the two equations the transformation $\boldsymbol{F}^+ = \boldsymbol{Q}\boldsymbol{F}$ was used. These equations have to hold for arbitrary $\boldsymbol{Q}$ and $\boldsymbol{s}$. In order to satisfy this, the constitutive response must be constructed in terms of quantities that are invariant with respect to the superimposed rotation and translation.

Consider now a constitutive response which is formulated in terms of the invariance of the arguments given in (3.29). The invariance of a vector field, such as the deformation map $\boldsymbol{\varphi}$, is its norm, i.e. the length. Since the norm is not invariant with respect to the superimposed translation $\boldsymbol{s}(t)$, the constitutive response can not be a function of the deformation map $\boldsymbol{\varphi}$. On the other hand the dependence of the constitutive response on the deformation gradient $\boldsymbol{F}$ can be kept. This tensorial argument must only be invariant with respect to a superimposed rotation. This can be achieved using invariances of a tensor. The interested reader is refereed to Spencer 2004 or Schröder and Neff 2010. Finally, the constitutive free energy density can be written as

$$\psi(\boldsymbol{X}, t) = f\big(\boldsymbol{F}, \varrho^f, \nabla\varrho^f, \mathfrak{J}, \nabla\mathfrak{J}\big) = f^+\big(\boldsymbol{Q}\boldsymbol{F}, \varrho^f, \nabla\varrho^f, \mathfrak{J}, \nabla\mathfrak{J}\big) \tag{3.30}$$

and similarly the constitutive evolution of the internal variables reads

$$\dot{\mathfrak{J}}(\boldsymbol{X}, t) = g\big(\boldsymbol{F}, \varrho^f, \nabla\varrho^f, \mathfrak{J}, \nabla\mathfrak{J}\big) = g^+\big(\boldsymbol{Q}\boldsymbol{F}, \varrho^f, \nabla\varrho^f, \mathfrak{J}, \nabla\mathfrak{J}\big) \tag{3.31}$$

Note that for the constitutive response expressed in terms of the Cauchy-Green deformation tensor $\boldsymbol{C}$ the PMO is a priori satisfied. For the constitutive response expressed in terms of $\boldsymbol{F}$ it must be ensured especially by fulfilling the condition $(\cdot)(\boldsymbol{F}) \stackrel{!}{=} (\cdot)^+(\boldsymbol{Q}\boldsymbol{F})$.

3.3.5. Principle of Material Symmetry

Some materials have an anisotropic material behavior due to their microstructure. An anisotropic microstructure subject to a certain symmetry is considered a material symmetry. This symmetry can then be described by the rotations $\boldsymbol{Q}_{\mathcal{G}} \in \mathcal{G} \subset SO(3)$, where $\mathcal{G}$ is the symmetry group of the material. The principle of material symmetry (PMS) states that the constitutive response should be invariant with respect to the rotations $\boldsymbol{Q}_{\mathcal{G}}$ superimposed onto the reference configuration. This leads to

$$\psi(\boldsymbol{X}, t) = f\big(\boldsymbol{F}, \varrho^f, \nabla\varrho^f, \mathfrak{J}, \nabla\mathfrak{J}\big) = f^*\big(\boldsymbol{F}\boldsymbol{Q}_{\mathcal{G}}, \varrho^f, \nabla\varrho^f, \mathfrak{J}, \nabla\mathfrak{J}\big) \tag{3.32}$$

for the free energy density. The same argument holds also for the constitutive evolution of the internal variables

$$\dot{\mathfrak{J}}(\boldsymbol{X}, t) = g\big(\boldsymbol{F}, \varrho^f, \nabla\varrho^f, \mathfrak{J}, \nabla\mathfrak{J}\big) = g^*\big(\boldsymbol{F}\boldsymbol{Q}_{\mathcal{G}}, \varrho^f, \nabla\varrho^f, \mathfrak{J}, \nabla\mathfrak{J}\big). \tag{3.33}$$

Similar to the PMO the PMS is a priori satisfied for the constitutive response expressed in terms of $\boldsymbol{C}$. Otherwise $(\cdot)(\boldsymbol{F}) \stackrel{!}{=} (\cdot)^*(\boldsymbol{F}\boldsymbol{Q}_{\mathcal{G}})$ must be guaranteed especially.

3.3.6. Evaluation of the Dissipation Postulate

The constitutive response is *thermodynamically consistent* if it satisfies the dissipation postulate (2.63). To evaluate the dissipation postulate the time derivative of the free energy density in terms of the aforementioned arguments is needed. It reads

$$\begin{aligned}\dot{\psi}(\boldsymbol{F}, \varrho^f, \nabla\varrho^f, \mathfrak{I}, \nabla\mathfrak{I}) &= \frac{\mathrm{d}}{\mathrm{d}t}\psi(\boldsymbol{F}, \varrho^f, \nabla\varrho^f, \mathfrak{I}, \nabla\mathfrak{I}) \\ &= \partial_{\boldsymbol{F}}\psi : \dot{\boldsymbol{F}} + \partial_{\varrho^f}\psi\ \dot{\varrho}^f + \partial_{\nabla\varrho^f}\psi \cdot \nabla\dot{\varrho}^f + \partial_{\mathfrak{I}}\psi\ \dot{\mathfrak{I}} + \partial_{\nabla\mathfrak{I}}\psi \cdot \nabla\dot{\mathfrak{I}}.\end{aligned} \tag{3.34}$$

Inserting this into (2.63) and making use of the divergence and the localization theorem yields

$$\begin{aligned}(\boldsymbol{P} - \partial_{\boldsymbol{F}}\psi) : \dot{\boldsymbol{F}} + [\mu - \partial_{\varrho^f}\psi + \mathrm{Div}(\partial_{\nabla\varrho^f}\psi)]\dot{\varrho}^f \\ -[\partial_{\mathfrak{I}}\psi - \mathrm{Div}(\partial_{\nabla\mathfrak{I}}\psi)]\dot{\mathfrak{I}} \geq 0 \text{ in } \mathcal{B}_0, \\ \mathbb{B}\cdot\mathbb{H} \geq 0 \text{ in } \mathcal{B}_0, \\ (\partial_{\nabla\mathfrak{I}}\psi \cdot \boldsymbol{N})\ \dot{\mathfrak{I}} \geq 0 \text{ on } \partial\mathcal{B}_{0\mathfrak{k}} \\ (\partial_{\nabla\varrho^f}\psi \cdot \boldsymbol{N})\ \dot{\varrho}^f \geq 0 \text{ on } \partial\mathcal{B}_{0\mu}.\end{aligned} \tag{3.35}$$

Here $(3.35)_3$ and $(3.35)_4$ are constraints for the Neumann boundary conditions for the internal variables on the boundary $\mathcal{B}_{0\mathfrak{k}} \subset \mathcal{B}$ and for the mass flow on the boundary $\mathcal{B}_{0\mu} \subset \mathcal{B}$.

In order to fulfill the dissipation postulate the condition in $(3.35)_1$ and $(3.35)_2$ has to hold in the whole body $\mathcal{B}_0$. $(3.35)_1$ can be decomposed into two statements. The first statement gives the definition of the 1st Piola-Kirchhoff stress and the relation between the relative change of fluid mass and the chemical potential

$$\boldsymbol{P} - \partial_{\boldsymbol{F}}\psi = \boldsymbol{0} \quad \text{and} \quad \mu - \partial_{\varrho^f}\psi + \mathrm{Div}(\partial_{\nabla\varrho^f}\psi) = 0, \tag{3.36}$$

and the second statement represents a condition for the evolution of the internal variables

$$-\left[\partial_{\mathfrak{I}}\psi - \mathrm{Div}(\partial_{\nabla\mathfrak{I}}\ \psi)\right]\ \dot{\mathfrak{I}} \geq 0. \tag{3.37}$$

The relations in (3.36) are derived by the *Coleman-Noll procedure* due to Coleman and Noll 1959 and solve the initial closure problem in Section 3.2. They give a constitutive expression of the 1st Piola-Kirchhoff stress $\boldsymbol{P}$ in terms of the free energy density ψ and the deformation gradient $\boldsymbol{F}$ as well as a constitutive expression of the chemical potential in terms of the free energy density ψ and the relative change of fluid mass ϱ^f.

In order to satisfy the inequality $(3.35)_2$ and (3.37) a *dissipation potential density* is introduced. This is discussed in what follows.

Dissipation Potential Density. By introducing the functional derivative with respect to the quantity a as $\delta_a(\cdot) = \partial_a(\cdot) - \mathrm{Div}[\partial_{\nabla a}\ (\cdot)]$ the inequality (3.37) can be recast as

$$-\delta_{\mathfrak{I}}\psi\ \dot{\mathfrak{I}} \geq 0. \tag{3.38}$$

Considering now a dissipation potential density $\phi(\dot{\mathfrak{I}})$ an implicit definition of the evolution equation for $\mathfrak{I}$ can be given by

$$-\delta_{\mathfrak{I}}\psi(\boldsymbol{F}, \varrho^f, \nabla\varrho^f, \mathfrak{I}, \nabla\mathfrak{I}) \in \partial_{\dot{\mathfrak{I}}}\phi. \tag{3.39}$$

This equation is referred to as *Biot's equation*. For a more detailed explanation of the concept of a dissipation potential see Biot 1965b, Ziegler and Wehrli 1987 and Miehe 2002. In the case of a non-smooth dissipation potential density the functional derivative $-\delta_{\mathfrak{I}}\psi$ has to be part of the sub-differential of the dissipation potential density, see e.g. Frémond 2002.

If the potential density $\phi(\dot{\mathfrak{I}})$ is convex, positive and normalized, is can be show that the condition (3.37) and therefore the thermodynamical consistency is a priori satisfied.

In order to satisfy the inequality $(3.35)_2$ the same idea as for the evolution of the internal variables can be used. Hence to fulfill the condition

$$\mathbb{B} \cdot \mathbb{H} \geq 0, \tag{3.40}$$

an implicit definition of the fluid mass flow vector $\mathbb{H}$ is introduced by

$$\mathbb{B}(\boldsymbol{F}, \varrho^f, \nabla\varrho^f, \mathfrak{I}, \nabla\mathfrak{I}) \in \partial_{\mathbb{H}}\phi. \tag{3.41}$$

For a convex, positive and normalized potential density $\phi(\mathbb{H})$ the condition $(3.35)_2$ is a priori satisfied yielding thermodynamical consistency.

3.4. Governing Field Equations

In the subsequent treatment quasi-static conditions ($|\ddot{\boldsymbol{\varphi}}| \approx 0$, $|\dot{\boldsymbol{V}}| \approx 0$, $|\dot{\boldsymbol{a}}^f| \approx 0$) are assumed. Furthermore the body force is related to the gravitational force ($\boldsymbol{b} = \bar{\boldsymbol{g}}$) and a local response with respect to the relative change of fluid mass is adopted.

Hence with the aforementioned considerations at hand a free energy density $\psi(\boldsymbol{F}, \varrho^f, \mathfrak{I}, \nabla\mathfrak{I})$ as well as a dissipation potential density $\phi(\mathbb{H}, \dot{\mathfrak{I}})$ can be constructed. Thereby the free energy density has to satisfy the balance of angular momentum (2.51) where the relation $\boldsymbol{P} = \partial_{\boldsymbol{F}}\psi$ is used. The governing field equations are given as

balance of solid mass	$\varrho_0^s = J\varrho_t^s$	(3.42)
balance of fluid mass	$-\operatorname{Div}(\mathbb{H}) = \dot{\varrho}^f$	(3.43)
balance of linear momentum	$\operatorname{Div}(\partial_{\boldsymbol{F}}\psi) + \varrho_0\boldsymbol{b} = \boldsymbol{0}$	(3.44)
fluid mass flow vector	$\mathbb{B} \in \partial_{\mathbb{H}}\phi$	(3.45)
evolution of internal variables	$-\delta_{\mathfrak{I}}\psi \in \partial_{\dot{\mathfrak{I}}}\phi.$	(3.46)

The unknowns in these equations are

current mass density of solid	ϱ_t^s	(3.47)
relative change of fluid mass	ϱ^f	(3.48)
deformation map	$\boldsymbol{\varphi}$	(3.49)
fluid mass flow vector	$\mathbb{H}$	(3.50)
internal variables	$\mathfrak{I}.$	(3.51)

With n_{int} as the number of scalar internal variables there are $1+1+3+3+n_{\text{int}} = 8+n_{\text{int}}$ scalar equations and $1+1+3+3+n_{\text{int}} = 8+n_{\text{int}}$ scalar unknowns yielding a unique solution for the system of equations.

3.5. Variational Formulation

The governing equations (3.42)-(3.46) represent the closed form of the system of equations for the initial boundary value problem in Section 3.1. The balance of solid mass and therefore the current mass density of solid can be neglected for the representation of the problem in the reference configuration. The remaining governing equations (3.43)-(3.46) can be considered in an variational framework for the boundary value problem of two-component systems. The interested reader is referred to Miehe 2002, or Svendsen 2004. Basis of the variational formulation is the definition of the *rate–type potential* at a given state $\{\boldsymbol{\varphi}, \varrho^f, \mathfrak{I}\}$

$$\Pi_{\mathcal{B}_0}(\dot{\boldsymbol{\varphi}}, \mathbb{H}, \dot{\mathfrak{I}}; \boldsymbol{\varphi}, \varrho^f, \mathfrak{I}) = \frac{\mathrm{d}}{\mathrm{d}t} E_{\mathcal{B}_0}(\boldsymbol{\varphi}, \varrho^f, \mathfrak{I}) + D_{\mathcal{B}_0}(\mathbb{H}, \dot{\mathfrak{I}}) - P^{\mathrm{ext}}_{\mathcal{B}_0}(\dot{\boldsymbol{\varphi}}, \mathbb{H}, \dot{\mathfrak{I}}), \tag{3.52}$$

where $\frac{\mathrm{d}}{\mathrm{d}t} E_{\mathcal{B}_0}$ is the *rate of energy*, $D_{\mathcal{B}_0}$ the *dissipation potential* and $P^{\mathrm{ext}}_{\mathcal{B}_0}$ the *external load potential*. The rate of energy is given in terms of the free energy density ψ

$$\frac{\mathrm{d}}{\mathrm{d}t} E_{\mathcal{B}_0}(\boldsymbol{\varphi}, \varrho^f, \mathfrak{I}) = \frac{\mathrm{d}}{\mathrm{d}t} \int_{\mathcal{B}_0} \psi(\boldsymbol{F}, \varrho^f, \mathfrak{I}, \nabla\mathfrak{I}) \, \mathrm{d}V. \tag{3.53}$$

Applying the chain rule yields

$$\begin{aligned} \frac{\mathrm{d}}{\mathrm{d}t} E_{\mathcal{B}_0}(\boldsymbol{\varphi}, \varrho^f, \mathfrak{I}) &= \int_{\mathcal{B}_0} \partial_{\boldsymbol{F}}\psi : \nabla\dot{\boldsymbol{\varphi}} + \partial^f_\varrho\psi \; \dot{\varrho}^f + \partial_\mathfrak{I}\psi \; \dot{\mathfrak{I}} + \partial_{\nabla\mathfrak{I}}\psi \cdot \nabla\dot{\mathfrak{I}} \, \mathrm{d}V \\ &= \int_{\mathcal{B}_0} \partial_{\boldsymbol{F}}\psi : \nabla\dot{\boldsymbol{\varphi}} - \partial^f_\varrho\psi \; \mathrm{Div}(\mathbb{H}) + \partial_\mathfrak{I}\psi \; \dot{\mathfrak{I}} + \partial_{\nabla\mathfrak{I}}\psi \cdot \nabla\dot{\mathfrak{I}} \, \mathrm{d}V, \end{aligned} \tag{3.54}$$

where the balance of fluid mass (3.43) was inserted. The dissipation potential $D_{\mathcal{B}_0}$ is formulated in terms of the constitutive dissipation potential density $\phi(\mathbb{H}, \dot{\mathfrak{I}})$

$$D_{\mathcal{B}_0}(\mathbb{H}, \dot{\mathfrak{I}}) = \int_{\mathcal{B}_0} \phi(\mathbb{H}, \dot{\mathfrak{I}}) \, \mathrm{d}V. \tag{3.55}$$

The external load potential $P^{\mathrm{ext}}_{\mathcal{B}_0}$ is expressed in terms of the prescribed gravitational force $\bar{\boldsymbol{g}}$, the prescribed mechanical traction $\bar{\boldsymbol{T}}$, the prescribed traction like quantity $\bar{\mathfrak{k}}$ and the prescribed fluid potential $\bar{\mu}$. It reads

$$\begin{aligned} P^{\mathrm{ext}}_{\mathcal{B}_0}(\dot{\boldsymbol{\varphi}}, \dot{\mathfrak{I}}) = &\int_{\mathcal{B}_0} \varrho_0 \bar{\boldsymbol{g}} \cdot \dot{\boldsymbol{\varphi}} \, \mathrm{d}V + \int_{\mathcal{B}_{0\boldsymbol{T}}} \bar{\boldsymbol{T}} \cdot \dot{\boldsymbol{\varphi}} \, \mathrm{d}A + \int_{\mathcal{B}_{0\mathfrak{k}}} \bar{\mathfrak{k}} \; \dot{\mathfrak{I}} \, \mathrm{d}A \\ &+ \int_{\mathcal{B}_0} \bar{\boldsymbol{g}} \cdot (\boldsymbol{F}\mathbb{H}) \, \mathrm{d}V + \int_{\mathcal{B}_{0\mu}} \bar{\mu} \; \mathbb{H} \cdot \boldsymbol{N} \, \mathrm{d}A. \end{aligned} \tag{3.56}$$

Based on the rate potential $\Pi_{\mathcal{B}_0}$ (3.52) and the definition of the rate of energy, the dissipation potential and the external loading potential, the variational principle for a two-component system is given as

$$\boxed{\{\dot{\boldsymbol{\varphi}}^*, \mathbb{H}^*, \dot{\mathfrak{I}}^*\} = \arg\Big\{ \inf_{\dot{\boldsymbol{\varphi}} \in \mathcal{W}_{\dot{\boldsymbol{\varphi}}}} \inf_{\mathbb{H} \in \mathcal{W}_\mathbb{H}} \inf_{\dot{\mathfrak{I}} \in \mathcal{W}_\mathfrak{I}} \Pi_{\mathcal{B}_0}(\dot{\boldsymbol{\varphi}}, \mathbb{H}, \dot{\mathfrak{I}}; \boldsymbol{\varphi}, \varrho^f, \mathfrak{I}) \Big\}.} \tag{3.57}$$

Note that in here a minimization with respect to the evolution of the deformation map, the fluid mass flow and the evolution of the internal variables is used. This is considered

as minimization principle. However depending on the specific definition of the model problem, i.e. constitutive functions and internal variables, mixed variational principles can also be derived.

In (3.57) the admissible function space $\mathcal{W}_{\dot{\boldsymbol{\varphi}}}$, $\mathcal{W}_{\dot{\mathbb{H}}}$ and $\mathcal{W}_{\dot{\mathfrak{J}}}$ for the unknown rates are given as

$$\begin{aligned}
\mathcal{W}_{\dot{\boldsymbol{\varphi}}} &= \{\dot{\boldsymbol{\varphi}} \in H^1(\mathcal{B}_0) | \dot{\boldsymbol{\varphi}} = \dot{\bar{\boldsymbol{\varphi}}} \text{ on } \partial\mathcal{B}_{0\boldsymbol{\varphi}}\} \\
\mathcal{W}_{\dot{\mathbb{H}}} &= \{\dot{\mathbb{H}} \in H(\mathrm{Div}, \mathcal{B}_0) | \dot{\mathbb{H}} \cdot \boldsymbol{N} = \dot{\bar{\mathbb{H}}} \text{ on } \partial\mathcal{B}_{0H}\} \\
\mathcal{W}_{\dot{\mathfrak{J}}} &= \{\dot{\mathfrak{J}} \in H^1(\mathcal{B}_0)\}.
\end{aligned} \tag{3.58}$$

Here it is assumed that the function space $H^1(\mathcal{B}_0)$ satisfies the demands originating form the constitutive model formulation, clearly the construction of ψ and ϕ and the definition of the unknown fields.

Performing the variation of $\Pi_{\mathcal{B}_0}$ at a fixed state $\{\boldsymbol{\varphi}, \varrho^f, \mathfrak{J}\}$ and applying the fundamental lemma of the calculus of variations yields the Euler equations of (3.57)

$$\mathrm{Div}(\partial_{\boldsymbol{F}}\psi) + \varrho_0\bar{\boldsymbol{g}} = \boldsymbol{0} \qquad \text{in } \mathcal{B}_0, \tag{3.59}$$

$$\nabla[\partial_{\varrho^f}\psi - \bar{\boldsymbol{g}} \cdot \boldsymbol{\varphi}] + \partial_{\mathbb{H}}\phi \ni \boldsymbol{0} \qquad \text{in } \mathcal{B}_0, \tag{3.60}$$

$$\partial_{\mathfrak{J}}\psi - \mathrm{Div}(\partial_{\nabla\mathfrak{J}}\psi) + \partial_{\dot{\mathfrak{J}}}\phi \ni 0 \qquad \text{in } \mathcal{B}_0, \tag{3.61}$$

$$\partial_{\boldsymbol{F}}\psi\boldsymbol{N} - \bar{\boldsymbol{T}} = \boldsymbol{0} \qquad \text{on } \partial\mathcal{B}_{0\boldsymbol{T}}, \tag{3.62}$$

$$\partial_{\varrho^f}\psi - \bar{\mu} = 0 \qquad \text{on } \partial\mathcal{B}_{0\mu}, \tag{3.63}$$

$$\partial_{\nabla\mathfrak{J}}\psi\boldsymbol{N} - \bar{\mathfrak{k}} = 0 \qquad \text{on } \partial\mathcal{B}_{0\mathfrak{k}}. \tag{3.64}$$

Note that the Euler equations of the variational principle are the governing field equations (3.43)-(3.46) and the Neumann boundary conditions (3.6), (3.8) and $(3.35)_2$. This allows for the conclusion that the variational principle in (3.57) fully characterizes the initial boundary value problem of continuum mechanics of solid-fluid systems.

3.6. Numerical Treatment

Up to this point the initial boundary value problem of continuum mechanics of solid-fluid systems was closed by introducing the constitutive free energy density and the constitutive dissipation potential density. It is derived based on the physical balances laws. Furthermore the initial boundary value problem can be formulated in terms of a variational principle. The variational principle for dissipative solid-fluid systems is expressed as a rate–type formulation.

In order to arrive at a numerical implementation of the material model and the initial boundary value problem two additional steps have to be considered. Since the rate–type variational principle is continuous in time and space (i) a time-discretization has to be performed and then (ii) a space-discretization has to be applied. The time-discretization is based on an algorithmic time integration of the rate–type potential and yields an incremental variational formulation. Based on a finite-element discretization in space the incremental variational formulation can be formulated in terms of discrete values of the unknown fields (deformation map, fluid mass flow and internal variables). This finally leads to a set of linear systems of equations which can be solved by an appropriate algebraic solution scheme.

3.6.1. Incremental Variational Formulation

An algorithmic time integration scheme over a given time step $\tau = [t_n, t_{n+1})$, e.g. backward Euler method, is applied on the rate-type potential in (3.52). This yields the incremental potential $\Pi^{\tau}_{\mathcal{B}_0}$. For a pure Dirichlet problem ($P^{\text{ext}}_{\mathcal{B}_0} = 0$) it reads

$$\Pi^{\tau}_{\mathcal{B}_0}(\boldsymbol{\varphi}, \mathbb{H}, \mathfrak{I}; \mathfrak{I}_n) = \text{Algo}\Big\{ \int_{t_n}^{t_{n+1}} \Pi_{\mathcal{B}_0}(\dot{\boldsymbol{\varphi}}, \mathbb{H}, \dot{\mathfrak{I}}; \boldsymbol{\varphi}, \mathfrak{I}_n)\ \mathrm{d}t \Big\}. \tag{3.65}$$

The incremental potential can be expressed in terms of an incremental potential density π^{τ}

$$\Pi^{\tau}_{\mathcal{B}_0}(\boldsymbol{\varphi}, \mathbb{H}, \mathfrak{I}; \mathfrak{I}_n) = \int_{\mathcal{B}_0} \pi^{\tau}_{\mathcal{B}_0}(\boldsymbol{F}, \mathbb{H}, \mathfrak{I}, \nabla\mathfrak{I}; \mathfrak{I}_n)\ \mathrm{d}V. \tag{3.66}$$

Furthermore the incremental potential density is given in terms of the constitutive free energy density ψ and the incremental version of the constitutive dissipation potential density ϕ^{τ}

$$\int_{\mathcal{B}_0} \pi^{\tau}_{\mathcal{B}_0}(\boldsymbol{F}, \mathbb{H}, \mathfrak{I}, \nabla\mathfrak{I}; \mathfrak{I}_n) = \psi(\boldsymbol{F}, \varrho^f, \mathfrak{I}, \nabla\mathfrak{I}) + \phi^{\tau}(\mathbb{H}, \mathfrak{I}; \mathfrak{I}_n). \tag{3.67}$$

The time-discrete variational principle yields the deformation map, the fluid mass flow and the internal variables as solution of the initial boundary value problem

$$\boxed{\{\boldsymbol{\varphi}^*, \mathbb{H}^*, \mathfrak{I}^*\} = \arg\Big\{ \inf_{\boldsymbol{\varphi}\in\mathcal{W}_{\boldsymbol{\varphi}}} \inf_{\mathbb{H}\in\mathcal{W}_{\mathbb{H}}} \inf_{\mathfrak{I}\in\mathcal{W}_{\mathfrak{I}}} \Pi^{\tau}_{\mathcal{B}_0}(\boldsymbol{\varphi}, \mathfrak{I}; \mathfrak{I}_n) \Big\}.} \tag{3.68}$$

Here the admissible function space for the deformation map, the fluid mass flow vector and the internal variables are given as

$$\begin{aligned} \mathcal{W}_{\boldsymbol{\varphi}} &= \{\boldsymbol{\varphi} \in H^1(\mathcal{B}_0) | \boldsymbol{\varphi} = \bar{\boldsymbol{\varphi}} \text{ on } \partial\mathcal{B}_{0\boldsymbol{\varphi}}\} \\ \mathcal{W}_{\mathbb{H}} &= \{\mathbb{H} \in H(\text{Div}, \mathcal{B}_0) | \mathbb{H} \cdot \boldsymbol{N} = \bar{\mathbb{H}} \text{ on } \partial\mathcal{B}_{0H}\} \\ \mathcal{W}_{\mathfrak{I}} &= \{\mathfrak{I} \in H^1(\mathcal{B}_0)\}. \end{aligned} \tag{3.69}$$

Note that it is assumed that these spaces fulfill the requirements stemming from the constitutive model formulation. This means that the admissible function space in $(3.69)_3$ in particular strongly depends on the definition of the internal variable.

The Euler equations of (3.68) are obtained by applying the calculus of variations for a given $\mathfrak{I}_n$

$$\text{Div}(\partial_{\boldsymbol{F}}\psi) = \boldsymbol{0} \qquad \text{in } \mathcal{B}_0, \tag{3.70}$$

$$\tau\nabla\partial^f_{\varrho}\psi + \partial_{\mathbb{H}}\phi \ni \boldsymbol{0} \qquad \text{in } \mathcal{B}_0, \tag{3.71}$$

$$\partial_{\mathfrak{I}}\psi - \text{Div}(\partial_{\nabla\mathfrak{I}}\psi) + \partial_{\mathfrak{I}}\phi^{\tau} \ni 0 \qquad \text{in } \mathcal{B}_0. \tag{3.72}$$

These three equations are identified as the balance of linear momentum under quasi-static conditions and zero body force, the fluid flow equation under quasi-static conditions and zero body force as well as the evolution equation for the internal variables.

3.6.2. Space-Time-Discrete Finite-Element Formulation

Based on the triangulation $\mathcal{T}^h(\mathcal{B}_0)$ of the domain $\mathcal{B}_0$ a set of non-overlapping finite elements $\mathcal{B}_0^e$ are introduced. With this at hand the domain $\mathcal{B}_0$ can be approximated by $\mathcal{B}_0^h$ in terms of the union of the n_e finite elements

$$\mathcal{B}_0 \approx \mathcal{B}_0^h = \bigcup_{e=1}^{n_e} \mathcal{B}_0^e. \tag{3.73}$$

Within the finite-element method an ansatz for the continuous fields $\boldsymbol{\varphi}(\boldsymbol{X})$, $\mathbb{H}(\boldsymbol{X})$ and $\mathfrak{I}(\boldsymbol{X})$ is made. This yields to an approximation of these fields based on discrete values at given interpolation points and corresponding basis/shape functions

$$\begin{aligned}
\boldsymbol{\varphi}(\boldsymbol{X}) &\approx \boldsymbol{\varphi}^h(\boldsymbol{X}) = \sum_{i=1}^{n_{\boldsymbol{\varphi}}} N_{\boldsymbol{\varphi}}^i(\boldsymbol{X}) \boldsymbol{\varphi}^i, \\
\mathbb{H}(\boldsymbol{X}) &\approx \mathbb{H}^h(\boldsymbol{X}) = \sum_{i=1}^{n_{\mathbb{H}}} \boldsymbol{N}_{\mathbb{H}}^i(\boldsymbol{X}) H^i, \\
\mathfrak{I}(\boldsymbol{X}) &\approx \mathfrak{I}^h(\boldsymbol{X}) = \sum_{i=1}^{n_{\mathfrak{I}}} N_{\mathfrak{I}}^i(\boldsymbol{X}) \mathfrak{I}^i,
\end{aligned} \tag{3.74}$$

where $n_{\boldsymbol{\varphi}}$ is number of interpolation points of the deformation map within one element. The basis function for the i-th interpolation point of the deformation map is denoted as $N_{\boldsymbol{\varphi}}^i(\boldsymbol{X})$. The discrete value of the deformation map at the i-th interpolation point is given as $\boldsymbol{\varphi}^i$. Similarly the number of interpolation points, basis function and the discrete values of the fluid mass flow as well as the internal variables are denoted as $n_{\mathbb{H}}$, $\boldsymbol{N}_{\mathbb{H}}^i(\boldsymbol{X})$ and H^i and $n_{\mathfrak{I}}$, $N_{\mathfrak{I}}^i(\boldsymbol{X})$ and $\mathfrak{I}^i$.

Note that the basis functions of the fluid mass flow are vectors while the discrete values are scalars, representing the flux over the element edges. This arises from the definition of the admissible function space for the fluid mass flow in (3.69) yielding a Raviart–Thomas–type finite element formulation.

The basis functions can be represented as a matrix. For a quantity a of the dimension s_a and with n_a interpolation points this matrix representation reads

$$\mathbf{N}_a(\boldsymbol{X}) = \begin{bmatrix} N_1(\boldsymbol{X}) & 0 & 0 & & N_{n_a}(\boldsymbol{X}) & 0 & 0 \\ 0 & \ddots & \vdots & \dots & 0 & \ddots & \vdots \\ 0 & \cdots & N_1(\boldsymbol{X}) & & 0 & \cdots & N_{n_a}(\boldsymbol{X}) \end{bmatrix} \tag{3.75}$$

The corresponding vector of the discrete values for a quantity a reads

$$\mathbf{d}_a = \begin{bmatrix} a_1^1 & a_2^1 & \dots & a_{s_a}^{n_a} \end{bmatrix}^T. \tag{3.76}$$

The definition of the matrix representation of the basis functions and the vector representation of the discrete values allows for a compact notation for the interpolation of the discrete values of the deformation map and the internal variables. Hence, the approximated fields in (3.74) can be represented as

$$\begin{bmatrix} \boldsymbol{\varphi}^h(\boldsymbol{X}) \\ \mathbb{H}^h(\boldsymbol{X}) \\ \mathfrak{I}^h(\boldsymbol{X}) \end{bmatrix} = \mathbf{N}\mathbf{d} \quad \text{with} \quad \mathbf{N} = \begin{bmatrix} \mathbf{N}_{\boldsymbol{\varphi}}(\boldsymbol{X}) \\ \mathbf{N}_{\mathbb{H}}(\boldsymbol{X}) \\ \mathbf{N}_{\mathfrak{I}}(\boldsymbol{X}) \end{bmatrix} \quad \text{and} \quad \mathbf{d} = \begin{bmatrix} \mathbf{d}_{\boldsymbol{\varphi}} \\ \mathbf{d}_{\mathbb{H}} \\ \mathbf{d}_{\mathfrak{I}} \end{bmatrix}. \tag{3.77}$$

Here the global interpolation matrix $\mathbf{N}$ and the global discrete values vector $\mathbf{d}$ was introduced. Inserting the latter definition of the interpolation into the incremental potential (3.66) yields the *space-time-discrete potential* $\Pi^{\tau h}$

$$\Pi^{\tau h}_{\mathcal{B}_0}(\mathbf{d}) = \int_{\mathcal{B}_0} \pi^{\tau h}_{\mathcal{B}_0}(\mathfrak{C}^h)\, \mathrm{d}V \quad \text{with} \quad \mathfrak{C}^h = \mathbf{B}\mathbf{d} \tag{3.78}$$

It is expressed in terms of the space-time-discrete potential density $\pi^{\tau h}_{\mathcal{B}_0}$ and the generalized interpolation matrix $\mathbf{B}$. The latter is given as

$$\mathbf{B} = \begin{bmatrix} \partial_{\boldsymbol{X}} \mathrm{N}_{\boldsymbol{\varphi}}(\boldsymbol{X}) \\ \boldsymbol{N}_{\mathbb{H}}(\boldsymbol{X}) \\ \mathrm{Div}\left(\boldsymbol{N}_{\mathbb{H}}(\boldsymbol{X})\right) \\ \mathrm{N}_{\mathfrak{I}}(\boldsymbol{X}) \\ \partial_{\boldsymbol{X}} \mathrm{N}_{\mathfrak{I}}(\boldsymbol{X}) \end{bmatrix} \quad \text{and} \quad \mathfrak{C}^h = \begin{bmatrix} \boldsymbol{F}^h \\ \mathbb{H}^h \\ \mathrm{Div}(\mathbb{H}^h) \\ \mathfrak{I}^h \\ \nabla \mathfrak{I}^h \end{bmatrix} = \mathbf{B}\mathbf{d} \tag{3.79}$$

It is used to obtain also the gradients of the unknown fields based on the derivative of the basis functions. Note that the definition and shape of the generalized interpolation matrix $\mathbf{B}$ is strongly dependent on the definition of the constitutive free energy density and the constitutive dissipation potential density.

Based on the definition of space-time-discrete potential the variational principle for the space-time-discrete problem can be stated as

$$\boxed{\mathbf{d}^* = \arg\left\{ \inf_{\mathbf{d}} \Pi^{\tau h}_{\mathcal{B}_0}(\mathbf{d}) \right\}.} \tag{3.80}$$

Solving the latter algebraic minimization principle yields the discrete values $\mathbf{d}^*$. Applying the calculus of variations on (3.80) leads to the following condition

$$\mathbf{R} := \Pi^{\tau h}_{\mathcal{B}_0,\mathbf{d}} = \int_{\mathcal{B}_0} \mathbf{B}^T \mathbf{S}\, \mathrm{d}V = \boldsymbol{0}, \tag{3.81}$$

where the array $\mathbf{S}$ contains the partial derivatives of the space-time-discrete potential density $\pi^{\tau h}_{\mathcal{B}_0}$. Under the assumption of a smooth dissipation potential density it is derived as

$$\mathbf{S} := \partial_{\mathfrak{C}^h} \pi^{\tau h}_{\mathcal{B}_0} = \begin{bmatrix} \psi_{,\boldsymbol{F}^h} \\ \tau \nabla \psi_{,\mathrm{Div}(\mathbb{H}^h)} \\ \phi^{\tau}_{,\mathbb{H}^h} \\ \psi_{,\mathfrak{I}^h} + \phi^{\tau}_{,\mathfrak{I}^h} \\ \psi_{,\nabla \mathfrak{I}^h} \end{bmatrix} \tag{3.82}$$

Since the system of equations (3.81) is in general a non–linear system a linearization is applied on (3.81) yielding

$$\mathrm{Lin}(\mathbf{R}) = \mathbf{R}(\mathbf{d}^i) + \partial_{\mathbf{d}} \mathbf{R}(\mathbf{d}^i) \cdot (\mathbf{d}^{i+1} - \mathbf{d}^i) = \boldsymbol{0}. \tag{3.83}$$

where the index i is the iteration counter. The linearized problem is solved by a Newton–Raphson-type iteration

$$\mathbf{d} \leftarrow \mathbf{d} - \mathbf{K}^{-1}\mathbf{R} \quad \text{with} \quad \mathbf{K} := \partial_{\mathbf{d}} \mathbf{R} = \Pi^{\tau h}_{\mathcal{B}_0,\mathbf{d}\mathbf{d}} = \int_{\mathcal{B}} \mathbf{B}^T \mathbf{C} \boldsymbol{B}\, \mathrm{d}V. \tag{3.84}$$

The array $\mathbf{C}$ contains the second derivatives of the space-time-discrete potential density. These are identical to the first derivatives of $\mathbf{S}$. Under the assumption of a smooth dissipation potential density it is given as

$$
\begin{aligned}
\mathbf{C} :&= \partial^2_{\boldsymbol{\mathcal{C}}^h} \pi^{\tau h}_{\mathcal{B}_0} \\
&= \partial_{\boldsymbol{\mathcal{C}}^h} \mathbf{S} \\
&= \begin{bmatrix}
\psi_{,\boldsymbol{F}^h \boldsymbol{F}^h} & \tau \psi_{,\boldsymbol{F}\,\mathrm{Div}(\mathbb{H}^h)} & 0 & \psi_{,\boldsymbol{F}^h \mathfrak{J}^h} & \psi_{,\boldsymbol{F}^h \nabla \mathfrak{J}^h} \\
\tau \psi_{,\mathrm{Div}(\mathbb{H}^h)\boldsymbol{F}^h} & \tau \psi_{,\mathrm{Div}(\mathbb{H}^h)\,\mathrm{Div}(\mathbb{H}^h)} & 0 & 0 & 0 \\
0 & 0 & \psi_{,\mathbb{H}^h \mathbb{H}^h} & 0 & 0 \\
\psi_{,\mathfrak{J}^h \boldsymbol{F}^h} & 0 & 0 & \psi_{,\mathfrak{J}^h \mathfrak{J}^h} + \phi^{\tau}_{,\mathfrak{J}^h \mathfrak{J}^h} & \psi_{,\mathfrak{J}^h, \nabla \mathfrak{J}^h} \\
\psi_{,\nabla \mathfrak{J}^h \boldsymbol{F}^h} & 0 & 0 & \psi_{,\nabla \mathfrak{J}^h \mathfrak{J}^h} & \psi_{,\nabla \mathfrak{J}^h \nabla \mathfrak{J}^h}
\end{bmatrix} .
\end{aligned}
\tag{3.85}
$$

Note that for the general case of a non–smooth dissipation potential density an additional algorithmic treatment (such as return mapping schemes, active-set methods, etc.) has to be applied, see Simo and Taylor 1986, Hintermüller et al. 2002 or Heister et al. 2015.

The matrix $\mathbf{K}$ has a sparse nature. In order to solve the system for one iteration step, direct spares solvers can be used. However by increasing the problem size by a fine discretization in space it might become insufficient to use such solvers. Then other techniques such as iterative solvers or matrix-free methods can be used, see e.g. Axelsson 1976, Wriggers 2008 or Arndt et al. 2020.

Bibliography

Abbo, A. J. and S. W. Sloan (1995). "A smooth hyperbolic approximation to the Mohr-Coulomb yield criterion". In: *Computers & Structures* 54.3, pp. 427–441.

Adachi, J., E. Siebrits, A. Peirce, and J. Desroches (2007). "Computer simulation of hydraulic fractures". In: *International Journal of Rock Mechanics & Mining Sciences* 44, pp. 739–757.

Aldakheel, F., N. Noii, T. Wick, and P. Wriggers (2020). "A global-local approach for hydraulic phase-field fracture in poroelastic media". In: *arXiv preprint arXiv:2001.06055*.

Alessi, R., J.-J. Marigo, and S. Vidoli (2015). "Gradient damage models coupled with plasticity: Variational formulation and main properties". In: *Mechanics of Materials* 80, pp. 351–367.

Ambati, M., T. Gerasimov, and L. de Lorenzis (2015). "Phase-field modeling of ductile fracture". In: *Computational Mechanics* 55, pp. 1017–1040.

Ambati, M., R. Kruse, and L. de Lorenzis (2016). "A phase-field model for ductile fracture at finite strains and its experimental verification". In: *Computational Mechanics* 57.1, pp. 149–167.

Ambrosio, L. and V. M. Tortorelli (1990). "Approximation of functionals depending on jumps by elliptic functionals via Γ-convergence". In: *Communications on Pure and Applied Mathematics* 43, pp. 999–1036.

Arndt, D., W. Bangerth, B. Blais, T. C. Clevenger, M. Fehling, A. V. Grayver, T. Heister, L. Heltai, M. Kronbichler, M. Maier, et al. (2020). "The deal. II library, version 9.2". In: *Journal of Numerical Mathematics* 28.3, pp. 131–146.

Aslan, O., N. Cordero, A. Gaubert, and S. Forest (2011). "Micromorphic approach to single crystal plasticity and damage". In: *International Journal of Engineering Science* 49, pp. 1311–1325.

Axelsson, O. (1976). "A class of iterative methods for finite element equations". In: *Computer Methods in Applied Mechanics and Engineering* 9.2, pp. 123–137.

Babuška, I. (1973). "The finite element method with Lagrangian multipliers". In: *Numerische Mathematik* 20, pp. 179–192.

Bear, J. (1972). *Dynamics of Fluids in Porous Media*. Dover Publications, New York.

Bear, J. and Y. Bachmat (1991). *Introduction to modelling of transport phenomena in porous media*. Kluwer Academic Publishers, Dordrecht.

Belytschko, T., J. Fish, and E. Engelmann (1988). "A Finite Element with Embedded Localization Zones". In: *Computer Methods in Applied Mechanics and Engineering* 70, pp. 59–89.

Besson, J. (2010). "Continuum Models of Ductile Fracture: A Review". In: *International Journal of Damage Mechanics* 19, pp. 3–52.

Biot, M. A. (1941). "General theory of three-dimensional consolidation". In: *Journal of Applied Physics* 12, pp. 155–164.

Biot, M. A. (1965a). *Mechanics of Incremental Deformations*. John Wiley & Sons Inc., New York.

Biot, M. A. (1965b). *Mechanics of incremental deformations*. Wiley.

Biot, M. A. (1977). "Variational Lagrangian-thermodynamics of nonisothermal finite strain mechanics of porous solids and thermomolecular diffusion". In: *International Journal of Solids and Structures* 13.6, pp. 579–597.

Bluhm, J. and R. de Boer (1997). "The volume fraction concept in the porous media theory". In: *ZAMM-Journal of Applied Mathematics and Mechanics/Zeitschrift für Angewandte Mathematik und Mechanik* 77.8, pp. 563–577.

Bourdin, B., G. A. Francfort, and J.-J. Marigo (2008). *The Variational Approach to Fracture*. Springer.

Bourdin, B., C. P. Chukwudozie, and K. Yoshioka (2012). "A variational approach to the numerical simulation of hydraulic fracturing". In: *SPE Annual Technical Conference and Exhibition*. Society of Petroleum Engineers.

Brezzi, F. (1974). "On the existence, uniqueness and approximation of saddle-point problems arising from lagrangian multipliers". In: *Revue française d'automatique, informatique, recherche opérationnelle. Analyse numérique* 8, pp. 129–151.

Cajuhi, T., L. Sanavia, and L. de Lorenzis (2018). "Phase-field modeling of fracture in variably saturated porous media". In: *Computational Mechanics* 61.3, pp. 299–318.

Castonguay, S. T., M. E. Mear, R. H. Dean, and J. H. Schmidt (2013). "Predictions of the growth of multiple interacting hydraulic fractures in three dimensions". In: *SPE annual technical conference and exhibition*. Society of Petroleum Engineers.

Chaboche, J. L. (1981). "Continuous Damage Mechanics – A Tool to Describe Phenomena Before Crack Initiation". In: *Nuclear Engineering and Design* 64, pp. 233–247.

Chaboche, J. L. (1988). "Continuum Damage Mechanics: Part 1 – General Concepts". In: *Journal of Applied Mechanics* 55, pp. 59–72.

Chukwudozie, C., B. Bourdin, and K. Yoshioka (2019). "A variational phase-field model for hydraulic fracturing in porous media". In: *Computer Methods in Applied Mechanics and Engineering* 347, pp. 957–982.

Coleman, B. D. and W. Noll (1959). "On the thermostatics of continuous media". In: *Archive for rational mechanics and analysis* 4.1, pp. 97–128.

Comi, C. (1999). "Computational modelling of gradient-enhanced damage in quasi-brittle materials". In: *Mechanics of Cohesive-frictional Materials* 4.1, pp. 17–36. ISSN: 1099-1484.

Coulomb, C. A. (1776). "Essai sur une application des regles de maximis et minimis a quelques problemes de statique relatifs a l'architecture". In: *Mémoires de l'Academie Royale Des Sciences* 7, pp. 343–387.

Coussy, O. (2004). *Poromechanics*. John Wiley & Sons, Chichester.

Dahi-Taleghani, A. and J. E. Olson (2011). "Numerical modeling of multistranded-hydraulic-fracture propagation: accounting for the interaction between induced and natural fractures". In: *SPE journal* 16.03, pp. 575–581.

Damjanac, B., I. Gil, M. Pierce, M. Sanchez, A. Van As, and J. McLennan (2010). "A new approach to hydraulic fracturing modeling in naturally fractured reservoirs". In: *44th US Rock Mechanics Symposium and 5th US-Canada Rock Mechanics Symposium*. American Rock Mechanics Association.

Darcy, H. (1856). *Les fountaines publiques de la ville de Dijon*. Victor Dalmont, Paris.

de Boer, R. (1988). "On plastic deformation of soils". In: *International Journal of Plasticity* 4.4, pp. 371–391.

de Boer, R. (2000). *Theory of Porous Media*. Springer, Berlin.

de Borst, R., J. Pamin, and M. G. D. Geers (1999). "On coupled gradient-dependent plasticity and damage theories with a view to localization analysis". In: *European Journal of Mechanics - A/Solids* 18, pp. 939–962.

de Borst, R. and C. V. Verhoosel (2016). "Gradient damage vs phase-field approaches for fracture: Similarities and differences". In: *Computer Methods in Applied Mechanics and Engineering* 312, pp. 78–94.

Detournay, E. and A. H.-D. Cheng (1993). "Fundamentals of poroelasticity". In: *Comprehensive Rock Engineering: Principles, Practice and Projects, Vol. II, Analysis and Design Method*. Ed. by C. Fairhurst. Pergamon Press. Chap. 5, pp. 113–171.

Dimitrijevic, B. J. and K. Hackl (2011). "A regularization framework for damage-plasticity models via gradient enhancement of the free energy". In: *International Journal for Numerical Methods in Biomedical Engineering* 27, pp. 1199–1210.

Drucker, D. C. and W. Prager (1952). "Soil mechanics and plastic analysis or limit design". In: *Quarterly of applied mathematics* 10.2, pp. 157–165.

Duda, F. P., A. Ciarbonetti, P. J. Sánchez, and A. E. Huespe (2015). "A phase-field/gradient damage model for brittle fracture in elastic-plastic solids". In: *International Journal of Plasticity* 65, pp. 269–296.

Ehlers, W. (1995). "A single-surface yield function for geomaterials". In: *Archive of Applied Mechanics* 65.4, pp. 246–259.

Ehlers, W. (2002). "Foundations of multiphasic and porous materials". In: *Porous Media: Theory, Experiments and Numerical Applications*. Ed. by W. Ehlers and J. Bluhm. Springer-Verlag, Berlin, pp. 3–86.

Ehlers, W. and C. Luo (2017). "A phase-field approach embedded in the Theory of Porous Media for the description of dynamic hydraulic fracturing". In: *Computer Methods in Applied Mechanics and Engineering* 315, pp. 348–368.

Ehlers, W. and C. Luo (2018). "A phase-field approach embedded in the Theory of Porous Media for the description of dynamic hydraulic fracturing, Part II: The crack-opening indicator". In: *Computer Methods in Applied Mechanics and Engineering* 341, pp. 429–442.

Francfort, G. A. and J.-J. Marigo (1998). "Revisiting brittle fracture as an energy minimization problem". In: *Journal of the Mechanics and Physics of Solids* 46, pp. 1319–1342.

Frémond, M. (2002). *Non-Smooth Thermomechanics*. Springer.

Frémond, M. and B. Nedjar (1996). "Damage, gradient of damage, and principle of virtual power". In: *International Journal of Solids and Structures* 33, pp. 1083–1103.

Gajo, A. and R. Denzer (2011). "Finite element modelling of saturated porous media at finite strains under dynamic conditions with compressible constituents". In: *International journal for numerical methods in engineering* 85.13, pp. 1705–1736.

Gordeliy, E. and A. Peirce (2013a). "Coupling schemes for modeling hydraulic fracture propagation using the XFEM". In: *Computer Methods in Applied Mechanics and Engineering* 253, pp. 305–322.

Gordeliy, E. and A. Peirce (2013b). "Implicit level set schemes for modeling hydraulic fractures using the XFEM". In: *Computer Methods in Applied Mechanics and Engineering* 266, pp. 125–143.

Griffith, A. A. (1920). "The phenomena of rupture and flow in solids". In: *Philosophical Transactions of the Royal Society London A* 221, pp. 163–198.

Griffith, A. A. (1924). "The Theory of Rupture". In: *Proceedings of the First International Congress for Applied Mechanics, Delft*. Ed. by C. B. Biezeno and J. M. Burgers, pp. 55–63.

Gupta, P. and C. A. Duarte (2014). "Simulation of non-planar three-dimensional hydraulic fracture propagation". In: *International Journal for numerical and analytical methods in geomechanics* 38, pp. 1397–1430.

Gurson, A. L. (1975). "Plastic flow and fracture behavior of ductile materials incorporating void nucleation, growth and coalescence". PhD thesis. Division of Engineering, Brown University.

Gurtin, M. E., E. Fried, and L. Anand (2010). *The Mechanics and Thermodynamics of Continua*. Cambridge University Press.

Hakim, V. and A. Karma (2009). "Laws of crack motion and phase-field models of fracture". In: *Journal of the Mechanics and Physics of Solids* 57, pp. 342–368.

Heider, Y. and B. Markert (2017). "A phase-field modeling approach of hydraulic fracture in saturated porous media". In: *Mechanics Research Communications* 80, pp. 38–46.

Heister, T., M. F. Wheeler, and T. Wick (2015). "A primal-dual active set method and predictor-corrector mesh adaptivity for computing fracture propagation using a phase-field approach". In: *Computer Methods in Applied Mechanics and Engineering* 290, pp. 466–495.

Hill, R. (1950). *The Mathematical Theory of Plasticity*. Oxford University Press.

Hintermüller, M., K. Ito, and K. Kunisch (2002). "The primal-dual active set strategy as a semismooth Newton method". In: *SIAM Journal on Optimization* 13.3, pp. 865–888.

Holzapfel, G. A. (2000). *Nonlinear solid mechanics*. John Wiley & Sons.

Irwin, G. R. (1957). "Analysis of stresses and strains near the end of a crack traversing a plate". In: *Journal of Applied Mechanics* 24, pp. 361–364.

Irwin, G. R. (1958). "Fracture". In: *Encyclopedia of Physics*. Ed. by S. Flügge. Vol. 6, Elasticity and Plasticity. Springer, pp. 551–590.

Johnson, E. and M. P. Cleary (1991). "Implications of recent laboratory experimental results for hydraulic fractures". In: *Low permeability reservoirs symposium*. Society of Petroleum Engineers.

Johnson, G. and W. Cook (1985). "Fracture characteristics of three metals subjected to various strains, strain rates, temperatures and pressures". In: *Engineering Fracture Mechanics* 21, pp. 31–48.

Kachanov, L. (1986). *Introduction to continuum damage mechanics*. Vol. 10. Springer Science & Business Media.

Kienle, D., F. Aldakheel, and M.-A. Keip (2019). "A finite-strain phase-field approach to ductile failure of frictional materials". In: *International Journal of Solids and Structures* 172, pp. 147–162.

Kuhn, C. and R. Müller (2010). "A continuum phase field model for fracture". In: *Engineering Fracture Machanics* 77, pp. 3625–3634.

Lambrecht, M. and C. Miehe (1999). "Two non-associated isotropic elastoplastic hardening models for frictional materials". In: *Acta Mechanica* 135, pp. 73–90.

Lambrecht, M. and C. Miehe (2001). "A note on formulas for localized failure of frictional materials in compression and biaxial loading modes". In: *International Journal for Numerical and Analytical Methods in Geomechanics* 25, pp. 955–971.

Leblond, J., G. Perrin, and P. Suquet (1994). "Exact results and approximate models for porous viscoplastic solids". In: *International Journal of Plasticity* 3, pp. 213–235.

Lemaitre, J. (1984). "How to Use Damage Mechanics". In: *Nuclear Engineering and Design* 80, pp. 233–245.

Lemaitre, J. (1985). "A Continuous Damage Mechanics Model for Ductile Fracture". In: *Journal of Engineering Materials and Technology* 107, pp. 83–89.

Lemaitre, J. and J.-L. Chaboche (1990). *Mechanics of Solid Materials*. Cambridge University Press.

Li, H., M. Fu, J. Lu, and H. Yang (2011). "Ductile fracture: Experiments and computations". In: *International Journal of Plasticity* 27, pp. 147–180.

Malvern, L. E. (1969). "Introduction to the Mechanis of a Continous Medium". In: *Prentice-Hall, New Jersey*.

Marsden, J. E. and T. J. R. Hughes (1983). *Mathematical foundations of elasticity*. Prentice-Hall.

Mauthe, S. (2017). *Variational multiphysics modeling of diffusion in elastic solids and hydraulic fracturing in porous media*. Institut für Mechanik (Bauwesen), Lehrstuhl für Kontinuumsmechanik, Universität Stuttgart.

Mauthe, S. and C. Miehe (2017). "Hydraulic fracture in poro-hydro-elastic media". In: *Mechanics Research Communications* 80, pp. 69–83.

Miehe, C. (2002). "Strain-driven homogenization of inelastic microstructures and composites based on an incremental variational formulation". In: *International Journal for Numerical Methods in Engineering* 55, pp. 1285–1322.

Miehe, C. (2005). "Einführung in die Kontinuumsmechanik und Materialtheorie". In: *Lecture Notes, Universität Stuttgart*.

Miehe, C. (2006). "Geometrische Methoden der Nichtlinearen Kontinuumsmechanik und Kontinuumsthermodynamik". In: *Lecture Notes, Universität Stuttgart*.

Miehe, C., M. Hofacker, L.-M. Schänzel, and F. Aldakheel (2015a). "Phase Field Modeling of Fracture in Multi-Physics Problems. Part II. Brittle-to-Ductile Failure Mode Transition and Crack Propagation in Thermo-Elastic-Plastic Solids". In: *Computer Methods in Applied Mechanics and Engineering* 294, pp. 486–522.

Miehe, C., D. Kienle, F. Aldakheel, and S. Teichtmeister (2016). "Phase field modeling of fracture in porous plasticity: A variational gradient-extended Eulerian framework for the macroscopic analysis of ductile failure". In: *Computer Methods in Applied Mechanics and Engineering* 312, pp. 3–50.

Miehe, C., S. Mauthe, and S. Teichtmeister (2015b). "Minimization principles for the coupled problem of Darcy-Biot-type fluid transport in porous media linked to phase field modeling of fracture". In: *Journal of the Mechanics and Physics of Solids* 82, pp. 186–217.

Miehe, C., F. Welschinger, and M. Hofacker (2010). "Thermodynamically consistent phase-field models of fracture: Variational principles and multi-field FE implementations". In: *International Journal for Numerical Methods in Engineering* 83, pp. 1273–1311.

Mikelić, A., M. F. Wheeler, and T. Wick (2015a). "A Phase-Field Method for Propagating Fluid-Filled Fractures Coupled to a Surrounding Porous Medium". In: *SIAM Multiscale Modeling Simulation* 13.1, pp. 367–398.

Mikelić, A., M. F. Wheeler, and T. Wick (2015b). "Phase-field modeling of a fluid-driven fracture in a poroelastic medium". In: *Computational Geosciences*.

Mikelić, A., M. F. Wheeler, and T. Wick (2015c). "A phase-field method for propagating fluid-filled fractures coupled to a surrounding porous medium". In: *Multiscale Modeling & Simulation* 13.1, pp. 367–398.

Mumford, D. and J. Shah (1989). "Optimal approximations by piecewise smooth functions and associated variational problems". In: *Communications on Pure and Applied Mathematics* 42, pp. 577–685.

Nedjar, B. (2001). "Elastoplastic-damage modelling including the gradient of damage: formulation and computational aspects". In: *Inernational Journal of Solids and Structures* 38, pp. 5421–5451.

Needleman, A. and V. Tvergaard (1984). "An analysis of ductile rupture in notched bars". In: *Journal of the Mechanics and Physics of Solids* 32.6, pp. 461–490.

Peerlings, R. H. J., R. de Borst, W. A. M. Brekelmans, and J. H. P. de Vree (1996). "Gradient Enhanced Damage for Quasi–Brittle Materials". In: *International Journal for Numerical Methods in Engineering* 39, pp. 3391–3403.

Pham, K., H. Amor, J.-J. Marigo, and C. Maurini (2011). "Gradient damage models and their use to approximate brittle fracture". In: *International Journal of Damage Mechanics* 20.4, pp. 618–652.

Pise, M., J. Bluhm, and J. Schröder (2019). "Elasto-plastic phase-field model of hydraulic fracture in saturated binary porous media". In: *International Journal for Multiscale Computational Engineering* 17.2.

Ponte Castañeda, P. and M. Zaidman (1994). "Constitutive models for porous materials with evolving microstructure". In: *Journal of the Mechanics and Physics of Solids* 42, pp. 1459–1497.

Raviart, P. A. and J. M. Thomas (1977). "Primal hybrid finite element methods for 2nd order elliptic equations". In: *Mathematics of computation* 31.138, pp. 391–413.

Reusch, F., B. Svendsen, and D. Klingbeil (2003). "A non-local extension of Gurson-based ductile damage modeling". In: *Computational Materials Science* 26, pp. 219–229.

Rice, J. R. and D. M. Tracey (1969). "On the ductile enlargement of voids in triaxial stress fields". In: *Journal of the Mechanics and Physics of Solids* 17, pp. 201–217.

Rousselier, G. (1987). "Ductile fracture models and their potential in local approach of fracture". In: *Nuclear Engineering and Design* 105, pp. 97–111.

Saanouni, K. and M. Hamed (2013). "Micromorphic approach for finite gradient-elasto-plasticity fully coupled with ductile damage: Formulation and computational aspects". In: *International Journal of Solids and Structures* 50, pp. 2289–2309.

Santillán, D., R. Juanes, and L. Cueto-Felgueroso (2017). "Phase field model of fluid-driven fracture in elastic media: Immersed-fracture formulation and validation with analytical solutions". In: *Journal of Geophysical Research: Solid Earth* 122.4, pp. 2565–2589.

Schröder, J. and P. Neff (2010). *Poly-, quasi-and rank-one convexity in applied mechanics*. Vol. 516. Springer Science & Business Media.

Shauer, N. and C. A. Duarte (2019). "Improved algorithms for generalized finite element simulations of three-dimensional hydraulic fracture propagation". In: *International Journal for Numerical and Analytical Methods in Geomechanics* 43.18, pp. 2707–2742.

Simo, J. C. and J. W. Ju (1987a). "Strain– and Stress–Based Continuum Damage Models– I. Formulation". In: *International Journal of Solids and Structures* 23, pp. 821–840.

Simo, J. C. and J. W. Ju (1987b). "Strain– and Stress–Based Continuum Damage Models– II. Computational Aspects". In: *International Journal of Solids and Structures* 23, pp. 841–869.

Simo, J. C. and G. Meschke (1993). "A new class of algorithms for classical plasticity extended to finite strains. Application to geomaterials". In: *Computational Mechanics* 11.4, pp. 253–278.

Simo, J. C. and R. L. Taylor (1986). "A return mapping algorithm for plane stress elastoplasticity". In: *International Journal for Numerical Methods in Engineering* 22.3, pp. 649–670.

Sneddon, I. N. and M. Lowengrub (1969). *Crack problems in the classical theory of elasticity*. John Wiley & Sons, Inc., New York.

Spencer, A. J. M. (2004). *Continuum mechanics*. Courier Corporation.

Suquet, P. (1992). "On Bounds for the Overall Potential of Power Law Materials Containing Voids with an Arbitrary Shape". In: *Mechanics Research Communications* 19, pp. 51–58.

Svendsen, B. (2004). "On thermodynamic- and variational-based formulations of models for inelastic continua with internal lengthscales". In: *Computer Methods in Applied Mechanics and Engineering* 193.48–51, pp. 5429–5452.

Teichtmeister, S., S. Mauthe, and C. Miehe (2019). "Aspects of finite element formulations for the coupled problem of poroelasticity based on a canonical minimization principle". In: *Computational Mechanics* 64.3, pp. 685–716.

Terzaghi, K. (1925). *Erdbaumechanik auf bodenphysikalischer Grundlage*. F. Deuticke.

Tresca, H. E. (1864). *Sur l'ecoulement des corps solides soumis a de fortes pressions*. Imprimerie de Gauthier-Villars, successeur de Mallet-Bachelier, rue de Seine-Saint-Germain.

Truesdell, C. and W. Noll (1965). "Handbuch der Physik Bd. III/3". In: ed. by S. Flügge. Springer, Berlin. Chap. The nonlinear field theories of mechanics.

Vermeer, P. and R. de Borst (1984). "Non-associated plasticity for soils, concrete and rock". In: *Heron* 29.3, pp. 1–64.

von Mises, R. (1913). "Mechanik der festen Körper im plastisch-deformablen Zustand". In: *Nachrichten von der Gesellschaft der Wissenschaften zu Göttingen, Mathematisch-Physikalische Klasse* 1913, pp. 582–592.

Whitaker, S. (1986). "Flow in porous media I: A theoretical derivation of Darcy's law". In: *Transport in porous media* 1.1, pp. 3–25.

Wilson, Z. A. and C. M. Landis (2016). "Phase-Field Modeling of Hydraulic Fracture". In: *ICES Report* 16-10.

Wriggers, P. (2008). *Nonlinear finite element methods*. Springer Science & Business Media.

Wu, T. and L. de Lorenzis (2016). "A phase-field approach to fracture coupled with diffusion". In: *Computer Methods in Applied Mechanics and Engineering* 312, pp. 196–223.

Ziegler, H. and C. Wehrli (1987). "The derivation of constitutive relations from the free energy and the dissipation function". In: *Advances in Applied Mechanics* 25, pp. 183–238.

Zienkiewicz, O. C., C. Humpheson, and R. W. Lewis (1975). "Associated and non-associated visco-plasticity and plasticity in soil mechanics". In: *Geotechnique* 25.4, pp. 671–689.

— Part II —

Publications

In this part follwing publications are provided:

- Miehe, C., Kienle, D., Aldakheel, F. & Teichtmeister, S. [2016], *Phase field modeling of fracture in porous plasticity: A variational gradient-extended Eulerian framework for the macroscopic analysis of ductile failure.* Computer Methods in Applied Mechanics and Engineering, 312: 3–50, **published (03.10.2016)**

- Kienle, D., Aldakheel, F. & Keip, M.-A. [2019] *A finite-strain phase-field approach to ductile failure of frictional materials.* International Journal of Solids and Structures, 172: 147–162, **published (01.11.2019)**

- Kienle, D. & Keip, M.-A. [2021] *A variational minimization formulation for hydraulically induced fracturing in elastic-plastic solids.* International Journal of Fracture, 237: 203–227 **published (15.05.2021)**

Chapter 4

Phase Field Modeling of Fracture in Porous Plasticity: A Variational Gradient-Extended Eulerian Framework For the Macroscopic Analysis of Ductile Failure

C. Miehe*, D. Kienle, F. Aldakheel & S. Teichtmeister

Institute of Applied Mechanics, Chair I

University of Stuttgart, 70550 Stuttgart, Pfaffenwaldring 7, Germany

Abstract This work outlines a rigorous variational-based framework for the phase field modeling of fracture in isotropic porous solids undergoing large elastic-plastic strains. It extends the recent works Miehe et al. 2015a, 2016b to a particular formulation of isotropic porous plasticity. The phase field approach regularizes sharp crack surfaces within a pure continuum setting by a specific *gradient damage modeling* with geometric features rooted in fracture mechanics. A *gradient plasticity model* for porous plasticity with a simple growth law for the evolution of the void fraction is developed, and linked to a failure criterion in terms of the local elastic-plastic work density that drives the fracture phase field. It is shown that this approach is able to model basic phenomena of ductile failure such as *cup-cone failure surfaces* in terms of only two material parameters on the side of damage mechanics: a *critical work density* that triggers the onset of damage and a *shape parameter* that governs the postcritical damage up to fracture. The formulation includes two independent length scales which regularize both the plastic response as well as the crack discontinuities. This allows to design damage zones of ductile fracture to be inside of plastic zones or vice versa, and guarantees on the computational side a mesh objectivity in post-critical ranges. The key aspect that allows to construct a *variational theory for*

*Corresponding Author. Tel.: +4971168566379, Fax: +4971168566347. E-mail address: cm@mechbau.uni-stuttgart.de (C. Miehe)

porous plasticity at fracture is the use of an *Eulerian constitutive setting*, where the yield function is formulated in terms of the *Kirchhoff stress*. Here, we exploit the fact that this stress approximates an *effective stress* that drives the plasticity in the matrix of the porous solid. The coupling of gradient plasticity to gradient damage is realized by a constitutive work density function that includes the stored elastic energy and the dissipated work due to plasticity and fracture. The latter represents a coupled resistance to plasticity and damage, depending on the gradient-extended internal variables which enter the plastic yield function and the fracture threshold function. The canonical theory proposed is shown to be governed by a rate-type minimization principle, which fully determines the coupled multi-field evolution problem, and provides inherent symmetries with regard to a finite element implementation. The robust computational setting proposed includes (i) a general return scheme of plasticity in the spectral space of logarithmic principal strains and dual Kirchhoff stresses, (ii) the micromorphic regularization of the gradient plastic evolution and (iii) a history-field-driven update of the linear phase field equation.

Keywords: Porous plasticity, Ductile fracture, Phase-field modeling, Strain gradient plasticity, Gradient damage mechanics, Variational principles.

4.1. Introduction

Fracture in the form of evolving crack surfaces in ductile solid materials is preceded by significant plastic distortion. The prediction of failure mechanisms due to crack initiation and growth coupled with elastic-plastic deformations is an intriguingly challenging task, and plays an extremely important role in various engineering applications. This covers machining, cutting and forming of ductile metals and polymers, i.e. applications at the core of automobile, aerospace or heavy industries which significantly benefit from precisely predictive computational tools to model ductile fracture in the design phase of products. To this end, a rigorous variational-based framework is presented for an innovative phase field modeling of ductile fracture in *porous* elastic-plastic solids at large strains.

4.1.1. Plasticity, Damage and Fracture in Ductile Materials

Ductile fracture is a phenomenon that couples at the macroscopic level *plastic deformations* with the *accumulation of damage* and *crack propagation*. The process of damage that follows extensive plastic deformations covers the macroscopic effects of degrading stiffness, strength and ductility up to a critical state where rupture occurs. Damage is caused by deformation mechanisms at the microscopic level, such as void nucleation, growth and coalescence, the formation of micro-shear-bands and micro-cracks. A great number of pure phenomenological and micro-mechanically motivated approaches exists for the continuum modeling of ductile fracture, see for example Besson 2010 and Li et al. 2011 for overviews. The simplest approaches provide *estimates* for the local initiation of fracture *uncoupled* from the plastic deformation, for example by introducing a damage field variable that counts towards the local initiation of fracture, see Johnson and Cook 1985. In contrast, *coupled formulations* link the evolution of damage to the evolution of plastic deformation. This covers on the one side the pure phenomenological macro-models of *continuum damage mechanics*, see for example Lemaitre 1985 and Lemaitre and Chaboche 1990. On the other side, models of *porous plasticity* describe micro-mechanical mecha-

nisms such as void growth, and obtain macroscopic constitutive expressions by analytical homogenization techniques. This includes early investigations such as Rice and Tracey 1969 on exponential growth of voids in an ideal plastic matrix under remote strain action. Gurson 1975 obtained a macroscopic yield surface by homogenization of a porous RVE with assumed rigid plastic flow, that degrades with increasing void fraction. It was enhanced by Needleman and Tvergaard 1984 and many follow-up works to include effects of void nucleation and coalescence. A conceptual similar model for porous plasticity is suggested by Rousselier 1987 with numerical implementation discussed in Lorentz et al. 2008. Alternative homogenization-based models for porous plasticity are suggested for example in Ponte Castañeda and Zaidman 1994 and Leblond et al. 1994. There is a constantly evolving vast literature on improved damage models for porous materials, see for example Nahshon and Hutchinson 2008 and Danas and Ponte Castañeda 2012 for recent contributions.

However, in these *local models* of plasticity coupled with damage, the strong softening behavior induces *localization* of plastic and damage zones. The accompanying loss of ellipticity or hyperbolicity in quasi-static or dynamic cases results in the pathological mesh dependence of finite element implementations, where localized zones are determined by the element size of spatial discretizations. A way to overcome this problem is the construction of *gradient plasticity* and *gradient damage* models which *limit the width* of localized plastic and damage zones due to their inherent *length scales* and *size effects* of the dissipative response. Pure phenomenologically-based theories of gradient plasticity often use plastic length scales as limiters of localized zones determined by macroscopic experiments, see for example Mühlhaus and Aifantis 1991, Geers 2004 and Reddy et al. 2008. Recently Miehe 2011, 2014 proposed a unified framework of strain-gradient plasticity based on multi-field variational principles for both geometrically linear and non-linear setting. On the side of damage mechanics, formulations of gradient-enhanced models are mostly applied to the modeling of degradation effects in brittle or quasi-brittle materials, see for example Peerlings et al. 1996, Frémond and Nedjar 1996 and Comi 1999. Here, a *damage length scale* that limits localized zones is introduced, determined by macroscopic experiments. The recent works Miehe et al. 2010b and Pham et al. 2011 apply gradient damage models to the regularized description of Griffith-type brittle fracture. The coupling of *local* plasticity with gradient-damage models have already been used extensively to model ductile fracture, see for example de Borst et al. 1999, Nedjar 2001, Reusch et al. 2003, Alessi et al. 2015 and Ambati et al. 2015a. As noted by Alessi et al. 2015, a model of gradient damage coupled with plasticity allows the *nucleation of cohesive cracks*, i.e. the existence of a surface of discontinuity of displacements with non-vanishing stress. By defining length scales and limiters for *both* the plastic as well as the damage zones one can ensure that the damage zone evolves inside of a plastic zone and vice versa. Recent works in this direction are Aslan et al. 2011, Dimitrijevic and Hackl 2011, Saanouni and Hamed 2013 and Miehe et al. 2015a. In this work, we develop a rigorous variational foundation for the coupling of porous gradient plasticity to gradient damage models at finite strains.

4.1.2. Variational Phase Field Modeling of Ductile Fracture

Recently developed phase field approaches to fracture regularize sharp crack discontinuities within a pure continuum formulation. This *diffusive* crack modeling allows the

resolution of complex failure topologies, such as crack branching phenomena in dynamic fracture of brittle solids, see Hofacker and Miehe 2012 and references cited therein. In contrast to computational models which model sharp cracks, see e.g. Simo et al. 1993, Belytschko and Black 1999, Linder and Raina 2013, Miehe and Gürses 2007 and many others, the phase field approach is a spatially smooth continuum formulation that avoids the modeling of discontinuities and can be implemented in a straightforward manner by coupled multi-field finite element solvers. Three basic approaches to the regularized modeling of Griffith-type *brittle fracture* in elastic solids may be distinguished: (i) The phase field approach by Karma et al. 2001 and Hakim and Karma 2009 apply a Ginzburg-Landau-type evolution of an unconstrained crack phase field, using a non-convex degradation function that separates unbroken and broken states. It *lacks explicit definitions of irreversibility constraints* for the crack evolution. (ii) The approach of Francfort and Marigo 1998, Bourdin et al. 2000, 2008, adopts the variational structure and Γ-convergent regularization of image segmentation developed by Mumford and Shah 1989 and Ambrosio and Tortorelli 1990 for the analysis of finite increments in quasi-static crack evolution. The irreversibility of the fracture process is modeled by *evolving Dirichlet-type boundary conditions*, while the scalar auxiliary field used for the regularization is un-constrained. This needs the implementation of non-standard code structures in typical finite element solvers. (iii) The phase field approach by Miehe et al. 2010a,b is a gradient damage theory with a *local irreversibility constraint* on the crack phase field, however, equipped with constitutive structures rooted in fracture mechanics. It incorporates regularized crack surface density functions as central constitutive objects, which is motivated in a descriptive format based on geometric considerations. Such a formulation can easily be implemented by a multi-field finite element solver with monolithic or staggered solution of the coupled problem. Recent works on brittle fracture along this third line are Amor et al. 2009, Pham et al. 2011, Borden et al. 2012 and Verhoosel and de Borst 2013.

Extensions to the phase field modeling of ductile fracture are exclusively related to the third line, representing conceptually a coupling of gradient damage mechanics with models of elasto-plasticity. Duda et al. 2015 investigate a setting of brittle fracture in elastic-plastic solids. Variational-based approaches to combined brittle-ductile fracture are outlined in Ulmer et al. 2013 and Alessi et al. 2015. The model suggested in Ambati et al. 2015a uses a characteristic degradation function that couples damage to plasticity in a multiplicative format. However, these settings combine *local models* of plasticity to the gradient-damage-type phase field modeling of fracture and do not meet the demands mentioned above, i.e. related plastic and damage length scales. Furthermore, settings outlined in Ambati et al. 2015a do not provide a canonical structure based on variational principles. This is achieved in the recent work Miehe et al. 2015a that couples gradient plasticity to gradient damage at finite strains.

This paper presents a consistent variational-based framework for the phase field modeling of ductile fracture in elastic-plastic porous solids undergoing large strains. It links a formulation of *variational gradient plasticity*, as recently outlined in Miehe 2011, 2014, to a specific setting of *variational gradient damage*, rooted in the phase field approach of fracture suggested by Miehe et al. 2010a,b. Such a formulation has conceptually been outlined in Miehe et al. 2015a and was recast in Miehe et al. 2016a,b into a canonical variational formulation. It is extended in this work to a particular formulation of porous plasticity in an Eulerian geometric setting. The basic structural ingredients of the formulation proposed here are:

- A phase field model for ductile fracture that combines ingredients of porous gradient plasticity and gradient damage, offering a *scaling of plastic to damage length scales*.
- A thermodynamic framework that is fully variational in nature, based on a split of a *work density function* into energetic and dissipative parts, and a *dissipation function* with separate thresholds for plasticity and damage.

The approach is embedded in the theory of *gradient-extended continuum modeling*, as outlined in the general context by Maugin 1990, Capriz 1989, Mariano 2001 and Frémond 2002. The gradient plasticity-damage coupling is conceptually based on a *work density function* that governs the rate-independent part of a solid undergoing elastic-plastic deformations at fracture. It assumes a *phase transition* of the elastic-plastic work density towards a given critical value, that provides locally a *threshold for brittle or ductile fracture*. The constitutive structure of the work density function includes in a modular format separate constitutive functions with a clear physical meaning. On the side of the elastic-plastic bulk response, this covers the *elastic work density function* and the *plastic work density function* of an undamaged material. On the side of regularized fracture mechanics, a *crack surface density function* is introduced that can be geometrically motivated by a regularization of a sharp crack. Finally, the elastic-plastic-damage coupling is governed by a *degradation function*, that is assumed to be convex as used previously in damage mechanics. For this canonically simple model, the coupling of gradient plasticity and gradient damage is realized by only two material parameters: a critical elastic-plastic work density w_c that governs the onset of fracture and a parameter ζ that controls the shape of the post-critical range of damage.

Here, we propose a canonically simple *model of porous plasticity in an Eulerian geometric setting* relative to the current configuration. The elastic energy is formulated by the elastic Finger tensor and the dual Kirchhoff stress tensor, which automatically induces an isotropic representation. The formulation focuses on a combination of ingredients obtained from microscopic porous plasticity with purely macroscopic criteria for the onset of fracture. To this end, a standard growth of voids is considered, that is *assumed to be driven by the total volumetric deformation*. This is a simple micro-mechanically motivated assumption reasonable for small elastic strains combined with large plastic strains. A key observation related to this assumption is that the *Kirchhoff stress can be considered as an effective stress acting on the matrix material*. This provides the key assumption for formulating a consistent formulation of isotropic porous plasticity based on a variational principle, where the above mentioned *work density is not a function of the void volume fraction*.

A further split of the work density function into an energetic part that is stored and a dissipative part provides the thermodynamic foundation of the model. Here, the energetic part is defined to be exclusively elastic in nature, representing a degraded elastic free energy density. Besides the constitutive expression for the stresses, it provides locally *energetic driving forces* of plasticity as well as regularized fracture. The dissipative part governs *plastic and fracture resistances*, each equipped with length scales l_p and l_f, which includes the coupling between gradient plasticity and gradient damage. This viewpoint settles the general *framework of gradient extended modeling*. The variables responsible for the length scale effects are the equivalent plastic strain and the fracture phase field. They are considered to be *passive in nature*, i.e. governed by Dirichlet and Neumann-type boundary conditions which do not allow an independent load-type driving. Hence,

micro-balance-type theories such as considered in full generality by Gurtin 1996, 2003 or Forest 2009 are avoided in this setting. Due to the specific split of the work density function into energetic and dissipative part, the *dissipation is defined fully local in nature*. This allows a decomposition into plastic and fracture parts, defining separate energetic driving forces for the evolution of plastic deformation and the accumulation of fracture. A numerical integration of these separate plastic and fracture contributions to the dissipation then allows a decomposition of the dissipative part of the work density function into contributions due to plasticity and fracture.

This decomposition of the dissipation into plastic and fracture parts offers a clear structure for the constitutive modeling of the evolution equations. Here, a formulation is constructed based on *two separate threshold functions for plasticity and fracture*, each driven by the driving forces which govern the dissipation due to plasticity and fracture. The associated resistances are defined by variational derivatives of the dissipative part of the work density function. On the side of plasticity, we develop a modified Gurson-type yield criterion in the Eulerian Kirchhoff stress space that governs the evolution of the macroscopic plastic flow. Furthermore, the void fraction is considered in the modified yield function as a *state variable*, i.e. the yield function is evaluated at a given state of the void fraction. These two ingredients allow to construct a minimization principle for the problem of isotropic porous plasticity at finite strains coupled to the phase field modeling of fracture. It allows by coupling ingredients of micromechanical porous plasticity to the gradient-damage response of fracture the analysis of basic phenomena in ductile plasticity, such as the cup-cone response. With these two additional threshold functions at hand, a *dissipation potential function* is constructed that additively splits into plastic and regularized fracture parts. It is shown that the coupled plasticity-damage model is thermodynamically consistent. A detailed analysis comments on the role of the material parameters and points out for a one-dimensional problem the characteristics of the modeling concept. The approach models both brittle as well as ductile fracture. The occurrence and sequence of these phenomena depends on the choice of the material parameters.

A further important aspect is the *micromorphic regularization* of the model with a structure such as outlined in Forest 2009. This is achieved by considering an extended set of plastic and damage variables which are linked by penalty terms in a modified work density function. The advantage of such a formulation lies on the computational side, in particular on the side of gradient plasticity. It allows a straightforward finite element formulation of gradient plasticity that does not need to account of sharp plastic boundaries. The structure of the evolution equations for the two scalar internal variables, the equivalent plastic strain and the fracture phase field, is analyzed for both the canonical gradient formulation as well as for its micromorphic regularization, and shown to have a formally similar structure. In particular, we consider possible modifications of the phase field equation that accounts for fracture in tension. Finally, the modeling performance of the formulation is underlined by characteristic benchmark problems. Here, the need of the coupling of gradient plasticity–damage is highlighted in order to obtain a mesh-objective post-critical response as well as physically reasonable results with regard to the diffuse distribution of localized plastic strains and damage.

In summary, the following sections outline aspects and details with regard to the development of a variational based theory of phase field fracture coupled with gradient plasticity in porous solids, as well as its numerical implementation. The work contains:

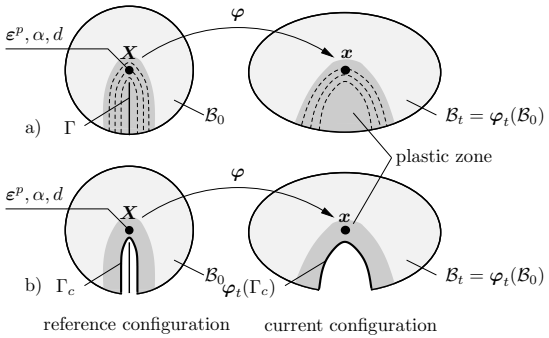

Figure 4.1: Finite deformation of a solid with a regularized crack *inside* of a plastic zone. The *deformation map* $\boldsymbol{\varphi}$ maps at time t the reference configuration $\mathcal{B}_0$ onto the current configuration $\mathcal{B}_t$. a) The *crack phase field* $d \in [0, 1)$ defines a regularized crack surface functional $\Gamma_l(d)$ that converges in the limit $l \to 0$ to the sharp crack surface Γ. b) The level set $\Gamma_c = \{\boldsymbol{X} \,|\, d = c\}$ defines for a constant $c \approx 1$ the crack faces in the regularized setting. Parts of the continuum with $d > c$ are considered to be free space and are not displayed.

- An Eulerian formulation of multiplicative porous plasticity linked to the phase field modeling of fracture.
- A modified Gurson-type yield function, formulated in terms of the Kirchhoff stresses, combined with a growth law in terms of the total Jacobian.
- A minimization principle for the coupled problem of isotropic porous gradient plasticity coupled to phase field fracture.
- An algorithmic setting of the minimization problem in the spectral space of Eulerian Hencky strains and Kirchhoff stresses.
- Efficient spatial discretization based on a micromorphic regularization of gradient plasticity and a history-variable-driven linear update of the linear fracture phase field equation.

4.2. Introduction of Primary Field Variables

This section introduces all state variables used in the subsequent treatment. This covers the specific representation of *isotropic multiplicative plasticity in the Eulerian geometric setting* proposed by Simo and Miehe 1992 and Simo 1992, its extension to porous microstructures and the coupling to a phase field modeling of fracture.

4.2.1. Isotropic Multiplicative Finite Plasticity with Plastic Metric

Finite Deformations. Let $\boldsymbol{\varphi}(\boldsymbol{X}, t)$ with initial condition $\boldsymbol{\varphi}(\boldsymbol{X}, t_0) = \boldsymbol{X}$ be the deformation map at time t that maps material positions $\boldsymbol{X} \in \mathcal{B}_0$ of the reference configuration

$\mathcal{B}_0 \in \mathcal{R}^3$ onto points $\boldsymbol{x} = \boldsymbol{\varphi}_t(\boldsymbol{X}) \in \mathcal{B}_t$ of the current configuration $\mathcal{B}_t \in \mathcal{R}^3$ as visualized in Figure 4.1. The material deformation gradient is defined by $\boldsymbol{F} := \nabla \boldsymbol{\varphi}_t(\boldsymbol{X})$ with $J := \det[\boldsymbol{F}] > 0$. The solid is loaded by prescribed deformations and external traction on the boundary, defined by time-dependent ("active") Dirichlet- and Neumann conditions

$$\boldsymbol{\varphi} = \bar{\boldsymbol{\varphi}}(\boldsymbol{X}, t) \text{ on } \partial\mathcal{B}_0^{\varphi} \quad \text{and} \quad \boldsymbol{P}\boldsymbol{n}_0 = \bar{\boldsymbol{t}}_0(\boldsymbol{X}, t) \text{ on } \partial\mathcal{B}_0^{t} \tag{4.1}$$

on the surface $\partial\mathcal{B}_0 = \partial\mathcal{B}_0^{\varphi} \cup \partial\mathcal{B}_0^{t}$ of the undeformed configuration. The first Piola stress tensor $\boldsymbol{P}$ is the thermodynamic dual to $\boldsymbol{F}$.

Macroscopic Plastic Metric and Elastic Deformation. We introduce a *co-variant Lagrangian plastic metric* $\boldsymbol{G}^p \in Sym_+(3)$ as an internal variable that evolves in time. It is considered as a purely phenomenological object for the description of the plastic deformation. The plastic metric can be motivated by a multiplicative split $\boldsymbol{F} = \boldsymbol{F}^e\boldsymbol{F}^p$ of the deformation gradient into plastic and elastic parts, as introduced by Kröner 1958, Lee, E. H. 1969 and Mandel J. 1972. Then, an elastic deformation measure is the *contravariant Eulerian elastic Finger tensor* $\boldsymbol{b}^e = \boldsymbol{F}^e\boldsymbol{F}^{eT}$ that provides the definition

$$\boldsymbol{b}^e := \boldsymbol{F}\boldsymbol{G}^{p-1}\boldsymbol{F}^T \quad \text{with} \quad \boldsymbol{G}^p(\boldsymbol{X}, t_0) = \boldsymbol{1} \ , \tag{4.2}$$

when the Lagrangian plastic metric is identified by $\boldsymbol{G}^p = \boldsymbol{F}^{pT}\boldsymbol{F}^p$. As underlined in Miehe 1998, the a priori use of $\boldsymbol{G}^p \in Sym_+(3)$ instead of $\boldsymbol{F}^p \in GL(3)_+$ restricts the subsequent setting to a theory of finite plasticity that *excludes the influence of plastic rotations*. Accompanied by the elastic deformation measure is the multiplicative split

$$J^e := JJ^{p-1} \quad \text{with} \quad J^p := \sqrt{\det[\boldsymbol{G}^p]} \ , \tag{4.3}$$

of the volumetric deformation into plastic and elastic parts. The evolution of the plastic metric in time is described by the *Eulerian plastic rate of deformation tensor*

$$\boldsymbol{d}^p := -\tfrac{1}{2}(\boldsymbol{\pounds}_{\boldsymbol{v}}\boldsymbol{b}^e)\boldsymbol{b}^{e-1} = \boldsymbol{F}\boldsymbol{D}^p\boldsymbol{F}^{-1} \quad \text{with} \quad \boldsymbol{D}^p = -\tfrac{1}{2}\dot{\boldsymbol{G}}^{p-1}\boldsymbol{G}^p \tag{4.4}$$

first introduced in Simo and Miehe 1992, where $\boldsymbol{\pounds}_{\boldsymbol{v}}\boldsymbol{b}^e := \boldsymbol{F}\dot{\boldsymbol{G}}^{p-1}\boldsymbol{F}^T$ is the Lie derivative or Oldroyd rate of $\boldsymbol{b}^e$. Note that $\boldsymbol{d}^p$ corresponds to the evolution $\dot{\boldsymbol{G}}^p$ of the Lagrangian plastic metric. From the perspective of multiplicative plasticity, this definition follows from the push-forward $\boldsymbol{d}^p = \boldsymbol{F}^e\text{sym}[\boldsymbol{L}^p]\boldsymbol{F}^{e-1}$ of the *symmetric part* of the plastic evolution operator $\boldsymbol{L}^p = \dot{\boldsymbol{F}}^p\boldsymbol{F}^{p-1}$ from a fictitious plastic intermediate configuration to the current configuration. This underlines the fact that the theory of multiplicative plasticity under consideration uses a *zero plastic spin* $\text{skew}[\boldsymbol{L}^p] = \boldsymbol{0}$. For the *isotropic elastic response* under consideration, the *symmetry* of the Eulerian rate of deformation tensor $\boldsymbol{d}^{pT} = \boldsymbol{d}^p$, where $\boldsymbol{\pounds}_{\boldsymbol{v}}\boldsymbol{b}^e$ *commutes with* $\boldsymbol{b}^e$, is realized by a normality rule for the plastic flow in terms of the symmetric Kirchhoff stress $\boldsymbol{\tau}$ considered below. The evolution of the volumetric plastic deformation takes the form

$$\dot{J}^p = J^p \,\text{tr}[\boldsymbol{d}^p] \quad \text{with} \quad \text{tr}[\boldsymbol{d}^p] = \text{tr}[\boldsymbol{D}^p] \ . \tag{4.5}$$

Note that all kinematic quantities introduced above are functions of the Lagrangian plastic metric $\boldsymbol{G}^p$ and its rate, which describe the macroscopic plastic state and its evolution.

4.2.2. Evolution of an Isotropic Porous Microstructure

Volume Fraction of Voids. The subsequent modeling accounts for a microstructure with an *isotropic* distribution of voids embedded into a matrix, that is restricted to *isochoric plastic flow*. The porosity is described by the *void volume fraction*

$$f \in [f_0, 1) \quad \text{with} \quad f(\boldsymbol{X}, t_0) = f_0 > 0 \tag{4.6}$$

that evolves due to the plastic deformation of the matrix from a given initial value f_0. When restricting to scenarios of metal or polymer plasticity with *small elastic strains*, we estimate

$$J^p \approx J \quad \text{and} \quad \dot{J}^p \approx \dot{J} = J \operatorname{tr}[\boldsymbol{L}] \,, \tag{4.7}$$

where $\boldsymbol{L} = \dot{\boldsymbol{F}}\boldsymbol{F}^{-1}$ is the spatial velocity gradient. As a consequence, the void volume fraction f is assumed to be in a *one-to-one relationship to the total volumetric macrodeformation*. Its evolution is obtained from the mass balance of the matrix material, that approximately reads

$$\frac{d}{dt}\int_{\mathcal{B}_t} \rho_M (1-f) dv = 0 \tag{4.8}$$

with constant density ρ_M and the volume element $dv = JdV$ of deformed configuration $\mathcal{B}_t$. This global statement results into the *growth-type evolution equation*

$$\dot{f} = (1-f)\frac{\dot{J}}{J} = (1-f)\operatorname{tr}[\boldsymbol{L}] \tag{4.9}$$

for void fractions above the lower bound $f_0 > 0$. Its integration results into the closed-form relationship

$$f = \widehat{f}(J) = \max[\, f_0, 1 - \frac{1-f_0}{J}\,] \tag{4.10}$$

between the void fraction and the Jacobian of the deformation gradient. Hence, the void fraction f is assumed to be a function of the Jacobian J of the deformation gradient.*

An Effective Cauchy Stress. Let $\boldsymbol{\sigma} \in Sym_+(3)$ be the macroscopic true Cauchy stress tensor defined on the deformed manifold $\mathcal{B}_t$. In order to define an *effective stress tensor* $\widetilde{\boldsymbol{\sigma}}$ that drives the plastic deformation of the matrix, an estimate for the Jacobian J is introduced obtained form the inverse representation of (4.10)

$$J \approx \frac{1-f_0}{1-f} \approx \frac{1}{1-f} \,, \tag{4.11}$$

that holds for small initial void fractions $f_0 << 1$. This approximation is then used to estimate the effective Cauchy stress

$$\widetilde{\boldsymbol{\sigma}} := \frac{\boldsymbol{\sigma}}{1-f} \;\approx\; \boldsymbol{\tau} := J\boldsymbol{\sigma} \tag{4.12}$$

*The assumption (4.8) is consistent with a classical growth law already considered in Gurson 1975. We view it here as a particular *constitutive definition* of an effective void fraction. In this sense, it is open for a modification conceptually for considering void coalescence such as conceptually outlined in Tvergaard 1982.

by the Kirchhoff stress $\boldsymbol{\tau}$. Hence, for the growth-type porosity evolution (4.9) suitable for a matrix material undergoing small elastic and large isochoric plastic strains, the *Kirchhoff tensor* $\boldsymbol{\tau}$ *defined in (4.12)*$_2$ *can be considered as an effective Cauchy stress acting on the matrix material.* This observation is a key ingredient of the subsequent work. It provides a clear physical motivation for the use of the Eulerian Kirchhoff stress $\boldsymbol{\tau}$ in yield functions of isotropic porous plasticity, and characterizes $\boldsymbol{\tau}$ as the driving force for the plasticity of the matrix material consistent with the void growth assumption (4.9). This result is crucial for the setting up of the subsequent variational framework for porous plasticity at fracture in a consistent geometric setting with respect to the current configuration.

Strain-Gradient Hardening of Matrix. In order to set up a length scale for the plastic response, we consider a formulation of isotropic gradient plasticity. To this end, a scalar *microstructural hardening variable*

$$\alpha \in [0, \infty) \quad \text{with} \quad \alpha(\boldsymbol{X}, t_0) = 0 \tag{4.13}$$

is introduced that defines an equivalent plastic strain in the matrix material. Its evolution is derived by postulating the equivalence of the microscopic plastic hardening power of the matrix and the macroscopic plastic power per unit of the reference volume

$$\int_{\mathcal{B}_t} r^p \dot{\alpha}(1-f) dv = \int_{\mathcal{B}_t} \boldsymbol{\sigma} : \boldsymbol{d}^p dv \ , \tag{4.14}$$

where $r^p(\alpha, \nabla\alpha)$ is a given isotropic *hardening function* of the matrix material. $\boldsymbol{\sigma} : \boldsymbol{d}^p$ is the macroscopic plastic power with respect to the volume of the current configuration, where $\boldsymbol{\sigma}$ is the Cauchy stress and $\boldsymbol{d}^p$ the plastic evolution operator defined in (4.4). Taking the local form of (4.14), dividing it by the factor $1-f$ and integrating it over the reference volume $\mathcal{B}_0$ gives the alternative form

$$\int_{\mathcal{B}_0} r^p \dot{\alpha} dV = \int_{\mathcal{B}_0} \boldsymbol{\tau} : \boldsymbol{d}^p dV \ , \tag{4.15}$$

when the approximation (4.12) of the effective Cauchy stress by the Kirchhoff stress is inserted. Note carefully that the void fraction f does not explicitly appear in this statement, because it is covered by the Kirchhoff stress $\boldsymbol{\tau}$. This provides the foundation of the subsequent development of a variational formulation of porous plasticity. Here, we formulate yield functions in terms of the Kirchhoff stress such that the variational-based evolution of the microstructural hardening variable takes the form

$$\dot{\alpha} = \frac{1}{r^p} \boldsymbol{\tau} : \boldsymbol{d}^p \geq 0 \ . \tag{4.16}$$

In the subsequent treatment, we introduce the *plastic length scale* l_p that accounts for size effects to overcome the non-physical mesh sensitivity in ductile fracture. To this end, we focus on a first order setting of gradient plasticity where the gradient $\nabla\alpha(\boldsymbol{X}, t)$ enters the constitutive functions. The generalized internal variable field α is considered to be passive in the sense that an external driving is not allowed. This is consistent with the time-independent ("passive") Dirichlet- and Neumann conditions

$$\alpha = 0 \text{ on } \partial\mathcal{B}_0^{\alpha} \quad \text{and} \quad \nabla\alpha \cdot \boldsymbol{n}_0 = \boldsymbol{0} \text{ on } \partial\mathcal{B}_0^{\nabla\alpha} \tag{4.17}$$

on the surface $\partial\mathcal{B}_0 = \partial\mathcal{B}_0^{\alpha} \cup \partial\mathcal{B}_0^{\nabla\alpha}$ of the undeformed configuration, defining "micro-clamped" and "free" constraints for the evolution of the plastic deformation.

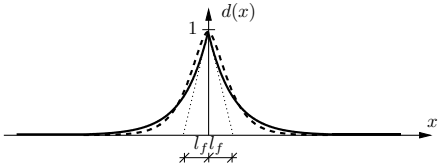

Figure 4.2: Diffusive crack modeling at $x = 0$ modeled with the length scale $l_f \leq l_p$. Regularized curves obtained from minimization principle of diffusive crack topology $\int_{\mathcal{B}_0} \gamma_l dV \rightarrow Min!$ with crack surface density function γ_l. Thick line: $\gamma_l = d^2/2l_f + l_f|\nabla d|^2/2$ with regularization profile $exp[-|x|/l_f]$ satisfying $d(0) = 1$, dotted line: $\gamma_l = d^2/2l_f + l_f|\nabla d|^2/4 + l_f^3(\Delta d)^2/32$ with regularization profile $exp[-2|x|/l_f](1 + 2|x|/l_f)$ satisfying $d(0) = 1$ and $d'(0) = 0$.

4.2.3. The Phase Field Approximation of Sharp Macro-Cracks

Following previous treatments of Miehe et al. 2010b, we consider the phase field approach to fracture as a specific formulation of gradient damage mechanics. It is based on a geometric regularization of sharp crack discontinuities that is governed by a *crack phase field*

$$d \in [0, 1] \quad \text{with} \quad \dot{d} \geq 0 \quad \text{and} \quad d(\boldsymbol{X}, t_0) = 0 \tag{4.18}$$

as indicated in Figure 4.2. It characterizes locally for the initial condition $d(\boldsymbol{X}, t) = 0$ the unbroken and for $d(\boldsymbol{X}, t) = 1$ the fully broken state of the material. In contrast to traditional approaches to gradient damage mechanics, the crack phase field d is considered to have a purely geometric meaning. It governs the *regularized crack surface*

$$\Gamma_l(d) = \int_{\mathcal{B}_0} \widehat{\gamma}(d, \nabla d)\, dV \quad \text{with} \quad \widehat{\gamma}(d, \nabla d) = \frac{1}{2l_f} d^2 + \frac{l_f}{2} |\nabla d|^2 \tag{4.19}$$

that is formulated in terms of an isotropic *crack surface density function* per unit volume of the solid. The regularization is governed by a *fracture length scale*

$$l_f \leq l_p \quad \text{or} \quad l_f \geq l_p \tag{4.20}$$

such that the regularized crack zone lies inside of the plastic zone or vice versa. The function $\widehat{\gamma}$ in (4.15) already appears in the approximation by Ambrosio and Tortorelli 1990 of the Mumford and Shah 1989 functional of image segmentation. The functional $\Gamma_l(d)$ converges to a sharp-crack topology for vanishing fracture length scale $l_f \rightarrow 0$ as schematically visualized in Figure 4.2, which depicts in addition a possible higher order approximation suggested by Borden et al. 2014. When assuming a given sharp crack surface topology by prescribing the Dirichlet condition $d = 1$ on $\Gamma \subset \mathcal{B}_0$, the regularized crack phase field d in the full domain $\mathcal{B}_0$ is obtained by a *minimization principle of diffusive crack topology* with the limit

$$\lim_{l_f \rightarrow 0} \left\{ \inf_d \Gamma_l(d) \right\} = \Gamma(t) \ , \tag{4.21}$$

see Miehe et al. 2010b for more details. Figure 4.3 depicts numerical solutions of this variational problem in a two-dimensional setting, which demonstrate the influence of the fracture length scale l_f. Note that the limit for vanishing fracture length scale $l_f \rightarrow 0$ gives the sharp crack surface Γ. The crack phase field d is passive in the sense that

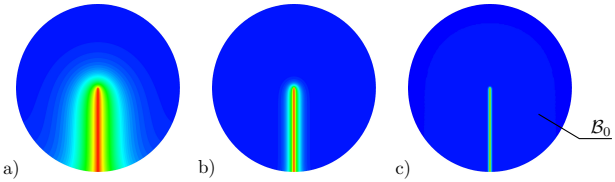

Figure 4.3: Continuum approximation of crack discontinuities. Solutions of the variational problem (4.8) of diffusive crack topology for a circular specimen with a given sharp crack Γ, prescribed by the Dirichlet condition $d = 1$. Crack phase field $d \in [0, 1]$ for different length scales $l_f^a > l_f^b > l_f^c$. The sequence of plots visualizes the limit $\Gamma_l \to \Gamma$ of the regularized crack surface functional (4.8) towards the sharp crack surface.

an external driving is not allowed. Only time-independent ("passive") Dirichlet- and Neumann conditions

$$d = 1 \text{ on } \Gamma \subset \mathcal{B}_0 \quad \text{and} \quad \nabla d \cdot \boldsymbol{n}_0 = \boldsymbol{0} \text{ on } \partial\mathcal{B}_0 \tag{4.22}$$

are allowed, defining a sharp "initial crack" and "free" evolution of the crack phase field on the full boundary.

4.2.4. Global Primary Fields and Constitutive State Variables

The above introduced variables will characterize a multi-field setting of gradient plasticity at fracture based on three *global primary fields*

$$\mathfrak{U} := \{\boldsymbol{\varphi}, \alpha, d\} \ , \tag{4.23}$$

the finite deformation map $\boldsymbol{\varphi}$, the strain-hardening variable α and the crack phase field d. In addition, the Lagrangian plastic metric field $\boldsymbol{G}^{p-1}$ serves as an additional *local primary field*. The subsequent constitutive approach to the phase field modeling of ductile fracture focuses on the set

$$\mathfrak{C} := \{\nabla\boldsymbol{\varphi}, \boldsymbol{G}^{p-1}, \alpha, \nabla\alpha, d, \nabla d\} \ , \tag{4.24}$$

reflecting a combination of first-order gradient plasticity with a first-order gradient damage modeling. The subsequent theory of gradient plasticity at fracture uses this set of constitutive state variables.

4.3. Variational Phase Field Approches to Brittle Fracture

The section provides an overview of different approaches to the phase field modeling of brittle fracture found in the literature, which provide the starting point for the subsequent extension to ductile fracture. The differences between approaches are best understood by considering an incremental setting. To this end, consider the interval $[t_n, t]$ of a process parameter t (time or load parameter), and assume all variables at t_n to be given. The process is driven by the Dirichlet conditions on the current deformation field $\boldsymbol{\varphi}$ defined in $(4.2)_1$. Important differences appear in the *formulation the irreversibility constraints*, which have a strong influence to the characterization on the fracture phase field variable.

4.3.1. The Fundamental Variational Theory of Brittle Fracture

Fundamental Variational Theory of Brittle Fracture. In Griffith-type fracture, the current deformation $\boldsymbol{\varphi}$ and sharp crack surface Γ in a brittle elastic solid are determined by the incremental minimization problem

$$E_1(\boldsymbol{\varphi}, \Gamma) = \int_{\mathcal{B}_0 \setminus \Gamma} \widehat{\psi}(\nabla \boldsymbol{\varphi})\, dV \;+\; g_c\, \mathcal{H}(\Gamma) \rightarrow \text{Min!} \quad \text{for} \quad \Gamma \supset \Gamma_n \tag{4.25}$$

developed by Francfort and Marigo 1998. The functional E_1 represents the total work needed for the deformation and cracking of the solid, consisting of the stored elastic strain energy and the energy release due to fracture. $\mathcal{H}(\Gamma)$ is the Hausdorff surface measure of the crack set Γ, and g_c the critical surface energy release. The functional E_1 has a structure identical to that for image segmentation developed by Mumford and Shah 1989. Note that the variable for the description of the crack evolution is the *current crack surface* Γ *itself*, that is *constraint to include the sharp crack surface* Γ_n *obtained in the previous step* at time t_n. This irreversibility condition can be viewed as a Dirichlet condition for the current sharp crack surface Γ, that advances in the incremental loading process.

Regularized Variational Theory. For the numerical implementation of the incremental minimization problem (4.25), Bourdin et al. 2008 used the Γ-convergent approximation of (4.25) developed in the field of image segmentation by Ambrosio and Tortorelli 1990. It can be represented in the form

$$E_2(\boldsymbol{\varphi}, d) = \int_{\mathcal{B}_0} \widehat{W}(\nabla \boldsymbol{\varphi}, d, \nabla d)\, dV \rightarrow \text{Min!} \quad \text{for} \quad d \in \mathcal{W}_n^d \tag{4.26}$$

where $d \in [0, 1]$ is an auxiliary field that we here denote as the fracture phase field. The total work density function

$$\widehat{W} = \widehat{g}(d)\widehat{\psi}(\nabla \boldsymbol{\varphi}) + g_c \widehat{\gamma}(d, \nabla d) \tag{4.27}$$

contains a degraded elastic work density and the crack energy release per unit volume. $\widehat{g} = (1 - d)^2 + k$ is a degrading function and $\widehat{\gamma}$ the crack surface density function. The irreversibility is achieved by *evolving Dirichlet conditions* on the auxiliary field d with

$$\mathcal{W}_n^d := \{d |\; d(\boldsymbol{X}, t) = 1 \text{ in } \mathcal{B}_0|_{d_n(\boldsymbol{X}, t)=1}\}\ . \tag{4.28}$$

Note carefully that the auxiliary field d is *not locally constrained*, i.e. d can increase as well as decrease as shown in Figure 4.4a. The irreversibility is incorporated by an incremental evolution of Dirichlet conditions: Once the auxiliary field d reaches within an incremental load step at a local point $\boldsymbol{X} \in \mathcal{B}_0$ the value $d = 1$, that point carries in the subsequent incremental steps the Dirichlet-type condition (4.28). For the 1D tension test shown in Figure 4.4a, the phase field d increases in the full domain and remains homogeneous until an imperfection-driven localization starts in the middle of the 1D bar at $X = 0$. Subsequently, after localization, the phase field in the outer regions decreases back again up to zero. A characteristic profile with a non-differentiable point at $X = 0$ is obtained. As indicated in Figure 4.4a, the formulation by Bourdin et al. 2008 provides a Γ-*convergent regularization of a sharp crack* at $X = 0$ for the limit $l_f \rightarrow 0$ of the length scale in the crack density function $\widehat{\gamma}$.

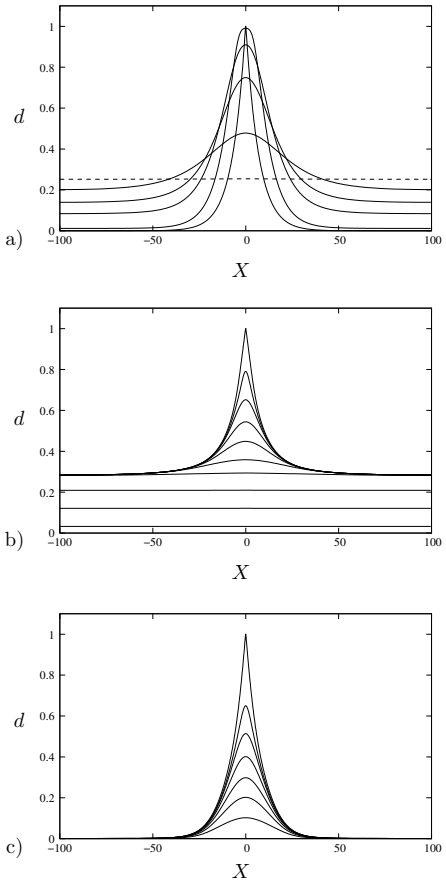

Figure 4.4: Evolution of the fracture phase field d in a 1d tension test for different approaches. a) Regularized variational theory (4.26) by Bourdin et al. 2000 without local irreversibility. b) Gradient damage formulation *without threshold* (4.30) by Amor et al. 2009 and Miehe et al. 2010b with local irreversibility. c) Gradient damage formulation *with threshold* based on (4.32) by Pham et al. 2011 and Miehe et al. 2015b with local irreversibility and elastic domain. Formulations a) and c) are convergent to the a crack for the limit $l_f \to 0$.

4.3.2. Variational Gradient Damage Approaches to Brittle Fracture

Formulation without Threshold. A locally irreversible phase field evolution developed by Amor et al. 2009 and Miehe et al. 2010b considers the minimization of the incremental energy functional

$$E_3(\boldsymbol{\varphi}, d) = \int_{\mathcal{B}_0} [\, \widehat{W}(\nabla\boldsymbol{\varphi}, d, \nabla d) + \int_{t_n}^{t} \widehat{V}(\dot{d}) dt \,]\, dV \to \text{Min!} \tag{4.29}$$

with the total work density $\widehat{W}$ defined in (4.27) and the dissipation potential density

$$\widehat{V} = \frac{\eta}{2}\dot{d}^2 + \widehat{I}(\dot{d}) \quad \text{with} \quad \widehat{I} = \begin{cases} 0 \text{ for } \dot{d} \geq 0 \\ \infty \text{ otherwise} \end{cases} . \tag{4.30}$$

Here, a *local irreversibility constraint* $\dot{d} \geq 0$ and a *viscous effect* of crack propagation is enforced by the dissipation function $\widehat{V}$. The functional E_3 is considered to be an algorithmic expression that approximates the time integration by the closed-form incremental expression

$$E_3(\boldsymbol{\varphi}, d) = \int_{\mathcal{B}_0} [\, \widehat{W}(\nabla\boldsymbol{\varphi}, d, \nabla d) + \frac{\eta}{2\tau}(d - d_n)^2 + \widehat{I}(d - d_n) \,] \, dV \to \text{Min!} \tag{4.31}$$

In contrast to (4.26) with evolving boundary conditions on d, the irreversibility is realized by the contribution of the indicator function $\widehat{I}$ to the local constitutive dissipation function. This is a classical ingredient of gradient damage theories, accounting for fracture by locally irreversible damage of the material. Such a formulation with a non-smooth evolution of the phase field can be implemented in a straightforward manner by finite element multifield solvers. The difference to the formulation of Bourdin et al. 2008 is depicted in Figure 4.4b for a one-dimensional tensile test. First, the phase field growths and remains homogeneous up to the same level as in Figure 4.4a. However, due to the local irreversibility constraint, the phase does subsequently not decrease in zones aside from the crack localization. As a consequence, these zones remain partially damaged. Such a formulation is not Γ-*convergent to a sharp crack* at $X = 0$ for the limit $l_f \to 0$ of the length scale in the crack density function $\widehat{\gamma}$, as numerically investigated by May et al. 2015. However, very reasonable results are obtained for inhomogeneous multi-dimensional problem, where the evolution of the crack phase field is a priori localized, see Miehe et al. 2010a,b.

Formulation with Threshold. The problem of missing convergence of the gradient damage formulation to the sharp crack limit can be overcome by an inclusion of a fracture threshold, i.e. an elastic domain in the space of the crack driving forces with zero evolution related to zero evolution of the phase field d. This is a classical ingredient of gradient damage theories, see for example Frémond and Nedjar 1996 and Miehe 2011. Recent formulations outlined in Pham et al. 2011 and Miehe et al. 2015b combine it with the functions $\widehat{g}$ and $\widehat{\gamma}$ related to the functional of Ambrosio and Tortorelli 1990. The formulation considered in Miehe et al. 2015b again bases on the incremental minimization principle (4.31) that *accounts locally for irreversibility* of the phase field d by the indicator function $\widehat{I}$. However, it uses a modification of the total energy density function (4.27)

$$\widehat{W}(\nabla\boldsymbol{\varphi}, d, \nabla d) = \widehat{g}(d)\widehat{\psi}(\nabla\boldsymbol{\varphi}) + [1 - \widehat{g}(d)]w_c + (2w_c l_f)\widehat{\gamma}(d, \nabla d) \tag{4.32}$$

where the material parameter w_c plays the role of a *fracture energy threshold*. * The effect of this modification is demonstrated in Figure 4.4c for a one-dimensional test. In contrast

* The function (4.32) can be recast into the form

$$\widehat{W}(\nabla\boldsymbol{\varphi}, d, \nabla d) = \widehat{g}(d)\widehat{\psi}(\nabla\boldsymbol{\varphi}) + 2w_c[\, d + \frac{l_f^2}{2}|\nabla d|^2 \,] \tag{4.33}$$

that appears already in formulation of gradient damage by Frémond and Nedjar 1996.

to the Figure 4.4b, the phase field d starts to develop at the same time as it localizes, and is *restricted to a damaged zone* of width depending on the length scale l_f. For $\psi < w_c$, the fracture phase field is equal to zero. The final distribution of the phase field over the cracked bar is then similar to the distribution in Figure 4.4a obtained by the formulation of Bourdin et al. 2008. Such a formulation with thresholds combines advantages of a description that is convergent to the sharp crack limit with a simple implementation by finite element solvers for multi-field problems. As a consequence, we subsequently extend this gradient damage formulation with threshold to the modeling of ductile fracture in elastic-plastic solids.

4.4. Variational Phase Field Approach to Ductile Fracture

This section outlines a theory for the coupling of gradient plasticity coupled with a phase field modeling of fracture that is fully variational in nature. It is based on the definition of constitutive work density and threshold functions, which define a *minimization principle* for the coupled evolution system.

4.4.1. Coupling Gradient Plasticity to Gradient Damage Mechanics

Consider the stress power $\mathcal{P} := \boldsymbol{\tau} : \boldsymbol{d}$ per unit volume of the reference configuration, acting on a local material element that undergoes elastic-plastic deformation and fracture. It is the inner product of the stress and a rate of deformation, the thermodynamic external variables acting on the material element. We use the Eulerian rate of deformation $\boldsymbol{d} := \mathrm{sym}[\boldsymbol{L}]$, i.e. the symmetric part of the spatial velocity gradient $\boldsymbol{L} := \dot{\boldsymbol{F}}\boldsymbol{F}^{-1}$, and its dual stress tensor, the symmetric Eulerian Kirchhoff stress $\boldsymbol{\tau}$. Let W denote the time-accumulated work per unit volume and $\boldsymbol{\mathcal{W}}$ its accumulation in space

$$W := \int_0^T \mathcal{P}\, dt \quad \text{and} \quad \boldsymbol{\mathcal{W}} := \int_{\mathcal{B}_0} W\, dV \ , \tag{4.34}$$

i.e. the total work needed to deform and crack the solid $\mathcal{B}_0$ within the process time $[0, T]$. We base the subsequent development of a phase field approach on a constitutive representation of this work

$$\boldsymbol{\mathcal{W}} = \int_{\mathcal{B}_0} [\, \widehat{W}(\boldsymbol{\mathfrak{C}}) + D_{vis} \,] dV \ . \tag{4.35}$$

It is governed by a *constitutive work density function* $\widehat{W}$ that describes the *rate-independent part* of the global work $\boldsymbol{\mathcal{W}}$. The a priori dissipative *rate-dependent part* D_{vis} due to viscous resistance forces vanishes in the rate-independent limit. Equation (4.35) holds for particular boundary conditions of the "non-local" generalized internal variable fields α and d. These must be "passive" in the sense that an external driving of these fields is not allowed, which is consistent with (i) *constant Dirichlet data* and (ii) *zero Neumann data* of α and d on the surface $\partial\mathcal{B}_0$ of the solid, as defined in (4.5) and (4.9) above. The rate-independent part $\widehat{W}$ is assumed to depend on the array $\boldsymbol{\mathfrak{C}}$ of constitutive state variables introduced in (4.11). We focus on the particular structure

$$\widehat{W}(\boldsymbol{\mathfrak{C}}) = \widehat{g}(d)\widehat{w}_0^{ep}(\boldsymbol{b}^e, \alpha, \nabla\alpha) + (1 - \widehat{g}(d))w_c + 2\frac{w_c}{\zeta} l_f \widehat{\gamma}(d, \nabla d) \tag{4.36}$$

as conceptually suggested already in Miehe et al. 2015a, which provides a particular coupling of gradient plasticity with gradient damage mechanics. The function $\widehat{w}_0^{ep}$ splits up into elastic and plastic contributions according to

$$\widehat{w}_0^{ep}(\boldsymbol{b}^e, \alpha, \nabla\alpha) = \widehat{w}_0^{e}(\boldsymbol{b}^e) + \widehat{w}_0^{p}(\alpha, \nabla\alpha) \ . \tag{4.37}$$

The derivatives of the potential density $\widehat{W}$ determine the rate-independent parts of stresses, the driving forces and the thresholds for the evolution of the plastic strains and the fracture phase field. It is based on four constitutive functions with a clear physical meaning:

F1 The *effective elastic work density function* $\widehat{w}_0^e$ models the macroscopic stress response of the undamaged material.

F2. The *effective plastic work density function* $\widehat{w}_0^p$ models local and strain gradient plastic hardening response of the undamaged matrix material.

F3. The *degradation function* $\widehat{g}$ describes the transition of the work density $\widehat{w}_0^{ep}$ towards the constant crack threshold parameter w_c.

F4. The *crack surface density function* $\widehat{\gamma}$ provides the geometric regularization of a sharp crack topology as already discussed above.

The work-density function $\widehat{W}$ models for $d \in [0,1]$ with the first two terms a phase transition of the effective elastic-plastic work density $\widehat{w}_0^{ep}$ towards the constant threshold value w_c, and with the third term the accumulated fracture work density. Here, $w_c > 0$ is a *specific critical fracture energy* per unit volume, that enters the formulation as the key material parameter on the side of fracture mechanics. The second material parameter ζ *controls the post-critical range* after crack initialization by scaling the work needed for the generation of the regularized crack surface. Figure 4.12 below gives a visual interpretation of the parameters w_c and ζ for a local homogeneous response, where $D^{pf} := (1 + 1/\zeta)w_c$, defined in (4.49), is the maximum dissipated work density at fracture $d = 1$. The constitutive representation for $\widehat{W}$ in (4.36) provides the basis for the coupling of a model of gradient plasticity (governed by $\widehat{w}_0^p$) with a gradient damage formulation (governed by $\widehat{\gamma}$), realized by the degradation function $\widehat{g}$.

4.4.2. Choice of Effective Work Density and Degradation Functions

Effective Elastic Work Density. The effective elastic work density function $\widehat{w}_0^e$ in (4.37) models the stored elastic energy of the unbroken material. The dependence on the Eulerian elastic Finger tensor $\boldsymbol{b}^e$ defined in (4.2) *restricts the model to isotropy*. This is a consequence of the *objectivity constraint* $\widehat{w}_0^e(\boldsymbol{Q}\boldsymbol{b}^e\boldsymbol{Q}^T) = \widehat{w}_0^e(\boldsymbol{b}^e)$ for all $\boldsymbol{Q} \in SO(3)$. For the subsequent model problems, the elastic work density is assumed to have the simple quadratic form

$$\widehat{w}_0^e(\boldsymbol{b}^e) = \frac{\lambda}{2}\mathrm{tr}^2[\boldsymbol{h}^e] + \mu\,\mathrm{tr}[(\boldsymbol{h}^e)^2] \quad \text{with} \quad \boldsymbol{h}^e := \tfrac{1}{2}\ln[\boldsymbol{b}^e] \tag{4.38}$$

of the Eulerian elastic Hencky tensor $\boldsymbol{h}^e$. It characterizes an isotropic, linear stress response in the logarithmic strain space. $\lambda > 0$ and $\mu > 0$ are the Lame constants. The

function provides a structure identical to the geometrical linear theory of elasticity at small strains. Note that $\widehat{w}_0^e$ is *convex* with respect to $\boldsymbol{h}^e$, however, due to the nonlinear relationship (4.2), *not poly-convex* with respect to $\boldsymbol{F}$. This restricts the model of elasto-plasticity under consideration to a range of small elastic strains $||\boldsymbol{h}^e|| < \epsilon$, however, accompanied by large plastic strains. This is a typical scenario applicable to metal plasticity.

Effective Plastic Work Density. The effective plastic work density function $\widehat{w}_0^p$ in (4.37) models the dissipated plastic work of the unbroken matrix material per unit volume of the reference configuration, consistent with the argumentation that led to (4.15). For the modeling of length scale effects in isotropic gradient plasticity, we focus on the equivalent plastic strain α and its gradient. It is assumed to have the form

$$\widehat{w}_0^p(\alpha, \nabla\alpha) = \int_0^\alpha \widehat{y}_M(\widetilde{\alpha}) d\widetilde{\alpha} + y_0 \frac{l_p^2}{2} |\nabla\alpha|^2 \,, \tag{4.39}$$

where $l_p \geq 0$ is a plastic length scale related to a strain-gradient hardening effect. $\widehat{y}_M(\alpha)$ is an isotropic local hardening function obtained form homogeneous experiments of the matrix material. We use in what follows the saturation-type function

$$\widehat{y}_M(\alpha) = y_0 + (y_\infty - y_0)(\,1 - \exp[-\eta\alpha]\,) \,+\, h\alpha \tag{4.40}$$

in terms of the four material parameters $y_0 > 0$, $y_\infty \geq y_0$, $\eta > 0$ and $h \geq 0$, where the initial yield stress y_0 determines the threshold of the effective elastic response.

Degradation Function. The degradation function $\widehat{g}(d)$ in (4.36) models the degradation of the elastic-plastic work density due to fracture. It interpolates between the unbroken response for $d = 0$ and the fully broken state at $d = 1$ by satisfying the constraints $\widehat{g}(0) = 1$, $\widehat{g}(1) = 0$, $\widehat{g}'(d) \leq 0$ and $\widehat{g}'(1) = 0$. In particular, the last constraint ensures that the local driving force dual to d ensures an upper bound of the phase field $d \in [0, 1]$. A function that satisfies this constraint is

$$\widehat{g}(d) = (1 - d)^2 \,. \tag{4.41}$$

The quadratic nature of this function is an important ingredient for the construction of a *linear equation* for the evolution of the phase field d. Note that the total work density $\widehat{W}$ introduced in (4.36) applies the same degradation function $\widehat{g}(d)$ on the three functions $\widehat{w}_0^e$, $\widehat{w}_0^p$ and $\widehat{w}_0^f$, respectively. This is an important assumption with regard to the subsequent construction of a *gradient plasticity model related to the effective quantities* of the undamaged material, where the effective plastic work density $\widehat{w}_0^p$ serves as a ductile contribution to the crack driving force.*

*The functions $\widehat{g}$ defined in (4.41) appears in the Γ-convergent regularization by Ambrosio and Tortorelli 1990 of the Mumford-Shah functional in image segmentation, see Mumford and Shah 1989. Subsequently, it has been used by Bourdin et al. 2000 in the incremental approximation of their variational theory of brittle fracture, Francfort and Marigo 1998, see also Comi 1999 for an early application in gradient damage mechanics. Note that the function (4.35) is *convex* with $\widehat{g}'' > 0$. This is in contrast to the non-convex function $\widehat{g}(d) = 4(1-d)^3 - 3(1-d)^4$ used in the phase field model of Hakim and Karma 2009 in brittle fracture mechanics.

4.4.3. Stored Energy, Dissipation and Thermodynamic Consistency

Energetic-Dissipative Split. In order to quantify both the energy stored in the material and the dissipation, a further assumption is needed that postulates a split of the work density function $\widehat{W}$ into energetic and dissipative parts. To this end, (4.36) is decomposed

$$\widehat{W}(\boldsymbol{\mathfrak{C}}) = \widehat{\psi}^e(\boldsymbol{b}^e, d) + \widehat{D}^{pf}(\alpha, \nabla\alpha, d, \nabla d) \tag{4.42}$$

into a *stored energy density* $\widehat{\psi}^e$ and the *accumulated dissipative part* $\widehat{D}^{pf}$ due to plasticity and fracture. This split assumes that the macroscopic elastic strain energy is the only part of the total work density that is stored in the material. The constitutive expression for this part obtained from (4.36) is

$$\widehat{\psi}^e(\boldsymbol{b}^e, d) = \widehat{g}(d)\widehat{w}_0^e(\boldsymbol{b}^e) \tag{4.43}$$

governed by the degrading function $\widehat{g}$ and the elastic strain energy function $\widehat{w}_0^e$ of the unbroken material.* Consequently, the remaining part of the work density function (4.36)

$$\widehat{D}^{pf}(\alpha, \nabla\alpha, d, \nabla d) = \widehat{g}(d)\widehat{w}_0^p(\alpha, \nabla\alpha) + (1 - \widehat{g}(d))w_c + 2\frac{w_c}{\zeta} l_f \widehat{\gamma}(d, \nabla d) \tag{4.44}$$

models the accumulated dissipation in terms of the plastic work density function $\widehat{w}_0^p$ of the unbroken material and the crack surface density function $\widehat{\gamma}$.

Plasticity-Fracture Split. Note that $\widehat{D}^{pf}$ provides a constitutive expression for the accumulated dissipation due to plasticity *and* fracture. It does not allow to separate both contributions. In order to investigate this, define the dissipation *locally* as the difference of the external stress power and the evolution of the energy storage, by the standard Clausius-Planck inequality

$$\mathcal{D}^{pf} := \boldsymbol{\tau} : \boldsymbol{d} - \frac{d}{dt}\widehat{\psi}^e \geq 0 \ . \tag{4.45}$$

The evolution of the elastic stored energy $\widehat{\psi}^e$ can be expressed in terms of the material time derivative $\dot{\boldsymbol{b}}^e = \boldsymbol{l}\boldsymbol{b}^e + \boldsymbol{b}^e\boldsymbol{l}^T + \boldsymbol{\pounds}_{\boldsymbol{v}}\boldsymbol{b}^e$. Exploiting the fact that $\boldsymbol{b}^e$ and $\partial_{\boldsymbol{b}^e}\widehat{\psi}^e$ *commute* as a consequence of the elastic isotropy, a standard argument identifies the constitutive equation for the Kirchhoff stress

$$\boldsymbol{\tau} = \widehat{g}(d)\boldsymbol{\tau}_0 \quad \text{with} \quad \boldsymbol{\tau}_0 = 2\boldsymbol{b}^e\partial_{\boldsymbol{b}^e}\widehat{w}_0^e = \partial_{\boldsymbol{h}^e}\widehat{w}_0^e \ . \tag{4.46}$$

The remaining reduced dissipation expression splits up into plastic and fracture parts

$$\mathcal{D}^{pf} := \mathcal{D}^p + \mathcal{D}^f \geq 0 \ \text{ with } \ \mathcal{D}^p := \mathfrak{f}^p : \boldsymbol{d}^p \geq 0 \ \text{ and } \ \mathcal{D}^f := \mathfrak{f}^f \dot{d} \geq 0 \tag{4.47}$$

where $\boldsymbol{d}^p$ is the Eulerian plastic rate of deformation tensor introduced in (4.4). The energetic plastic and fracture *driving forces* are

$$\mathfrak{f}^p := \boldsymbol{\tau} \quad \text{and} \quad \mathfrak{f}^f := -\widehat{g}'(d)\widehat{w}_0^e \tag{4.48}$$

*This assumption does not specify the stored energy due to cold (plastic) work, that is difficult to quantify by caloric experiments. In that sense, (4.43) provides a convenient mathematical definition suitable for *pure mechanical* analyses.

obtained from the energy storage function $\widehat{\psi}^e$ in (4.43). The plastic driving force $\mathfrak{f}^p$ is the Kirchhoff stress $\boldsymbol{\tau}$. The fracture driving force $\mathfrak{f}^f$ is related to the effective elastic energy $\widehat{w}_0^e$. When introducing the time- and space-accumulated dissipative work

$$D^{pf} := \int_0^T \mathcal{D}^{pf}\, dt \quad \text{and} \quad \mathfrak{D}^{pf} := \int_{\mathcal{B}_0} D^{pf}\, dV \ , \tag{4.49}$$

in analogy to (4.34), insertion of (4.47) allows a *separate identification* of the contributions due to plasticity and fracture. In particular, we have

$$D^{pf} := D^p + D^f \tag{4.50}$$

with the definitions

$$D^p := \int_0^T \mathcal{D}^p\, dt \quad \text{and} \quad D^f := \int_0^T \mathcal{D}^f\, dt \ . \tag{4.51}$$

These expressions can numerically be evaluated and provide for a rate-independent model with $D_{vis} = 0$ in (4.35) under homogeneous conditions with $\nabla\alpha = \nabla d = \boldsymbol{0}$ the closed form $\widehat{D}^{pf}$ in (4.44). The split (4.50) is visualized in Figure 4.12 below for a one-dimensional model problem of non-hardening ideal plasticity.

4.4.4. Driving, Resistance and Thresholds for Plasticity and Fracture

The evolutions of the plastic strains and fracture phase field are constructed in a normal-dissipative format related to threshold functions. These functions are formulated in terms of energetic driving forces $\mathfrak{f}^p$ and $\mathfrak{f}^f$ defined in (4.48) and dissipative resistance forces obtained from the dissipative part $\widehat{D}^{pf}$ of the work density function $\widehat{W}$.

Threshold for Plasticity. The rate independent part of the dissipative resistance dual to the hardening variable α is defined

$$r^p := \delta_\alpha \widehat{D}^{pf} = \partial_\alpha \widehat{D}^{pf} - \mathrm{Div}[\partial_{\nabla\alpha} \widehat{D}^{pf}] \tag{4.52}$$

in terms of the variational derivative of $\widehat{D}^{pf}$ by α, reflecting the characteristics of the gradient-extended plasticity model under consideration. An *elastic domain* associated with the plastic deformation in the space of the plastic driving force $\mathfrak{f}^p \equiv \boldsymbol{\tau}$ is defined by

$$\mathbb{E}_{plas} := \{\ (\mathfrak{f}^p, r^p)\ |\ \widehat{\phi}^p(\mathfrak{f}^p, r^p; f) \leq 0\ \} \tag{4.53}$$

in terms of the *plastic yield function* $\widehat{\phi}^p$. It depends on the current microstructural void fraction f, which was in (4.10) assumed to be a *function of the current deformation state*. We focus on a specific class of yield functions for porous materials formulated in terms of the Kirchhoff stresses

$$\widehat{\phi}^p(\mathfrak{f}^p, r^p; f) = \widehat{\chi}^p(\mathfrak{f}^p; f) - \sqrt{\tfrac{2}{3}}\, r^p \tag{4.54}$$

with the *generalized norm of the plastic driving force* $\mathfrak{f}^p \equiv \boldsymbol{\tau}$, which is *positively homogeneous of the degree one*. This provides the property

$$\mathfrak{f}^p : \partial_{\mathfrak{f}^p} \widehat{\chi}^p = \widehat{\chi}^p \tag{4.55}$$

for the normal to the yield function, that is subsequently exploited. A function that satisfies these properties is the *modified Gurson function*

$$\widehat{\chi}^p(\mathfrak{f}^p; f) = \sqrt{(||\operatorname{dev}[\mathfrak{f}^p]||)^2 + \tfrac{1}{3} f\,(\operatorname{tr}[\mathfrak{f}^p])^2} \tag{4.56}$$

in the Kirchhoff stress space derived in Section 4.4.7 below, which degenerates for $f = 0$ to the classical von Mises function.*

Threshold for Fracture. The rate-independent part of the dissipative resistance dual to the fracture phase field d is defined by

$$r^f := \delta_d \widehat{D}^{pf} = \partial_d \widehat{D}^{pf} - \operatorname{Div}[\partial_{\nabla d} \widehat{D}^{pf}] \,. \tag{4.60}$$

in terms of the variational derivative of $\widehat{D}^{pf}$ by d, characterizes the phase field model of fracture as a gradient-extended damage formulation. A *crack threshold domain* in the space of the crack driving force $\mathfrak{f}^f$ is defined by

$$\mathbb{E}_{frac} := \{\, (\mathfrak{f}^f - r^f) \,|\, \widehat{\phi}^f(\mathfrak{f}^f - r^f) \leq 0 \,\} \tag{4.61}$$

in terms of the *crack threshold function* $\widehat{\phi}^f$. We focus on the constitutive representation

$$\widehat{\phi}^f(\mathfrak{f}^f - r^f) = \mathfrak{f}^f - r^f \,. \tag{4.62}$$

where the energetic driving force $\mathfrak{f}^f$ is bounded by the crack resistance r^f.

4.4.5. Evolution Equations for the Generalized Internal Variables

Introduction of a Dissipation Potential Function. With the above introduced threshold and resistance functions at hand, a dissipation potential function can be constructed based on the standard concept of maximum dissipation. For a rate-independent evolution of the inelastic state, this defines the potential function

$$\widehat{V}(\dot{\mathfrak{E}}; f) = \sup_{(\mathfrak{f}^p, r^p) \in \mathbb{E}_{plas}} \; \sup_{(\mathfrak{f}^f - r^f) \in \mathbb{E}_{frac}} [\, \mathfrak{f}^p : \boldsymbol{d}^p - r^p \dot{\alpha} + (\mathfrak{f}^f - r^f)\dot{d} \,] \tag{4.63}$$

* When using the constitutive structure for $\widehat{W}$ in (4.36), note that the above yield function (4.54) can be recast into the form

$$\widehat{\phi}^p(\mathfrak{f}^p, r^p; f) = \widehat{g}(d)\, \widehat{\phi}^p_0(\mathfrak{f}^p_0, r^p_0; f) \quad \text{with} \quad \widehat{\phi}^p_0 = \widehat{\chi}^p(\mathfrak{f}^p_0; f) - \sqrt{\tfrac{2}{3}}\, r^p_0 \tag{4.57}$$

with the degradation function $\widehat{g}(d)$ defined in (4.41) and the *effective plastic yield function* $\widehat{\phi}^p_0$ formulated in terms of the *effective stress-like variables*

$$\mathfrak{f}^p_0 := \frac{1}{\widehat{g}(d)} \mathfrak{f}^p \quad \text{and} \quad r^p_0 := \frac{1}{\widehat{g}(d)} r^p \,. \tag{4.58}$$

This constitutive structure characterizes a formulation of gradient plasticity related to the effective state variables of the undamaged material. Hence, $\mathbb{E}_{plas}$ in (4.53) can be interpreted to bound the domain

$$\mathbb{E}^0_{plas} := \{\, (\mathfrak{f}^p_0, r^p_0) \,|\, \widehat{\phi}^p_0(\mathfrak{f}^p_0, r^p_0; f) \leq 0 \,\} \tag{4.59}$$

in the *effective stress space*.

related to the two elastic domains $\mathbb{E}_{plas}$ and $\mathbb{E}_{frac}$ defined in (4.53) and (4.61), respectively. Note that this normal-dissipative evolution response is governed by only two scalar functions.

F5. The *plastic yield function* $\widehat{\phi}^p(\mathfrak{f}^p, r^p; f)$ that determines the elastic domain in terms of the plastic driving force $\mathfrak{f}^p \equiv \boldsymbol{\tau}$.

F6. The *fracture threshold function* $\widehat{\phi}^f(\mathfrak{f}^f - r^f)$ that determines the initiation of fracture in terms of the fracture driving force $\mathfrak{f}^f$.

These two functions, defined for the model problem under consideration in (4.54) and (4.62), supplement the four constitutive functions $\widehat{w}_0^e$, $\widehat{w}_0^p$, $\widehat{g}$ and $\widehat{\gamma}$ in the total work density function (4.34) and complete the proposed phase field model of fracture.

Rate-Independent Evolution. For the rate-independent evolution, the constrained optimization problem (4.63) is solved via an extended Lagrange functional

$$\widehat{V}(\dot{\boldsymbol{\mathfrak{e}}}; f) = \sup_{\mathfrak{f}^p, r^p, \mathfrak{f}^f - r^f} \sup_{\lambda^p, \lambda^f} [\, \mathfrak{f}^p : \boldsymbol{d}^p - r^p\dot{\alpha} + (\mathfrak{f}^f - r^f)\dot{d} - \lambda^p\widehat{\phi}^p(\mathfrak{f}^p, r^p; f) - \lambda^f\widehat{\phi}^f(\mathfrak{f}^f - r^f) \,] \,, \quad (4.64)$$

where the Lagrange parameters λ^p and λ^f control the non-smooth evolution of the plasticity and the fracture, respectively. The necessary conditions of the local optimization problem (4.64) determine the *plastic flow rules*

$$\boldsymbol{d}^p = \lambda^p\, \partial_{\mathfrak{f}^p}\widehat{\phi}^p \quad \text{and} \quad \dot{\alpha} = -\lambda^p\, \partial_{r^p}\widehat{\phi}^p \quad (4.65)$$

and the normal-dissipative *evolution equation for the crack phase field*

$$\dot{d} = \lambda^f\, \partial_{\mathfrak{f}^f - r^f}\widehat{\phi}^f \,. \quad (4.66)$$

along with the two loading-unloading conditions

$$\lambda^p \geq 0 \,,\ \widehat{\phi}^p \leq 0 \,,\ \lambda^p\widehat{\phi}^p = 0 \quad \text{and} \quad \lambda^f \geq 0 \,,\ \widehat{\phi}^f \leq 0 \,,\ \lambda^f\widehat{\phi}^f = 0 \,. \quad (4.67)$$

of the plastic and fracture response, respectively.

Viscous Regularized Evolution. In this work, we consider *viscous regularizations* for both dissipation mechanisms. This allows the definition of a dissipation potential function in a non-constrained manner

$$\widehat{V}(\dot{\boldsymbol{\mathfrak{e}}}; f) = \sup_{\mathfrak{f}^p, r^p, \mathfrak{f}^f - r^f} [\, \mathfrak{f}^p : \boldsymbol{d}^p - r^p\dot{\alpha} + (\mathfrak{f}^f - r^f)\dot{d} - \widehat{V}^*(\mathfrak{f}^p, r^p, \mathfrak{f}^f - r^f; f) \,] \,, \quad (4.68)$$

in terms of the *dual dissipation potential function*

$$\widehat{V}^*(\mathfrak{f}^p, r^p, \mathfrak{f}^f - r^f; f) = \frac{3}{4\eta_p}\left\langle \widehat{\phi}^p(\mathfrak{f}^p, r^p; f) \right\rangle^2 + \frac{1}{2\eta_f}\left\langle \widehat{\phi}^f(\mathfrak{f}^f - r^f) \right\rangle^2 \quad (4.69)$$

where $\langle x \rangle := (x + |x|)/2$ is the Macaulay bracket. η_p and η_f are additional material parameters which characterize viscosity of the plastic deformation and the crack propagation. Note that the dual dissipation potential $\widehat{V}^*$ in (4.68) can mathematically be interpreted

as a quadratic penalty term, that enforces approximately the threshold conditions (4.53) and (4.61). The necessary conditions of the local optimization problem (4.68) yield the *plastic flow rules* (4.65) and the *evolution equation for the crack phase field* (4.66), where the loading-unloading conditions (4.67) are replaced by the viscous constitutive functions

$$\lambda^p := \frac{3}{2\eta_p} \left\langle \widehat{\phi}^p \right\rangle \geq 0 \quad \text{and} \quad \lambda^f := \frac{1}{\eta_f} \left\langle \widehat{\phi}^f \right\rangle \geq 0 \,. \tag{4.70}$$

Furthermore, note that the positiveness of the parameters λ^p and λ^f imply via (4.65) and (4.66) a *monotonic growth*

$$\dot{\alpha} \geq 0 \quad \text{and} \quad \dot{d} \geq 0 \tag{4.71}$$

of the equivalent plastic strain and the fracture phase field.

4.4.6. Proof of Thermodynamic Consistency and its Consequences

The above evolution equations (4.65) and (4.66) satisfy the thermodynamic constraints (4.47). In particular, we have

$$\mathcal{D}^p = \widehat{\chi}^p(\mathfrak{f}^p; f)\, \lambda^p \geq 0 \quad \text{and} \quad \mathcal{D}^f = \mathfrak{f}^f \lambda^f \geq 0 \,. \tag{4.72}$$

This is obvious due to the a priori positive parameters λ^p and λ^f and the positive driving terms, caused by the *convexity of the threshold functions* $\widehat{\phi}^p$ and $\widehat{\phi}^f$ in (4.54) and (4.62), respectively. For the case of both plastic as well as fracture loading with $\widehat{\phi}^p \geq 0$ and $\widehat{\phi}^f \geq 0$, the driving forces can be expressed in terms of the rate-independent and rate-dependent resistances

$$\widehat{\chi}^p(\mathfrak{f}^p; f) = \sqrt{\tfrac{2}{3}}(r^p + \eta_p \dot{\alpha}) \quad \text{and} \quad \mathfrak{f}^f = r^f + \eta_f \dot{d} \,, \tag{4.73}$$

yielding the representation of the dissipation

$$\mathcal{D}^p = r^p \dot{\alpha} + \eta_p \dot{\alpha}^2 \geq 0 \quad \text{and} \quad \mathcal{D}^f = r^f \dot{d} + \eta_f \dot{d}^2 \geq 0 \,. \tag{4.74}$$

Hence, the total dissipation splits into rate-independent and rate-dependent parts

$$\mathcal{D} := \mathcal{D}^{pf} + \mathcal{D}_{vis} \geq 0 \quad \text{with} \quad \mathcal{D}^{pf} = r^p \dot{\alpha} + r^f \dot{d} \quad \text{and} \quad \mathcal{D}_{vis} := \eta_p \dot{\alpha}^2 + \eta_f \dot{d}^2 \,. \tag{4.75}$$

The viscous part is positive for positive material parameters $\eta_p > 0$ and $\eta_f > 0$. Using the definitions of r^p and r^f in (4.52) and (4.60) in terms of variational derivatives of the function $\widehat{D}^{pf}$, the integration over the volume of the solid gives

$$\int_{\mathcal{B}_0} \mathcal{D} dV = \int_{\mathcal{B}_0} [\, \frac{d}{dt} \widehat{D}^{pf} + \mathcal{D}_{vis} \,] dV - \int_{\partial \mathcal{B}_0} [\, \partial_{\nabla \alpha} \widehat{D}^{pf} \cdot \boldsymbol{n}_0 \dot{\alpha} + \partial_{\nabla d} \widehat{D}^{pf} \cdot \boldsymbol{n}_0 \dot{d} \,] dA \geq 0 \,. \tag{4.76}$$

Here, the surface term vanishes as a consequence of the restriction to "passive" boundary conditions, representing (i) *constant Dirichlet data* and (ii) *zero Neumann data* of α and d on the surface $\partial \mathcal{B}_0$ of the solid, see below for further details. When integrating over the process time $[0, T]$, we end up with the representation of the space-time-accumulated *total dissipative work* needed for the generation of plastic deformation and fracture

$$\mathfrak{D} := \int_{\mathcal{B}_0} [\, \widehat{D}^{pf}(\alpha, \nabla \alpha, d, \nabla d) + D_{vis} \,] dV \geq 0 \tag{4.77}$$

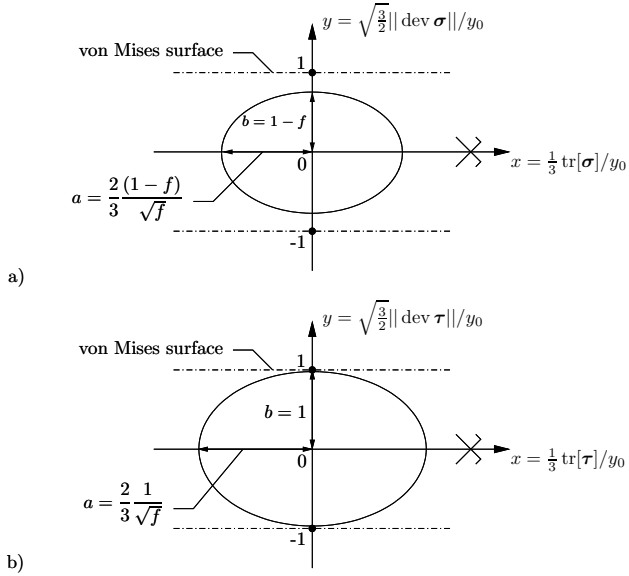

Figure 4.5: Yield surfaces for isotropic porous plasticity, visualized for non-hardening matrix response $r^p = y_0 = const.$ in 2d hydrostatic-deviatoric-stress plot. The void fraction is assumed to be governed by the growth condition (4.10), i.e.$f = 1-(1-f_0)/J$. a) Modified Gurson yield surface (4.80) in *Cauchy stress space* $\boldsymbol{\sigma}$. b) Modified Gurson yield surface (4.82) in *Kirchhoff stress space* $\boldsymbol{\tau}$, where the Kirchhoff stress plays for $f_0 << 1$ according to (4.12) the role of an *effective Cauchy stress*, i.e. $\boldsymbol{\tau} \approx \boldsymbol{\sigma}/(1-f)$.

with the definition

$$D_{vis} := \int_0^T \mathcal{D}_{vis} dt \geq 0 \ . \tag{4.78}$$

This identifies the dissipative part of the work density function $\widehat{W}$ introduced in (4.36) with decomposition (4.42) as the time-space-accumulated dissipative work done to the solid.

4.4.7. A Yield Function for Porous Plasticity in Kirchhoff Stress Space

This subsection comments on the choice of the yield functions for porous plasticity formulated in terms of the Kirchhoff stress $\boldsymbol{\tau}$. Recall that under the void growth assumption (4.10), the Kirchhoff stress plays the role of an effective Cauchy stress acting on the matrix material. Let us start form the classical Gurson yield hypersurface for a porous material

$$\widehat{\phi}^p_G(\boldsymbol{\sigma}, r^p; f) = \frac{\sigma^2_{eq}}{r^{p2}} + 2f\cosh\left[\frac{3}{2}\frac{\sigma_m}{r^p}\right] - (1+f^2) = 0 \tag{4.79}$$

in the space of the *true Cauchy stress* $\boldsymbol{\sigma}$, where $\sigma_{eq} := \sqrt{3/2}||\operatorname{dev}[\boldsymbol{\sigma}]||$ and $\sigma_m := \operatorname{tr}[\boldsymbol{\sigma}]/3$. Making the *approximation* $\cosh(x) \approx x^2/2 + 1$ and using some algebraic manipulations

yields the quadratic hypersurface

$$(||\operatorname{dev}[\boldsymbol{\sigma}]||)^2 + \frac{1}{6} f (\operatorname{tr}[\boldsymbol{\sigma}])^2 - (1-f)^2 \frac{2}{3} r^{p2} = 0 \ . \tag{4.80}$$

Dividing by the factor $(1-f)^2$ gives a surface

$$(||\operatorname{dev}[\widetilde{\boldsymbol{\sigma}}]||)^2 + \frac{1}{6} f (\operatorname{tr}[\widetilde{\boldsymbol{\sigma}}])^2 - \frac{2}{3} r^{p2} = 0 \tag{4.81}$$

in terms of the *effective Cauchy stress* $\widetilde{\boldsymbol{\sigma}} := \boldsymbol{\sigma}/(1-f)$. Finally, approximation of the effective Cauchy stress $\widetilde{\boldsymbol{\sigma}} \approx \boldsymbol{\tau}$ by the Kirchhoff stress $\boldsymbol{\tau}$ according to the result (4.12) gives the new surface

$$\widehat{\phi}^p(\boldsymbol{\tau}, r^p; f) = \widehat{\chi}^p(\boldsymbol{\tau}; f) - \sqrt{\frac{2}{3}} r^p = 0 \tag{4.82}$$

of the desired form (4.54) with the generalized norm of the Kirchhoff stress

$$\widehat{\chi}^p(\boldsymbol{\tau}; f) = \sqrt{(||\operatorname{dev}[\boldsymbol{\tau}]||)^2 + \frac{1}{6} f \, (\operatorname{tr}[\boldsymbol{\tau}])^2} \tag{4.83}$$

that satisfies the condition (4.56) of the homogeneity of the degree one. Note the simple dependence on the void fraction f that is due to the fact that the Kirchhoff stress $\boldsymbol{\tau}$ already includes a dependence on f through (4.12). This influence is highlighted in Figure 4.5 and 4.6 that compares the yield hypersurface in the Cauchy stress space with that in the Kirchhoff stress space. The plastic evolution equations (4.65) take for the function (4.82) the explicit form

$$\boldsymbol{d}^p = \lambda^p \frac{\operatorname{dev}[\boldsymbol{\tau}] + \frac{1}{6} f \ \operatorname{tr}[\boldsymbol{\tau}] \boldsymbol{1}}{\sqrt{(||\operatorname{dev}[\boldsymbol{\tau}]||)^2 + \frac{1}{6} f \, (\operatorname{tr}[\boldsymbol{\tau}])^2}} \quad \text{and} \quad \dot{\alpha} = \lambda^p \sqrt{\frac{2}{3}} \ . \tag{4.84}$$

The function (4.83) recovers for $f = 0$ the classical von Mises function for isochoric plastic flow. In this sense, (4.83) in combination with the simple void growth law (4.10) is considered as the simplest extension of the J_2-flow towards a volumetric plastic flow response in metallic or polymer materials. Note that this function is used here as a plasticity model in combination with a macroscopic fracture condition based on the phase field description. This justifies the simple form when compared with more complex functions describing both plastic deformation as well as ductile fracture.

4.4.8. Role of Material Parameters for Brittle and Ductile Fracture

The onset of fracture and plasticity is governed by the critical work density w_c in (4.36) and the initial yield stress y_0 in (4.40), respectively. The relationship of these two key material parameters on dissipative side to the elastic moduli κ and μ in (4.38) makes the difference between brittle or ductile fracture as indicated in Figure 4.7.

Brittle Fracture. Brittle fracture is initiated by a crack evolution that is followed by a plastic deformation. In other words, the elastic initial deformation reaches a critical state

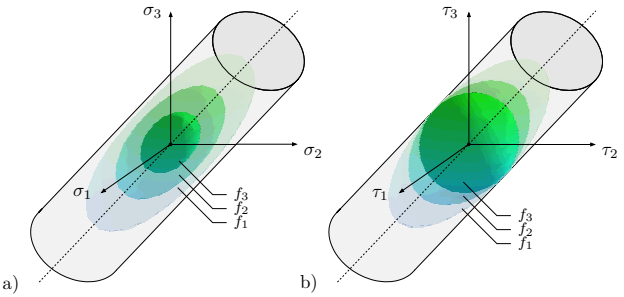

Figure 4.6: Yield surfaces for isotropic porous plasticity, visualized for non-hardening matrix response $r^p = y_0 = const.$ and different void fractions $f_1 < f_2 < f_3$ in 3d principal stress space. a) Modified Gurson yield surface (4.80) in *Cauchy stress space* $\boldsymbol{\sigma}$. b) Modified Gurson yield surface (4.82) in *Kirchhoff stress space* $\boldsymbol{\tau}$, where the Kirchhoff stress plays according to (4.12) the role of an *effective Cauchy stress*, i.e. $\boldsymbol{\tau} \approx \boldsymbol{\sigma}/(1-f)$.

that triggers a brittle crack before plasticity starts. This scenario comes for the condition at the onset of fracture

$$\widehat{\phi}^f(2\widehat{w}_0^e(\boldsymbol{h}) - 2w_c) = 0 \quad \text{and} \quad \widehat{\phi}^p(\partial_{\boldsymbol{h}}\widehat{w}_0^e(\boldsymbol{h}), y_0; \widehat{f}(J)) < 0 \tag{4.85}$$

of the threshold functions introduced above. The combination of these two conditions gives a constraint on the the material parameters

$$\text{Brittle E-F-P Response:} \quad w_c < \frac{1}{3}\frac{y_0^2}{2\mu} + \frac{\kappa}{2}\left(1 - 3\widehat{f}(J)\frac{\kappa}{2\mu}\right)(\ln[J])^2 \tag{4.86}$$

that depends on the volumetric deformation $J := \det[\boldsymbol{F}]$, with $\ln[J] = \operatorname{tr}[\boldsymbol{h}]$ and the elastic bulk modulus $\kappa = \lambda + 2\mu/3$. It states that a critical energy for fracture is less than the energy that triggers plasticity. The onsets of fracture and subsequent plasticity are then defined by the criteria

$$\text{Onset F: } \widehat{w}_0^e(\boldsymbol{h}) = w_c \quad \text{and} \quad \text{Onset P: } \widehat{\chi}^p(\partial_{\boldsymbol{h}}\widehat{w}_0^e(\boldsymbol{h}); \widehat{f}(J)) = \sqrt{2/3}y_0 \ . \tag{4.87}$$

The fracture starts when the elastic energy reaches the critical value w_c. A further increase of logarithmic strain $\boldsymbol{h}$ results in an evolving fracture phase field d. The subsequent onset of plasticity then occurs if the *effective* strain energy reaches the critical energy for plastic yielding.

Ductile Fracture. Ductile fracture is characterized by a plastic yielding before fracture. This scenario is associated with the condition at the onset of plasticity

$$\widehat{\phi}^p(\partial_{\boldsymbol{h}}\widehat{w}_0^e(\boldsymbol{h}), y_0; \widehat{f}(J)) = 0 \quad \text{and} \quad \widehat{\phi}^f(2\widehat{w}_0^e(\boldsymbol{h}) - 2w_c) < 0 \tag{4.88}$$

of the two threshold functions. The combination of these two conditions gives the constraint on the material parameters

$$\text{Ductile E-P-F Response:} \quad w_c > \frac{1}{3}\frac{y_0^2}{2\mu} + \frac{\kappa}{2}\left(1 - 3\widehat{f}(J)\frac{\kappa}{2\mu}\right)(\ln[J])^2 \ . \tag{4.89}$$

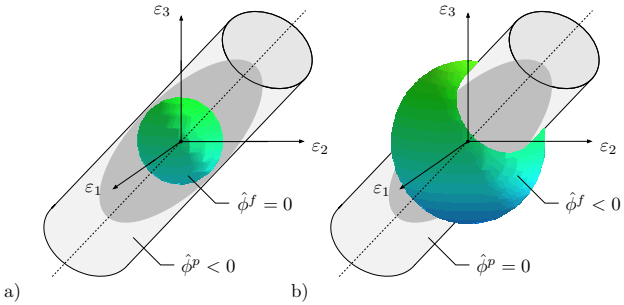

Figure 4.7: Plastic yield function $\widehat{\phi}^p = const.$ in (4.54) and fracture threshold surface $\widehat{\phi}^f = const$ in (4.62) visualized as hypersurfaces for non-hardening matrix response $r^p = y_0 = const.$ in the 3d logarithmic principal strain space. a) *Brittle* E-F-P response according to (4.86) with *active fracture surface* $\widehat{\phi}^f = 0$ at onset of fracture. b) *Ductile* E-P-F response according to (4.89) with *active yield surface* $\widehat{\phi}^p = 0$ at onset of plasticity.

Here, the critical energy that triggers fracture exceeds the energy at the onset of plasticity. The onsets of plasticity and subsequent fracture are then defined by

$$\text{Onset P: } \widehat{\chi}^p(\partial_{\boldsymbol{h}}\widehat{w}_0^e(\boldsymbol{h}); \widehat{f}(J)) = \sqrt{2/3}y_0 \quad \text{and} \quad \text{Onset F: } \widehat{w}_0^e(\boldsymbol{h}^e) + \widehat{w}_0^p(\alpha, \nabla\alpha) = w_c \ . \tag{4.90}$$

Plasticity starts if the elastic energy reaches the critical value for yielding. A further increase of logarithmic strain $\boldsymbol{h}$ results in evolving plastic deformation, characterized by the plastic metric $\boldsymbol{G}^p$ and the equivalent plastic strain α. The subsequent onset of fracture then occurs if the sum of *effective* elastic energy and *effective* plastic work density reaches the critical value for ductile fracture. For a highly ductile material with $\widehat{w}_0^e << \widehat{w}_0^p$ we may estimate for a given local hardening function $\widehat{y}(\alpha)$ a *critical value* α_c *of the equivalent plastic strain* in the matrix material by

$$\widehat{w}_0^p(\alpha_c, \boldsymbol{0}) = \int_0^{\alpha_c} \widehat{y}(\widetilde{\alpha}) d\widetilde{\alpha} \ \approx w_c \ . \tag{4.91}$$

The choice (4.41) of the degradation function $\widehat{g}$ allows a further interpretation of the material parameters w_c and ζ introduced in (4.36). A bound of the effective elastic-plastic work function $\widehat{w}_0^{ep}$ due to plasticity and fracture is per definition the work density function $\widehat{W}$ evaluated at $d = 1$. Hence,

$$\widehat{D}^{pf}(\alpha, \boldsymbol{0}, 1, \boldsymbol{0}) = (1 + \frac{1}{\zeta})w_c \tag{4.92}$$

is the maximum value of the dissipated work density for a *homogeneous rate-independent process*, see Figure 4.12 below. For a given fracture threshold parameter w_c, the parameter $\zeta \leq 1$ scales the dissipative work, providing for $\zeta < 1$ an increase of the dissipation due to fracture.

4.5. Minimization Principle for the Evolution Problem

4.5.1. Minimization Principle for the Multi-Field Evolution Problem

Minimization Problem. With the above introduced functions at hand, the boundary value problem is fully governed by a rate-type minimization principle for the quasi-static case, where inertia effects are neglected. In line with recent treatments on variational principles of gradient-extended materials outlined in Miehe 2011, consider the constitutive rate potential density

$$\pi(\dot{\mathfrak{E}}; f) = \frac{d}{dt}\widehat{W}(\mathfrak{E}) + \widehat{V}(\dot{\mathfrak{E}}; f) \tag{4.93}$$

in terms of the basic constitutive functions $\widehat{W}$ and $\widehat{V}$ defined in (4.36) and (4.68), respectively. The evolution of the boundary-problem of gradient plasticity coupled with gradient damage mechanics is then governed by the *global rate potential*

$$\Pi(\dot{\boldsymbol{\varphi}}, \dot{\alpha}, \dot{d}, \boldsymbol{d}^p) = \int_{\mathcal{B}_0} \pi(\dot{\mathfrak{E}}; f)\, dV \;-\; P_{ext}(\dot{\boldsymbol{\varphi}}) \tag{4.94}$$

where $P_{ext}(\dot{\boldsymbol{\varphi}}) := \int_{\mathcal{B}_0} \overline{\boldsymbol{\gamma}}_0 \cdot \dot{\boldsymbol{\varphi}}\, dV + \int_{\partial\mathcal{B}_0} \overline{\boldsymbol{t}}_0 \cdot \dot{\boldsymbol{\varphi}}\, dA$ is an external load functional. $\overline{\boldsymbol{\gamma}}_0$ is a given body force per unit volume of the reference configuration, $\overline{\boldsymbol{t}}_0$ a given traction field on the surface of the reference configuration. The evolution of all primary fields introduced in Section 4.2 at a given state is determined by the *minimization principle*

$$\{\dot{\boldsymbol{\varphi}}, \dot{\alpha}, \dot{d}, \boldsymbol{d}^p\} = \text{Arg}\{ \inf_{\dot{\boldsymbol{\varphi}}, \dot{\alpha}, \dot{d}, \boldsymbol{d}^p} \Pi(\dot{\boldsymbol{\varphi}}, \dot{\alpha}, \dot{d}, \boldsymbol{d}^p) \} \,. \tag{4.95}$$

Here, the evolutions $\{\dot{\boldsymbol{\varphi}}, \dot{\alpha}, \dot{d}\}$ of the global fields are constrained by Dirichlet-type boundary conditions defined in (4.2), (4.5) and (4.9) above. Note that the minimization structure of this variational principle is governed by the *convexity of the dissipation potential function* $\widehat{V}$ in (4.68), which states the thermodynamical consistency with the second axiom of thermodynamics.

Extended Problem. The combination of the global minimization principle (4.95) with the local maximum problem (4.68) for the definition of the dissipation potential $\widehat{V}$ provides a *mixed variational principle*, that defines all equations of the problem of gradient plasticity at fracture. Setting for compactness of the subsequent notation the *mixed variables*

$$A := r^p = \delta_\alpha \widehat{W} \quad \text{and} \quad D := \mathfrak{f}^f - r^f = \delta_d \widehat{W} \tag{4.96}$$

dual to the equivalent plastic strain α and the fracture phase field d and introducing the *mixed potential density*

$$\pi^* = \frac{d}{dt}\widehat{W}(\mathfrak{E}) + \boldsymbol{\tau} : \boldsymbol{d}^p - A\dot{\alpha} + D\dot{d} - \widehat{V}^*(\boldsymbol{\tau}, A, D; f) \,, \tag{4.97}$$

the Euler equations of the variational principle (4.95) appear in the form

$$\begin{array}{lll}
1. & \textit{Stress equilibrium} & \delta_{\boldsymbol{\varphi}}\pi^* \equiv \; -\mathrm{Div}\,[\,\partial_{\nabla\boldsymbol{\varphi}}\widehat{W}\,] = \overline{\boldsymbol{\gamma}}_0 \\
2. & \textit{Hardening force} & \delta_{\dot{\alpha}}\pi^* \equiv \; \partial_{\alpha}\widehat{W} - \mathrm{Div}\,[\,\partial_{\nabla\alpha}\widehat{W}\,] - A = 0 \\
3. & \textit{Fracture force} & \delta_{\dot{d}}\pi^* \equiv \; \partial_{d}\widehat{W} - \mathrm{Div}\,[\,\partial_{\nabla d}\widehat{W}\,] + D = 0 \\
4. & \textit{Plastic force} & \partial_{\boldsymbol{d}^p}\pi^* \equiv \; -\partial_{\boldsymbol{h}^e}\widehat{W} + \boldsymbol{\tau} = \boldsymbol{0} \\
5. & \textit{Plastic deformation} & \partial_{\boldsymbol{\tau}}\pi^* \equiv \; \boldsymbol{d}^p - \partial_{\boldsymbol{\tau}}\widehat{V}^* = \boldsymbol{0} \\
6. & \textit{Equivalent strain} & \partial_{A}\pi^* \equiv \; -\dot{\alpha} - \partial_{A}\widehat{V}^* = 0 \\
7. & \textit{Fracture phase field} & \partial_{D}\pi^* \equiv \; \dot{d} - \partial_{D}\widehat{V}^* = 0
\end{array} \tag{4.98}$$

along with Neumann-type boundary conditions of the form defined in (4.2), (4.5) and (4.9) above. Note that the above Euler equations are exclusively related to variational derivatives of the potential density π^* defined in (4.97). More details of the Euler equations associated with the variational principle (4.95) are outlined in Section 4.5.3 below.

4.5.2. Isotropic Plasticity Formulated in the Principal Strain Space

The isotropic elastic energy $\widehat{w}_0^e(\boldsymbol{h}^e)$ in (4.38) and the yield function $\widehat{\phi}^p$ in (4.54) can be formulated in terms of the elastic principal stretches and the principal stresses, respectively. To this end, solve the eigenvalue problem for the elastic Finger tensor in (4.2)

$$\left[\boldsymbol{b}^e - \lambda^{e2}\boldsymbol{1}\right]\boldsymbol{n}_i = \boldsymbol{0}\ , \tag{4.99}$$

where $\{\lambda_i^e\}_{i=1,3}$ are the elastic principal stretches and $\boldsymbol{n}_{i=1,3}$ the associated eigenvector triad. The Eulerian logarithmic Hencky tensor then takes the spectral form

$$\boldsymbol{h}^e := \tfrac{1}{2}\ln[\boldsymbol{b}^e] = \textstyle\sum_{i=1}^{3}\varepsilon_i^e\boldsymbol{n}_i\otimes\boldsymbol{n}_i \tag{4.100}$$

in terms of the *logarithmic elastic principle strains*

$$\varepsilon_i^e := \ln[\lambda_i^e]\ . \tag{4.101}$$

The spectral representation of the stored elastic energy functions $\widehat{w}_0^e$ results in the specific representation of the *work density function* (4.36)

$$\widehat{W} = \widehat{g}(d)[\ \widehat{w}_0^e(\varepsilon_1^e,\varepsilon_2^e,\varepsilon_3^e) + \widehat{w}_0^p(\alpha,\nabla\alpha)\ ] + (1-\widehat{g}(d))w_c + 2\frac{w_c}{\zeta}l_f\widehat{\gamma}(d,\nabla d)\ . \tag{4.102}$$

The straightforward exploitation of the hyperelastic stress function (4.46) then gives the spectral representation of the Kirchhoff stresses

$$\boldsymbol{\tau} = \textstyle\sum_{i=1}^{3}\tau_i\boldsymbol{n}_i\otimes\boldsymbol{n}_i \quad\text{with}\quad \tau_i = \widehat{W}_{,i} := \partial\widehat{W}/\partial\varepsilon_i^e \tag{4.103}$$

in terms of the *principal Kirchhoff stresses* τ_i. Furthermore, the spectral representation of the yield function $\widehat{\phi}^p$ results in the specific representation of the *dual dissipation potential function* (4.69)

$$\widehat{V}^* = \frac{3}{4\eta_p}\left\langle\widehat{\phi}^p(\tau_1,\tau_2,\tau_3,A;f)\right\rangle^2 + \frac{1}{2\eta_f}\left\langle\widehat{\phi}^f(D)\right\rangle^2 \tag{4.104}$$

where $\widehat{\phi}^p$ is evaluated at a given microstructural void state f. Then it can be shown that the Eulerian plastic flow rule (4.65) appears in the spectral form

$$\boldsymbol{d}^p = \textstyle\sum_{i=1}^{3}d_i^p\boldsymbol{n}_i\otimes\boldsymbol{n}_i \quad\text{with}\quad d_i^p = \widehat{V}_{,i}^* := \partial\widehat{V}^*/\partial\tau_i \tag{4.105}$$

in terms of the objective evolutions d_i^p in the directions of the principal axes.

4.5.3. Objective Exponential Integrator of the Plastic Metric

Consider a finite time increment $[t_n, t_{n+1}]$, where $\tau_{n+1} := t_{n+1} - t_n > 0$ denotes the step length, and all fields at time t_n are assumed to be *known*. An objective update algorithm for the Eulerian flow rule is obtained by integrating the Lagrangian counterpart of the rate equations (4.65) and transferring the result to the current configuration via a push-forward with the discrete map $\boldsymbol{F}_{n+1}$. The Lagrangian counterpart of (4.65) reads when using the transformation (4.4)

$$-\tfrac{1}{2}\dot{\boldsymbol{G}}^{p-1}\boldsymbol{G}^{p} = \boldsymbol{F}^{-1}\partial_{\boldsymbol{\tau}}\widehat{V}^{*}\boldsymbol{F}\ . \tag{4.106}$$

A backward Euler integrator with an exponential shift then yields the Lagrangian update algorithm

$$\boldsymbol{G}^{p-1}_{n+1} = \exp[\,-2\tau_{n+1}\boldsymbol{F}^{-1}_{n+1}\partial_{\boldsymbol{\tau}}\widehat{V}^{*}\boldsymbol{F}_{n+1}\,]\boldsymbol{G}^{p-1}_{n}\ . \tag{4.107}$$

In what follows, for convenience, all variables without subscript are understood to be evaluated at time t_{n+1}. Exploiting the algebraic result $\exp[\boldsymbol{F}^{-1}\boldsymbol{A}\boldsymbol{F}] = \boldsymbol{F}^{-1}\exp[\boldsymbol{A}]\boldsymbol{F}$, the transformation of (4.107) to the spatial configuration yields the objective update algorithm of the elastic Finger tensor

$$\boldsymbol{b}^{e} = \exp[-2\tau\partial_{\boldsymbol{\tau}}\widehat{V}^{*}]\boldsymbol{b}^{e*} \quad \text{with} \quad \boldsymbol{b}^{e*} := \boldsymbol{F}\boldsymbol{G}^{p-1}_{n}\boldsymbol{F}^{T}\ , \tag{4.108}$$

where the trial value $\boldsymbol{b}^{e*}$ was introduced. Recall that for the isotropic elastic response $\boldsymbol{\tau}$ and $\boldsymbol{b}^{e}$ commute. As a consequence, observe from (4.108) that also $\boldsymbol{b}^{e*}$ commutes with $\boldsymbol{b}^{e}$. Exploiting this *coaxiality of the incremental setting*, the current logarithmic elastic strains defined in (4.100) take the additive algorithmic form

$$\boldsymbol{h}^{e} = \boldsymbol{h}^{e*} - \tau\partial_{\boldsymbol{\tau}}\widehat{V}^{*} \quad \text{with} \quad \boldsymbol{h}^{e*} := \tfrac{1}{2}\ln[\boldsymbol{b}^{e*}] \tag{4.109}$$

for the elastic Hecnky tensor, similar to the small-strain update of the geometric linear theory. Hence, the integration of the flow rule (4.107) boils down to the update of the logarithmic principal elastic strains

$$\varepsilon^{e}_{i} = \varepsilon^{e*}_{i} - \tau\widehat{V}^{*}_{,i} \tag{4.110}$$

in the eigenvalue space of the trial elastic Finger tensor $\boldsymbol{b}^{e*}$ defined in (4.108). This holds in the current incremental step for *known* trail strains $\varepsilon^{e*}_{i} = \ln[\lambda^{e*}_{i}]$ and *known* eigenvectors $\boldsymbol{n}^{*}_{i=1,3}$ obtained form the eigenvalue problem $[\boldsymbol{b}^{e*} - \lambda^{e*2}_{i}\boldsymbol{1}]\boldsymbol{n}^{*}_{i} = \boldsymbol{0}$.

4.5.4. Numerical Implementation of the Minimization Problem

Incremental Potential Density. Next, a *mixed incremental potential density* per unit volume is defined by the algorithmic approximation

$$\pi^{*\tau} = Algo\{\int_{t_n}^{t_{n+1}} \pi^{*}\,dt\,\} \tag{4.111}$$

in terms of the the continuous rate-type potential π^{*} introduced in (4.97). A fully implicit Euler scheme consistent with the above exponential update (4.108) gives

$$\pi^{*\tau} = \widehat{W} + \textstyle\sum_{i=1}^{3}\tau_{i}\,[\,\varepsilon^{e*}_{i} - \varepsilon^{e}_{i}\,] - A(\alpha - \alpha_{n}) + D(d - d_{n}) - \tau\widehat{V}^{*} \tag{4.112}$$

Here, the work density function $\widehat{W}$ and the dual dissipation function $\widehat{V}^*$ are understood to be formulated in terms of principal strains and stresses according to (4.102) and (4.104), respectively. The second term in (4.112) expresses the plastic dissipation by the difference between the current elastic principal strains strains and its trial values. In order to obtain an incremental potential consistent with the continuous setting, the incremental potential *must* be evaluated for a microstructural void state f_n at time t_n.

Condensation of Local Variables. The first part of the incremental solution procedure consists of the condensation of the incremental potential density $\pi^{*\tau}$ in (4.112) by the set of local variables $\{\varepsilon_i^e, \sigma_i\}$, defining *condensed incremental work density*

$$(L^*): \quad \pi^{*\tau}_{red} = \inf_{\varepsilon_i^e} \sup_{\tau_i} \pi^{*\tau} \ . \tag{4.113}$$

The necessary conditions of this local problem

$$\partial_{\{\varepsilon_i^e, \tau_i\}} \pi^{*\tau} = \begin{bmatrix} \widehat{W}_{,i} - \tau_i \\ \varepsilon_i^{e*} - \varepsilon_i^e - \tau \widehat{V}^*_{,i} \end{bmatrix} = \boldsymbol{0} \ , \tag{4.114}$$

recovers the constitutive definition (4.103) of the principal plastic driving forces and the algorithmic update (4.110) of the logarithmic elastic principal strains. With known principal stresses σ_i, the stress tensor is defined by the algorithmic expression (4.103) for $\boldsymbol{n} = \boldsymbol{n}_i^*$.

Reduced Global Problem. With the condensed incremental work potential $\pi^{*\tau}_{red}$ in (4.113) at hand, define the reduced potential function

$$\Pi^{*\tau}_{red} = \int_{\mathcal{B}_0} \pi^{*\tau}_{red} \, dV \tag{4.115}$$

for pure Dirichlet problems with $P_{ext} = 0$ in (4.94). The second part of the incremental solution procedure consists of the solution of the mixed saddle point principle

$$(G^*): \quad \{\boldsymbol{\varphi}, \alpha, d, A, D\} = \mathrm{Arg}\{ \inf_{\boldsymbol{\varphi}, \alpha, d} \sup_{A, D} \Pi^{*\tau}_{red}(\boldsymbol{\varphi}, \alpha, d, A, D) \} \tag{4.116}$$

that determines the global fields and the associated driving forces. A straightforward finite element discretization of this problem based on interpolations

$$\mathfrak{C}_{G^*}(\boldsymbol{X}, t) := \{\nabla\boldsymbol{\varphi}, \alpha, \nabla\alpha, d, \nabla d, A, D\} = \boldsymbol{B}^*(\boldsymbol{X})\boldsymbol{d}^*(t) \tag{4.117}$$

with $\boldsymbol{d}^* := \{\boldsymbol{\varphi}, \alpha, d, A, D\}_{I=1}^{N_{node}}$ results in the necessary condition of the FE-discretized mixed variational principle (4.116), yielding the nonlinear algebraic system

$$\partial_{\boldsymbol{d}^*} \Pi^{*\tau h}_{red} = \int_{\mathcal{B}_0} \boldsymbol{B}^{*T} \boldsymbol{\mathcal{S}}^* \, dV = \boldsymbol{0} \ . \tag{4.118}$$

Here, $\mathfrak{S}^*$ may be viewed as a 'generalized stress array' dual to the global part $\mathfrak{C}_{G^*}$ of the state variables, defined by

$$\mathfrak{S}^* := \partial_{\mathfrak{C}_{G^*}} \pi^{*\tau}_{red} = \begin{bmatrix} \partial_{\nabla\boldsymbol{\varphi}} \widehat{W} \\ \partial_\alpha \widehat{W} - A \\ \partial_{\nabla\alpha} \widehat{W} \\ \partial_d \widehat{W} + D \\ \partial_{\nabla d} \widehat{W} \\ -(\alpha - \alpha_n) - \tau \partial_A \widehat{V}^* \\ (d - d_n) - \tau \partial_D \widehat{V}^* \end{bmatrix} . \tag{4.119}$$

A difficulty of the numerical solution of the mixed variational principle (4.116) is the appropriate interpolation of the dual-primal problem that includes the driving forces A and D associated with the gradient plastic and the gradient damage effects. For the phase field model of brittle fracture, such an implementation is outlined in Miehe et al. 2010b. For gradient plasticity, the recent sequence of works Miehe et al. 2013, 2015a discussed details of the mixed finite element formulations.

4.5.5. Micromorphic Regularization and Introduction of Crack History

The above outlined mixed implementation of coupled gradient plasticity-damage by finite element methods is demanding. A more convenient numerical implementation is achieved by two extensions of the above setting: (i) a *micromorphic regularization* on the side of gradient plasticity as recently suggested by Miehe et al. 2016b and (ii) the introduction of a *crack driving history field* on the side of gradient damage mechanics in line with Miehe et al. 2010b. These two modifications allow to defined a *further reduced global system*, where the mixed variables A and D in (4.116) are eliminated.

Micromorphic Regularization of Gradient Plasticity. The micromorphic setting, applied here in the generalized sense of Forest 2009 to the microstructural hardening variable, is based on an *extension* of the set (4.11) of state variables

$$\mathfrak{C} := \{\nabla\boldsymbol{\varphi}, \boldsymbol{G}^{p-1}, \bar{\alpha}, \alpha, \nabla\alpha, d, \nabla d\} \tag{4.120}$$

by the *local* equivalent plastic strain $\bar{\alpha}$. The dual *global* field α is then denoted as the micromorphic variable. The micromorphic regularization of the work density function $\widehat{W}$ in (4.102) affects only the microstructural work density $\widehat{w}^p_0(\alpha, \nabla\alpha)$, which is now extended towards a *micromorphic regularization*

$$\widehat{w}^p_0(\bar{\alpha}, \alpha, \nabla\alpha) = \int_0^{\bar{\alpha}} \widehat{y}(\widetilde{\bar{\alpha}}) d\widetilde{\bar{\alpha}} + y_0 \frac{l_p^2}{2} |\nabla\alpha|^2 + \frac{\epsilon_p}{2} (\bar{\alpha} - \alpha)^2 . \tag{4.121}$$

Here, the local slot α in (4.39) is *replaced* by the additional local variable $\bar{\alpha}$ introduced above. This variable is then linked to the global micromorphic field variable α by the quadratic penalty term, where ϵ_p is an additional material parameter. Note the for $\epsilon_p \to \infty$ the above micromorphic extension (4.121) recovers the original setting (4.39) of the gradient-extended theory in Section 4.3. The modification (4.121) by $\bar{\alpha}$ inserted into

(4.102) results in an extended work density function $\widehat{W}_m$. A further modification concerns the incremental potential in (4.112)

$$\pi_m^{*\tau} = \widehat{W}_m + \textstyle\sum_{i=1}^{3} \tau_i \, [\, \varepsilon_i^{e*} - \varepsilon_i^{e} \,] - A(\bar{\alpha} - \bar{\alpha}_n) + D(d - d_n) - \tau \widehat{V}^* \tag{4.122}$$

where the variable A is now considered to be dual to the *local* hardening variable $\bar{\alpha}$. These modifications relax the above mentioned problem of restricting the gradient variable to the plastic domain. Furthermore, the setting allows the use of *local* return algorithms for the update of the plastic state variables.

Condensation of Local Variables. With the micromorphic extension (4.121), an extension of the *condensed incremental work density* (4.113) is achieved

$$(L_m^*): \quad \pi_{m,red}^{*\tau} = \inf_{\varepsilon_i^e, \bar{\alpha} \tau_i, A} \sup \, \pi_m^{*\tau} \; . \tag{4.123}$$

which now determines in addition to (4.113) the local hardening variable $\bar{\alpha}$ and its dual driving force A. The necessary conditions of this extended problem are

$$\partial_{\{\varepsilon_i^e, \bar{\alpha}, \tau_i, A\}} \pi_m^{*\tau} = \begin{bmatrix} \widehat{W}_{m,i} - \tau_i \\ \widehat{W}_{m,\bar{\alpha}} - A \\ \varepsilon_i^{e*} - \varepsilon_i^e - \tau \widehat{V}_{,i}^* \\ -(\bar{\alpha} - \bar{\alpha}_n) - \tau \widehat{V}_{,A}^* \end{bmatrix} = \boldsymbol{0} \; . \tag{4.124}$$

The big advantage of this setting, when compared to (4.114), is that these equations characterize a setting of *local plasticity in the principal strain space with isotropic hardening* at frozen global micromorphic hardening variable α and fracture phase field variable d. Such a system can be solved by a *local return algorithm*. This local solution procedure is summarized in the two Boxes 4.1 and 4.2 below. Box 4.1 covers a pre- and post-processing, that first defines the trial state and finally determines the current stress state by a spectral representation. The core of the algorithm is summarized in Box 4.1, that concerns the solution in the eigenvalue space. It is a Newton-type solver of the system (4.124) with a particular structure providing closed forms of the current principal stresses and the elastic-plastic moduli. Note carefully that it is formulated such that the algorithm can be applied in the *rate-independent limit* $\eta_p = 0$.

Elimination of the Crack Driving Force. On the side of the phase field evolution, the mixed variable D can be eliminated as follows. From $(4.98)_7$ and $(4.98)_3$ one finds

$$\dot{d} = \frac{1}{\eta_f} \langle \, D \, \rangle \quad \text{with} \quad D = -\delta_d \widehat{W}_m \; . \tag{4.132}$$

The combination of of these equations characterizes a generalized Ginzburg-Landau- or Allen-Cahn-type equation for the evolution of the crack phase field d. It gives

$$\eta_f \dot{d} = \left\langle \, 2(1-d)[\, \widehat{w}_0^{ep} - w_c \,] - 2\frac{w_c}{\zeta} d + \mathrm{Div}[2\frac{w_c}{\zeta} l_f^2 \nabla d] \right\rangle \; . \tag{4.133}$$

Box 4.1: Stress Update Algorithm for Isotropic Visco-Elasto-Plasticity.

1. *Preprocessing.* $\boldsymbol{F}$ and $\{\boldsymbol{G}_n^{p-1}, \bar{\alpha}_n\}$ are given. Get trial value of Eulerian elastic Finger tensor $\boldsymbol{b}^{e*} := \boldsymbol{F}\boldsymbol{G}_n^{p-1}\boldsymbol{F}^T$, perform spectral decomposition $\boldsymbol{b}^{e*} = \sum_{i=1}^3 \lambda_i^{e*2} \boldsymbol{n}_i^* \otimes \boldsymbol{n}_i^*$ and compute trial logarithmic principal strains $\varepsilon_i^{e*} := \ln[\lambda_i^{e*}]$.

2. *Constitutive Box.* Compute elastic strains ε_i^e, principal stresses τ_i and algorithmic moduli $\mathbb{E}_{ij}^{ep}$ in eigenvalue space from the constitutive Box 4.2.

3. *Postprocessing.* Compute current elastic principal stretches $\lambda_i^e = \exp[\varepsilon_i^e]$, update Lagrangian plastic metric $\boldsymbol{G}^{p-1} = \boldsymbol{F}^{-1}[\sum_{i=1}^3 \lambda_i^{e2} \boldsymbol{n}_i^* \otimes \boldsymbol{n}_i^*]\boldsymbol{F}^{-T}$, get Kirchhoff stresses and algorithmic tangent moduli

$$\begin{array}{rl} \boldsymbol{\tau} & = \sum_{i=1}^3 \tau_i \boldsymbol{n}_i^* \otimes \boldsymbol{n}_i^* \\ \mathbb{E} & = \sum_i^3 \sum_j^3 [\, \mathbb{E}_{ij}^{ep} - 2\tau_i \delta_{ij} \,] \, \boldsymbol{n}_i^* \otimes \boldsymbol{n}_i^* \otimes \boldsymbol{n}_j^* \otimes \boldsymbol{n}_j^* \\ & \quad + \sum_i^3 \sum_{j \neq i}^3 \frac{\tau_i \lambda_j^{e*2} - \tau_j \lambda_i^{e*2}}{\lambda_i^{e*2} - \lambda_j^{e*2}} \boldsymbol{n}_i^* \otimes \boldsymbol{n}_j^* \otimes \boldsymbol{n}_i^* \otimes \boldsymbol{n}_j^* \end{array} \tag{4.125}$$

and compute nominal stresses and elastic-plastic tangent moduli

$$\boldsymbol{P} = \{\boldsymbol{\tau}\} \overset{2}{\circ} \boldsymbol{F}^{-T} \quad \text{and} \quad \boldsymbol{\mathcal{A}} = \{\, \mathbb{E} + \boldsymbol{1} \odot \boldsymbol{\tau} \,\} \overset{2}{\circ} \boldsymbol{F}^{-T} \overset{4}{\circ} \boldsymbol{F}^{-T} \tag{4.126}$$

In this equation, the effective work density $\widehat{w}_0^{ep}$ plays the role of the driving force. Crucial observation now is that $\widehat{w}_0^{ep}$ *does not depend of the phase field* d. As a consequence, we may recast the above equation into the form

$$\eta^f \dot{d} = 2(1-d)\mathcal{H}_0 - 2\frac{w_c}{\zeta} d + \mathrm{Div}[2\frac{w_c}{\zeta} l_f^2 \nabla d] \,, \tag{4.134}$$

where we introduced the *crack driving history field*

$$\mathcal{H}_0 = \max_{s \in [0,t]} \langle\, \widehat{w}_0^{ep} - w_c \,\rangle \tag{4.135}$$

It is the maximum value of the work density $\widehat{w}_0^{ep}$ due to elastic, plastic and microstructural fracture effects above the threshold w_c, obtained in the history of the deformation process. This field describes intrinsically the *local irreversibility* of the fracture process. Its introduction is very convenient for the numerical implementation, which is subsequently performed by considering the reduced equation (4.134) as the key governing equation for the fracture phase field evolution.

Reduced Global Problem. As a consequence of the micromorphic regularization on the side of gradient plasticity, and the above elimination of the variable D, the reduced global problem (4.116) takes the *pure minimization form structure*

$$(G_m^*): \quad \{\boldsymbol{\varphi}, \alpha, d\} = \mathrm{Arg}\{ \inf_{\boldsymbol{\varphi}, \alpha, d} \Pi_{m,red}^{\tau}(\boldsymbol{\varphi}, \alpha, d) \} \,. \tag{4.136}$$

Box 4.2: Return Algorithm and Tangent Moduli in Eigenvalue Space.

1. Set initial values $\varepsilon_i^e = \varepsilon_i^{e*}$ for $i = 1...3$, $\bar{\alpha} = \bar{\alpha}_n$ and $\gamma^p = 0$.

2. Compute derivatives of work function $\widehat{W}_m$ and plastic yield function $\widehat{\phi}^p$

$$\begin{array}{ll} \widehat{W}_m(\varepsilon_1^e, \varepsilon_2^e, \varepsilon_3^e, \bar{\alpha}, \alpha, \nabla\alpha, d, \nabla d; f_n) & \widehat{\phi}^p(\tau_1, \tau_2, \tau_3, A; f_n) \\ \begin{bmatrix} \tau_i \\ A \end{bmatrix} = \begin{bmatrix} \widehat{W}_{m,i} \\ \widehat{W}_{m,\bar{\alpha}} \end{bmatrix} & \underline{\boldsymbol{n}}^p := \begin{bmatrix} \widehat{\phi}^p_{,i} \\ \widehat{\phi}_{,A} \end{bmatrix} \\ \underline{\mathbb{E}}^e := \begin{bmatrix} \widehat{W}_{m,ij} & \widehat{W}_{m,i\bar{\alpha}} \\ \widehat{W}_{m,\bar{\alpha}j} & \widehat{W}_{m,\bar{\alpha}\bar{\alpha}} \end{bmatrix} & \underline{\mathbb{F}}^p := \begin{bmatrix} \widehat{\phi}^p_{,ij} & \widehat{\phi}^p_{,iA} \\ \widehat{\phi}^p_{,Aj} & \widehat{\chi}^p_{,AA} \end{bmatrix} \end{array} \tag{4.127}$$

3. For elastic step ($\widehat{\phi}^p < 0$): Set stresses $\tau_i = \widehat{W}_{m,i}$, moduli $\mathbb{E}^{ep}_{ij} = \widehat{W}_{m,ij}$ and exit.

4. Compute residuals and check tolerance

$$\underline{\boldsymbol{r}}^p := \begin{bmatrix} \varepsilon_i^e - \varepsilon_i^{e*} \\ \bar{\alpha} - \bar{\alpha}^* \end{bmatrix} + \gamma^p \underline{\boldsymbol{n}}^p \ . \quad \text{If } [\ \sqrt{\underline{\boldsymbol{r}}^{pT}\underline{\boldsymbol{r}}^p + [\ \widehat{\phi}^p - \frac{2\eta_p}{3\tau}\gamma^p\ ]^2} < tol\ ] \text{ go to 6.} \tag{4.128}$$

5. Set $\underline{\mathbb{X}}^p := [\ \underline{\mathbb{E}}^{e-1} + \gamma^p \underline{\mathbb{F}}^p\ ]^{-1}$, compute incremental plastic parameter

$$\Delta\gamma^p = \frac{1}{D^p}[\ \widehat{\phi}^p - \underline{\boldsymbol{n}}^{pT}\underline{\mathbb{X}}^p\,\underline{\boldsymbol{r}}^p\ ] \quad \text{with} \quad D^p := \underline{\boldsymbol{n}}^{pT}\underline{\mathbb{X}}^p\,\underline{\boldsymbol{n}}^p \ , \tag{4.129}$$

incremental strains

$$\begin{bmatrix} \Delta\varepsilon_i^e \\ \Delta\bar{\alpha} \end{bmatrix} = -\underline{\mathbb{E}}^{e-1}\underline{\mathbb{X}}^p\ [\ \underline{\boldsymbol{r}}^p + \Delta\gamma^p\,\underline{\boldsymbol{n}}^p\ ] \ , \tag{4.130}$$

perform the updates $\varepsilon_i^e \Leftarrow \varepsilon_i^e + \Delta\varepsilon_i^e$, $\bar{\alpha} \Leftarrow \bar{\alpha} + \Delta\bar{\alpha}$, $\gamma^p \Leftarrow \gamma^p + \Delta\gamma^p$ and go to 2.

6. Obtain stresses and consistent moduli in eigenvalue space

$$\tau_i = \widehat{W}_{m,i} \quad \text{and} \quad \mathbb{E}^{ep}_{ij} = \mathbb{X}^p_{ij} - \frac{1}{D^p}[\,\mathbb{X}^p_{ik}\widehat{\phi}^p_{,k} + \mathbb{X}^p_{iA}\widehat{\phi}^p_{,A}\,] \otimes [\,\widehat{\phi}^p_{,l}\mathbb{X}^p_{lj} + \widehat{\phi}^p_{,A}\mathbb{X}^p_{Aj}\,] \tag{4.131}$$

A finite element discretization of this problem based on interpolations

$$\mathfrak{C}_{G_m^*}(\boldsymbol{X},t) := \{\nabla\boldsymbol{\varphi}, \alpha, \nabla\alpha, d, \nabla d\} = \boldsymbol{B}(\boldsymbol{X})\boldsymbol{d}(t) \tag{4.137}$$

with $\boldsymbol{d} := \{\boldsymbol{\varphi}, \alpha, d\}_{I=1}^{N_{node}}$. This results in the reduction of the algebraic finite element problem (4.118) that reads

$$\partial_{\boldsymbol{d}}\Pi_{m,red}^{\tau h} = \int_{\mathcal{B}_0} \boldsymbol{B}^T \boldsymbol{\mathcal{S}}\, dV = \boldsymbol{0}\ . \tag{4.138}$$

in terms of the reduced 'generalized stress operator'

$$\boldsymbol{\mathcal{S}} := \partial_{\mathfrak{C}_{G_m^*}} \pi_{m.red}^{\tau} = \begin{bmatrix} \boldsymbol{P} \\ \epsilon_p(\bar{\alpha} - \alpha) \\ y_0\, l_p^2\, \nabla\alpha \\ \frac{\eta_f}{\tau}(d - d_n) - [\,(2(1-d)\mathcal{H}_0 - 2\frac{w_c}{\zeta}d\,] \\ 2\,\frac{w_c}{\zeta}\, l_f^2\, \nabla d \end{bmatrix}\ . \tag{4.139}$$

The fist Piola nominal stress $\boldsymbol{P}$ is provided by the local return algorithm in Box 4.1. It is a convenient reduction of the original operator of the mixed setting defined in (4.119), where the mixed variables A and D are eliminated based on (i) the micromorphic gradient plastic setting in (4.121) and (ii) the introduction of the history field in (4.135). Note that the last two entries in (4.139) are obtained as the weak form of equation (4.134). Observe furthermore that the formulation can be applied in the *rate-independent limit* $\eta_f = 0$ of the crack evolution.

4.5.6. The Three Governing PDEs of the Multi-Field Problem

In order to make the three governing equations $(4.98)_{1-3}$ more transparent, we comment in what follows on their detailed structure and possible modifications.

The Stress Equilibrium Equation. The first Euler equation $(4.98)_1$ of the variational principle (4.95) is the quasi-static form of the balance of momentum, which follows by taking the variation of the potential Π in (4.94) with respect to $\dot{\boldsymbol{\varphi}}$, yielding

$$\mathrm{Div}\,[(1-d)^2\boldsymbol{\tau}_0\boldsymbol{F}^{-T}] + \overline{\boldsymbol{\gamma}}_0 = \boldsymbol{0}\ . \tag{4.140}$$

The argument of material divergence operator is the first Piola nominal stress $\boldsymbol{P}$, obtained from the potential $\widehat{W}$ in (4.36) by

$$\boldsymbol{P} = \partial_{\boldsymbol{F}}\widehat{W} = \boldsymbol{\tau}\boldsymbol{F}^{-T} \quad \text{with} \quad \boldsymbol{\tau} = \partial_{\boldsymbol{h}^e}\widehat{W}\ , \tag{4.141}$$

for the isotropic case under consideration, where the Eulerian Kirchhoff stress $\boldsymbol{\tau}$ follows from the general return algorithm in Box 4.1. It is related by

$$\boldsymbol{\tau} = (1-d)^2\boldsymbol{\tau}_0 \quad \text{with} \quad \boldsymbol{\tau}_0 := \kappa\,\mathrm{tr}[\boldsymbol{h}^e]\boldsymbol{1} + 2\mu\,\mathrm{dev}[\boldsymbol{h}^e] \tag{4.142}$$

to the effective Kirchhoff stress $\boldsymbol{\tau}_0$ dual to the elastic Eulerian Hencky strain $\boldsymbol{h}^e$.

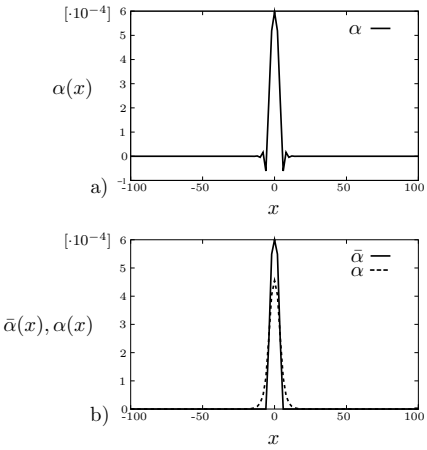

Figure 4.8: Canonical versus micromorphic formulation of gradient plasticity. Standard one-dimensional finite element solutions of gradient plasticity for a) canonical setting in equation (4.146) results in nonphysical oscillations at the elastic-plastic boundary, which are relaxed in b) by the micromorphic approach according to equations (4.148) and (4.149).

Gradient Plastic Evolution. The second Euler equation $(4.98)_2$ of the variational principle (4.95) determines the PDE for the strain gradient plastic evolution of the equivalent plastic strain. It defines the microstructural plastic hardening force

$$A = \delta_\alpha \widehat{W} = (1-d)^2 A_0 \quad \text{with} \quad A_0 := \widehat{y}(\alpha) - y_0 l_p^2 \Delta\alpha \tag{4.143}$$

in terms of the given *local* hardening function $\widehat{y}$ and the strain gradient term, governed by the Laplacian $\Delta\alpha$ of the equivalent plastic strain. It characterizes a combination of nonlinear local hardening with linear gradient hardening consistent with approaches by Aifantis 1987 and Mühlhaus and Aifantis 1991. The above PDE is accompanied by the Euler equations $(4.98)_{4,5,6}$ for the evolution equations of the plastic state, which give for particular model of porous plasticity

$$\dot{\alpha} = \lambda^p \sqrt{\tfrac{2}{3}} \quad \text{with} \quad \lambda^p := \frac{3}{2\eta^p} \left\langle \, \widehat{\chi}^p(\boldsymbol{\tau}; f) - \sqrt{\tfrac{2}{3}}\, A \, \right\rangle \tag{4.144}$$

as already stated in (4.84). Note that the degradation function $(1-d)^2$ acts on both the stresses (4.142) and as well as hardening variable (4.143), i.e. $\widehat{\chi}^p(\boldsymbol{\tau}; f) = (1-d)^2 \widehat{\chi}^p(\boldsymbol{\tau}_0; f)$ and $A = (1-d)^2 A_0$. As a consequence, the formulation models a *plastic response in the effective stress space* related to $\boldsymbol{\tau}_0$ and A_0. This response is completely independent of the fracture phase field for a state-dependent choice

$$\eta^p = (1-d)^2 \eta_0^p \, . \tag{4.145}$$

of the plastic viscosity. The combination of $(4.144)_2$ with (4.145) and (4.143) results in the PDE for the strain gradient evolution of the hardening variable

$$\dot{\alpha} = \frac{1}{\eta_0^p} \left\langle \, \sqrt{\tfrac{3}{2}} \widehat{\chi}^p(\boldsymbol{\tau}_0; f) - \left[\, \widehat{y}(\alpha) - y_0 l_p^2 \Delta\alpha \, \right] \right\rangle \tag{4.146}$$

where the Macaulay bracket ensures the irreversibility of the isotropic hardening variable. Clearly, the plastic hardening variable is driven by an equivalent effective stress, and has the typical gradient-type regularization. For the micromorphic regularization discussed above, the microstructural plastic hardening force appears in in the local equation

$$A = \partial_{\bar{\alpha}} \widehat{W} = (1-d)^2 A_0 \quad \text{with} \quad A_0 := \widehat{y}(\bar{\alpha}) + \epsilon_p(\bar{\alpha} - \alpha) \tag{4.147}$$

in terms of the additional local variable $\bar{\alpha}$. It recasts (4.143) into a local equation. The evolution equation $(4.144)_2$ now holds for the variable $\bar{\alpha}$ and modifies (4.146) towards the local equation

$$\dot{\bar{\alpha}} = \frac{1}{\eta_0^p} \left\langle \sqrt{\tfrac{3}{2}} \widehat{\chi}^p(\boldsymbol{\tau}_0; f) - [\, \widehat{y}(\bar{\alpha}) + \epsilon_p(\bar{\alpha} - \alpha) \,] \right\rangle \,. \tag{4.148}$$

The micromorphic variable α in the above equation is determined by a separate PDE obtained form the equilibrium condition $\delta_\alpha \widehat{W} = 0$ which gives

$$\alpha - \bar{l}_p^2 \, \Delta\alpha = \bar{\alpha} \quad \text{with} \quad \bar{l}_p = l_p \, \sqrt{y_0/\epsilon_p} \,, \tag{4.149}$$

where $\bar{l}_p$ is the plastic length scale of the micromorphic theory. The above two equations provide a modification of (4.146) based on an extended set of variables. As already mentioned, this has several advantages. It allows the application of the local stress return scheme in Box 4.1 at frozen micromorphic variable α, which is of particular convenience for a staggered local-global update of the hardening variable. Furthermore, note carefully that the evolution of the micromorphic variable in (4.149) is not restricted to the plastic domain as the original evolution in (4.146). This allows a straightforward finite element implementation without tracking of elastic-plastic boundaries.

The Fracture Phase Field Equation. The third Euler equation $(4.98)_3$ of the variational principle (4.95) determines the PDE for fracture phase field evolution equation. It has already considered in (4.133). Setting for convenience

$$\eta^f = 2 \frac{w_c}{\zeta} \eta_0^f \,, \tag{4.150}$$

(4.133) may be recast into the dimensionless evolution equation for the evolution of the crack phase field d

$$\dot{d} = \frac{1}{\eta_0^f} \left\langle \, (1-d)\, \zeta [\, \frac{\widehat{w}_0^{epf}}{w_c} - 1 \,] - [\, d - l_f^2 \Delta d \,] \right\rangle \tag{4.151}$$

Note the formal analogy to (4.146). The fracture phase field is driven by the effective elastic-plastic work function $\widehat{w}_0^{epf}$ that is independent of d. Following the notation of the recent work Miehe et al. 2015a, we may recast (4.151) into

$$\underbrace{\eta_0^f \dot{d}}_{evolution} = \underbrace{(1-d)\widetilde{\mathcal{H}}_0}_{crack\ force} - \underbrace{[\, d - l_f^2 \Delta d \,]}_{crack\ resistance} \tag{4.152}$$

with the dimensionless modification $\widetilde{\mathcal{H}}_0 = \zeta \mathcal{H}_0 / w_c$ of the history field $\mathcal{H}_0$ introduced in (4.135).

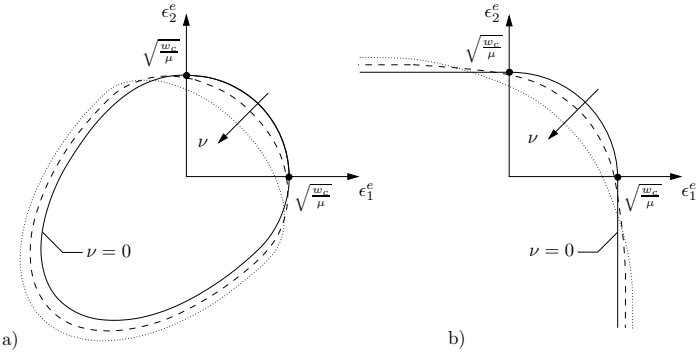

Figure 4.9: Modification of fracture threshold surface in (4.62) accounting for *brittle fracture in tension*, visualized in 2 d elastic principal strain space for different Poisson ratios ν. $\widehat{\phi}^f = 2\widehat{w}_0^{e+}(\boldsymbol{\varepsilon}^e) - 2w_c = 0$ for *brittle crack driving* in (4.157) for a) decomposition (4.155) of only the volumeteric term considered in Amor et al. 2009 and b) decomposition (4.154) of both Lame terms considered in Miehe et al. 2010b.

4.5.7. Modified Phase Field Equation for Brittle Fracture in Tension

Note that the above definition of the crack driving state function does not differentiate between tension and compression. In order to enforce a brittle crack evolution only in tension, we consider modifications of the crack driving forces as follows. A first variationally consistent approach is based on a modified representation of the work density function introduced in (4.36)

$$\widehat{W} = \widehat{g}\,[\,\widehat{w}_0^{e+} + \widehat{w}_0^{p}\,] + \widehat{w}_0^{e-} + (1-\widehat{g})w_c + 2\frac{w_c}{\zeta} l_f \widehat{\gamma} \tag{4.153}$$

where only a *tensile part* of the stored elastic energy $\widehat{w}_0^{e+}$ degrades due to fracture and the *compression part* $\widehat{w}_0^{e-}$ remains. As considered in Miehe et al. 2010b, the decomposition of the elastic work density function (4.38) into these contributions can be defined by

$$\widehat{w}_0^{e} = \widehat{w}_0^{e+} + \widehat{w}_0^{e-} \quad \text{with} \quad \widehat{w}_0^{e+}(\boldsymbol{h}^e) := \frac{\lambda}{2}\,\langle \mathrm{tr}[\boldsymbol{h}^e]\rangle^2 + \mu\,\mathrm{tr}[(\boldsymbol{h}^{e+})^2] \tag{4.154}$$

Here, $\boldsymbol{h}^{e+} := \sum_{a=1}^{3} \langle \varepsilon_a^e \rangle \; \boldsymbol{n}_a \otimes \boldsymbol{n}_a$ is the positive elastic Hencky tensor defined by a spectral decomposition.* Note that the definition (4.154) contains separate positive volumetric and isochoric contributions. As a consequence, the Kirchhoff stresses in (4.142) takes the modified form

$$\boldsymbol{\tau} = (1-d)^2 \boldsymbol{\tau}_0^+ + \boldsymbol{\tau}_0^- \quad \text{with} \quad \boldsymbol{\tau}_0^+ := \lambda\,\langle \mathrm{tr}[\boldsymbol{h}^e]\rangle\,\boldsymbol{1} + 2\mu \boldsymbol{h}^{e+} \tag{4.156}$$

*A simplification of the function $(4.154)_2$ is considered in Amor et al. 2009

$$\widehat{w}_0^{e+}(\boldsymbol{h}^e) := \frac{\kappa}{2}\,\langle \mathrm{tr}[\boldsymbol{h}^e]\rangle^2 + \mu\,\mathrm{tr}(\mathrm{dev}[(\boldsymbol{h}^e)^2])\;, \tag{4.155}$$

where only the volumetric contribution to the elastic strain energy accounts for a decomposition.

where only the tensile part degrades. Following the same steps as outlined above, we end up with the modification of the crack driving history field (4.135)

$$\mathcal{H}_0 = \max_{s\in[0,t]} \left\langle\, \widehat{w}_0^{e+}(\boldsymbol{h}^e) + \widehat{w}_0^p(\alpha, \nabla\alpha) - w_c \,\right\rangle \tag{4.157}$$

where the brittle contribution accounts only for the positive elastic energy $\widehat{w}_0^{e+}$. The brittle contributions to the driving state functions defined in (4.154) and (4.155) are visualized in Figure 4.9.

4.6. Model Investigations I: Local Coaxial Response

As a first model investigation, features of the proposed framework for coupling porous plasticity to phase field fracture is demonstrated for a local setting with *coaxial total and plastic deformation* $\boldsymbol{F}$ and $\boldsymbol{G}^p$, where the elastic Hencky strain $\boldsymbol{h}^e = \boldsymbol{h} - \boldsymbol{h}^p$ decomposes additively into total and plastic parts $\boldsymbol{h} := \frac{1}{2}\ln[\boldsymbol{F}^T\boldsymbol{F}]$ and $\boldsymbol{h}^p := \frac{1}{2}\ln[\boldsymbol{G}^p]$, respectively. The subsequent treatment provides a conceptual view on the material parameters used.

4.6.1. Constitutive Functions for Isochoric and Volumetric Response

Isochoric Case. Consider a reformulation of the above constitutive model for an isochoric coaxial process, that results in a one dimensional setting. To this end, introduce the amounts ε and ε^p of total and plastic logarithmic strains deviators by setting $\boldsymbol{h} = \varepsilon\boldsymbol{a}$ and $\boldsymbol{h}^p = \varepsilon^p\boldsymbol{a}$ with $||\boldsymbol{a}|| = 1$ and $\mathrm{tr}[\boldsymbol{a}] = 0$. This pure isochoric deformation is shown in Figure 4.10a. The work density function for a homogeneous ideal plastic state is

$$\widehat{W}(\varepsilon - \varepsilon^p, \alpha, d) = (1-d)^2\,[\,\mu(\varepsilon-\varepsilon^p)^2 + y_0\alpha - w_c] + w_c + \frac{w_c}{\zeta}d^2 \tag{4.158}$$

in the rate-independent setting. In the co-axial loading process, this function determines the constitutive expressions for the amount of the deviatoric stress $\mathrm{dev}[\boldsymbol{\tau}] = \tau\boldsymbol{a}$ and the driving forces A and D for plasticity and fracture

$$\begin{aligned} \tau &= \partial_\varepsilon\widehat{W} = (1-d)^2\,2\mu(\varepsilon-\varepsilon^p)\ , \\ A &:= \partial_\alpha\widehat{W} = (1-d)^2\,y_0\ , \\ D &:= -\partial_d\widehat{W} = 2(1-d)[\,\mu(\varepsilon-\varepsilon^p)^2 + y_0\alpha - w_c\,] - 2w_c d/\zeta\ . \end{aligned} \tag{4.159}$$

The evolution of the plastic strains and the fracture phase field is governed by the two threshold functions

$$\widehat{\phi}^p(\tau, A; f_0) = ||\tau|| - \sqrt{\tfrac{2}{3}}\,A \quad \text{and} \quad \widehat{\phi}^f(D) = D \tag{4.160}$$

for a constant initial void volume fraction f_0. The response of this one-dimensional scenario is visualized in Figure 4.11a for a monotonous increasing loading process.

Volumetric Case. Now let ε and ε^p be the amounts of volumetric total and plastic strains by setting $\boldsymbol{h} = \varepsilon\boldsymbol{a}$ and $\boldsymbol{h}^p = \varepsilon^p\boldsymbol{a}$ with $\boldsymbol{a} = \boldsymbol{1}$. This deformation is depicted in Figure 4.10b. The work density function for an ideal plastic homogeneous state is

$$\widehat{W}(\varepsilon - \varepsilon^p, \alpha, d) = (1-d)^2\,[\,\frac{\kappa}{2}(\varepsilon-\varepsilon^p)^2 + y_0\alpha - w_c\,] + w_c + \frac{w_c}{\zeta}d^2\ . \tag{4.161}$$

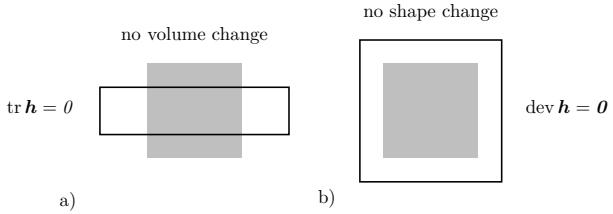

Figure 4.10: Homogeneous isochoric and volumetric deformations with coaxial total and plastic logarithmic strains $\boldsymbol{h} := \frac{1}{2}\ln[\boldsymbol{F}^T\boldsymbol{F}] = \varepsilon\boldsymbol{a}$ and $\boldsymbol{h}^p := \frac{1}{2}\ln[\boldsymbol{G}^p] = \varepsilon^p\boldsymbol{a}$, respectively. a) *Isochoric case* for $||\boldsymbol{a}|| = 1$ and $\mathrm{tr}[\boldsymbol{a}] = 0$. b) *Volumetric case* for $\boldsymbol{a} = \boldsymbol{1}$.

This function determines the volumetric stress $\frac{1}{3}\mathrm{tr}[\boldsymbol{\tau}]\boldsymbol{1} = \tau\boldsymbol{a}$ and the driving forces A and D for plasticity and fracture

$$\begin{aligned} \tau &= \partial_\varepsilon \widehat{W} = (1-d)^2\,\kappa\,(\varepsilon - \varepsilon^p)\ , \\ A &:= \partial_\alpha \widehat{W} = (1-d)^2\,y_0\ , \\ D &:= -\partial_d \widehat{W} = 2(1-d)\,[\,\kappa(\varepsilon-\varepsilon^p)^2/2 + y_0\alpha - w_c\,] - 2w_c d/\zeta\ . \end{aligned} \tag{4.162}$$

The two threshold functions for plasticity and fracture

$$\widehat{\phi}^p(\tau, A; f) = \sqrt{\tfrac{3}{2}f}\ ||\tau|| - \sqrt{\tfrac{2}{3}}\,A \quad \text{and} \quad \widehat{\phi}^f(D) = D \tag{4.163}$$

now depend on the current state of void fraction

$$f = \widehat{f}(\varepsilon) = \max[\ f_0, 1 - (1-f_0)\,\exp[-\varepsilon]\ ]\ , \tag{4.164}$$

which was assumed in (4.10) to be a function of total volumetric deformation, i.e. the macroscopic logarithmic strain ε. The response for a monotonous loading process is depicted in Figure 4.11b.

4.6.2. Role of Material Parameters at the Onset of Ductile Fracture

The onset of plasticity and fracture for the pure isochoric and volumetric responses is governed by the initial yield stress y_0 and the critical work density w_c, respectively. Ductile fracture is characterized by a *plastic yielding before fracture*. This scenario is associated with the condition at the onset of plasticity

$$\widehat{\phi}^p(\tau, y_0; \widehat{f}(\varepsilon)) = 0 \quad \text{and} \quad \widehat{\phi}^f(D) < 0 \tag{4.165}$$

of the two threshold functions at $\varepsilon^p = \alpha = d = 0$.

Isochoric Case. The combination of the two conditions (4.165) gives for the isochoric functions (4.159) the constraint on the material parameters

$$\text{Ductile Isochoric E-P-F Response:} \quad w_c > \mu\varepsilon_y^2 = \frac{1}{6}\,\frac{y_0^2}{\mu} \tag{4.166}$$

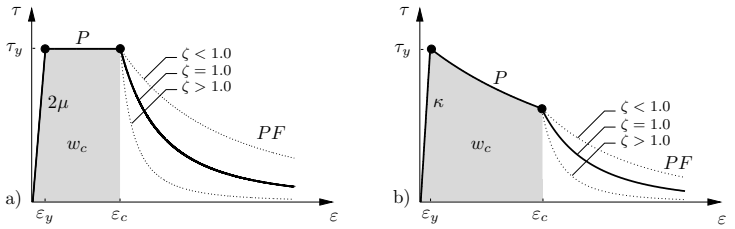

Figure 4.11: Local response for ideal plasticity coupled with fracture. Kirchhoff stress versus logarithmic strain: a) For purely *isochoric response* with onsets ε_y and $\varepsilon_c = \varepsilon_y + \varepsilon_y^p$ of plasticity and damage obtained from (4.166)–(4.167) and yield stress $\tau_y = 2\mu\varepsilon_y$. b) For purely *volumetric response* with onsets ε_y–ε_c of plasticity and damage obtained from (4.168)–(4.169) and yield stress $\tau_y = \kappa\varepsilon_y$. The stress softening is due to the void growth for the non-hardening matrix response under consideration. The threshold parameter w_c determines the onset of fracture and the parameter ζ the shape of the softening due to fracture.

at the onset of plasticity (P) and the condition

$$\frac{1}{6}\frac{y_0^2}{\mu} + y_0\alpha_c = w_c \quad \text{with} \quad \alpha_c = \sqrt{\tfrac{2}{3}}\varepsilon_c^p \,. \tag{4.167}$$

for the subsequent onset of fracture (F). These conditions determine a strain $\varepsilon = \varepsilon_y$, where plasticity starts, and a critical plastic strain $\varepsilon^p = \varepsilon_c^p$, where the ductile fracture is initiated. Figure 4.11a shows the ductile response for pure isochoric response, where the fracture threshold parameter w_c bounds the total work density after a considerable amount of plastic deformation.

Volumetric Case. The combination of the two conditions (4.165) gives for the volumetric functions (4.162) the constraint on the material parameters

$$\text{Ductile Volumetric E-P-F Response:} \quad w_c > \frac{\kappa}{2}\varepsilon_y^2 = \frac{1}{9}\frac{1}{\widehat{f}(\varepsilon_y)}\frac{y_0^2}{\kappa} \tag{4.168}$$

at the onset of plasticity (P) and the condition

$$\frac{1}{9}\frac{1}{\widehat{f}(\varepsilon_c)}\frac{y_0^2}{\kappa} + y_0\alpha_c = w_c \quad \text{with} \quad \alpha_c = \sqrt{\frac{2}{3}}\frac{1}{\sqrt{3\widehat{f}(\varepsilon_c)}}\varepsilon_c^p \,. \tag{4.169}$$

for the subsequent onset of fracture (F). These conditions can iteratively be solved for a strain $\varepsilon = \varepsilon_y$, where plasticity starts, and a strain $\varepsilon = \varepsilon_c$, where the ductile fracture is initiated. Figure 4.11b shows the ductile response with the strain-softening effect due to void growth, where the fracture threshold parameter w_c bounds total work density after a considerable amount of plastic deformation. Again the shape parameter ζ determines the slope of the post-critical range of fracture.

4.6.3. Plastic and Damage Dissipation in Brittle and Ductile Fracture

Figure 4.12 investigates the split of the dissipation into plastic and damage contribution for the case of brittle and ductile fracture. The investigation is performed for an *isochoric*

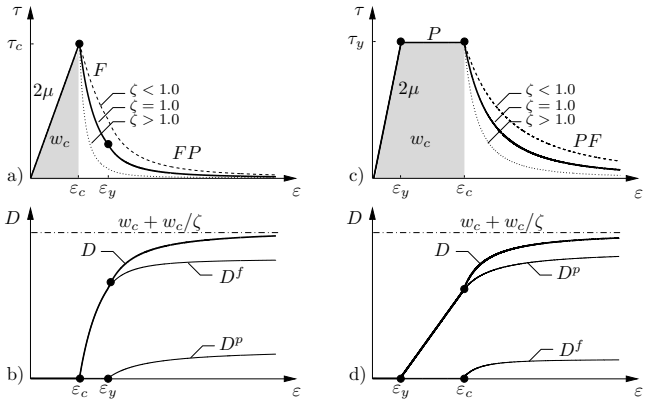

Figure 4.12: Dissipated work density for brittle and ductile isochoric response. Kirchhoff stress τ and dissipated work D^{pf} for homogeneous test with a-b) *brittle E-F-P response* and for c-d) *ductile E-P-F response*. The plastic yield stress $\tau_y = 2\mu\varepsilon_y$ bounds the effective stress. The fracture threshold parameter w_c determines the onset of fracture and the parameter ζ the shape of the softening due to fracture with the critical stress $\tau_c = \sqrt{2Ew_c}$. The dissipated work $D^{pf} = D^p + D^f$ contains contributions due to plasticity and fracture and converges to the value $w_c + w_c/\zeta$ at the fully broken state.

homogeneous test with constitutive functions summarized in (4.159) and (4.160). Figure 4.12a depicts the *brittle stress response* for $w_c < \frac{1}{6}\frac{y_0^2}{\mu}$ according to (4.166). Observe that the fracture threshold parameter w_c *bounds the elastic response* and determines the onset of fracture. The shape parameters ζ controls the shape of the post-critical range. It reduces the stress softening due to fracture $\zeta < 1$, where the resistance function $\widehat{D}^{pf}$ in (4.44) is convex, and provides more pronounced stress softening due to fracture for $\zeta > 1$, where $\widehat{D}^{pf}$ is non-convex. Figure 4.12b reports on the evolution of the dissipated work density D^{pf} evaluated by numerical integration of the integral expressions (4.51). Note that D^{pf} converges to the maximum value $w_c + w_c/\zeta$, which gives an additional meaning to the two material parameters w_c and ζ. Furthermore, observe that the dissipated work D^f due to fracture dominates in this case of brittle fracture, while the subsequently evolving dissipative work D^p due to plasticity is small. Figure 4.12c shows the ductile response for $w_c > \frac{1}{6}\frac{y_0^2}{\mu}$ in (4.166), where the fracture threshold parameter w_c bounds total work density after a considerable amount of plastic deformation. Again the shape parameter ζ determines the slope of the post-critical range of fracture, with $\zeta < 1$ for a convex and $\zeta > 1$ for a non-convex resistance function $\widehat{D}^{pf}$: Figure 4.12d shows the evolution of the dissipated work density D^{pf} up to the limit $w_c + w_c/\zeta$, where now the plastic contribution D^p dominates, successively raising the fracture contribution D^f.

4.7. Model Investigations II: Inhomogeneous IBV-Problems

Next, the performance of the proposed framework of phase field ductile fracture coupled with porous plastic solids is demonstrated by means of representative boundary-value problems. Section 4.7.1 demonstrates the influence of the plastic length scale l_p and the

Table 4.3: Material parameters used for the length scales study.

No.	Parameter	Name	Value	Unit
1.	κ	bulk modulus	164.2	GPa
2.	μ	shear modulus	80.2	GPa
3.	y_0	initial yield stress	0.2	GPa
4.	w_c	critical work density	0.005	GPa
5.	ϵ_p	penalty parameter	2.6	GPa
6.	l_f	fracture length scale	0.3/0.0	mm
7.	l_p	plastic length scale	0.0/0.3	mm
8.	ζ	fracture parameter	1.0	–

fracture length scale l_f on the final failure response. In Section 4.7.2, the formation of *cup–cone* fracture in 2D axisymmetric tensile specimen and extension to 3D setting are analyzed. Finally, a three dimensional tension test of a double notched bar is investigated in Section 4.7.3

4.7.1. Investigation of the Plastic and the Fracture Length Scales Influence

The first example shows a inhomogeneous tensile test that demonstrates the influence of the plastic and damage length scales l_p and l_f, respectively. To this end, we restrict conceptually the material response to the isochoric von Mises plasticity by setting the void volume fraction $f = f_0 = 0$. Furthermore, we focus on a non-hardening matrix response of ideal plasticity.

The geometry of the specimen is depicted in Figure 4.13a. It has a hyperbolic axis-symmetric shape, where plastic deformation and ductile fracture are initiated in the center of the specimen. The size of the specimen is chosen to be : $W = 3$ mm, $l = 1.5$ mm and

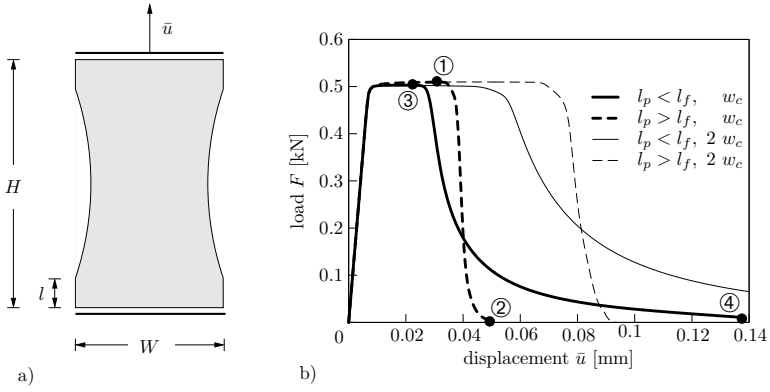

Figure 4.13: Inhomogeneous tensile test. a) Geometry and boundary conditions and b) load-deflection curves for the cases $l_p > l_f$ and $l_p < l_f$ in combination with two different fracture onset parameters w_c.

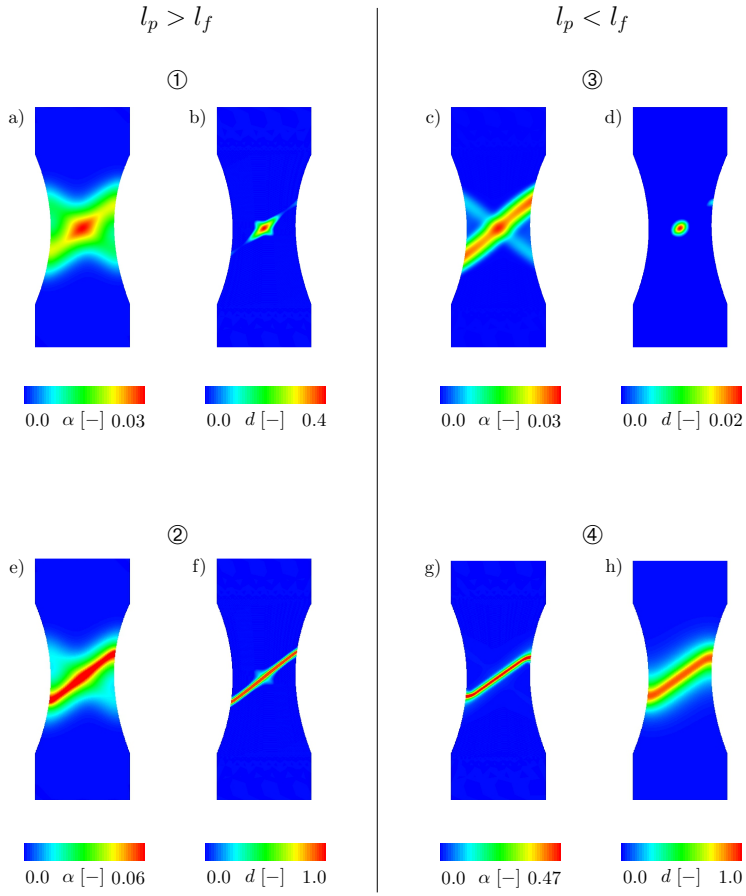

Figure 4.14: Inhomogeneous tensile test. Contour plots of the hardening variable α and the crack phase field variable d for two different deformation stages up to final rapture for the two cases $l_p > l_f$ and $l_p < l_f$, corresponding to the load-deflection curves plotted in Figure 4.13b.

$H = 7.75$ mm. We fixed the bottom edge of the specimen vertically and applied tension loading to the top edge as plotted in Figure 4.13a. The material parameters used are given in Table 4.3. The specimen is discretized with a mesh size of $h_e = 0.03$ mm in the expected fracture zone.

Figure 4.13b shows different load deflection curves for the cases $l_p > l_f$ and $l_p < l_f$, where an emphasize is put on the influence of the fracture onset parameter w_c. Herein, by increasing the critical fracture energy w_c a delayed onset of fracture is observed. The evolution of the crack phase field d compared with the evolution of the equivalent plastic strain α is reported in Figure 4.14 for the cases $l_p > l_f$ and $l_p < l_f$. Figure 4.14 ①-② demonstrates the contour plots for two different stages of the deformation up to final

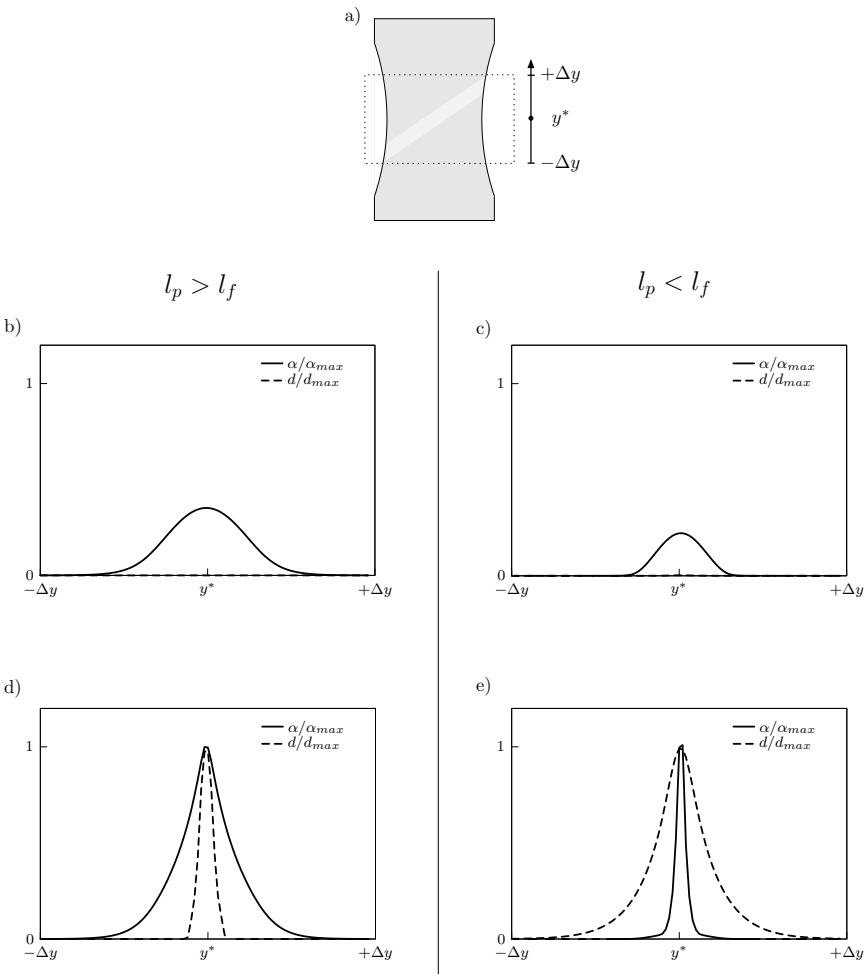

Figure 4.15: Inhomogeneous tensile test. a) A zoom out at the center of the specimen for visualization of the cross section of the plastified fracture zone. b) and d) Evolution of the fracture zone inside the plastic zone for $l_p > l_f$, whereas in c) and e) the fracture zone evolves outside the plastic zone for $l_p < l_f$.

rapture, where $l_p > l_f$. We observe that α and d start initially from the center and propagate outwards forming the sharp fracture zone which lies inside the plastic zone corresponding to the load-deflection *dashed-curves* plotted in Figure 4.13b. However, for the other case $l_p < l_f$, the sharp plastic shear band lies inside the fracture zone as demonstrated in Figure 4.14 ③-④ which corresponds to the load-deflection *solid-curves*

Table 4.4: Material parameters used for the axisymmetric tension test.

No.	Parameter	Name	Value	Unit
1.	κ	bulk modulus	164.2	GPa
2.	μ	shear modulus	80.2	GPa
3.	y_0	initial yield stress	0.45	GPa
4.	y_∞	infinite yield stress	0.715	GPa
5.	η	saturation parameter	16.93	–
6.	h	hardening parameter	0.13	GPa
7.	ϵ_p	penalty parameter	2.6	GPa
8.	f_0	initial void fraction	0.004	–
9.	l_f	fracture length scale	0.22	mm
10.	w_c	critical work density	0.32/0.42/0.52	GPa
11.	ζ	fracture parameter	1.0/3.0/7.0	–

plotted in Figure 4.13b. In this case, one notices a delayed failure response combined with huge plastic deformation compared with the cases $l_p > l_f$.

For visualization of plastic and fracture zones, a zoom out at the center of the specimen in the range between $[\, -\Delta y, +\Delta y \,]$ is illustrated in Figure 4.15a. We plot the normalized equivalent plastic strain α/α_{max} versus the normalized crack phase field d/d_{max} for two cases at the onset of fracture in Figure 4.15b-c and final failure in Figure 4.15d-e. Herein, for $l_p > l_f$ the fracture zone lies inside the plastic zone as shown in Figure 4.15d. Whereas for the case $l_p < l_f$, we observe an evolution of the fracture zone out side the plastic zone as plotted in Figure 4.15e. This shows conceptually the ability of controlling length scales in the proposed test.

4.7.2. Analysis of the Cup–Cone Fracture in Axisymmetric Tension Test

The second benchmark test is concerned with the simulation of a *cup–cone* failure mechanism in a cylindrical bar under tension. This is a classical failure mechanism of ductile metals, such as experimentally observed e.g. in the recent works of Li et al. 2011 and Kamat et al. 2011. The modeling and simulation of this phenomenon has a long history. We refer to the representative works of Tvergaard and Needleman 1984, Besson et al. 2001, Benzerga and Leblond 2010 and the recent comprehensive work by Huespe et al. 2012. The problem provides a very demanding example that shows the development of large plastic zone in a neck, followed by the initiation of a ductile crack zone with onset in the center of the specimen, that successively develops a *cup–cone fracture surface*.

The above mentioned modeling and simulation approaches use the Gurson-Tvergaard-Needelman (GTN) framework, that models void nucleation, growth and coalescence. Hence the ductile crack is locally triggered by a critical void fraction, that may be considered as a micromechanical criterion. We demonstrate in this example, that our proposed model based on the simplified Gurson yield surface with the canonical void growth condition provides an excellent fit to the experimentally observed *cup–cone* failure mechanism, when combined with the macroscopic fracture criterion characterized by the two fracture material parameters w_c and ζ.

We analyse this example for a relationship between the plastic and fracture length

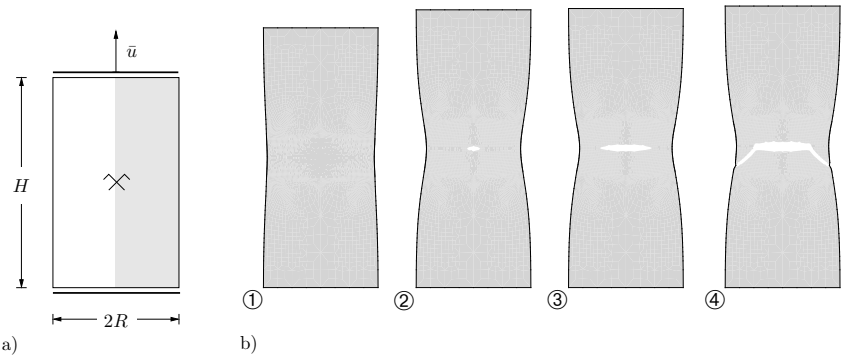

Figure 4.16: Axisymmetric tension test. a) Geometry and boundary conditions. b) Evolution of crack phase field d for four different states of the deformation up to final rapture: ① $\bar{u} = 6$ mm, ② $\bar{u} = 8.3$ mm, ③ $\bar{u} = 8.5$ mm and ④ $\bar{u} = 9$ mm, corresponding to the load-deflection curves plotted in Figure 4.18.

scales $l_p << l_f$ with $l_p \to 0$, yielding a pronounced and sharp crack surface geometry as observed in experiments. The geometric setup and the loading conditions of the specimen are depicted in Figure 4.16. The length of the specimen is chosen to be $H = 26$ mm and the radius is $R = 7.5$ mm, adopted from the benchmark in Huespe et al. 2012. The bottom edge of the specimen is fixed vertically and applied tension loading to the top edge. Due to the underlying symmetry, only one half of the specimen is discretized using enhanced assumed strain type finite elements. The mesh size of the specimen is chosen to be $h_e = 0.1$ mm in the expected fracture zone. To trigger localization in the center of the specimen, a geometrical imperfection is introduced in the central zone of the bar. Here, a reduction of the specimen net section at the central zone of height $H/7$ is applied, in which the radius at the center is chosen to be $r_c = 0.993\,R$. The material parameters used are given in Table 4.4.

The evolution of the crack phase field d in comparison to the evolution of the equivalent plastic strain α and the void volume fraction f for four different deformation states up to final rapture are depicted in Figures 4.16b–4.17. Here, we observe a huge plastic deformation as a necking zone at the center of the specimen as shown in Figure 4.16 ① and Figure 4.17a. Thereafter the void volume fraction starts to evolve from the center of the specimen as plotted in Figure 4.17e resulting in a crack initiation at the center zone as demonstrated in Figure 4.16b. The crack phase field d then propagates horizontally from the center outward following the equivalent plastic strain α evolution path in Figure 4.17b-d and the void volume fraction evolution path in Figure 4.17f-h, forming the *cup–cone* fracture surface as demonstrated in Figure 4.16b and Figure 4.17l. Note that, the void volume fraction starts to evolve from the initial value f_0 up to the maximum value $f_c = 0.15$ where the fracture starts. The evolution of the crack phase field d corresponding to the load-deflection curves plotted in Figure 4.18, is plotted for different stages of deformation up to final failure as in Figure 4.16b as follows: at ① the displacement is $\bar{u} = 6$ mm where large plastic deformation occurs, subsequently fracture starts at ② with $\bar{u} = 8.3$ mm. Observe that the crack phase field increases horizontally up to ③ where

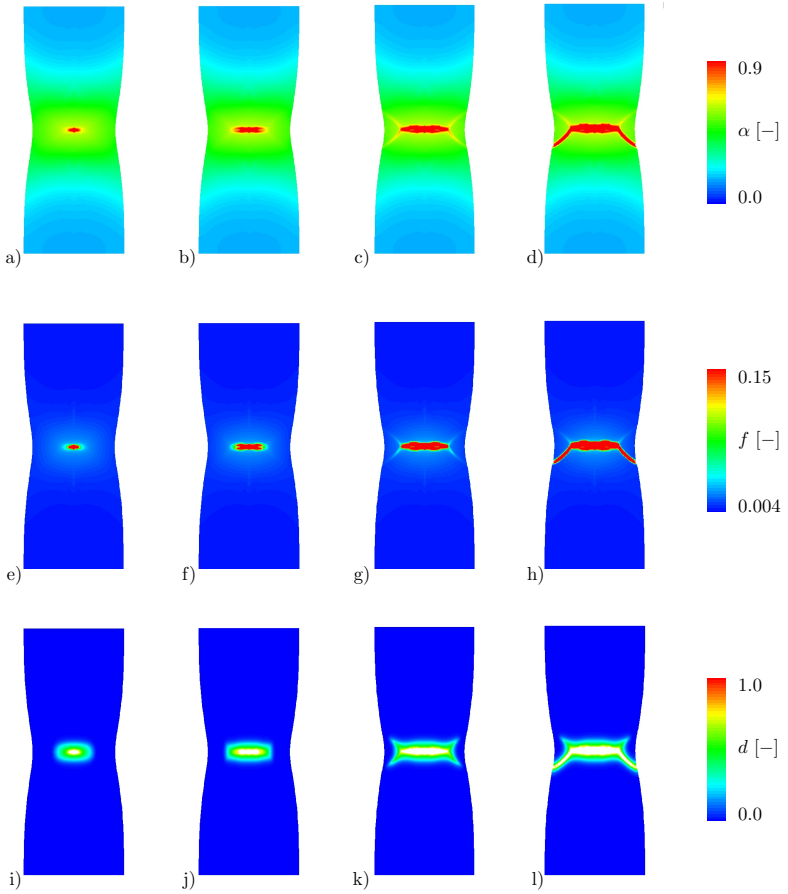

Figure 4.17: Axisymmetric tension test. Contour plots of the hardening variable α in (a)-(d); the void volume fraction f in (e)-(h) and the fracture phase field d in (i)-(l) for four different deformation states up to final rapture.

$\bar{u} = 8.5$ mm. Thereafter the crack propagates about 135° from the loading direction to follow the equivalent plastic strain and the void fraction path as shown in ④ corresponds to $\bar{u} = 9$ mm. For visualization of the crack surface, deformed regions with a crack phase field $d \approx 1$ are not plotted.

Each of the parameters f_0, w_c and ζ have a pronounced influence on the crack initiation and propagation as shown in the load-deflection curves in Figure 4.18. For higher initial void volume fraction f_0, an overall softening response is observed resulting in a faster failure behavior as shown in Figure 4.18a. The critical fracture energy w_c characterizes in the load-deflection diagram Figure 4.18b the onset of fracture, corresponding to its

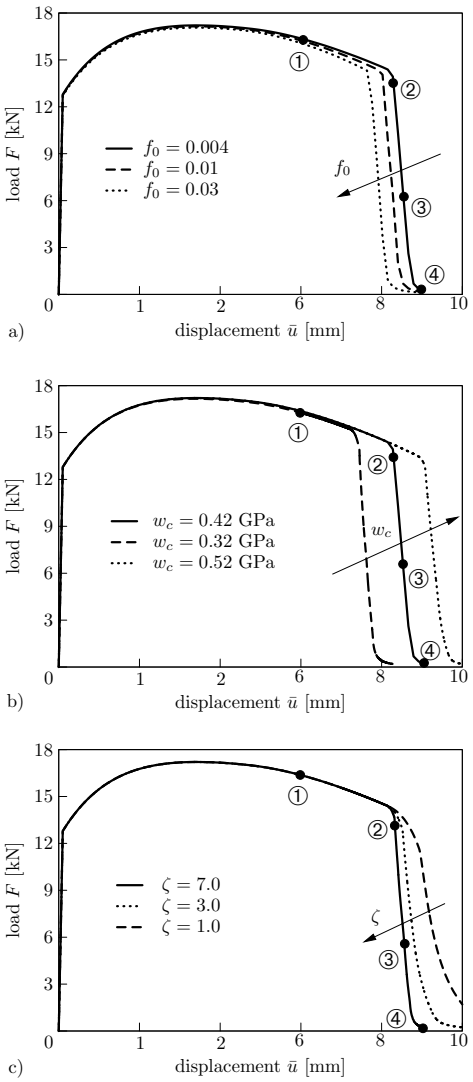

Figure 4.18: Load–displacement responses for axisymmetric tension test. Effects of a) three different initial void volume fractions f_0, b) three different critical work densities w_c and c) three different fracture parameters ζ on the crack initiation and load-displacement response.

local criterion as demonstrated in the homogeneous test in Figure 4.11. By increasing the value of w_c, one observes the expected delayed on-set of fracture. The fracture slope parameter ζ influences the post-critical range after the onset of fracture, by controlling

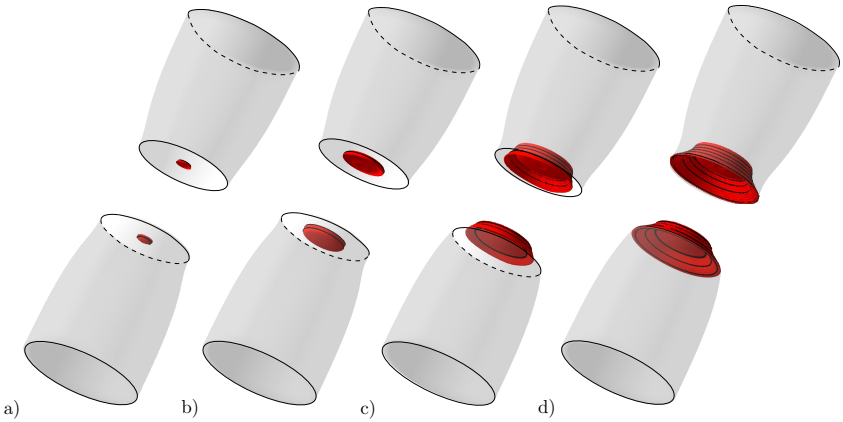

Figure 4.19: Three dimensional necking of a cylindrical bar. Evolution of the *cup–cone* failure mechanism in (a)-(d).

the dissipation of the fracture process. For larger values of ζ, a faster failure response is noticed as illustrated in Figure 4.18c.

To illustrate the *evolution* of the *cup–cone failure mechanism* in the cylindrical bar under tension loading, we extend the two dimensional BVP introduced in Figure 4.16 to three dimensional setting. Figure 4.19 demonstrates the crack phase field d evolution for four different stages of deformation up to final rupture. As documented in the 2D case, the fracture starts to initiate from the center of bar, see Figure 4.19a and propagates outward to form the *cup–cone* fracture surface, as shown in Figure 4.19b-d, where we used transparency effect and separation at the center of the bar to show the failure surface for $d \geq c \approx 1$.

The analysis shows that the proposed new model is competitive with Gurson-Needelman-Tvergaard (GTN) model, when focus is put on the macroscopic failure response. Let us emphasize at this stage that the proposed model is much simpler in structure than the GTN model, and based on a rigorous variational principle.

4.7.3. Three Dimensional Tension Test of a Double Notched Bar

The last model problem is concerned with analyzing the fracture phenomena of a double notched bar under tensile loading made of Al-alloy (Al-5005) as reported in the experiments of Li et al. 2011 and Ambati et al. 2015b. Similar to the necking example 4.7.2, we also use the following relationship between the plastic and the fracture length scales $l_p << l_f$ with $l_p \to 0$, yielding a pronounced and sharp crack surface geometry as observed in experiments. The geometric setup and the loading conditions of the specimen are depicted in Figure 4.20a. The size of the specimen is chosen to be : $H = 110$ mm, $W = 22$ mm, $l_1 = 25$ mm, $l_2 = 25$ mm, $l_3 = 10$ mm, $r_1 = 3.625$ mm and the radius of the two notches is $r_2 = 2.5$ mm, adopted from the benchmark in Ambati et al. 2015b.

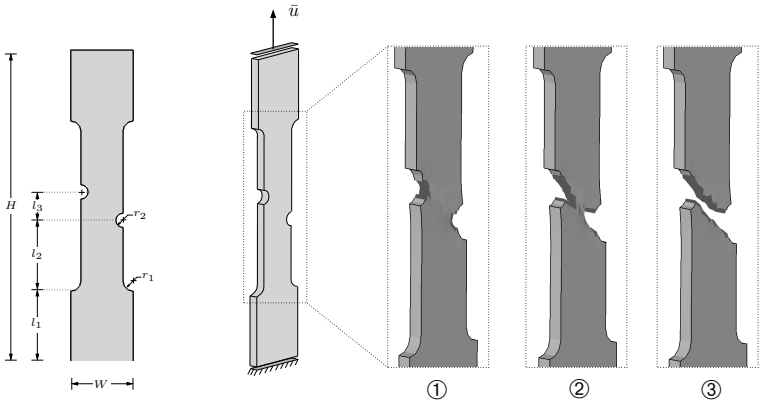

Figure 4.20: Tension test of a double notched bar. a) Geometry and boundary conditions. b) Evolution of the crack phase field d for three different states of the deformation up to final rapture: ① $\bar{u} = 3.0$ mm, ② $\bar{u} = 3.6$ mm, ③ $\bar{u} = 4.0$ mm, corresponding to the load-deflection curves plotted in Figure 4.22.

The same material parameters are used as in Li et al. 2011 and listed in Table 4.5. The mesh size of the specimen is chosen to be $h_e = 0.5$ mm in the expected fracture zone. The computation is performed by fixing the bottom edge of the specimen and applying the displacement $\bar{u}$ on the top vertical boundary as shown in Figure 4.20a.

The contour plots of the equivalent plastic strain α, the void volume fraction f and the fracture phase field d for different deformation stages up to final failure is depicted in Figure 4.21 on the undeformed configuration using the transparency effects to illustrate the evolution of the crack phase field at a zoom out in the specimen as plotted in Figure 4.20b. The crack phase field d initiates at the two notch tips, see Figure 4.21i where the maximum equivalent plastic strain and void fraction develops as shown in Figure 4.21a, and Figure 4.21e, respectively. Thereafter, they propagate from the notches

Table 4.5: Material parameters used for the notched specimen: Al-5005.

No.	Parameter	Name	Value	Unit
1.	κ	bulk modulus	73.854	GPa
2.	μ	shear modulus	26.455	GPa
3.	y_0	initial yield stress	0.113	GPa
4.	y_∞	infinite yield stress	0.135	GPa
5.	η	saturation parameter	24.5	–
6.	h	hardening parameter	0.1	GPa
7.	ϵ_p	penalty parameter	2.0	GPa
8.	f_0	initial void fraction	0.01	–
9.	l_f	fracture length scale	1.0	mm
10.	w_c	critical work density	0.06/0.08/0.1	GPa
11.	ζ	fracture parameter	1.0/50.0/100	–

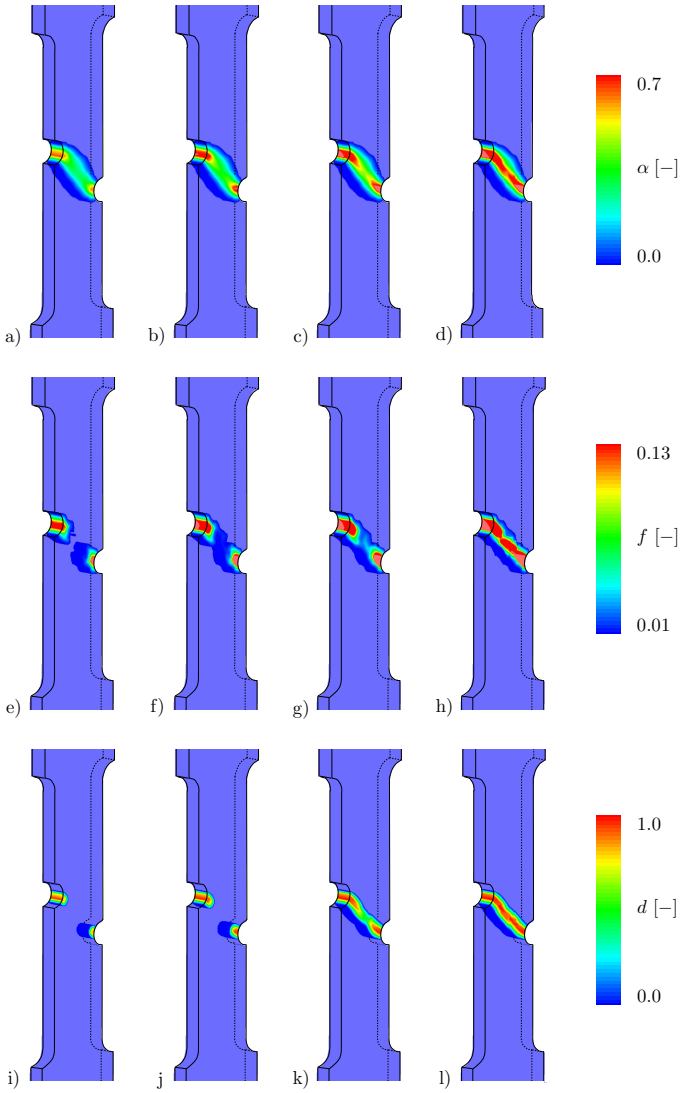

Figure 4.21: Three dimensional tension test of a double notched bar Tensile test on a double notched specimen. Contour plots of the hardening variable α in (a)-(d); the void volume fraction f in (e)-(h) and the fracture phase field d in (i)-(l) plotted on the undeformed configuration for four different deformation states up to final rapture.

inwards at an angle about 45° from the loading direction to follow the equivalent plastic strain and the void fraction path till the complete failure as shown in Figure 4.21j-l

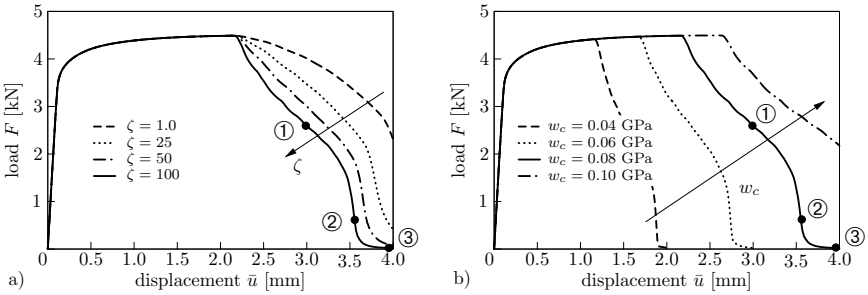

Figure 4.22: Load–displacement responses for tension test on a double notched specimen. Effects of four different fracture parameters ζ in a) and four different critical work densities w_c in b) on the crack initiation and propagation.

The evolution of the crack phase field d in the deformed configuration corresponding to the load-deflection curves in Figure 4.22, is plotted for three different stages of deformation up to final rupture in Figure 4.20 ①-③. For visualization of crack surface, deformed regions with a crack phase field $d \approx 1$ are not shown.

To illustrate the *influence of the fracture parameter* ζ and *the critical fracture energy* w_c on the crack initiation and propagation, Figure 4.22 plots the load-displacement response for four different values of ζ and w_c. One observes the expected delayed failure behavior by decreasing the value of ζ as in Figure 4.22b and by increasing the value of w_c as demonstrated in Figure 4.22a.

4.8. Conclusion

A variational-based framework for the phase field modeling of fracture in isotropic porous solids was proposed. The phase field approach regularizes sharp crack surfaces within a pure continuum setting by a specific gradient damage modeling with constitutive terms rooted in fracture mechanics. It was linked to a formulation of porous gradient plasticity at finite strains. As a consequence, the formulation includes two independent length scales which regularize both the plastic response as well as the crack discontinuities. This ensures that the damage zones of ductile fracture are inside of plastic zones or vice versa, and guarantees on the computational side a mesh objectivity in post-critical ranges. The proposed gradient plasticity model for porous plasticity was based on a simple growth law for the evolution of the void fraction, and linked to a failure criterion in terms of the local elastic-plastic work density that drives the fracture phase field. It was shown that this approach is able to model basic phenomena of ductile failure such as *cup-cone failure surfaces* in terms of only two material parameters on the side of damage mechanics: a *critical work density* that triggers the onset of damage and a *shape parameter* that governs the postcritical damage up to fracture. An important aspect was a precise representation of the framework within a canonical minimization principle. The key point that allows to construct such a principle was the use of an *Eulerian constitutive setting*, where the yield function was formulated in terms of the *Kirchhoff stress*. Here, we exploited the fact that this stress approximates an *effective stress* that drives the plasticity in the matrix

of the porous solid. The coupling of gradient plasticity to gradient damage was realized by a constitutive work density function that includes the stored elastic energy and the dissipated work due to plasticity and fracture. The latter represents a coupled resistance to plasticity and damage, depending on the gradient-extended internal variables which enter the plastic yield function and the fracture threshold function. The robust computational setting proposed included (i) a general return scheme of plasticity in the spectral space of logarithmic strains and dual Kirchhoff stresses, (ii) the micromorphic regularization of the gradient plastic evolution and (iii) a history-field-driven update of the linear phase field equation. The performance of the formulation was underlined by means of representative examples, which demonstrated the ability to model typical macroscopic failure phenomena of ductile fracture.

Acknowledgment. Support for this research was provided by the German Research Foundation (DFG) within the Cluster of Excellence Exc 310 *Simulation Technology* at the University of Stuttgart.

Bibliography

Aifantis, E. C. (1987). "The physics of plastic deformation". In: *International Journal of Plasticity* 3, pp. 211–247.

Alessi, R., J.-J. Marigo, and S. Vidoli (2015). "Gradient damage models coupled with plasticity: Variational formulation and main properties". In: *Mechanics of Materials* 80, pp. 351–367.

Ambati, M., T. Gerasimov, and L. de Lorenzis (2015a). "Phase-field modeling of ductile fracture". In: *Computational Mechanics* 55, pp. 1017–1040.

Ambati, M., R. Kruse, and L. de Lorenzis (2015b). "A phase-field model for ductile fracture at finite strains and its experimental verification". In: *Computational Mechanics* in press.

Ambrosio, L. and V. M. Tortorelli (1990). "Approximation of functionals depending on jumps by elliptic functionals via Γ-convergence". In: *Communications on Pure and Applied Mathematics* 43, pp. 999–1036.

Amor, H., J.-J. Marigo, and C. Maurini (2009). "Regularized formulation of the variational brittle fracture with unilateral contact: Numerical experiments". In: *Journal of the Mechanics and Physics of Solids* 57, pp. 1209–1229.

Aslan, O., N. Cordero, A. Gaubert, and S. Forest (2011). "Micromorphic approach to single crystal plasticity and damage". In: *International Journal of Engineering Science* 49, pp. 1311–1325.

Belytschko, T. and T. Black (1999). "Elastic crack growth in finite elements with minimal remeshing". In: *International Journal for Numerical Methods in Engineering* 45, pp. 601–620.

Benzerga, A. and J. Leblond (2010). "Ductile Fracture by Void Growth to Coalescence". In: *Advances in Applied Mechanics* 44, pp. 169–305.

Besson, J. (2010). "Continuum Models of Ductile Fracture: A Review". In: *International Journal of Damage Mechanics* 19, pp. 3–52.

Besson, J., D. Steglich, and W. Brocks (2001). "Modeling of crack growth in round bars and plane strain specimens". In: *International Journal of Solids and Structures* 38, pp. 8259–8284.

Borden, M. J., T. J. R. Hughes, C. M. Landis, and C. V. Verhoosel (2014). "A higher-order phase-field model for brittle fracture: Formulation and analysis within the isogeometric analysis framework". In: *Computer Methods in Applied Mechanics and Engineering* 273, pp. 100–118. ISSN: 0045-7825.

Borden, M. J., C. V. Verhoosel, M. A. Scott, T. J. R. Hughes, and C. M. Landis (2012). "A phase-field description of dynamic brittle fracture". In: *Computer Methods in Applied Mechanics and Engineering* 217-220, pp. 77–95.

Bourdin, B., G. A. Francfort, and J.-J. Marigo (2000). "Numerical experiments in revisited brittle fracture". In: *Journal of the Mechanics and Physics of Solids* 48, pp. 797–826.

Bourdin, B., G. A. Francfort, and J.-J. Marigo (2008). *The Variational Approach to Fracture*. Springer.

Capriz, G. (1989). "Continua with Microstructure. Springer Tracts in Natural Philosophy". In:

Comi, C. (1999). "Computational modelling of gradient-enhanced damage in quasi-brittle materials". In: *Mechanics of Cohesive-frictional Materials* 4.1, pp. 17–36. ISSN: 1099-1484.

Danas, K. and P. Ponte Castañeda (2012). "Influence of the Lode parameter and the stress triaxiality on the failure of elasto-plastic porous materials". In: *International Journal of Solids and Structures* 49, pp. 1325–1342.

de Borst, R., J. Pamin, and M. G. D. Geers (1999). "On coupled gradient-dependent plasticity and damage theories with a view to localization analysis". In: *European Journal of Mechanics - A/Solids* 18, pp. 939–962.

Dimitrijevic, B. J. and K. Hackl (2011). "A regularization framework for damage-plasticity models via gradient enhancement of the free energy". In: *International Journal for Numerical Methods in Biomedical Engineering* 27, pp. 1199–1210.

Duda, F. P., A. Ciarbonetti, P. J. Sánchez, and A. E. Huespe (2015). "A phase-field/gradient damage model for brittle fracture in elastic–plastic solids". In: *International Journal of Plasticity* 65, pp. 269–296.

Forest, S. (2009). "Micromorphic approach for gradient elasticity, viscoplasticity, and damage". In: *Journal of Engineering Mechanics* 135, pp. 117–131.

Francfort, G. A. and J.-J. Marigo (1998). "Revisiting brittle fracture as an energy minimization problem". In: *Journal of the Mechanics and Physics of Solids* 46, pp. 1319–1342.

Frémond, M. (2002). *Non-Smooth Thermomechanics*. Springer.

Frémond, M. and B. Nedjar (1996). "Damage, gradient of damage, and principle of virtual power". In: *International Journal of Solids and Structures* 33, pp. 1083–1103.

Geers, M. G. D. (2004). "Finite strain logarithmic hyperelasto-plasticity with softening: a strongly non-local imlicit gradient framework". In: *Computer Methods in Applied Mechanics and Engineering* 193, pp. 3377–3401.

Gurson, A. L. (1975). "Plastic flow and fracture behavior of ductile materials incorporating void nucleation, growth and coalescence". PhD thesis. Division of Engineering, Brown University.

Gurtin, M. E. (1996). "Generalized Ginzburg-Landau and Cahn-Hilliard equations based on a microforce balance". In: *Physica D* 92.3-4, pp. 178–192.

Gurtin, M. E. (2003). "On a framework for small-deformation viscoplasticity: free energy, microforces, strain gradients". In: *International Journal of Plasticity* 19, pp. 47–90.

Hakim, V. and A. Karma (2009). "Laws of crack motion and phase-field models of fracture". In: *Journal of the Mechanics and Physics of Solids* 57, pp. 342–368.

Hofacker, M. and C. Miehe (2012). "Continuum phase field modeling of dynamic fracture: variational principles and staggered FE implementation". In: *International Journal of Fracture* 178, pp. 113–129.

Huespe, A., A. Needleman, J. Oliver, and Sánchez (2012). "A finite strain, finite band method for modeling ductile fracture". In: *International Journal of Plasticity* 28, pp. 53–69.

Johnson, G. and W. Cook (1985). "Fracture characteristics of three metals subjected to various strains, strain rates, temperatures and pressures". In: *Engineering Fracture Mechanics* 21, pp. 31–48.

Kamat, S., M. Srinivas, and P. R. Rao (2011). "Effect of temperature on the mode I and mixed mode I/III fracture toughness of SA333 steel". In: *Materials Science and Engineering: A* 528.12.

Karma, A., D. A. Kessler, and H. Levine (2001). "Phase-field model of mode III dynamic fracture". In: *Physical Reviev Letters* 87, p. 045501.

Kröner, E. (1958). "Kontinuumstheorie der Versetzungen und Eigenspannungen". In: *Ergebnisse der angewandten Mathematik*. Ed. by L. Collatz and F. Lösch. Vol. 5, Springer.

Leblond, J., G. Perrin, and P. Suquet (1994). "Exact results and approximate models for porous viscoplastic solids". In: *International Journal of Plasticity* 3, pp. 213–235.

Lee, E. H. (1969). "Elastic-plastic deformation at finite strains". In: *Journal of Applied Mechanics, ASME* 36, pp. 1–6.

Lemaitre, J. (1985). "A Continuous Damage Mechanics Model for Ductile Fracture". In: *Journal of Engineering Materials and Technology* 107, pp. 83–89.

Lemaitre, J. and J.-L. Chaboche (1990). *Mechanics of Solid Materials*. Cambridge University Press.

Li, H., M. Fu, J. Lu, and H. Yang (2011). "Ductile fracture: Experiments and computations". In: *International Journal of Plasticity* 27, pp. 147–180.

Linder, C. and A. Raina (2013). "A strong discontinuity approach on multiple levels to model solids at failure". In: *Computer Methods in Applied Mechanics and Engineering* 253, pp. 558–583.

Lorentz, E., J. Besson, and V. Cano (2008). "Numerical simulation of ductile fracture with the Rousselier constitutive law". In: *Computer Methods in Applied Mechanics and Engineering* 197, pp. 1965–1982.

Mandel J. (1972). *Plasticité clasique et viscoplasticité,* CISM Courses and Lectures No.97. Springer.

Mariano, P. M. (2001). "Multifield theories in mechanics of solids". In: *Adv. App]. Mech* 38, pp. 1–93.

Maugin, G. A. (1990). "Internal variables and dissipative structures". In: *Journal of Non-Equilibrium Thermodynamics* 15, pp. 173–192.

May, S., J. Vignollet, and R. de Borst (2015). "A numerical assessment of phase-field models for brittle and cohesive fracture: Gamma-convergence and stress oscillations". In: *European Journal of Mechanics - A/Solids* 52, pp. 72–84.

Miehe, C. (1998). "A constitutive frame of elastoplasticity at large strains based on the notion of a plastic metric". In: *International Journal of Solids and Structures* 35, pp. 3859–3897.

Miehe, C. (2011). "A multi-field incremental variational framework for gradient-extended standard dissipative solids". In: *Journal of the Mechanics and Physics of Solids* 59, pp. 898–923.

Miehe, C. (2014). "Variational gradient plasticity at finite strains. Part I: Mixed potentials for the evolution and update problems of gradient-extended dissipative solids". In: *Computer Methods in Applied Mechanics and Engineering* 268, pp. 677–703.

Miehe, C., F. Aldakheel, and S. Mauthe (2013). "Mixed variational principles and robust finite element implementations of gradient plasticity at small strains". In: *International Journal for Numerical Methods in Engineering* 94, pp. 1037–1074.

Miehe, C., F. Aldakheel, and A. Raina (2016a). "Phase Field Modeling of Ductile Fracture at Finite Strains. A Variational Gradient-Extended Plasticity-Damage Theory". In: *International Journal of Plasticity* in press.

Miehe, C. and E. Gürses (2007). "A robust algorithm for configurational-force-driven brittle crack propagation with R-adaptive mesh alignment". In: *International Journal for Numerical Methods in Engineering* 72, pp. 127–155.

Miehe, C., M. Hofacker, L.-M. Schänzel, and F. Aldakheel (2015a). "Phase Field Modeling of Fracture in Multi-Physics Problems. Part II. Brittle-to-Ductile Failure Mode Transition and Crack Propagation in Thermo-Elastic-Plastic Solids". In: *Computer Methods in Applied Mechanics and Engineering* 294, pp. 486–522.

Miehe, C., M. Hofacker, and F. Welschinger (2010a). "A phase field model for rate-independent crack propagation: Robust algorithmic implementation based on operator splits". In: *Computer Methods in Applied Mechanics and Engineering* 199, pp. 2765–2778.

Miehe, C., L. Schänzel, and H. Ulmer (2015b). "Phase field Modeling of Fracture in Multi-Physics Problems. Part I. Balance of Crack Surface and Failure Criteria for Brittle Crack Propagation in Thermo-Elastic Solids". In: *Computer Methods in Applied Mechanics and Engineering* 294, pp. 449–485.

Miehe, C., S. Teichtmeister, and F. Aldakheel (2016b). "Phase-Field Modeling of Ductile Fracture: A Variational Gradient-Extended Plasticity-Damage Theory and its Micromorphic Regularization". In: *Philisophical Transactions of the Royal Society A* 374.

Miehe, C., F. Welschinger, and M. Hofacker (2010b). "Thermodynamically consistent phase-field models of fracture: Variational principles and multi-field FE implementations". In: *International Journal for Numerical Methods in Engineering* 83, pp. 1273–1311.

Mühlhaus, H.-B. and E. C. Aifantis (1991). "A variational principle for gradient plasticity". In: *International Journal of Solids and Structures* 28, pp. 845–857.

Mumford, D. and J. Shah (1989). "Optimal approximations by piecewise smooth functions and associated variational problems". In: *Communications on Pure and Applied Mathematics* 42, pp. 577–685.

Nahshon, K. and J. Hutchinson (2008). "Modification of the Gurson Model for shear failure". In: *European Journal of Mechanics A/Solids* 27, pp. 1–17.

Nedjar, B. (2001). "Elastoplastic-damage modelling including the gradient of damage: formulation and computational aspects". In: *Inernational Journal of Solids and Structures* 38, pp. 5421–5451.

Needleman, A. and V. Tvergaard (1984). "An analysis of ductile rupture in notched bars". In: *Journal of the Mechanics and Physics of Solids* 32.6, pp. 461–490.

Peerlings, R. H. J., R. de Borst, W. A. M. Brekelmans, and J. H. P. de Vree (1996). "Gradient Enhanced Damage for Quasi–Brittle Materials". In: *International Journal for Numerical Methods in Engineering* 39, pp. 3391–3403.

Pham, K., H. Amor, J.-J. Marigo, and C. Maurini (2011). "Gradient damage models and their use to approximate brittle fracture". In: *International Journal of Damage Mechanics* 20.4, pp. 618–652.

Ponte Castañeda, P. and M. Zaidman (1994). "Constitutive models for porous materials with evolving microstructure". In: *Journal of the Mechanics and Physics of Solids* 42, pp. 1459–1497.

Reddy, B., F. Ebobisse, and A. McBride (2008). "Well-posedness of a model of strain gradient plasticity for plastically irrotational materials". In: *International Journal of Plasticity* 24, pp. 55–73.

Reusch, F., B. Svendsen, and D. Klingbeil (2003). "A non-local extension of Gurson-based ductile damage modeling". In: *Computational Materials Science* 26, pp. 219–229.

Rice, J. R. and D. M. Tracey (1969). "On the ductile enlargement of voids in triaxial stress fields". In: *Journal of the Mechanics and Physics of Solids* 17, pp. 201–217.

Rousselier, G. (1987). "Ductile fracture models and their potential in local approach of fracture". In: *Nuclear Engineering and Design* 105, pp. 97–111.

Saanouni, K. and M. Hamed (2013). "Micromorphic approach for finite gradient-elasto-plasticity fully coupled with ductile damage: Formulation and computational aspects". In: *International Journal of Solids and Structures* 50, pp. 2289–2309.

Simo, J. C. (1992). "Algorithms for static and dynamic multiplicative plasticity that preserve the classical return mapping schemes of the infinitesimal theory". In: *Computer Methods in Applied Mechanics and Engineering* 99.

Simo, J. C., J. Oliver, and F. Armero (1993). "An analysis of strong discontinuities induced by strain-softening in rate-independent inelastic solids". In: *Computational Mechanics* 12, pp. 277–296.

Simo, J. and C. Miehe (1992). "Associative coupled thermoplasticity at finite strains: formulation, numerical analysis and implementation". In: *Computer Methods in Applied Mechanics and Engineering* 98.1, pp. 41–104.

Tvergaard, V. and A. Needleman (1984). "Analysis of the cup-cone fracture in a round tensile bar". In: *Acta Metall* 32, pp. 157–169.

Tvergaard, V. (1982). "On localization in ductile materials containing spherical voids". In: *International Journal of Fracture* 18, pp. 237–252.

Ulmer, H., M. Hofacker, and C. Miehe (2013). "Phase Field Modeling of Brittle and Ductile Fracture". In: *Proceedings in Applied Mathematics and Mechanics* 13, pp. 533–536.

Verhoosel, C. V. and R. de Borst (2013). "A phase-field model for cohesive fracture". In: *International Journal for Numerical Methods in Engineering* 96, pp. 43–62. ISSN: 1097-0207.

Chapter 5

A finite-strain phase-field approach large to ductile failure of frictional materials

Daniel Kienle[1,*], Fadi Aldakheel[2] & Marc-André Keip[1]

[1]Institute of Applied Mechanics

University of Stuttgart, 70569 Stuttgart, Pfaffenwaldring 7, Germany

[2]Institute of Continuum Mechanics

Leibniz Universität Hannover, 30167 Hannover, Appelstraße 11, Germany

Abstract This work presents a modeling framework for the ductile failure of frictional materials undergoing large deformations with a focus on soil mechanics. Crack formation and propagation in soil can be modeled in a convenient way by the recently developed continuum phase-field approach to fracture. Within this approach sharp crack discontinuities are regularized. It allows the use of standard discretization methods for crack discontinuities and is able to account for complex crack paths. In the present contribution, we develop a computational modeling framework for the phase-field approach to ductile fracture in frictional materials. It combines a *non-associative* Drucker-Prager-type elastic-plastic constitutive model with an evolution equation for the crack phase field in terms of an elastic-plastic energy density. An important aspect of this work is the development of an isotropic hardening mechanism that accounts for both *friction* and *cohesion hardening*. In order to guarantee a locking- and hourglass-free response, a *modified* enhanced element formulation, namely the consistent gradient formulation, is proposed as a key feature of the finite-element implementation. The performance of the formulation is demonstrated by means of representative numerical examples that describe soil crack formation rooted in elastic-plastic fracture mechanics.

[*]Corresponding author.
E-mail address: kienle@mechbau.uni-stuttgart.de

Keywords: Elastic-plastic material, ductile fracture, phase-field modeling, soil mechanics.

5.1. Introduction

Understanding and predicting the initiation and propagation of fracture in materials has been a topic of intensive research over the last decades. This also covers failure of frictional materials like soils and rocks, which are applications at the core of geo-technical and civil engineering. Concepts for describing the classical theory of brittle fracture are outlined in Griffith 1921 and Irwin 1958. Different approaches to the regularized modeling of Griffith-type brittle fracture in elastic solids have been introduced by, for example, Francfort and Marigo 1998, Bourdin et al. 2000, Bourdin et al. 2008, Amor et al. 2009, Kuhn and Müller 2010, Miehe et al. 2010b, Pham et al. 2011 and Borden et al. 2012. The mentioned works rely on Griffith-type theories for predicting crack initiation and propagation by a diffuse phase field that represents fracture. Recent extensions of these general approaches to brittle fracture are devoted, for example, towards the incorporation of cohesive-zone models Verhoosel and de Borst 2013, the fracturing of soft materials Miehe and Schänzel 2014, shells Reinoso et al. 2017 and anisotropic solids Teichtmeister et al. 2017 as well as towards fatigue fracture Alessi et al. 2018b, just to name a few. Thanks to its universal structure and numerical robustness the phase-field approach to fracture has proven a versatile and powerful tool for the description of failure of materials. Applications cover a wide range of scenarios and materials, for example, given by rupturing of arterial walls Gültekin et al. 2016; Raina and Miehe 2016 or hydraulically driven fracturing Ehlers and Luo 2017; Heider and Markert 2017; Miehe et al. 2015b; Mikelić et al. 2015; Wilson and Landis 2016. We refer to Pham et al. 2017 for experimental validations of the phase-field approach to brittle fracture.

By coupling gradient-damage mechanics with models of elasto-plasticity, the phase-field modeling can be extended towards *ductile fracture*. Associated formulations are able to account for plastic deformations coupled with crack evolution. In that respect, we refer to Duda et al. 2015, who propose a framework of ductile fracture based on the classical theory of continua with microstructure in the sense of Gurtin-type microforce balances. In their formulation, crack initiation and propagation are modeled in the sense of brittle fracture in elastic-plastic materials. In contrast to that, the modeling framework provided by Miehe et al. 2015a, takes into account the full elastic-plastic energy in the fracture driving force and allows for a transition from brittle to ductile fracture. Along similar lines, Ambati et al. 2015 developed an elastic-plastic phase-field formulation of ductile fracture by postulating a characteristic degradation function that incorporates the amount of plastic deformation. We refer to Ambati et al. 2016 for experimental verification. The important aspect of stress triaxiality has been incorporated by Borden et al. 2016, in the sense of a modified expression for the effective plastic work. For variationally consistent formulations we refer to the works of Miehe et al. 2016a,c that couple gradient plasticity with gradient damage at finite strains. We further highlight the recent variational approach of Alessi et al. 2018a which combines brittle, cohesive and ductile fracture in an illustrative one-dimensional setting. We emphasize that above models rely on von-Mises-type plasticity formulations coupled with fracture. Thus, they are not suitable for describing plastic deformations driven by volumetric stresses. This has

motivated Miehe et al. 2016b to extend the phase-field modeling of fracture towards porous finite plasticity accounting for growth of micro-voids. For associated augmentations with respect to void nucleation and coalescence see Aldakheel et al. 2017. The effects of nucleation, growth and coalescence of micro-voids play a crucial role in metal plasticity.

To describe the plastic deformation of frictional or granular materials a plasticity model is required, in which the yield criterion is a function of both the deviatoric and the volumetric stress. Such kinds of plasticity models have been proposed, for example, by Drucker and Prager 1952, Zienkiewicz et al. 1975, Vermeer and de Borst 1984, de Boer 1988, Simo and Meschke 1993, and Ehlers 1995. Among the plasticity formulations for frictional materials, the Drucker–Prager plasticity model shows good agreement with experimental observations for various applications in computational geo-mechanics, see Drucker and Prager 1952, Loret and Prevost 1986, Hjiaj et al. 2003, and Zreid and Kaliske 2016. In the numerical setting of these models the problem of singularity arises for tensile stress conditions. Therefore, the return-mapping scheme often fails to converge. In many works a tension cut-off is introduced to get rid of the singularity at the peak of the cone. However, this results in a non-differential formulation of the cone and could still cause convergence issues. This has encouraged Abbo and Sloan 1995 and Lambrecht and Miehe 1999, 2001 to introduce an additional term in the Drucker–Prager-type yield criterion and plastic-potential function based on a constant perturbation-type parameter that causes a smoothing-out of the peak of the classic cone. With regard to the failure description of geological materials we refer to the recent work of Choo and Sun 2018 who proposed a modeling framework based on a pressure-sensitive plasticity employing a modified Drucker–Prager yield surface.

The goal of the present contribution is to derive a theoretical and a computationally efficient framework for ductile fracture in soil mechanics at finite strains. To this end, we couple the phase-field approach to fracture with a *non-associative* Drucker–Prager-type elastic-plastic constitutive model, suitable for a wide range of applications in computational geo-mechanics. The soil is assumed to be an idealized material which behaves elastically up to some state of stress at which yielding occurs. An important aspect of our investigation is the development of two types of isotropic hardening mechanisms, namely the *cohesion* and *friction* hardening mechanism. A further key feature is the introduction of a phase-field driving force as function of an elastic-plastic energy density.

The outline of the paper is as follows. Section 5.2 summarizes the variational formulation of the fracture phase field in the context of a gradient-damage model incorporating a local irreversibility constraint preventing crack healing. In Section 5.3 we introduce the global unknowns and the kinematic fields of ductile fracture in frictional materials. We also show the key aspects of the multiplicative split of the deformation in an Eulerian setting. Hereby the Eulerian elastic Finger tensor is used as an elastic deformation measure. Based on this split the elastic-plastic energy contribution, the yield function and the plastic potential are introduced as constitutive functions. The algorithmic treatment of these equations is also shown in Section 5.3, followed by the formulation of the failure criterion which is used to drive the fracture phase field. Section 5.4 documents a well suited finite-element formulation for the proposed model that overcomes typical locking phenomena as well as zero-energy (hourglass) modes. Numerical examples showing the capabilities of the proposed model are presented in Section 5.5, considering a shear-band formation under compressive loading and the pullout behavior of an anchor plate. Section 5.6 closes

the contribution with a short summary.

5.2. Regularized crack surface topology

Following Miehe et al. 2010a this section discusses the basic ingredients of a purely geometric approach to the phase-field modeling of fracture. Consider a material body $\mathcal{B}_0 \subset \mathcal{R}^\delta$ with the dimension $\delta \in [2,3]$ in space and its surface $\partial\mathcal{B}_0 \subset \mathcal{R}^{\delta-1}$, see Figure 5.1. Let $\boldsymbol{X} \in \mathcal{B}_0$ be a point in this body at time $t \in \mathcal{T}$. Then, the crack phase field $d : \mathcal{B}_0 \times \mathcal{T} \to [0,1]$ denotes with $d(\boldsymbol{X},t) = 0$ the intact and with $d(\boldsymbol{X},t) = 1$ the broken material. Based on that, a sharp crack surface Γ can be approximated by the regularized crack surface Γ_l

$$\Gamma_l(d) = \int_{\mathcal{B}_0} \gamma_l(d,\nabla d)\,\mathrm{d}V \quad \text{with} \quad \gamma_l(d,\nabla d) = \frac{1}{2l}d^2 + \frac{l}{2}|\nabla d|^2 \,, \tag{5.1}$$

in terms of the crack-surface density γ_l per unit volume. This regularization is controlled by the length-scale parameter l. The sharp crack surface is gained from a crack-surface functional for vanishing length scale $l \to 0$. With prescribed Dirichlet condition $d = 1$ on $\Gamma \subset \mathcal{B}_0$ the regularized phase field d can then be obtained by a variational principle of diffuse crack topology $d = \mathrm{Arg}\{\inf_d \Gamma_l(d)\}$. The minimization yields the Euler equation $d - l^2\Delta d = 0$ in $\mathcal{B}_0$. The profile of the phase field d is governed by the solution of this partial differential equation, which is an exponential function. A more detailed illustration can be found in Miehe et al. 2010b for a second-order phase field and in Borden et al. 2014 for a fourth-order phase field. Taking the derivative w.r.t. time of the regularized crack surface yields

$$\frac{\mathrm{d}}{\mathrm{d}t}\Gamma_l(d) = \int_{\mathcal{B}_0} \delta_d\gamma_l(d,\nabla d)\,\dot{d}\,\mathrm{d}V \,, \tag{5.2}$$

where $\delta_d\gamma_l := \partial_d\gamma_l - \mathrm{Div}(\partial_{\nabla d}\gamma_l)$ is the variational derivative of the crack-surface density. The evolution of the regularized crack surface (5.2) is governed by a constitutive function. By postulating this constitutive function we can write

$$\frac{\mathrm{d}}{\mathrm{d}t}\Gamma_l(d) = \frac{1}{l}\int_{\mathcal{B}_0} [(1-d)\mathcal{H} - \eta\dot{d}]\dot{d}\,\mathrm{d}V \geq 0 \,, \tag{5.3}$$

where the viscosity of crack propagation is denoted as $\eta \geq 0$. According to Miehe et al. 2010a the crack driving force $\mathcal{H}$ is given by

$$\mathcal{H} = \max_{s\in[0,t]} D(\mathrm{state}(\boldsymbol{X},s)) \geq 0 \,, \tag{5.4}$$

where the crack driving state function D represents a constitutive function, which will be specified for the presented model in Section 5.3. The maximum over time of this function guarantees the irreversibility of the fracture phase field. The expression "state" stands for additional variables determined by the model for the elastic-plastic response in soil mechanics undergoing large strains considered in Section 5.3 below.

Combining the evolution equations (5.2, 5.3) and applying the localization theorem yields the local evolution of the crack phase field

$$\eta\dot{d} = (1-d)\mathcal{H} - (d - l^2\Delta d) \quad \text{with} \quad \nabla d \cdot \boldsymbol{n}_0 = 0 \ \text{ on } \partial\mathcal{B}_0 \,, \tag{5.5}$$

and the homogeneous Neumann condition with $\boldsymbol{n}_0$ as the outward unit normal on $\partial\mathcal{B}_0$.

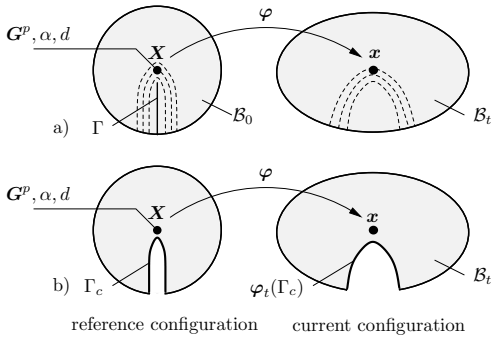

Figure 5.1: Primary variables of the model ($\boldsymbol{\varphi}$, $\boldsymbol{G}^p$, α, d): The crack phase-field d for different lengths scales l in a). $\Gamma_l(d)$ converges in the limit $l \to 0$ to the sharp crack surface Γ. In b) parts of the continuum with $d > c$ with $c \approx 1$ are considered to be free space and are not displayed. $\Gamma_c = \{\boldsymbol{X} \,|\, d = c\}$ defines the crack faces in the regularized setting.

5.3. Non-associative elastic-plastic hardening model coupled with a phase-field model of fracturing

This section combines the aforementioned phase-field approach to fracturing with a *non-associative* Drucker-Prager-type elastic-plastic constitutive model. When postulating the constitutive functions, the phase field d is considered as a generalized internal variable.

5.3.1. Introduction of kinematic and state variables

Deformation map. The deformation map at time t is denoted as $\boldsymbol{\varphi}(\boldsymbol{X}, t)$ and maps material positions $\boldsymbol{X} \in \mathcal{B}_0$ of the reference configuration $\mathcal{B}_0 \in \mathcal{R}^\delta$ onto points $\boldsymbol{x} = \boldsymbol{\varphi}_t(\boldsymbol{X}) \in \mathcal{B}_t$ of the current configuration $\mathcal{B}_t \in \mathcal{R}^\delta$, see Figure 5.1. The initial condition is given by $\boldsymbol{\varphi}(\boldsymbol{X}, t_0) = \boldsymbol{X}$. The deformation gradient is $\boldsymbol{F} := \nabla \boldsymbol{\varphi}_t(\boldsymbol{X})$ with its determinant $J := \det \boldsymbol{F} > 0$. Prescribed deformations and external tractions on the boundary are defined by the time-dependent Dirichlet- and Neumann conditions

$$\boldsymbol{\varphi} = \bar{\boldsymbol{\varphi}}(\boldsymbol{X}, t) \text{ on } \partial\mathcal{B}_0^{\boldsymbol{\varphi}} \quad \text{and} \quad \boldsymbol{P}\boldsymbol{n}_0 = \bar{\boldsymbol{t}}_0(\boldsymbol{X}, t) \text{ on } \partial\mathcal{B}_0^t \,, \tag{5.6}$$

where $\partial\mathcal{B}_0 = \partial\mathcal{B}_0^{\boldsymbol{\varphi}} \cup \partial\mathcal{B}_0^t$ is the surface of the undeformed configuration and $\boldsymbol{P}$ is the first Piola stress tensor defined as thermodynamic dual to $\boldsymbol{F}$.

Elastic Finger tensor. To describe the plastic deformation, the plastic metric $\boldsymbol{G}^p \in Sym^+(3)$ in the Lagrangian configuration is introduced as an internal variable, that evolves in time with $\boldsymbol{G}^p(\boldsymbol{X}, t_0) = \boldsymbol{1}$ as the initial state. Here $Sym^+(3) := \{\boldsymbol{A} \in \mathbb{K}^{3\times3} \mid \boldsymbol{A} = \boldsymbol{A}^T \mid \det \boldsymbol{A} > 0\}$ denotes the set of symmetric, real 3×3 matrices with a positive determinant. It can be constituted by a multiplicative split $\boldsymbol{F} = \boldsymbol{F}^e \boldsymbol{F}^p$ of the deformation gradient into plastic and elastic parts suggested by Kröner 1958, Lee, E. H. 1969 and Mandel J. 1972. Hence, an elastic deformation measure is the *Eulerian elastic*

Finger tensor defined as

$$\boldsymbol{b}^e = \boldsymbol{F}^e(\boldsymbol{F}^e)^T := \boldsymbol{F}(\boldsymbol{G}^p)^{-1}\boldsymbol{F}^T \quad \text{with} \quad \boldsymbol{G}^p = (\boldsymbol{F}^p)^T\boldsymbol{F}^p \ . \tag{5.7}$$

Note that the use of $\boldsymbol{G}^p \in Sym^+(3)$ instead of $\boldsymbol{F}^p \in GL^+(3)$ neglects plastic rotations (Miehe 1998a). Here $GL^+(3) := \{\boldsymbol{A} \in \mathbb{K}^{3\times 3} \mid \det \boldsymbol{A} > 0\}$ denotes the set of real 3×3 matrices with a positive determinant. The evolution of the Lagrangian plastic metric is governed by the *Eulerian plastic rate-of-deformation tensor* (Simo and Miehe 1992)

$$\boldsymbol{d}^p := -\tfrac{1}{2}(\pounds_{\boldsymbol{v}}\boldsymbol{b}^e)(\boldsymbol{b}^e)^{-1} = \boldsymbol{F}\boldsymbol{D}^p\boldsymbol{F}^{-1} \text{ with } \pounds_{\boldsymbol{v}}\boldsymbol{b}^e := \boldsymbol{F}\dot{\overline{(\boldsymbol{G}^p)^{-1}}}\boldsymbol{F}^T \text{ and } \boldsymbol{D}^p := -\tfrac{1}{2}\dot{\overline{(\boldsymbol{G}^p)^{-1}}}\boldsymbol{G}^p \ , \tag{5.8}$$

where $\pounds_{\boldsymbol{v}}\boldsymbol{b}^e$ denotes the Lie derivative of $\boldsymbol{b}^e$. The mapping properties of used tensors $\boldsymbol{G}^P$, $\boldsymbol{b}^e$, $\boldsymbol{d}^p$ and $\boldsymbol{D}^P$ are show in Figure 5.2.

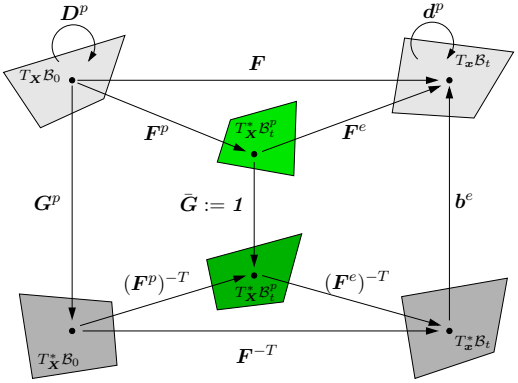

Figure 5.2: Visualization of the plastic metric $\boldsymbol{G}^p$, the elastic Finger tensor $\boldsymbol{b}^e$ and the Eulerian and Lagrangian plastic rate-of-deformation tensor $\boldsymbol{d}^p$ and $\boldsymbol{D}^p$. Given are the three covariant spaces for the Lagrangian ($T_{\boldsymbol{X}}\mathcal{B}_0$), intermediate plastic ($T_{\boldsymbol{X}}\mathcal{B}^p_t$) and Eulerian ($T_{\boldsymbol{x}}\mathcal{B}_t$) configuration and the three contravariant spaces for the Lagrangian ($T^*_{\boldsymbol{X}}\mathcal{B}_0$), intermediate plastic ($T^*_{\boldsymbol{X}}\mathcal{B}^p_t$) and Eulerian ($T^*_{\boldsymbol{x}}\mathcal{B}_t$) configuration.

Constitutive state variables. The *non-associative* elastic-plastic hardening model at finite strains is described by the deformation map $\boldsymbol{\varphi}$ as a global primary field. In addition, we introduce the equivalent plastic strain α as a local internal variable, which is associated with the plastic evolution and the plastic hardening mechanism. The Lagrangian plastic metric $\boldsymbol{G}^p$ serves as an additional local primary field. Consequently, the constitutive state is defined by

$$\text{state} := \{\nabla\boldsymbol{\varphi}, \boldsymbol{G}^p, \alpha\} \ . \tag{5.9}$$

5.3.2. Energetic storage function

The energy-storage function $\widehat{\Psi}$ is decomposed into an elastic and a plastic contribution. It is defined as

$$\widehat{\Psi}(\text{state}; d) = g(d)\big[\psi^e(\boldsymbol{b}^e) + \psi^p(\alpha)\big] \quad \text{with} \quad g(d) := (1-d)^2 + k \ , \tag{5.10}$$

which depends on the introduced state variables in (5.9) and the phase field d. Note that in case of fracture, the whole energetic response gets degraded by the degradation function $g(d)$. The residual stiffness that keeps the problem well posed is denoted as k with $k \in \mathcal{R}_+$.

Elastic contribution. The isotropic stored elastic energy of the solid is assumed to have the simple quadratic form

$$\psi^e(\boldsymbol{h}^e) := \frac{\lambda}{2}(\mathrm{tr}\boldsymbol{h}^e)^2 + \mu\,\mathrm{tr}[(\boldsymbol{h}^e)^2] \;, \tag{5.11}$$

in terms of the Eulerian elastic Hencky strain tensor $\boldsymbol{h}^e := \frac{1}{2}\ln \boldsymbol{b}^e$ and the Lamé constants $\lambda > -\frac{2}{3}\mu$ and $\mu > 0$. The above energy function defines an isotropic and linear stress-strain response in the logarithmic strain space.

In the present work a spectral representation of isotropic non-associative elasto-plasticity is considered. It provides a compact setting of the model problem formulated in terms of principal strains and principal stresses. We consider the eigenvalue problem for the elastic Finger tensor in (5.7)

$$[\boldsymbol{b}^e - (\lambda_i^e)^2\boldsymbol{1}]\,\boldsymbol{n}_i = \boldsymbol{0} \;, \tag{5.12}$$

in terms of the elastic principal stretches $\{\lambda_i^e\}_{i=1,2,3}$ and the corresponding eigenvectors $\{\boldsymbol{n}_i\}_{i=1,2,3}$. Hence, the spectral form of the Eulerian logarithmic Hencky tensor reads

$$\boldsymbol{h}^e = \tfrac{1}{2}\ln \boldsymbol{b}^e = \textstyle\sum_{i=1}^3 \varepsilon_i^e\, \boldsymbol{n}_i \otimes \boldsymbol{n}_i \quad \text{with} \quad \varepsilon_i^e := \ln \lambda_i^e \;, \tag{5.13}$$

where ε_i^e are the logarithmic elastic principle strains. This results in a spectral representation of the stored elastic energy function $\psi^e(\varepsilon_1^e, \varepsilon_2^e, \varepsilon_3^e)$. Following the Coleman-Noll procedure we obtain the Kirchhoff stresses $\boldsymbol{\tau}$ in the spectral representation τ_i as the first derivative of the energy function (5.10) with respect to the principle elastic strains

$$\boldsymbol{\tau} = \textstyle\sum_{i=1}^3 \tau_i\, \boldsymbol{n}_i \otimes \boldsymbol{n}_i \quad \text{with} \quad \tau_i = g(d)\,\widetilde{\tau}_i \quad \text{and} \quad \widetilde{\tau}_i = \psi^e_{,i} := \partial\psi^e/\partial\varepsilon_i^e \;. \tag{5.14}$$

Here $\widetilde{\tau}_i$ denotes the *effective principal Kirchhoff stresses*.

Plastic contribution. Focusing on an isotropic local plastic hardening mechanism, the plastic part of the energy function reads

$$\psi^p(\alpha) = \tfrac{1}{2}h\alpha^2 + \tau_y\big[\alpha + \tfrac{1}{\omega}\exp(-\omega\alpha) - \tfrac{1}{\omega}\big] \;, \tag{5.15}$$

where $h \geq 0$ is the hardening modulus, τ_y is the saturated yield shift and w is the saturation parameter which controls the saturation of the hardening mechanism. The derivative of the plastic energy with respect to the equivalent plastic strain α yields the hardening function $\widehat{\beta} := \beta(\alpha, d)$ which takes the form of a saturation-type function

$$\beta(\alpha, d) := g(d)\partial_\alpha\psi^p(\alpha) \quad \text{with} \quad \partial_\alpha\psi^p(\alpha) = h\alpha + \tau_y\big[1 - \exp(-\omega\alpha)\big] \;. \tag{5.16}$$

A graphical representation of this function is given in Figure 5.3.

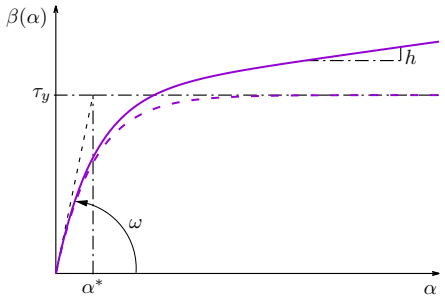

Figure 5.3: Hardening function $\beta(\alpha; d = 0)$ with linear hardening $h \neq 0$ (solid line) and without linear hardening $h = 0$ (dashed line), where $\alpha^* = (\frac{h}{\tau_y} + \omega)^{-1}$.

5.3.3. Yield function in Kirchhoff-stress space

Within the present work the classical Drucker-Prager yield criterion with an additional *regularization of the non-smooth peak* as introduced by Lambrecht and Miehe 1999, 2001 is considered. In addition, we propose an isotropic hardening mechanism that accounts for both *friction* and *cohesion hardening*. More details on the physical motivation of these hardening mechanisms can be found in the work of Vermeer and de Borst 1984.The yield criterion employed in the present work is an open-surface model which excludes plastic yielding under pure hydrostatic loading conditions. Furthermore, the cross section of the yield surface along the deviatoric plane is a circle which limits the model to isotropic response for different deviatoric stress states. More advances models of the elasto-plastic behavior of geomaterials have been proposed, for example, by Desai 1980; Ehlers 1995; Lade and Kim 1988, 1995.

The yield criterion function is formulated in terms of the Kirchhoff stresses $\boldsymbol{\tau}$ and reads

$$\widehat{\Phi}(\boldsymbol{\tau}, \widehat{\beta}) = \sqrt{\tfrac{3}{2}}\sqrt{||\operatorname{dev}[\boldsymbol{\tau}]||^2 + M_\phi^2 q_1^2} - M_\phi(p_{\max} - \tfrac{1}{3}\operatorname{tr}\boldsymbol{\tau}) - \widehat{\beta} M_h(\boldsymbol{\tau}) \; . \tag{5.17}$$

In the subsequent part a spectral representation of the yield function (5.17) is considered. It is represented in terms of the *principal stresses* τ_i with $\boldsymbol{\tau} = \sum_{i=1}^{3} \tau_i \, \boldsymbol{n}_i \otimes \boldsymbol{n}_i$

$$\widehat{\Phi}(\tau_1, \tau_2, \tau_3, \widehat{\beta}) = \sqrt{\tfrac{3}{2}}\sqrt{\tau_i' \tau_i' + M_\phi^2 q_1^2} - M_\phi(p_{\max} + p) - \widehat{\beta} M_h(\tau_i) \; , \tag{5.18}$$

where $p := -\frac{1}{3}\sum_{i=1}^{3} \tau_i$ is the hydrostatic pressure and $\tau_i' := \tau_i + p$ are the deviatoric principle stresses. The yield function represents for $\widehat{\beta} = q_1 = 0$ the classical Drucker-Prager cone, see Figure 5.4.

It is expressed in terms of the material parameters M_ϕ, $p_{\max}$, q_1, controlling the ideal plastic behavior, and the two material functions $\widehat{\beta} := \beta(\alpha, d)$, $M_h(\boldsymbol{\tau})$ accounting for the hardening response. Thereby M_ϕ is the slope of the Drucker-Prager cone in the view of the hydrostatic-deviatoric stress plot and $p_{\max}$ gives the position of the peak of the cone. Both can be expressed in terms of the *friction angle* ϕ and the *cohesion* c referring to the

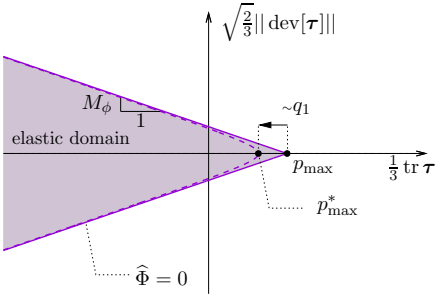

Figure 5.4: Yield surface (solid) and regularized yield surface (dashed) in two-dimensional hydrostatic-deviatoric stress plot. The position of the peak is given by $p^*_{\max} = \sqrt{3/2}q_1$.

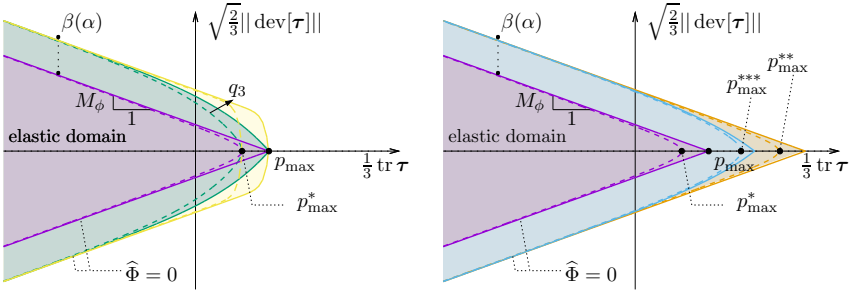

a) friction hardening
$q_2 = \exp(\sqrt{3/2}q_1q_3)$

b) cohesion/mixed-type hardening
$q_2 = 0/q_2 = 0.5\exp(\sqrt{3/2}q_1q_3)$

Figure 5.5: Yield surface in two-dimensional hydrostatic-deviatoric stress plot with and without regularization (dashed/solid lines). In a) with friction hardening for $q_3 = 10\bar{q}_3$ in yellow, for $q_3 = \bar{q}_3$ in green and no hardening in purple. In b) with cohesion hardening in orange, mixed-type hardening in blue and no hardening in purple.

Mohr-Coulomb criterion as

$$M_\phi = \frac{6\sin\phi}{3 \pm \sin\phi} \quad \text{and} \quad p_{\max} = c\cot\phi\ , \tag{5.19}$$

where $\pm$ is used for the different matching (compressive or tensile meridian) of the Drucker-Prager model with the Mohr-Coulomb model. In addition, q_1 controls the *smoothing-out of the peak* as a perturbation parameter Lambrecht and Miehe 1999, see Figure 5.4. This regularization is crucial for a robust numerical implementation.

The material function $M_h(\boldsymbol{\tau})$ introduced in (5.17) is chosen as

$$M_h(\boldsymbol{\tau}) = 1 - q_2\exp[q_3(\tfrac{1}{3}\operatorname{tr}\boldsymbol{\tau} - p_{max})] \quad \text{with} \quad q_2 \in [0, \exp(\sqrt{\tfrac{3}{2}}q_1q_3)]. \tag{5.20}$$

Here, q_3 controls the transition zone of the hardening, see Figure 5.5a. The influence of this parameter is not further investigated in this work. For simplicity, it is chosen

as $\frac{1}{2}\kappa^{-1}$ in what follows, where κ is the bulk modulus given by $\kappa = (3\lambda + 2\mu)/3$. The parameter q_2 is related to the different types of material hardening as follows: For i) $q_2 = \exp(\sqrt{3/2}\ q_1 q_3)$ a *friction hardening* behavior is obtained, where the position of peak $p_{\max}$ of the cone does not change due to hardening. With ii) $q_2 = 0$ it results in *cohesion hardening* and iii) $0 < q_2 < \exp(\sqrt{3/2}\ q_1 q_3)$ yields *mixed-type hardening*. In the latter two cases the peak moves due to hardening.

i) For the case of *friction hardening* the position $p^*_{\max}$ of the regularized peak is obtained by

$$p^*_{\max} = p_{\max} - \sqrt{\tfrac{3}{2}}\ q_1 \quad \text{with} \quad q_1 \in \big[0, \sqrt{\tfrac{2}{3}}\ p_{\max}\big]. \tag{5.21}$$

Note that the regularization parameter q_1 is bounded to guarantee a physically admissible behavior by satisfying $p^*_{\max} \geq 0$.

ii) In the case of *cohesion hardening* the position of the peak $p^{**}_{\max}$ is given by

$$\begin{aligned} p^{**}_{\max}(\widehat{\beta}) &= p_{\max} - \sqrt{\tfrac{3}{2}} q_1 + \tfrac{1}{M_\phi}\widehat{\beta} \\ &= p^*_{\max} + \tfrac{1}{M_\phi}\widehat{\beta}. \end{aligned} \tag{5.22}$$

iii) In the case of *mixed-type hardening* the position of the peak $p^{***}_{\max}$ can be computed according to

$$p^{***}_{\max}(\widehat{\beta}) = p^{**}_{\max}(\widehat{\beta}) - \tfrac{1}{q_3} W(z) \quad \text{with} \quad z = \tfrac{\widehat{\beta} q_2 q_3}{M_\phi} \exp\Big[q_3\big(p^{**}_{\max}(\widehat{\beta}) - p_{\max}\big)\Big], \tag{5.23}$$

where $W(x)$ is the inverse of the function $f(x) = x\exp(x)$, also called the Lambert-W function.

A graphical representation of the yield surface for the cohesion, friction and mixed-type hardening is illustrated in Figure 5.5.

5.3.4. Plastic potential function

To define the flow direction of the *non-associative* elastic-plastic hardening model for frictional materials, we introduce the plastic potential function in its spectral form as

$$\widehat{\chi}(\tau_1, \tau_2, \tau_3, \widehat{\beta}) = \sqrt{\tfrac{3}{2}}\sqrt{\tau'_i \tau'_i + M^2_\chi q^2_1} - M_\chi(p_{\max} + p) - \widehat{\beta} M_h(\tau_i)\ . \tag{5.24}$$

It is plotted in the two-dimensional hydrostatic-deviatoric stress plot in Figure 5.6. Note that its shape is analogous to the yield function in (5.17) and it incorporates the same hardening mechanism. The difference is the material parameter M_χ as the constant slope of the cone which characterizes the plastic potential hyper-surface. M_χ has to satisfy the condition $M_\chi \leq M_\phi$ and can be represented by

$$M_\chi = \frac{6\sin\theta}{3 \pm \sin\theta}\ . \tag{5.25}$$

Here θ denotes the *angle of dilatancy* representing the ratio of plastic volume change over the plastic shear strain. Note carefully that the slope of the plastic potential has to be smaller or equal than the slope of the yield function to be consistent with experimental

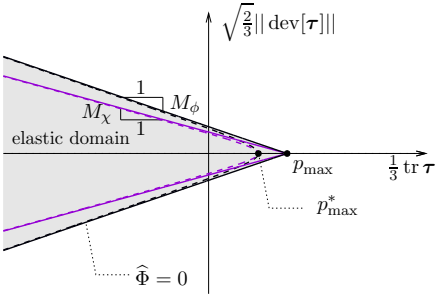

Figure 5.6: Plastic potential in two-dimensional hydrostatic-deviatoric stress plot with and without regularization (dashed/solid line) and the initial yield surface $\widehat{\Phi}(\boldsymbol{\tau};\hat{\beta}=0)$ in black.

results and to ensure, in case of cohesionless material ($c=0 \rightarrow p_{\max}=0$), the dissipative nature of plasticity as outlined by Vermeer and de Borst 1984.

With the plastic potential function at hand, we can define the Eulerian plastic flow rule in the spectral form as

$$\boldsymbol{d}^p := \dot{\lambda}\,\partial_{\boldsymbol{\tau}}\widehat{\chi} = \dot{\lambda}\sum_{i=1}^{3} d_i^p\,\boldsymbol{n}_i\otimes\boldsymbol{n}_i \quad \text{with} \quad d_i^p := \partial\widehat{\chi}/\partial\tau_i = \widehat{\chi}_{,i}. \tag{5.26}$$

Here, the Eulerian plastic rate of deformation tensor is given in terms of the plastic rate $\dot{\lambda}$ and the direction of plastic flow d_i^p. The evolution of the equivalent plastic strain α as an internal variable is considered in the same manner as in metal plasticity

$$\dot{\alpha} := \sqrt{\tfrac{2}{3}}\,||\boldsymbol{d}^p|| = -\dot{\lambda}\,d_{\hat{\beta}} \quad \text{with} \quad d_{\hat{\beta}} := -\sqrt{\tfrac{2}{3}}\sqrt{(\widehat{\chi}_{,1}^2+\widehat{\chi}_{,2}^2+\widehat{\chi}_{,3}^2)}. \tag{5.27}$$

5.3.5. Algorithmic treatment in the spectral space

For compactness the implementation is performed in the spectral space. Therefore, the evolution equation (5.26) must be recast. To this end a backward Euler time integration is used such that the total time is split into finite time increments $[t_n, t_{n+1}]$, where $\tau := t_{n+1}-t_n > 0$ is the time step size. All fields at time t_n are assumed to be known. With the rate equation (5.26) and its Lagrangian counterpart (5.8) at hand we can write

$$-\tfrac{1}{2}\,\overline{(\dot{\boldsymbol{G}^p})^{-1}}\boldsymbol{G}^p = \boldsymbol{F}^{-1}\dot{\lambda}\partial_{\boldsymbol{\tau}}\widehat{\chi}\boldsymbol{F}\ . \tag{5.28}$$

A backward Euler integrator with an exponential shift Miehe 1995; Miehe and Stein 1992; Simo 1992; Weber and Anand 1990 is taken as an approximated solution of (5.28), yielding the Lagrangian update

$$(\boldsymbol{G}^p_{n+1})^{-1} = \exp[\,-2\gamma_{n+1}\boldsymbol{F}^{-1}_{n+1}\partial_{\boldsymbol{\tau}}\widehat{\chi}\boldsymbol{F}_{n+1}\,](\boldsymbol{G}^p_n)^{-1} \quad \text{with} \quad \gamma_{n+1}=\tau\dot{\lambda} \tag{5.29}$$

in terms of the incremental plastic parameter γ_{n+1}. In what follows the subscript $n+1$ will be dropped, so that all quantities without subscript are evaluated at time t_{n+1}.

Using the property $\exp[\boldsymbol{F}^{-1}\boldsymbol{A}\boldsymbol{F}] = \boldsymbol{F}^{-1}\exp[\boldsymbol{A}]\boldsymbol{F}$ of the matrix exponential the Lagrangian update (5.29) can be recast into an Eulerian update of the elastic Finger tensor

$$\boldsymbol{b}^e = \exp[-2\gamma\partial_{\boldsymbol{\tau}}\widehat{\chi}]\boldsymbol{b}^{e,tr} \quad \text{with} \quad \boldsymbol{b}^{e,tr} := \boldsymbol{F}(\boldsymbol{G}^p_n)^{-1}\boldsymbol{F}^T\ , \tag{5.30}$$

where $\boldsymbol{b}^{e,tr}$ is the elastic trial Finger tensor. Since $\boldsymbol{\tau}$ and $\boldsymbol{b}^e$ commute for the underlying *isotropic elastic* material law and $\partial_{\boldsymbol{\tau}}\widehat{\chi}$ commutes with $\boldsymbol{b}^e$ for the underlying *isotropic plastic* material law, $\boldsymbol{b}^{e,tr}$ also commutes with $\boldsymbol{b}^e$, see (5.30). Taking then the logarithm of (5.30) yields the additive update of the elastic Eulerian logarithmic Hencky tensor defined in (5.13)

$$\boldsymbol{h}^e = \boldsymbol{h}^{e,tr} - \gamma\partial_{\boldsymbol{\tau}}\widehat{\chi} \quad \text{with} \quad \boldsymbol{h}^{e,tr} := \tfrac{1}{2}\ln[\boldsymbol{b}^{e,tr}] \,. \tag{5.31}$$

Note that this update is similar to a small-strain update of the geometric linear theory. Transforming the update into the spectral space of the trial elastic Finger tensor $\boldsymbol{b}^{e,tr}$, the Lagrangian flow rule (5.29) is reduced to the update of the logarithmic principal elastic strains

$$\varepsilon_i^e = \varepsilon_i^{e,tr} - \gamma\widehat{\chi}_{,i} \quad \text{with} \quad \partial_{\boldsymbol{\tau}}\widehat{\chi} = \textstyle\sum_{i=1}^{3}\widehat{\chi}_{,i}\boldsymbol{n}_i \otimes \boldsymbol{n}_i \,. \tag{5.32}$$

Here we assume that the trial strains $\varepsilon_i^{e,tr} = \ln[\lambda_i^{e,tr}]$ and the eigenvectors $\{\boldsymbol{n}_i^{tr}\}_{i=1,2,3}$ can be obtained from the eigenvalue problem $[\boldsymbol{b}^{e,tr} - (\lambda_i^{e,tr})^2\boldsymbol{1}]\boldsymbol{n}_i^{tr} = \boldsymbol{0}$ and are thus known.

The flow rule (5.27) can be integrated in a straightforward way. We define a generalized residual vector for updating the local internal variables of the plastic strain and the equivalent plastic strain as

$$\begin{aligned} r_i &:= \varepsilon_i^e - \varepsilon_i^{e,tr} + \gamma\widehat{\chi}_{,i}(\tau_1,\tau_2,\tau_3,\widehat{\beta}) = 0, \\ r_{\widehat{\beta}} &:= \alpha - \alpha^{tr} + \gamma d_{\widehat{\beta}}(\tau_1,\tau_2,\tau_3,\widehat{\beta}) = 0, \\ r_{\widehat{\Phi}} &:= \widehat{\Phi}(\tau_1,\tau_2,\tau_3,\widehat{\beta}) - \tfrac{2\tilde{\eta}}{3\tau}\gamma = 0, \end{aligned}$$

where we introduced in $(5.33)_3$ the *plastic viscosity* $\tilde{\eta}$ in order to arrive at a better numerical performance.

Equations (5.33) are solved by a local return mapping scheme, in line with the recent work Miehe et al. 2016b. The two Boxes 5.1 and 5.2 summarize this local solution scheme. Box 5.1 defines the trial state and the final stress state by a spectral representation. The actual return mapping scheme with the update of stress and tangent moduli are shown in Box 5.2. Note carefully that the use of a non associative plasticity formulation leads to non-symmetric consistent moduli, see Box 5.2, point 4.

5.3.6. Balance and evolution equations of the multi-field problem

In this section the local form of the balance and evolution equations for the multi-field approach to phase-field modeling of ductile fracture of soils is given.

Mechanical equilibrium. The balance of linear momentum in quasi-static form reads

$$\text{Div}\,\boldsymbol{P} + \bar{\boldsymbol{\gamma}}_0 = \boldsymbol{0}, \tag{5.33}$$

where $\bar{\boldsymbol{\gamma}}_0$ denotes a given body force per unit volume of the reference configuration. The argument of the referential divergence operator "Div" is the first Piola-Kirchhoff stress $\boldsymbol{P}$, obtained from the energy storage function (5.10) by

$$\boldsymbol{P} = \partial_{\boldsymbol{F}}\widehat{\Psi} = \boldsymbol{\tau}\boldsymbol{F}^{-T} \quad \text{with} \quad \boldsymbol{\tau} = \partial_{\boldsymbol{h}^e}\widehat{\Psi}. \tag{5.34}$$

1. *Get trial states.* $\boldsymbol{F}$ and $\{\boldsymbol{G}_n^p, \alpha_n\}$ are given. Get trial value of Eulerian elastic Finger tensor $\boldsymbol{b}^{e,tr} := \boldsymbol{F}(\boldsymbol{G}_n^p)^{-1}\boldsymbol{F}^T$, do spectral decomposition $\boldsymbol{b}^{e,tr} = \sum_{i=1}^3 (\lambda_i^{e,tr})^2 \boldsymbol{n}_i^{tr} \otimes \boldsymbol{n}_i^{tr}$, compute trial logarithmic principal strains $\varepsilon_i^{e,tr} := \ln[\lambda_i^{e,tr}]$.

2. *Constitutive material response.* Compute elastic strains ε_i^e, principal stresses τ_i and algorithmic moduli $\mathbb{E}_{ij}^{ep}$ in spectral space, see Box 5.2.

3. *Get strain, stress and tangent.* Get current elastic principal stretches $\lambda_i^e = \exp[\varepsilon_i^e]$, update Lagrangian plastic metric $\boldsymbol{G}^p = (\boldsymbol{F}^{-1}[\sum_{i=1}^3 (\lambda_i^e)^2 \boldsymbol{n}_i^{tr} \otimes \boldsymbol{n}_i^{tr}]\boldsymbol{F}^{-T})^{-1}$, get Kirchhoff stresses and algorithmic tangent moduli

$$
\begin{aligned}
\boldsymbol{\tau} &= \textstyle\sum_{i=1}^3 \tau_i \boldsymbol{n}_i^{tr} \otimes \boldsymbol{n}_i^{tr} \\
\mathbb{E} &= \textstyle\sum_{i=1}^3 \sum_{j=1}^3 [\, \mathbb{E}_{ij}^{ep} - 2\tau_i \delta_{ij} \,] \, \boldsymbol{n}_i^{tr} \otimes \boldsymbol{n}_i^{tr} \otimes \boldsymbol{n}_j^{tr} \otimes \boldsymbol{n}_j^{tr} \\
&\quad + \textstyle\sum_{i=1}^3 \sum_{j \neq i}^3 \frac{\tau_i (\lambda_j^{e,tr})^2 - \tau_j (\lambda_i^{e,tr})^2}{(\lambda_i^{e,tr})^2 - (\lambda_j^{e,tr})^2} \boldsymbol{n}_i^{tr} \otimes \boldsymbol{n}_j^{tr} \otimes \boldsymbol{n}_i^{tr} \otimes \boldsymbol{n}_j^{tr}
\end{aligned}
$$

and compute nominal stresses and elastic-plastic tangent moduli

$$
\boldsymbol{P} = \boldsymbol{\tau}\boldsymbol{F}^{-T} \quad \text{and} \quad \boldsymbol{\mathcal{A}} = \{\, \mathbb{E} + \boldsymbol{1} \odot \boldsymbol{\tau} \,\} \overset{2}{\circ} \boldsymbol{F}^{-T} \overset{4}{\circ} \boldsymbol{F}^{-T}
$$

$$
\boldsymbol{A} \odot \boldsymbol{B} \to \textstyle\sum_{i,j,k,l=1}^3 \boldsymbol{A}_{ik} \boldsymbol{B}_{jl} \boldsymbol{e}_i \otimes \boldsymbol{e}_j \otimes \boldsymbol{e}_k \otimes \boldsymbol{e}_l \qquad \mathbb{A} \overset{2}{\circ} \boldsymbol{B} \to \textstyle\sum_{i,j,k,l,m=1}^3 \mathbb{A}_{imkl} \boldsymbol{B}_{mj} \boldsymbol{e}_i \otimes \boldsymbol{e}_j \otimes \boldsymbol{e}_k \otimes \boldsymbol{e}_l
$$

$$
\mathbb{A} \overset{4}{\circ} \boldsymbol{B} \to \textstyle\sum_{i,j,k,l,m=1}^3 \mathbb{A}_{ijkm} \boldsymbol{B}_{ml} \boldsymbol{e}_i \otimes \boldsymbol{e}_j \otimes \boldsymbol{e}_k \otimes \boldsymbol{e}_l
$$

Box 5.1: Stress update scheme for plasticity. For more details see Miehe 1998b.

1. Set initial values $\varepsilon_i^e = \varepsilon_i^{e,tr}$ for $i = 1...3$, $\alpha = \alpha_n$ and $\gamma = 0$.

2. Get derivatives of energy-storage function, yield function and plastic potential

$$\widehat{\Psi}(\varepsilon_1^e, \varepsilon_2^e, \varepsilon_3^e, \alpha; d) \qquad \boldsymbol{s} = \begin{bmatrix} \widehat{\Psi}_{,i} \\ \widehat{\Psi}_{,\alpha} \end{bmatrix} \quad \mathbb{E} = \begin{bmatrix} \widehat{\Psi}_{,ij} & \widehat{\Psi}_{,i\alpha} \\ \widehat{\Psi}_{,\alpha j} & \widehat{\Psi}_{,\alpha\alpha} \end{bmatrix}$$

$$\widehat{\Phi}(\tau_1, \tau_2, \tau_3, \widehat{\beta}) \qquad \boldsymbol{n} = \begin{bmatrix} \widehat{\Phi}_{,i} \\ \widehat{\Phi}_{,\widehat{\beta}} \end{bmatrix}$$

$$\widehat{\chi}(\tau_1, \tau_2, \tau_3, \widehat{\beta}) \qquad \boldsymbol{v} = \begin{bmatrix} \widehat{\chi}_{,i} \\ d_{\tilde{\beta}} \end{bmatrix} \quad \mathbb{F} = \begin{bmatrix} \widehat{\chi}_{,ij} & \widehat{\chi}_{,i\widehat{\beta}} \\ d_{\tilde{\beta},j} & d_{\tilde{\beta},\widehat{\beta}} \end{bmatrix}$$

3. Check for yielding. If yielding do a local Newton iteration

if $\widehat{\Phi} < 0$ **then** `// elastic step`
- set $\tau_i = \widehat{\Psi}_{,i}$ and $\mathbb{E}_{ij}^{ep} = \widehat{\Psi}_{,ij}$
- **return**

else `// plastic step`
- **compute** residual vector
  - $\boldsymbol{r} := \left[(\varepsilon_i^e - \varepsilon_i^{e,tr});\ (\alpha - \alpha^{tr})\right]^T + \gamma\, \boldsymbol{v}$
- **check** if local Newton is converged
  - if $[\ \sqrt{\boldsymbol{r}^T\boldsymbol{r} + \ [\widehat{\Phi} - \frac{2\tilde{\eta}}{3\tau}\gamma]^2} < tol\ ]$ go to **4.**
- **compute** incremental plastic parameter
  - $\Delta\gamma = \frac{1}{C}[\ \widehat{\Phi} - \boldsymbol{n}^T\mathbb{X}\,\boldsymbol{r}\ ]$ with $C := \boldsymbol{n}^T\mathbb{X}\,\boldsymbol{v}$ and $\mathbb{X} := [\ \mathbb{E}^{-1} + \gamma\mathbb{F}\ ]^{-1}$
- **compute** incremental strains and hardening variable
  - $[\Delta\varepsilon_i^e;\ \Delta\alpha]^T = -\mathbb{E}^{-1}\mathbb{X}\ [\ \boldsymbol{r} + \Delta\gamma\, \boldsymbol{n}\ ]$
- **update** elastic/plastic quantities
  - $\varepsilon_i^e \Leftarrow \varepsilon_i^e + \Delta\varepsilon_i^e;\ \ \alpha \Leftarrow \alpha + \Delta\alpha,\ \ \gamma \Leftarrow \gamma + \Delta\gamma$
- go to **2**.

4. For plastic step: Obtain stresses and consistent moduli in eigenvalue space

$$\tau_i = \widehat{\Psi}_{,i} \quad \text{and} \quad \mathbb{E}_{ij}^{ep} = \mathbb{X}_{ij} \ - \ \frac{1}{C}\,[\,\mathbb{X}_{ik}\widehat{\chi}_{,k} + \mathbb{X}_{i\widehat{\beta}}d_{\tilde{\beta}}\,] \otimes [\,\widehat{\Phi}_{,l}\mathbb{X}_{lj} + \widehat{\Phi}_{,\widehat{\beta}}\mathbb{X}_{\widehat{\beta}j}\,]$$

Box 5.2: Return mapping and tangent moduli in spectral space. For more details see Miehe 1998b.

The Eulerian Kirchhoff stress $\boldsymbol{\tau}$ follows from the general return algorithm in Box 5.2. It is related to the effective Kirchhoff stress $\widetilde{\boldsymbol{\tau}}$ dual to the elastic Eulerian Hencky strain $\boldsymbol{h}^e$ by

$$\boldsymbol{\tau} = g(d)\,\widetilde{\boldsymbol{\tau}} \quad \text{with} \quad \widetilde{\boldsymbol{\tau}} := \lambda\,\mathrm{tr}\boldsymbol{h}^e\,\boldsymbol{1} + 2\mu\,\boldsymbol{h}^e. \tag{5.35}$$

Evolution of the fracture phase field. Recalling the definition of the crack driving force (5.4), the phase-field evolution (5.5) and the constitutive state (5.9), we can define the crack driving state function $D(\text{state}(\boldsymbol{X}), s)$ for ductile failure in frictional material as

$$\eta\dot{d} = (1-d)\mathcal{H} - (d - l^2\Delta d) \quad \text{with} \quad \mathcal{H} = \max_{s\in[0,t]} \underbrace{\zeta \left\langle \frac{\psi^e + \psi^p}{\psi_c} - 1 \right\rangle_+}_{:=D(\text{state}(\boldsymbol{X},s))}, \tag{5.36}$$

in terms of the critical fracture energy per unit volume ψ_c, a fracture parameter ζ controlling the post-critical range after crack initialization and the ramp function $\langle x\rangle_+ := (x + |x|)/2$. For the rate-independent case ($\eta \to 0$) the evolution equation reads

$$0 = (1-d)\mathcal{H} - (d - l^2\Delta d)\ . \tag{5.37}$$

The representation of the evolution equation $(5.36)_1$ is obtained from a generalized Ginzburg–Landau- or Allen–Cahn-type equation, see Miehe et al. 2010a and its extension to ductile fracture Miehe et al. 2015a. From $(5.36)_2$ it can be seen that the crack is driven by the effective elastic and plastic energy densities. These functions do not depend on d.

The crack driving state function D in $(5.36)_2$ does not differentiate between tension and compression. In order to enforce crack evolution only under tension, we modify the crack driving state function according to Miehe et al. 2010b as

$$D = \zeta \left\langle \frac{\psi^e_+ + \psi^p}{\psi_c} - 1 \right\rangle_+ \quad \text{with} \quad \psi^e_+(\boldsymbol{h}^e) := \frac{\lambda}{2}\langle \mathrm{tr}[\boldsymbol{h}^e]\rangle^2_+ + \mu\,\mathrm{tr}[(\boldsymbol{h}^e_+)^2] \tag{5.38}$$

where the brittle contribution accounts only for the tensile elastic energy ψ^e_+. Here, $\boldsymbol{h}^e_+ := \sum_{i=1}^3 \langle\varepsilon^e_i\rangle_+\ \boldsymbol{n}_i \otimes \boldsymbol{n}_i$ is the positive elastic Hencky tensor defined by a spectral decomposition. For more details on the split of the elastic energy density we refer to Miehe et al. 2016b, 2010b.

Due to the biconvexity of the above governing equations a "one-pass" staggered scheme based on incrementally decoupled updates of the phase field d and the deformation map $\boldsymbol{\varphi}$ is used in order to solve the equations, see Miehe et al. 2015a, 2010a.

5.4. Choice of finite element formulation

This section discusses the finite-element formulation employed for the numerical discretization of the above governing equations. Our goal is to arrive at a stable and robust implementation free of locking. Associated phenomena are well-known in computational plasticity and lead in general to stiffing of the material response, for example when employing bilinear quadrilateral (Q_1) elements as most native conforming element formulation. As a remedy, a Taylor–Hood or a Mini element formulation with displacement and pressure as degree of freedoms are an often chosen option. However, these formulations are

not well suited due to the degradation of both the volumetric and the deviatoric stresses. A further attractive element formulation is given by the classical enhanced assumed strain element (EAS) Simo and Armero 1992; Simo and Rifai 1990; Wilson et al. 1973. Such formulation however shows hourglass modes under compressive loading and is thus not well-suited for the scenarios to be analyzed in the present context. We therefore implement a *modified* enhanced assumed strain element formulation given by the *consistent gradient* (CG) formulation advocated by Glaser and Armero 1997; Korelc et al. 2010; Korelc and Wriggers 1996. This very convenient element formulation overcomes hourglass modes and will be sketched briefly in this section.

5.4.1. Basic considerations of an enhanced strain formulation

A starting point to derive the governing equations of a *modified* EAS element is a three-field Hu–Washizu-type potential of an arbitrary non-linear elasticity model with a given constitutive free-energy function $\widehat{\Psi}(\boldsymbol{F})$. Without external loading the potential reads

$$\Pi(\boldsymbol{u},\boldsymbol{H},\boldsymbol{P}) = \int_{\mathcal{B}_0} [\widehat{\Psi}(\boldsymbol{F}) + \boldsymbol{P}\cdot(\nabla\boldsymbol{u}-\boldsymbol{H})]\,\mathrm{d}V \quad \text{with} \quad \boldsymbol{F} := \boldsymbol{1}+\boldsymbol{H}. \tag{5.39}$$

The variation of $\Pi(\boldsymbol{u},\boldsymbol{H},\boldsymbol{P})$ with respect to the independent variables yields the Euler equations

$$\begin{aligned} \operatorname{Div}\boldsymbol{P} &= \boldsymbol{0} \text{in } \mathcal{B}_0,\\ \nabla\boldsymbol{u}-\boldsymbol{H} &= \boldsymbol{0} \text{in } \mathcal{B}_0,\\ -\boldsymbol{P}+\partial_{\boldsymbol{F}}\widehat{\Psi} &= \boldsymbol{0} \text{in } \mathcal{B}_0, \end{aligned}$$

where boundary terms are ignored. Accordingly, we identify $\boldsymbol{H}$ as the displacement gradient $\nabla\boldsymbol{u}$ and $\boldsymbol{P}$ as the first Piola-Kirchhoff stress. Using a reparameterization of the displacement gradient $\boldsymbol{H}$ yields the *enhanced* deformation gradient $\boldsymbol{F}$

$$\boldsymbol{F} := \boldsymbol{1}+\boldsymbol{H} = \boldsymbol{1}+\nabla\boldsymbol{u}+\widetilde{\boldsymbol{H}} \quad \text{with} \quad \boldsymbol{H} = \nabla\boldsymbol{u}+\widetilde{\boldsymbol{H}}, \tag{5.40}$$

where $\widetilde{\boldsymbol{H}}$ is the *enhanced displacement gradient*. The variation of a modified three-field potential $\widetilde{\Pi}(\boldsymbol{u},\nabla\boldsymbol{u}+\widetilde{\boldsymbol{H}},\boldsymbol{P})$ then yields the Euler equations

$$\begin{aligned} \operatorname{Div}\boldsymbol{P} &= \boldsymbol{0} \text{in } \mathcal{B}_0,\\ \widetilde{\boldsymbol{H}} &= \boldsymbol{0} \text{in } \mathcal{B}_0,\\ -\boldsymbol{P}+\partial_{\boldsymbol{F}}\widehat{\Psi} &= \boldsymbol{0} \text{in } \mathcal{B}_0, \end{aligned}$$

where again boundary terms are ignored. From $(5.41)_2$ we observe that in a continuous setting the enhanced displacement gradient $\widetilde{\boldsymbol{H}}$ vanishes in $\mathcal{B}_0$. This is also referred to as orthogonality condition. However, in a *discrete setting* this will lead to an improved representation of the deformation gradient as defined in (5.40). Based on these considerations, a spatial discretization with an approximation of the enhanced displacement gradient $\widetilde{\boldsymbol{H}}$ by an interpolation of local parameters is performed. Furthermore, static condensation of the local parameters is employed, which leads to the final representation of the residual vector and the stiffness matrix.

Based on the above framework, the crucial steps to arrive at a *consistent gradient formulation* according to Glaser and Armero 1997; Korelc et al. 2010; Korelc and Wriggers 1996 are i) the spatial discretization and ii) the interpolation of the local parameters. Therefore, we focus on these two steps in the subsequent sections.

5.4.2. Spatial discretization and interpolation

Based on above considerations and the introduction of the triangulation of the domain $\mathcal{B}_0$ into n_{nel} elements $\mathcal{B}_0^e$ such that

$$\mathcal{B}_0 \approx \bigcup_{e=1}^{n_{\text{el}}} \mathcal{B}_0^e, \tag{5.41}$$

the deformation gradient at $\boldsymbol{X} \in \mathcal{B}_0^e$ can be approximated by

$$\boldsymbol{F}(\boldsymbol{X}) \approx \boldsymbol{F}^h(\boldsymbol{\xi}) = \boldsymbol{1} + \underbrace{\sum_{I=1}^{n_{\text{node}}} \boldsymbol{d}_I \otimes \nabla_{\boldsymbol{X}} N^I(\boldsymbol{\xi})}_{\boldsymbol{H}^h \text{ (compatible)}} + \underbrace{\sum_{I=1}^{n_{\text{enh}}} \boldsymbol{\alpha}_I \otimes \boldsymbol{G}^I(\boldsymbol{\xi})}_{\widetilde{\boldsymbol{H}}^h \text{ (enhanced)}}. \tag{5.42}$$

Here we introduced $\boldsymbol{\xi} \in \square$ as the coordinates in the isoparametric space and $\boldsymbol{d}_I$ as the vector of the nodal degrees of freedom at the node I. Second order Lagrange shape functions are chosen as nodal basis functions $N^I(\boldsymbol{\xi})$. Note that the computation of $\boldsymbol{H}^h$ involves the inverse of the Jacobian matrix $\boldsymbol{J}$ of the mapping $\boldsymbol{\xi} \in \square \to \boldsymbol{X} \in \mathcal{B}_0^e$. The vectors of the local parameters α_I^i are denoted as $\boldsymbol{\alpha}_I$ with $\boldsymbol{\alpha}_I = [\alpha_I^1, ..., \alpha_I^{n_{\text{dim}}}]^T$ and the vector of the interpolation functions for the enhanced modes is indicated as $\boldsymbol{G}^I(\boldsymbol{\xi})$. For the choice of $n_{\text{enh}} = n_{\text{dim}}$, this results in the classical EAS element with four enhanced modes in the two-dimensional case and nine enhanced modes in the three-dimensional case (Wilson et al. 1973). We will address the interpolation of the enhanced displacement gradient $\widetilde{\boldsymbol{H}}$ in more detail in the next subsection.

Interpolation of the enhanced part of the deformation gradient. For a simpler representation we introduce some abbreviations associated with the Jacobian $\boldsymbol{J}$ as

$$j(\boldsymbol{\xi}) := \det \boldsymbol{J}(\boldsymbol{\xi}), \quad j_0 := \det \boldsymbol{J}_0 \quad \text{with} \quad \boldsymbol{J}_0 := \boldsymbol{J}(\boldsymbol{\xi} = \boldsymbol{0}). \tag{5.43}$$

Based on that, the interpolation functions in $\boldsymbol{G}^I$ are defined in terms of the derivatives of the basis functions $\widetilde{N}^I$ of the enhanced modes

$$[\boldsymbol{G}^1, ..., \boldsymbol{G}^{n_{\text{enh}}}] := \frac{j_0}{j(\boldsymbol{\xi})} \boldsymbol{J}_0^{-T} \boldsymbol{E}(\boldsymbol{\xi}) \quad \text{with} \quad \boldsymbol{E}(\boldsymbol{\xi}) = [\partial_{\boldsymbol{\xi}} \widetilde{N}^1, ..., \partial_{\boldsymbol{\xi}} \widetilde{N}^{n_{\text{enh}}}]. \tag{5.44}$$

The formulation of the original EAS element uses the basis function of the incompatible mode element by Wilson et al. 1973, i.e. $\widetilde{N}^I = \frac{1}{2}(\xi_I^2 - 1)$. With equation (5.44) the term of the *enhanced displacement gradient* $\widetilde{\boldsymbol{H}}$ in (5.42) can be recast in a tensor product form as

$$\widetilde{\boldsymbol{H}}^h(\boldsymbol{\xi}) = \sum_{I=1}^{n_{\text{enh}}} \boldsymbol{\alpha}_I \otimes \boldsymbol{G}^I(\boldsymbol{\xi}) = \frac{j_0}{j(\boldsymbol{\xi})} \underbrace{\boldsymbol{E}(\boldsymbol{\xi}) \widetilde{\boldsymbol{\alpha}}}_{=: \boldsymbol{M}(\boldsymbol{\xi})} \boldsymbol{J}_0^{-1} \quad \text{with} \quad \widetilde{\boldsymbol{\alpha}} := [\boldsymbol{\alpha}_I, ..., \boldsymbol{\alpha}_{n_{\text{enh}}}]. \tag{5.45}$$

Modified interpolation for hourglass stabilization. In the *consistent gradient formulation* according to Glaser and Armero 1997; Korelc et al. 2010; Korelc and Wriggers

1996 the tensor $\boldsymbol{M}(\boldsymbol{\xi})$ is *modified* in order to overcome hourglass modes. The modified tensor is given as

$$\boldsymbol{M}_{\mathrm{CG}}(\boldsymbol{\xi}) := \boldsymbol{M}(\boldsymbol{\xi})^T = \widetilde{\boldsymbol{\alpha}}^T \boldsymbol{E}(\boldsymbol{\xi})^T. \tag{5.46}$$

We note that the representation of the interpolation of local parameters in (5.44) and (5.45) are based on an objective tensor transformation assuming a one-to-one relation of $\boldsymbol{M}(\boldsymbol{\xi})$ and $\boldsymbol{E}(\boldsymbol{\xi})$ with the gradient of the basis functions of the incompatible modes $\partial_{\boldsymbol{\xi}} \widetilde{N}^I$. This is the case when using the enhanced modes and interpolation from Wilson et al. 1973. However, since in the *consistent gradient formulation* the matrix $\boldsymbol{M}(\boldsymbol{\xi})$ of interpolation is modified, a full tensor transformation has to be used as follows

$$\widetilde{\boldsymbol{H}}^h(\boldsymbol{\xi}) = \frac{j_0}{j(\boldsymbol{\xi})} [\boldsymbol{J}(\boldsymbol{\xi})]^{-T} \boldsymbol{M}(\boldsymbol{\xi}) [\boldsymbol{J}(\boldsymbol{\xi})]^{-1}. \tag{5.47}$$

5.5. Representative numerical examples

We now demonstrate the features of the proposed framework by means of some representative numerical examples. The first example considers an element benchmark problem and shows the performance of the presented consistent-gradient (CG) element. In the second example a soil specimen under compressive loading is considered. Thereby the consequences of the non-associative plasticity are investigated by a parameter study of the angle of dilatancy θ. The third example deals with the pullout behavior of an anchor plate and shows the influence of the presented different hardening mechanisms and the friction angle ϕ.

5.5.1. Performance of the CG element

In the following benchmark test, we will show that the CG element is a convenient choice for the targeted applications in the present work. The geometry of the problem is given by a two-dimensional square-shaped column with dimensions $W = 0.1$ m and $H = 0.3$ m as depicted in Figure 5.7a. At its bottom edge, the column is completely fixed and at its top edge an increasing displacement $\bar{u}$ in negative vertical direction is prescribed such that the column is compressed. Here a load increment of $\Delta\bar{u} = 5 \cdot 10^{-3}$ mm is taken. In the center of the column the parameter defining the slope of the yield surface M_ϕ is reduced by 5% as an initial imperfection to induce the formation of a plastic shear band. The amplitude of this imperfection is sufficiently small so that it does not affect the overall structural response. The geometric setup and boundary conditions are shown in Figure 5.7a. The simulation is performed under plain-strain conditions.

Lamé parameter	$\lambda = 117.0$	MN/m^2	friction, dilatancy	$M_{\phi;\chi} = 0.98$	–
Lamé parameter	$\mu = 80.0$	MN/m^2	position of peak	$p_{\max} = 0.2$	MN/m^2
hardening modulus	$h = 0.0$	MN/m^2	perturbation	$q_1 = 1.0$	N/m^2
saturated yield shift	$\tau_y = 37.0$	MN/m^2	hardening switch	$q_2 = \exp(\sqrt{3/8}\,\frac{q_1}{\kappa})$	–
saturation	$\omega = 2.0$	–	transition zone	$q_3 = 0.5\kappa^{-1}$	m^2/MN

Table 5.3: Parameters for the benchmark problem of the CG element.

In the numerical analysis, we are focusing on locking phenomena induced by the plastic deformation. No fracturing will take place yet. The material parameters are given in Table 5.3. The simulations are performed with bilinear quadrilateral (Q_1), quadratic triangular (P_2), EAS and CG elements. For the test with the Q_1, EAS and CG element formulations the domain was discretized by 893 elements, while 1110 elements were used for the P_2 formulation. In Figure 5.7b the distribution of the hydrostatic pressure in the domain and the corresponding load-deflection curves are shown for the four tested element formulations.

From the load-deflection curves it can be seen that the Q_1 formulation results in an overstiff response. This is also reflected by the deformation of the domain, where no buckling is observed. The P_2 formulation yields a softer response but the hydrostatic pressure is oscillating within the domain. The EAS formulation also shows a softer response than the Q_1 element but hourglass modes are observed as illustrated in the zoom of the bottom edge in Figure 5.7b. As can be seen from Figure 5.7b, the CG formulation gives a reasonable load deflection response and also a convenient hydrostatic pressure distribution. Based on these observations, we conclude that the CG formulation satisfies the demands of the presented model. It will be used in the following simulations.

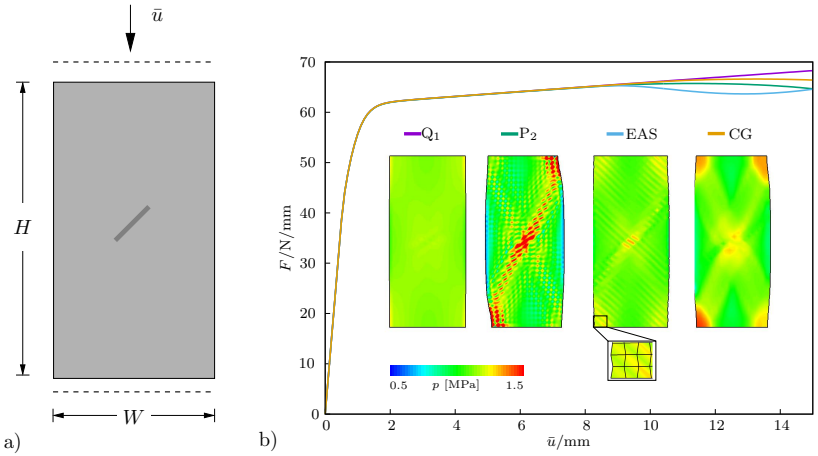

Figure 5.7: Results of the benchmark test: Geometry and boundary conditions in a). The area with the reduced material parameter M_ϕ is shown in dark gray. b) The load-deflection curves and the distributions of the hydrostatic pressure within the domain for the four tested element formulations.

5.5.2. Shear band formation in soil specimen

In the present test, we consider a similar geometry and loading as in the previous benchmark test. The dimensions of the specimen are again given as $W = 0.1$ m, $H = 0.3$ m, see Figure 5.8a. The specimen is discretized with 19,844 quadrilateral elements with an

effective element size of $h_e = 1.25$ mm. Due to the used "one-pass" staggered solution scheme, the solution during the fracture process may depend on the load increment $\Delta\bar{u}$. Therefore, the load increment is chosen based on a convergence study. The chosen load increment ($\Delta\bar{u} = 5 \cdot 10^{-3}$ mm) seems to be small enough to capture the fracture behavior correctly. The corresponding load deflection curves for this study are shown in Figure 5.8b.

Lamé parameter	$\lambda = 117.0$	MN/m^2	friction	$M_\phi = 0.98$	–
Lamé parameter	$\mu = 80.0$	MN/m^2	dilatancy I	$M_\chi^I = 0.97$	–
hardening modulus	$h = 0.035$	MN/m^2	dilatancy II	$M_\chi^{II} = 0.8$	–
saturated yield shift	$\tau_y = 0.5$	MN/m^2	dilatancy III	$M_\chi^{III} = 0.7$	–
saturation	$\omega = 0.1$	–	position of peak	$p_{\max} = 0.2$	MN/m^2
length scale	$l = 2.5$	mm	perturbation	$q_1 = 1.0$	N/m^2
crit. fracture energy	$\psi_c = 0.07$	MN/m^2	hardening switch	$q_2 = \exp(\sqrt{3/8}\frac{q_1}{\kappa})$	–
fracture parameter	$\zeta = 1.0$	–	transition zone	$q_3 = 0.5\kappa^{-1}$	m^2/MN

Table 5.4: Parameters employed in the simulation of the shear-band formation in a soil specimen.

The simulation is run with three different angles of dilatancy θ relating to the material parameter $M_\chi = 6\sin\theta/(3 \pm \sin\theta)$. The remaining material parameters are given in Table 5.4. Figure 5.9 shows the corresponding load-deflection curves. In Figure 5.10 the fracture phase field is visualized for two different deflection states and the three different M_χ. Figure 5.11 shows the evolution of the equivalent plastic strain α depending on M_χ. In the first test we deal with an almost associative plasticity formulation ($M_\chi^I = 0.97 \approx M_\phi$). In the remaining two tests ($M_\chi^{II} = 0.8$, $M_\chi^{III} = 0.7$) the angle of dilatancy θ differs more from the angle of friction ϕ, hence corresponding to more pronounced non-associative formulations.

The consequence of the non-associative character of the plasticity formulation is now investigated by examining the load-deflection curves in Figure 5.9. Comparing the force at a displacement of about 2 mm, where plastic yielding occurs, we observe that the maximum force sustained by the specimen decreases with M_χ. This means that non-associative plasticity goes along with a softer response of the material. By increasing the load the plastic deformation grows until the onset of fracture at a total top displacement of about 19 mm. This finally leads to a complete rupture of the solid.

Taking a closer look at the developed fracture phase field in Figure 5.10a-c for a top displacement of $\bar{u} = \bar{u}_1 = 19.24$ mm one observes the most pronounced crack for M_χ^I. Under the same applied displacement M_χ^{II} shows the smallest crack. At a displacement $\bar{u} = \bar{u}_2 = 20.88$ mm the state of final rupture is reached for all samples, see 5.10d–f. Note that the final crack path is influenced by M_χ.

We now take a closer look at the evolution of the equivalent plastic strain α and the fracture phase field d for the three different M_χ. Figure 5.11 shows four states of deformation identified as "localization of plasticity" (Figures 5.11a,e,i), "onset of fracture" (Figures 5.11b,f,j), "fracture propagation" (Figure 5.11c,g,k) and "final rupture" (Figure 5.11d,h,l). All four states are plotted for the three given M_χ. In Figure 5.11a–d one can see the evolution of plastic strain α and the fracture phase field d for $M_\chi^I = 0.97$, in

Figure 5.11e–h for $M_\chi^{II} = 0.8$ and in Figure 5.11i–l for $M_\chi^{III} = 0.7$.

The distribution of the equivalent plastic strain α at the localization of plasticity (Figure 5.11a,e,i) is similar for M_χ^I and M_χ^{II}, but for M_χ^{III} the plasticity is more concentrated in the center of the specimen.

At the onset of fracture (Figures 5.11b,f,j) a more diffuse distribution of the equivalent plastic strain α with M_χ^I is present. For M_χ^{II} the upper part of the specimen tends to slide to the left side (Figure 5.11f). This effect becomes even more clear at the next state shown in Figures 5.11c,g,k. There we notice that for M_χ^I the specimen *buckles over the full height*, for M_χ^{II} the upper part slides to the left, and for M_χ^{III} the specimen *buckles at about 2/3 of the height*. These deformation modes can also be observed in the last state showing the final rupture (Figure 5.11d,h,l). Note that a lower M_χ goes along with a sharper shear band and also a sharper crack interface.

5.5.3. Pullout behaviour of anchor plate in soil

As final numerical example, we consider the pullout behavior of an anchor plate in a soil specimen. The specimen is given in terms of a rectangular domain with dimensions of $H = 1$ m $L = 1.75$ m that contains a prescribed notch in its center. The left and right edge of the specimen are fixed in the horizontal direction. The bottom edge of the specimen is fixed completely. The anchor plate is loaded by a prescribed Dirichlet boundary condition $\bar{u}$ pointing in upward direction. Due to the used "one-pass" staggered solution scheme, the solution may depend on the load increment $\Delta\bar{u}$. Therefore, the load increment is chosen based on a convergence study. The chosen load increment ($\Delta\bar{u} = 6.25 \cdot 10^{-5}$ mm) seems to be small enough to capture the fracture behavior correctly. The corresponding load deflection curves for this study are shown in Figure 5.12b.

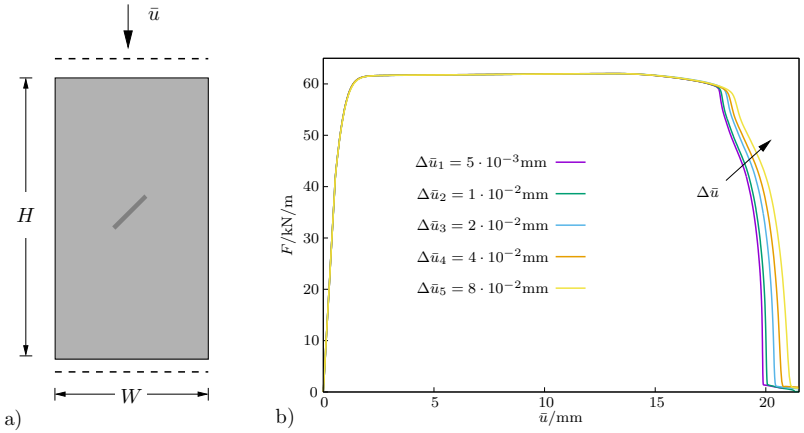

Figure 5.8: Shear band formation in soil specimen: Geometry and boundary condition in a). The area with the reduced material parameter M_ϕ is shown in dark gray. Corresponding load deflection curves for different load increments $\Delta\bar{u}$ are shown in b).

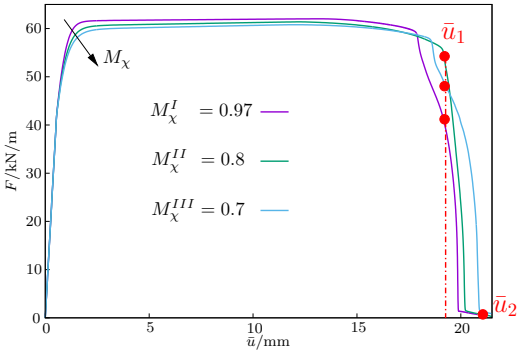

Figure 5.9: Shear band formation in soil specimen: Corresponding load deflection curves for different M_χ.

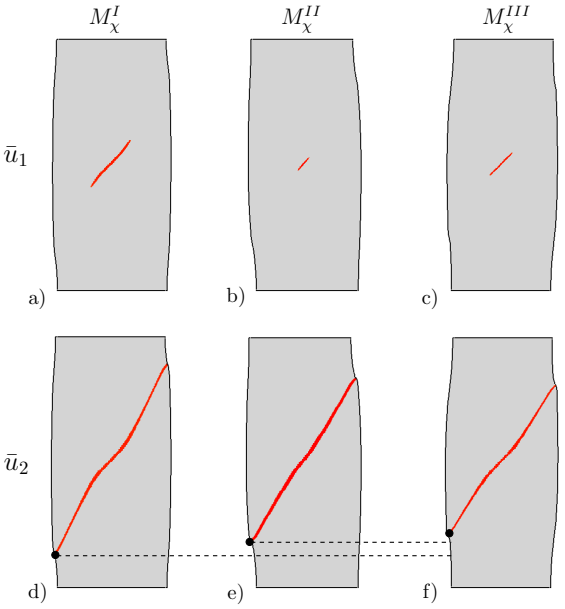

Figure 5.10: Shear band formation in soil specimen: Fracture phase-field for the three tested M_χ at two different displacements $\bar{u}_1$ and $\bar{u}_2$ (compare Figure 5.9). Areas with $d \approx 1$ are colored in red.

In order to allow for a straightforward detachment of the anchor plate from the below solid, we prescribe Dirichlet boundary conditions of the fracture phase field $d = 1$ for

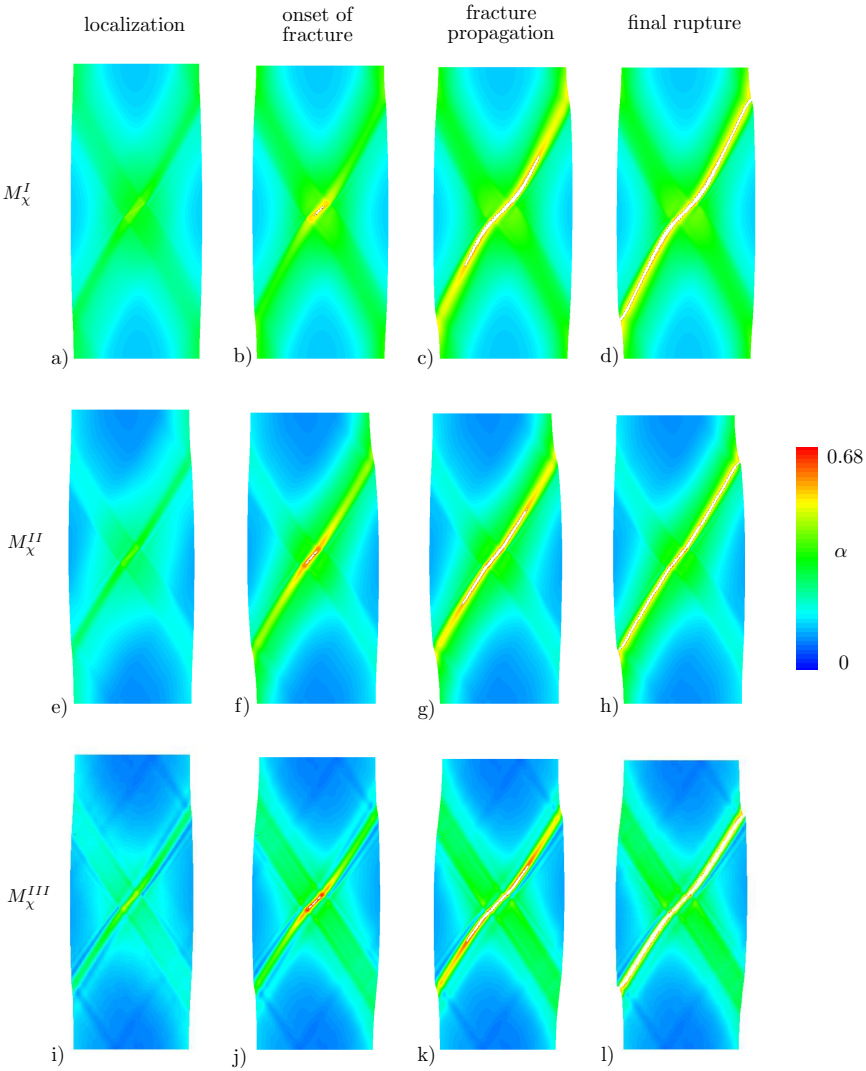

Figure 5.11: Shear band formation in soil specimen: Evolution of the equivalent plastic strain α where regions with a crack phase field $d \approx 1$ are not plotted for three different angles of dilatancy θ, respectively M_χ. From the localization of plasticity until final rupture in (a–d) for M_χ^I, in (e–h) for M_χ^{II} and in (i–l) for M_χ^{III}.

all nodes within some notched region directly below the plate. This guarantees that the anchor plate does not adhere to the soil matrix underneath it. The prescribed notch

Lamé parameter	$\lambda = 86.0$	MN/m^2	friction I/II	$M_\phi^{I;II} = 0.98;1.2$	–
Lamé parameter	$\mu = 58.0$	MN/m^2	dilatancy	$M_\chi = 0.7$	–
hardening modulus	$h = 0.0$	MN/m^2	position of peak	$p_{\max} = 1.6$	kN/m^2
saturated yield shift	$\tau_y = 6.0$	MN/m^2	perturbation	$q_1 = 1.0$	kN/m^2
saturation	$\omega = 1.0$	–	hardening switch I	$q_2^I = 0.0$	–
length scale	$l = 2.4$	cm	hardening switch II	$q_2^{II} = \exp(\sqrt{3/8}\frac{q_1}{\kappa})$	–
crit. fracture energy	$\psi_c = 10.0$	N/m^2	hardening switch III	$q_2^{III} = 0.5 q_2^{II}$	–
fracture parameter	$\zeta = 30.0$	–	transition zone	$q_3 = 0.5\kappa^{-1}$	m^2/MN

Table 5.5: Material parameters for pullout behaviour of an anchor plate in soil.

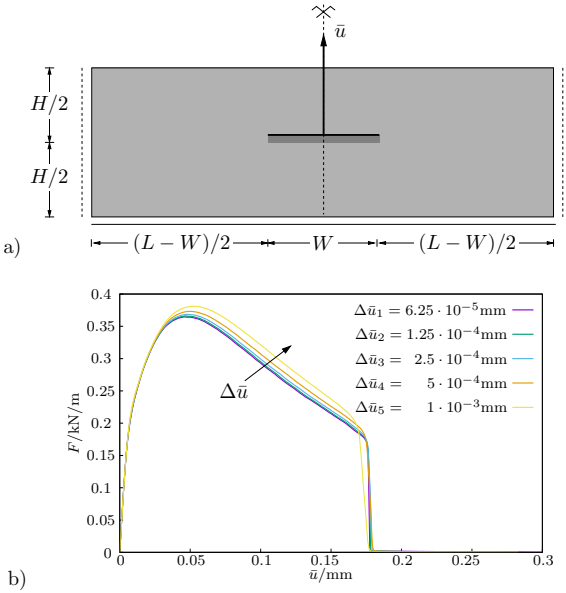

Figure 5.12: Pullout behavior of an anchor plate: a) Geometry and boundary conditions. The dark area indicates the prescribed notch. Corresponding load deflection curves for different load increments $\Delta\bar{u}$ are shown in b).

has the width $W = 0.4$ m and the height of one element $h_e = 1.2$ cm. Geometry and boundary conditions of the complete setting are visualized in Figure 5.12a. Due to the symmetry of both loading and geometry we discretize only one half of the specimen with 22,474 quadrilateral elements.

Our goal in the present simulation is to analyze the influence of the different hardening mechanisms (*cohesion, friction and mixed-type hardening*) in combination with the friction angle ϕ relating to the material parameter $M_\phi = 6\sin\phi/(3 \pm \sin\phi)$. We consider three different parameters q_2 defining either cohesion, friction or mixed-type hardening together with two different parameters M_ϕ defining the slope of the Drucker-Prager cone. The

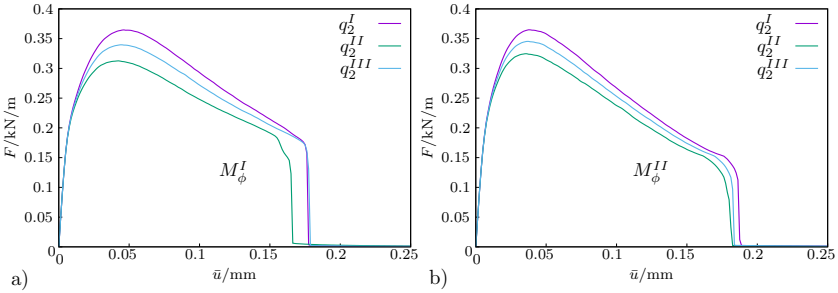

Figure 5.13: Pullout behavior of an anchor plate: The corresponding load deflection curves for the test with three different parameters q_2 and two different slopes M_ϕ^I in a) and M_ϕ^{II} b).

material parameters are given in Table 5.5.

Starting point of our investigations on the influence of different hardening mechanisms are the load-deflection curves, see Figure 5.13a and b. Here we took the load and the displacement of the nodes that represent the anchor plate. There, it can be observed that cohesion hardening ($q_2^I = 0$) leads to the stiffest material response for a given parameter M_ϕ. The softest response is associated with pure friction hardening ($q_2^{II} = \exp(\sqrt{3/8} q_1 \kappa^{-1})$. The mixed-type hardening ($q_2^{III} = 0.5\, q_2^{II}$) leads to an intermediate response. In the areas of the domain with a positive hydrostatic pressure the stress state is close to the peak of the yield surface, hence making it a big difference for the plastic yielding whether the peak moves due to hardening or not. Finally, this gives with cohesion hardening (peak moves, see (5.22)) the stiffest response.

The evolution of the hydrostatic pressure p and the equivalent plastic strain α are pictured in Figure 5.14. Taking a look at the evolution of hydrostatic pressure p shown in Figures 5.14a–c, we notice tensile stresses near the corners of the anchor at the beginning of the deformation (Figure 5.14a). The crack starts to initiate in that area. Furthermore, zones with compressive stresses are observed above the anchor, see Figure 5.14b. The crack propagates from the corners of the anchor plate to the boundaries of the domain with an angle of about 16° directed towards the upper edge. After a certain crack length, the crack kinks and develops a more direct path to the upper edge, as can be seen in Figure 5.14c. In the fully ruptured state, the compressive zones almost vanish. The evolution of the equivalent plastic strain α in Figures 5.14d–f indicates that the fracture follows the plastic deformation. Here the arrows show the direction of the displacement.

In Figure 5.15 the crack path and the distribution of the equivalent plastic strain α for the tested hardening mechanisms are depicted. As can be seen, the hardening mechanism has an influence on the crack path. Although the angle of the crack path stays the same, the kink of the crack path occurs closer to the anchor plate in case of friction hardening. As a result the point where the crack reaches the upper edge differs for the tested cases.

Finally, Figure 5.16 shows the crack path and the distribution of the equivalent plastic strain α for the tested slopes M_ϕ of the Drucker-Prager cone. Considering the influence of the slope of the Drucker-Prager cone M_ϕ, a higher slope results in a higher maximum force and a delayed final rupture, see Figure 5.13a and b. By comparing the crack paths for a

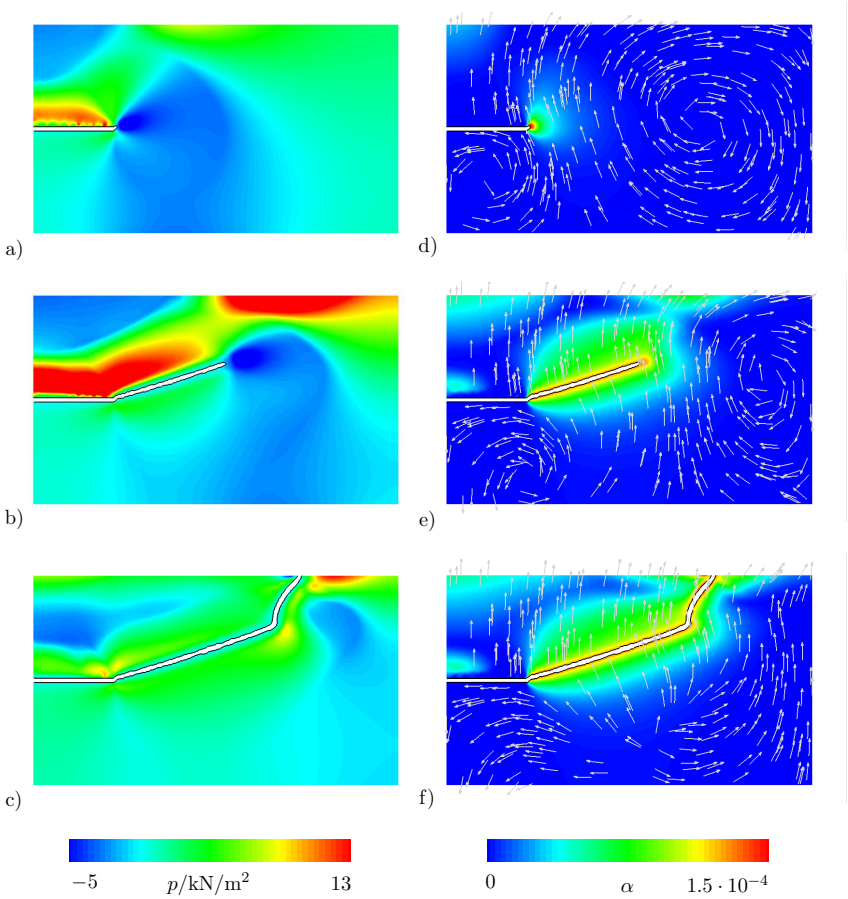

Figure 5.14: Pullout behavior of an anchor plate with M_ϕ^I and q_2^I (cohesion hardening): Evolution of the hydrostatic pressure $p = -\frac{1}{3}\operatorname{tr}\boldsymbol{\tau}$ in (a–c) and the evolution of the equivalent plastic strain α in (d–f) where the arrows indicate the direction of the displacement. Regions with a crack phase field $d \approx 1$ are not plotted.

chosen parameter q_2 and the tested slopes M_ϕ of the Drucker-Prager cone, an increasing slope M_ϕ yields a horizontally moved kinking point (Figure 5.16). This behavior is quite similar to the influence of the parameter q_2 on the crack path. The tested $M_\phi = 1.2$ leads to a crack path that ends almost at the top left and right corner of the specimen.

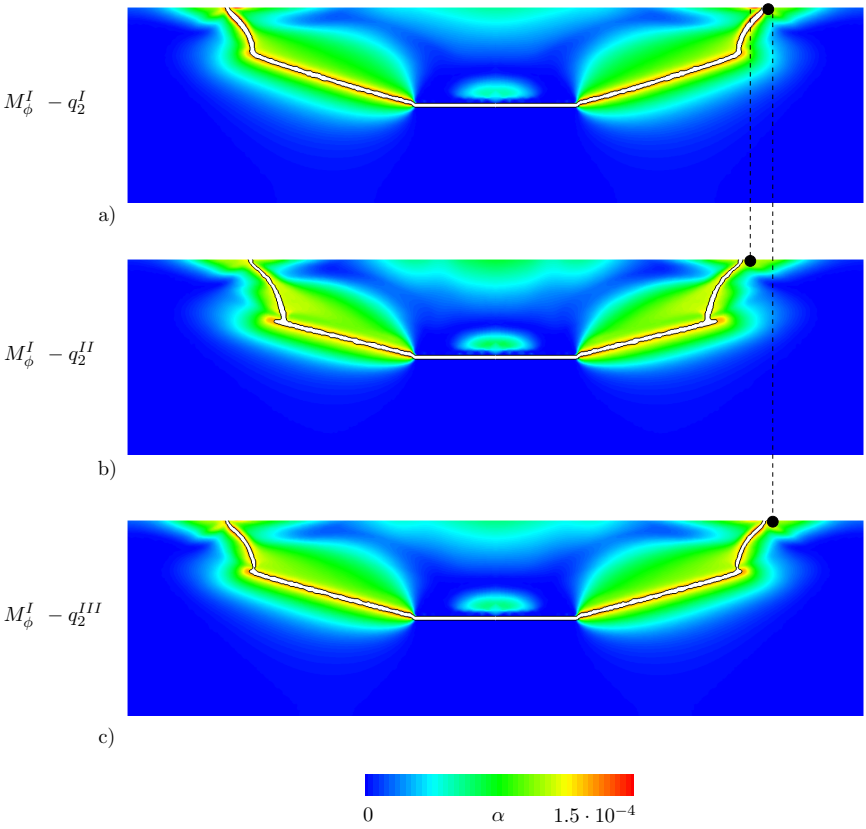

Figure 5.15: Pullout behavior of an anchor plate: Distribution of the equivalent plastic strain α at the final ruptured state with cohesion hardening in a), friction hardening in b) and mixed-type hardening in c). The black dot indicates the fracture tip. Regions with a crack phase field $d \approx 1$ are not plotted.

5.6. Conclusion

A phase-field model of ductile fracture in frictional materials based on the Drucker–Prager plasticity formulation was introduced within the present work. The proposed framework was formulated in a finite-strain setting where the material functions were formulated in the Eulerian space. The presented Drucker–Prager-type yield criterion has two key features. The first key feature is the regularization of the peak of the Drucker–Prager cone yielding a smooth and differentiable formulation which was implemented in a robust numerical procedure. The second key feature is the formulated isotropic hardening

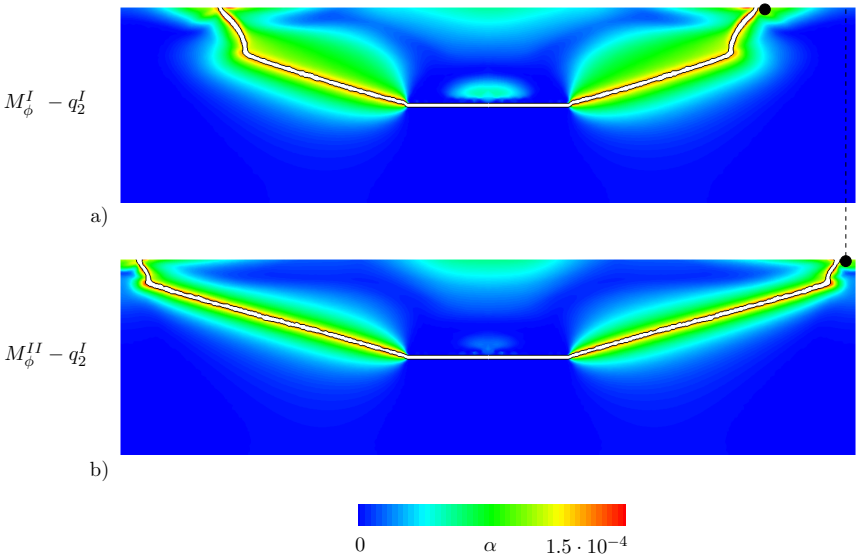

Figure 5.16: Pullout behavior of an anchor plate: Distribution of the equivalent plastic strain α at the final ruptured state with cohesion hardening and two different parameters M_ϕ in a)-b). The black dot indicates the fracture tip. Regions with a crack phase field $d \approx 1$ are not plotted.

mechanism representing both *cohesion and friction hardening*. The elastic-plastic material model was linked to a phase-field model for fracture by a failure criterion based on the elastic-plastic energy density to describe crack initiation and propagation in frictional materials undergoing large elastic-plastic deformations. The numerical treatment was formulated in the principal stress-strain space using a general return algorithm for the plastic flow. Furthermore, a consistent-gradient finite-element formulation was used to guarantee locking- and hourglassing-free material response. Finally, the capabilities of the proposed framework and the consequences of the incorporated hardening mechanisms were shown by means of representative numerical examples considering the shear band formation in a soil column and the pullout behavior of an anchor plate in a soil specimen.

Acknowledgments. M.-A.K. and D.K. gratefully acknowledge the financial support of the German Research Foundation (DFG) in the framework of SFB 1313 (Project B01) and within the Cluster of Excellence in *Simulation Technology* (EXC 310) at the University of Stuttgart. F.A. gratefully acknowledges support by the DFG within project WR 19/58-1.

We further note that the formulation proposed in the present work was numerically implemented into existing code structures designed by Christian Miehe. These code structures are available to the authors from earlier joint works on large-strain elasto-plasticity and fracture (e.g. Miehe et al. 2016b). This applies in particular to the long-standing and tested algorithms summarized in Box 1 and 2 originating from the contribution Miehe

1998b. These algorithms served as algorithmic basis for the numerical implementation of the constitutive model documented in the present work.

Bibliography

Abbo, A. J. and S. W. Sloan (1995). "A smooth hyperbolic approximation to the Mohr-Coulomb yield criterion". In: *Computers & Structures* 54.3, pp. 427–441.

Aldakheel, F., P. Wriggers, and C. Miehe (2017). "A modified Gurson-type plasticity model at finite strains: formulation, numerical analysis and phase-field coupling". In: *Computational Mechanics*, pp. 1–19.

Alessi, R., J.-J. Marigo, C. Maurini, and S. Vidoli (2018a). "Coupling damage and plasticity for a phase-field regularisation of brittle, cohesive and ductile fracture: One-dimensional examples". In: *International Journal of Mechanical Sciences* 149, pp. 559–576.

Alessi, R., S. Vidoli, and L. de Lorenzis (2018b). "A phenomenological approach to fatigue with a variational phase-field model: The one-dimensional case". In: *Engineering fracture mechanics* 190, pp. 53–73.

Ambati, M., T. Gerasimov, and L. de Lorenzis (2015). "Phase-field modeling of ductile fracture". In: *Computational Mechanics* 55, pp. 1017–1040.

Ambati, M., R. Kruse, and L. de Lorenzis (2016). "A phase-field model for ductile fracture at finite strains and its experimental verification". In: *Computational Mechanics* 57.1, pp. 149–167.

Amor, H., J.-J. Marigo, and C. Maurini (2009). "Regularized formulation of the variational brittle fracture with unilateral contact: Numerical experiments". In: *Journal of the Mechanics and Physics of Solids* 57, pp. 1209–1229.

Borden, M. J., T. J. R. Hughes, C. M. Landis, A. Anvari, and I. J. Lee (2016). "A phase-field formulation for fracture in ductile materials: Finite deformation balance law derivation, plastic degradation, and stress triaxiality effects". In: *Computer Methods in Applied Mechanics and Engineering* 312, pp. 130–166.

Borden, M. J., T. J. R. Hughes, C. M. Landis, and C. V. Verhoosel (2014). "A higher-order phase-field model for brittle fracture: Formulation and analysis within the isogeometric analysis framework". In: *Computer Methods in Applied Mechanics and Engineering* 273, pp. 100–118. ISSN: 0045-7825.

Borden, M. J., C. V. Verhoosel, M. A. Scott, T. J. R. Hughes, and C. M. Landis (2012). "A phase-field description of dynamic brittle fracture". In: *Computer Methods in Applied Mechanics and Engineering* 217-220, pp. 77–95.

Bourdin, B., G. A. Francfort, and J.-J. Marigo (2000). "Numerical experiments in revisited brittle fracture". In: *Journal of the Mechanics and Physics of Solids* 48, pp. 797–826.

Bourdin, B., G. A. Francfort, and J.-J. Marigo (2008). *The Variational Approach to Fracture*. Springer.

Choo, J. and W. Sun (2018). "Coupled phase-field and plasticity modeling of geological materials: From brittle fracture to ductile flow". In: *Computer Methods in Applied Mechanics and Engineering* 330, pp. 1–32.

de Boer, R. (1988). "On plastic deformation of soils". In: *International Journal of Plasticity* 4.4, pp. 371–391.

Desai, C. S. (1980). "A general basis for yield, failure and potential functions in plasticity". In: *International Journal for Numerical and Analytical Methods in Geomechanics* 4.4, pp. 361–375.

Drucker, D. C. and W. Prager (1952). "Soil mechanics and plastic analysis or limit design". In: *Quarterly of applied mathematics* 10.2, pp. 157–165.

Duda, F. P., A. Ciarbonetti, P. J. Sánchez, and A. E. Huespe (2015). "A phase-field/gradient damage model for brittle fracture in elastic-plastic solids". In: *International Journal of Plasticity* 65, pp. 269–296.

Ehlers, W. (1995). "A single-surface yield function for geomaterials". In: *Archive of Applied Mechanics* 65.4, pp. 246–259.

Ehlers, W. and C. Luo (2017). "A phase-field approach embedded in the Theory of Porous Media for the description of dynamic hydraulic fracturing". In: *Computer Methods in Applied Mechanics and Engineering* 315, pp. 348–368.

Francfort, G. A. and J.-J. Marigo (1998). "Revisiting brittle fracture as an energy minimization problem". In: *Journal of the Mechanics and Physics of Solids* 46, pp. 1319–1342.

Glaser, S. and F. Armero (1997). "On the formulation of enhanced strain finite elements in finite deformations". In: *Engineering computations* 14, pp. 759–791.

Griffith, A. A. (1921). "The phenomena of rupture and flow in solids". In: *Philosophical transactions of the royal society of london. Series A, containing papers of a mathematical or physical character*, pp. 163–198.

Gültekin, O., H. Dal, and G. Holzapfel (2016). "A phase-field approach to model fracture of arterial walls: Theory and finite element analysis". In: *Computer Methods in Applied Mechanics and Engineering* 312, pp. 542–566.

Heider, Y. and B. Markert (2017). "A phase-field modeling approach of hydraulic fracture in saturated porous media". In: *Mechanics Research Communications* 80, pp. 38–46.

Hjiaj, M., J. Fortin, and G. de Saxce (2003). "A complete stress update algorithm for the non-associated Drucker-Prager model including treatment of the apex". In: *International Journal of Engineering Science* 41.10, pp. 1109–1143.

Irwin, G. R. (1958). "Fracture". In: *Encyclopedia of Physics*. Ed. by S. Flügge. Vol. 6, Elasticity and Plasticity. Springer, pp. 551–590.

Korelc, J., S. Ursa, and P. Wriggers (Sept. 2010). "An improved EAS brick element for finite deformation". In: *Computational Mechanics* 46.4, pp. 641–659.

Korelc, J. and P. Wriggers (1996). "Consistent gradient formulation for a stable enhanced strain method for large deformations". In: *Engineering Computations* 13.1, pp. 103–123.

Kröner, E. (1958). "Kontinuumstheorie der Versetzungen und Eigenspannungen". In: *Ergebnisse der angewandten Mathematik*. Ed. by L. Collatz and F. Lösch. Vol. 5, Springer.

Kuhn, C. and R. Müller (2010). "A continuum phase field model for fracture". In: *Engineering Fracture Machanics* 77, pp. 3625–3634.

Lade, P. V. and M. K. Kim (1988). "Single hardening constitutive model for frictional materials II. Yield critirion and plastic work contours". In: *Computers and geotechnics* 6.1, pp. 13–29.

Lade, P. V. and M. K. Kim (1995). "Single hardening constitutive model for soil, rock and concrete". In: *International Journal of Solids and Structures* 32.14, pp. 1963–1978.

Lambrecht, M. and C. Miehe (1999). "Two non-associated isotropic elastoplastic hardening models for frictional materials". In: *Acta Mechanica* 135, pp. 73–90.

Lambrecht, M. and C. Miehe (2001). "A note on formulas for localized failure of frictional materials in compression and biaxial loading modes". In: *International Journal for Numerical and Analytical Methods in Geomechanics* 25, pp. 955–971.

Lee, E. H. (1969). "Elastic-plastic deformation at finite strains". In: *Journal of Applied Mechanics, ASME* 36, pp. 1–6.

Loret, B. and J. H. Prevost (1986). "Accurate numerical solutions for drucker-prager elastic-plastic models". In: *Computer Methods in Applied Mechanics and Engineering* 54.3, pp. 259–277.

Mandel J. (1972). *Plasticité clasique et viscoplasticité,* CISM Courses and Lectures No.97. Springer.

Miehe, C. (1995). "A theory of large-strain isotropic thermoplasticity based on metric transformation tensors". In: *Archive of Applied Mechanics* 66, pp. 45–64.

Miehe, C. (1998a). "A constitutive frame of elastoplasticity at large strains based on the notion of a plastic metric". In: *International Journal of Solids and Structures* 35, pp. 3859–3897.

Miehe, C. (1998b). "A formulation of finite elastoplasticity based on dual co- and contravariant eigenvector triads normalized with respect to a plastic metric". In: *Computer Methods in Applied Mechanics and Engineering* 159, pp. 223–260.

Miehe, C., F. Aldakheel, and A. Raina (2016a). "Phase Field Modeling of Ductile Fracture at Finite Strains. A Variational Gradient-Extended Plasticity-Damage Theory". In: *International Journal of Plasticity* in press.

Miehe, C., M. Hofacker, L.-M. Schänzel, and F. Aldakheel (2015a). "Phase Field Modeling of Fracture in Multi-Physics Problems. Part II. Brittle-to-Ductile Failure Mode Transition and Crack Propagation in Thermo-Elastic-Plastic Solids". In: *Computer Methods in Applied Mechanics and Engineering* 294, pp. 486–522.

Miehe, C., M. Hofacker, and F. Welschinger (2010a). "A phase field model for rate-independent crack propagation: Robust algorithmic implementation based on operator splits". In: *Computer Methods in Applied Mechanics and Engineering* 199, pp. 2765–2778.

Miehe, C., D. Kienle, F. Aldakheel, and S. Teichtmeister (2016b). "Phase field modeling of fracture in porous plasticity: A variational gradient-extended Eulerian framework for the macroscopic analysis of ductile failure". In: *Computer Methods in Applied Mechanics and Engineering* 312, pp. 3–50.

Miehe, C., S. Mauthe, and S. Teichtmeister (2015b). "Minimization principles for the coupled problem of Darcy-Biot-type fluid transport in porous media linked to phase field modeling of fracture". In: *Journal of the Mechanics and Physics of Solids* 82, pp. 186–217.

Miehe, C. and L. Schänzel (2014). "Phase field modeling of fracture in rubbery polymers. Part I: Finite elasticity coupled with brittle failure". In: *Journal of the Mechanics and Physics of Solids* 65, pp. 93–113.

Miehe, C. and E. Stein (1992). "A canonical model of multiplicative elasto-plasticity. Formulation and aspects of the numerical implementation". In: *European Journal of Mechanics A/Solids* 11, pp. 25–43.

Miehe, C., S. Teichtmeister, and F. Aldakheel (2016c). "Phase-Field Modeling of Ductile Fracture: A Variational Gradient-Extended Plasticity-Damage Theory and its Micromorphic Regularization". In: *Philisophical Transactions of the Royal Society A* 374.

Miehe, C., F. Welschinger, and M. Hofacker (2010b). "Thermodynamically consistent phase-field models of fracture: Variational principles and multi-field FE implementations". In: *International Journal for Numerical Methods in Engineering* 83, pp. 1273–1311.

Mikelić, A., M. F. Wheeler, and T. Wick (2015). "A Phase-Field Method for Propagating Fluid-Filled Fractures Coupled to a Surrounding Porous Medium". In: *SIAM Multiscale Modeling Simulation* 13.1, pp. 367–398.

Pham, K., H. Amor, J.-J. Marigo, and C. Maurini (2011). "Gradient damage models and their use to approximate brittle fracture". In: *International Journal of Damage Mechanics* 20.4, pp. 618–652.

Pham, K., K. Ravi-Chandar, and C. Landis (2017). "Experimental validation of a phase-field model for fracture". In: *International Journal of Fracture* 205.1, pp. 83–101.

Raina, A. and C. Miehe (2016). "A phase-field model for fracture in biological tissues". In: *Biomechanics and Modeling in Mechanobiology* 15, pp. 479–496.

Reinoso, J., M. Paggi, and C. Linder (2017). "Phase field modeling of brittle fracture for enhanced assumed strain shells at large deformations: formulation and finite element implementation". In: *Computational Mechanics* 59.6, pp. 981–1001.

Simo, J. C. (1992). "Algorithms for static and dynamic multiplicative plasticity that preserve the classical return mapping schemes of the infinitesimal theory". In: *Computer Methods in Applied Mechanics and Engineering* 99.

Simo, J. C. and F. Armero (1992). "Geometrically nonlinear enhanced strain mixed methods and the method of incompatible modes". In: *International Journal for Numerical Methods in Engineering* 33, pp. 1413–1449.

Simo, J. C. and G. Meschke (1993). "A new class of algorithms for classical plasticity extended to finite strains. Application to geomaterials". In: *Computational Mechanics* 11.4, pp. 253–278.

Simo, J. C. and M. S. Rifai (1990). "A class of mixed assumed strain methods and the method of incompatible modes". In: *International Journal for Numerical Methods in Engineering* 29, pp. 1595–1638.

Simo, J. and C. Miehe (1992). "Associative coupled thermoplasticity at finite strains: formulation, numerical analysis and implementation". In: *Computer Methods in Applied Mechanics and Engineering* 98.1, pp. 41–104.

Teichtmeister, S., D. Kienle, F. Aldakheel, and M.-A. Keip (2017). "Phase field modeling of fracture in anisotropic brittle solids". In: *International Journal of Non-Linear Mechanics* 97, pp. 1–21.

Verhoosel, C. V. and R. de Borst (2013). "A phase-field model for cohesive fracture". In: *International Journal for Numerical Methods in Engineering* 96, pp. 43–62. ISSN: 1097-0207.

Vermeer, P. and R. de Borst (1984). "Non-associated plasticity for soils, concrete and rock". In: *Heron* 29.3, pp. 1–64.

Weber, G. and L. Anand (1990). "Finite deformation constitutive equations and a time integration procedure for isotropic, hyperelastic-viscoplastic solids". In: *Computer Methods in Applied Mechanics and Engineering* 79, pp. 173–202.

Wilson, E. L., R. L. Taylor, W. P. Doherty, and J. Ghaboussi (1973). "Incompatible displacement models". In: *Numerical and Computer Methods in Structural Mechanics*. Ed. by S. J. Fenves. Academic Press, New York, pp. 43–57.

Wilson, Z. A. and C. M. Landis (2016). "Phase-Field Modeling of Hydraulic Fracture". In: *ICES Report* 16-10.

Zienkiewicz, O. C., C. Humpheson, and R. W. Lewis (1975). "Associated and non-associated visco-plasticity and plasticity in soil mechanics". In: *Geotechnique* 25.4, pp. 671–689.

Zreid, I. and M. Kaliske (2016). "An implicit gradient formulation for microplane Drucker-Prager plasticity". In: *International Journal of Plasticity* 83, pp. 252–272.

Chapter 6

A variational minimization formulation for hydraulically induced fracturing in elastic-plastic solids

Daniel Kienle* & Marc-André Keip

Institute of Applied Mechanics

Department of Civil and Environmental Engineering

University of Stuttgart

Abstract

A variational modeling framework for hydraulically induced fracturing of elastic-plastic solids is developed in the present work. The developed variational structure provides a global minimization problem. While fracture propagation is modeled by means of a phase-field approach to fracture, plastic effects are take into account by using a Drucker–Prager-type yield-criterion function. This yield-criterion function governs the plastic evolution of the fluid-solid mixture. Fluid storage and transport are described by a Darcy–Biot-type formulation. Thereby the fluid storage is decomposed into a contribution due to the elastic deformations and one due to the plastic deformations. A local return mapping scheme is used for the update of the plastic quantities. The global minimization structure demands a $H(\mathrm{div})$-conforming finite-element formulation. Furthermore this is combined with an enhanced-assumed-strain formulation in order to overcome locking phenomena arising from the plastic deformations. The robustness and capabilities of the presented framework will be shown in a sequence of numerical examples.

Keywords: Variational principles, porous media, ductile fracture, phase-field modeling.

*Corresponding author.
E-mail address: kienle@mechbau.uni-stuttgart.de

6.1. Introduction

One of the main applications for a model of hydraulically induced fractures can be found in the recently utilized oil-production technique called fracking. During this process a highly pressurized fluid is injected into a perforated bore hole. The goal is to induce fractures in layers of the earth's crust that store large amounts of oil and gas. The fractures are created to increase the fluid permeability of the present soil or rock, therewith leading to a higher flow of gas and oil into the bore hole where it is collected. The main criticisms of this technique are related to the inducement of fractures that could lead to environmental issues such as seismic activities or contamination of drinking water. Therefore, in recent years various attempts have been made to better capture and understand the underlying physical processes, for example the development of models that can be used in numerical simulations. The idea is that an accurate and robust model can help in forecasting both risks and the potential of such a technique. To be successful, such a model has to capture three distinct mechanisms: first, it has to describe the mechanical deformation of the present porous medium (which could be soil or rock); second, it has to describe the fluid transport throughout the intact and fractured porous medium; third, the model needs to be capable of describing fracture initiation and propagation, for example being driven by fluid pressure.

To embed the present work into the literature, we comment on recent development in the field. For the modeling of hydraulic fracturing, it is of substantial importance to describe the mechanical deformation of the underlying porous media. Powerful techniques in this direction are given on the one hand by model formulations within the context of the so-called Theory of Porous Media, see de Boer 2000, Ehlers 2002 and Bluhm and de Boer 1997. An alternative approach that is suitable for the description of fully saturated porous media with one fluid phase is formulated in the seminal works of Terzaghi 1925 and Biot 1941. Associated models reside in the area of the Biot theory of consolidation, see Detournay and Cheng 1993 and Bear 1972 for a general overview.

When it comes to the modeling of fluid flow within a porous medium, it is often made use of the law of Darcy 1856. Darcy's law provides a phenomenological approach to the modeling of fluid flux that is driven by gradients of fluid pressure or, more precisely, by gradients of the chemical potential. Darcy's law is often referred to as a macroscopic approach since it describes the fluid flow through the porous medium's pore scale in an averaged or homogenized sense. Fluid flow within fractures, i.e. regions without solid content, could directly be modeled based on the Navier–Stokes-equation. Associated simplifications can be based on the lubrication theory and lead to so-called Poiseuille-type flow models. While the first approach is often used in combination with models related to the Theory of Porous Media, the latter one can nicely be embedded in formulations that relate to Biot's theory of consolidation.

Since the present work aims at the description of fracturing processes in porous media, we briefly refer to some related literature. Fundamental concepts for the description of fracture were proposed by Griffith 1921 and Irwin 1958. These works provide energy-based fracture criteria for brittle materials and build the theoretical basis for the recently developed phase-field models of fracturing. With regard to the latter we highlight the contributions of Francfort and Marigo 1998, Bourdin et al. 2000, 2008, Amor et al. 2009, Kuhn and Müller 2010, Miehe et al. 2010a and Pham et al. 2011b. The phase-field

approach to fracture is extremely versatile and has been extended to the modeling of ductile fracture (Miehe et al. 2016a, 2015a, 2016b,c, Ambati et al. 2015, Borden et al. 2016, Alessi et al. 2018a, Steinke et al. 2020, Yin and Kaliske 2020), anisotropic fracturing (Li et al. 2015, Teichtmeister et al. 2017, Storm et al. 2020) and fatigue fracture (Alessi et al. 2018b, Lo et al. 2019, Schreiber et al. 2020, Carrara et al. 2020), just to name a few.

Next to the above mentioned extensions, the phase-field approach to fracture has also seen pronounced activity in the field of porous media. Here we highlight the contributions of Bourdin et al. 2012, Mikelić et al. 2019, 2015a,b; Mikelić et al. 2015c, Miehe et al. 2015b, Wilson and Landis 2016, Wu and Lorenzis 2016, Mauthe and Miehe 2017, and Cajuhi et al. 2018 that are embedded into Biot's theory of consolidation. We further highlight the recent work Wheeler et al. 2020 on the adaptive and parallel simulation of hydraulically induced fracture propagation as well as the contribution of Teichtmeister et al. 2019 on the numerical treatment of poro-elastic problems with an emphasis on suitable finite-element formulations. Combinations of the Theory of Porous Media with the phase-field approach to fracture have been provided by Ehlers and Luo 2017; Ehlers and Luo 2018; Heider and Markert 2017. Within the phase-field models for hydraulic fracturing Bourdin et al. 2012, Wilson and Landis 2016, Santillán et al. 2017 and Chukwudozie et al. 2019 compared their numerical solutions with analytical solutions obtained by Sneddon and Lowengrub 1969. For a recent monograph on the multiphysics of the phase-field modeling of fracturing we refer to Wick 2020.

Next to phase-field models for facturing of porous media there exist a number of alternative approaches to hydraulic fracturing. Here we explicitly mention the contribution of Adachi et al. 2007 giving a wide overview and discussion of so-called planar hydraulic fracturing models with its root in linear elastic fracture mechanics. Furthermore, Castonguay et al. 2013 treated fracturing in the framework of the boundary element method. The hydraulic fracture model by Damjanac et al. 2010 makes use of the discrete element method. Another established method for the modeling of cracks is given by the extended or generalized finite element method, see Dahi-Taleghani and Olson 2011, Gupta and Duarte 2014, Gordeliy and Peirce 2013a,b and Shauer and Duarte 2019 for applications to porous media.

We note that the above mentioned models all relate to elastic deformations of the material. However, there is experimental evidence that elastic material response alone cannot capture all relevant effects Johnson and Cleary 1991. This serves as a motivation to the develop models that incorporate elastic-plastic deformations. Here we would like to refer to the recent developments of Pise et al. 2019 and Aldakheel et al. 2020. In the given works, the plastic response is incorporated by introducing a Drucker–Prager-type yield criterion function Drucker and Prager 1952. We note that the works Pise et al. 2019, Aldakheel et al. 2020 are not variational and consider a yield-criterion function in terms of the effective stresses. The present work provides an alternative formulation of elastic-plastic hydraulic fracturing in a rigorously variational setting motivated by the ideas of Armero 1999. In the latter work, an additive split of the fluid content into an elastic and a plastic part is suggested, which leads to a constitutive fluid pressure as a function of only elastic quantities. This concept is perfectly suitable for a variational framework that combines the elastic-plastic deformation of the porous medium with the fluid transport on the one hand and the fracture initiation and evolution on the other.

The present work is structured as follows. In Section 6.2 the unknown fields and

associated kinematic relations are introduced. Thereafter, in 6.3, we provide the variational framework and the constitutive functions. Here, we make use of a Darcy–Biot-type formulation for the fluid transport in the porous medium and a Drucker–Prager-type yield-criterion function for plastic flow. This then leads to the set of Euler equations that describe the behavior of a fracturing porous-elastic-plastic solid. The numerical treatment of the problem is based on a time-discrete incremental variational formulation combined with a local return-mapping scheme and discussed in Section 6.4. We showcase the capabilities of the presented numerical framework for hydraulically induced fracturing of porous-elastic-plastic solids by means of some numerical examples to be discussed in Section 6.5. We consider a rigid-footing test as well as two fluid-injection tests in detail. A summary and an outlook will be provided in Section 6.6.

6.2. Independent and primary fields

In the present section we introduce the independent and primary fields of the porous-elastic-plastic fracture model. They account for the elastic-plastic deformation of a body $\mathcal{B}$, for the fluid flux and storage in $\mathcal{B}$ as well as for the fracture initiation and evolution in $\mathcal{B}$. The surface of the body will in the following be denotes as $\partial\mathcal{B}$.

Small-strain kinematics.. The model presented in this work is formulated in the context of the infinitesimal-strain theory. Hence, we consider the displacement field $\boldsymbol{u}(\boldsymbol{x}, t)$ at the material point $\boldsymbol{x} \in \mathcal{B}$ and time t

$$\boldsymbol{u} : \begin{cases} \mathcal{B} \times \mathcal{T} \to \mathcal{R}^3 \\ (\boldsymbol{x}, t) \mapsto \boldsymbol{u}(\boldsymbol{x}, t) \end{cases} \tag{6.1}$$

as independent field. Based on that, we introduce the infinitesimal strain tensor as a primary variable. It cam be computed from the displacement gradient by

$$\boldsymbol{\varepsilon} := \tfrac{1}{2}(\nabla \boldsymbol{u} + \nabla \boldsymbol{u}^T). \tag{6.2}$$

Plastic deformations.. Since we are interested in modeling ductile response of the material, we additively decompose the strain tensor (6.2) into elastic and plastic contributions

$$\boldsymbol{\varepsilon} = \boldsymbol{\varepsilon}^e + \boldsymbol{\varepsilon}^p, \tag{6.3}$$

wherein the plastic strain $\boldsymbol{\varepsilon}^p$ will be treated as a local internal variable. Further, to describe local isotropic hardening, we introduce a local hardening field α formally by

$$\alpha : \begin{cases} \mathcal{B} \times \mathcal{T} \to \mathcal{R} \\ (\boldsymbol{x}, t) \mapsto \alpha(\boldsymbol{x}, t). \end{cases} \tag{6.4}$$

Fluid mass and fluid flux.. The initial density (mass per unit volume) of the fluid-solid mixture is denoted by m_0. It can be computed from the densities of the fluid ρ_f and the solid ρ_s through the given porosity of the mixture φ as

$$m_0 = \rho_f \varphi + \rho_s (1 - \varphi) \quad \text{with} \quad \varphi = \tfrac{V_{\text{pore}}}{V_{\text{pore}} + V_{\text{solid}}}. \tag{6.5}$$

In the above equation, the porosity φ has been obtained from the given pore and solid volume V_{pore} and V_{solid}, respectively. The sum of solid and fluid volume is often denoted as bulk volume V_{bulk}.

Following Biot's approach to thermodynamically open systems, the mass balance in its global and local representation reads (Biot 1984)

$$\frac{\mathrm{d}}{\mathrm{d}t}\int_{\mathcal{B}} m_0 + m \,\mathrm{d}V = -\int_{\partial\mathcal{B}} \mathbb{h}\cdot\boldsymbol{n}\,\mathrm{d}A \qquad \Leftrightarrow \qquad \dot{m} = -\operatorname{div}\mathbb{h} \quad \text{in } \mathcal{B}. \tag{6.6}$$

Here, m denotes the change in the bulk's density, which is caused by fluid flux through the body's surface. Thus, the vector $\mathbb{h}$ given on the right-hand side of (6.6) denotes a fluid-flux vector. Formally, the latter two quantities can be introduced as

$$m : \left\{ \begin{array}{l} \mathcal{B}\times\mathcal{T}\to\mathcal{R} \\ (\boldsymbol{x},t)\mapsto m(\boldsymbol{x},t) \end{array} \right. \quad \text{and} \quad \mathbb{h} : \left\{ \begin{array}{l} \mathcal{B}\times\mathcal{T}\to\mathcal{R}^3 \\ (\boldsymbol{x},t)\mapsto \mathbb{h}(\boldsymbol{x},t). \end{array} \right. \tag{6.7}$$

In what follows we denote m as the change of fluid content. Analogous to the strain tensor, we decompose m into an elastic and a plastic part

$$m = m^e + m^p. \tag{6.8}$$

Here, the plastic contribution m^p describes a change in bulk density that is caused by plastic deformations. It is associated with fluid that is irreversibly squeezed out or soaked in due to plastic deformations.

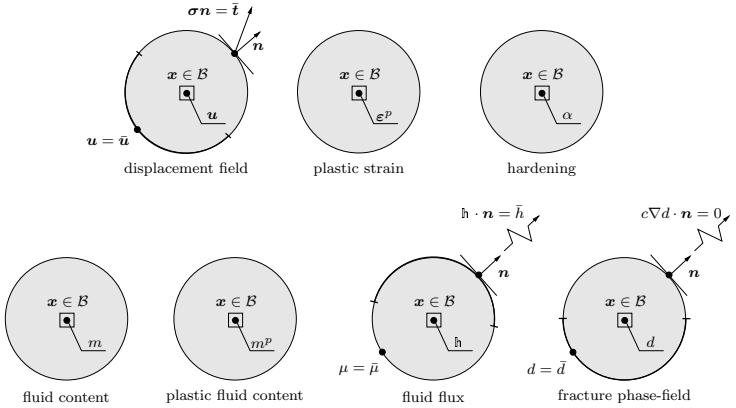

Figure 6.1: The unknown fields for porous-elastic-plastic solids at fracture. The boundary $\partial\mathcal{B}$ is decomposed into Dirichlet and Neumann parts for the *displacement* $\partial\mathcal{B}_{\boldsymbol{u}}\cup\partial\mathcal{B}_{\boldsymbol{t}}$, the *fluid flux* $\partial\mathcal{B}_{\mathbb{h}}\cup\partial\mathcal{B}_{\mu}$ and the *fracture phase-field* $\partial\mathcal{B}_{d}\cup\partial\mathcal{B}_{\mathfrak{t}}$. For the fracture phase-field, zero Neuman boundary conditions are assumed. Here c is a constant depending on the model formulation.

Fracture phase field.. As mentioned above, we will model cracks and their evolution based on the phase-field approach to fracture. The fracture phase field d is thus formally introduced as

$$d : \left\{ \begin{array}{l} \mathcal{B}\times\mathcal{T}\to[0,1] \\ (\boldsymbol{x},t)\mapsto d(\boldsymbol{x},t). \end{array} \right. \tag{6.9}$$

It denotes with $d = 0$ an intact state and with $d = 1$ a broken state of the material. The phase field is used to approximate a sharp crack interface Γ in a diffuse manner. This

results in the definition of a regularized crack surface Γ_l in terms of a crack-surface density γ and a corresponding length-scale parameter l given by

$$\Gamma \approx \Gamma_l(d) := \int_{\mathcal{B}} \gamma(d, \nabla d)\, \mathrm{d}V \quad \text{with} \quad \gamma(d, \nabla d) := \tfrac{1}{2l} d^2 + \tfrac{l}{2} |\nabla d|^2, \tag{6.10}$$

Note that the sharp crack surface is recovered for vanishing length-scale parameter ($l \to 0 \Rightarrow \Gamma_l \to \Gamma$). Here we follow the notation of Miehe et al. 2010b.

To sum up, the primary fields for porous-elastic-plastic solids at fracture and the corresponding Dirichlet and Neumann boundary are depicted in Figure 6.1

6.3. Variational formulation of fracturing porous-elastic-plastic solids

Based on the previous section, we are able to introduce the primary fields for the description of fracturing porous-elastic-plastic solids as

$$\mathfrak{U} := \{\boldsymbol{u}, \mathbb{h}, d, \boldsymbol{\varepsilon}^p, \alpha, m^p\}. \tag{6.11}$$

In order to formulate a rate-type variational principle we define the rate of the primary fields as

$$\dot{\mathfrak{U}} := \{\dot{\boldsymbol{u}}, \dot{\mathbb{h}}, \dot{d}, \dot{\boldsymbol{\varepsilon}}^p, \dot{\alpha}, \dot{m}^p\}. \tag{6.12}$$

Furthermore, we identify the constitutive state of the model and its evolution as

$$\mathfrak{C} := \{\boldsymbol{\varepsilon}, m, \mathbb{h}, d, \nabla d, \boldsymbol{\varepsilon}^p, \alpha, m^p\} \quad \text{and} \quad \dot{\mathfrak{C}} := \{\dot{\boldsymbol{\varepsilon}}, \dot{\mathbb{h}}, \operatorname{div} \dot{\mathbb{h}}, \dot{d}, \dot{\nabla} d, \dot{\boldsymbol{\varepsilon}}^p, \dot{\alpha}, \dot{m}^p\}, \tag{6.13}$$

respectively.

6.3.1. Formulation of the rate-type potential

The general form of the rate-type potential is given by

$$\Pi(\dot{\mathfrak{U}}; \mathfrak{U}) := \frac{\mathrm{d}}{\mathrm{d}t} E(\dot{\mathfrak{C}}; \mathfrak{C}) + D(\dot{\mathfrak{C}}) - P_{\text{ext}}(\dot{\mathfrak{U}}), \tag{6.14}$$

where $\frac{\mathrm{d}}{\mathrm{d}t} E(\dot{\mathfrak{C}}; \mathfrak{C})$ is the rate of the energy, $D(\dot{\mathfrak{C}})$ is the dissipation potential and $P_{\text{ext}}(\dot{\mathfrak{U}})$ is the potential of the external loading. The rate of the energy is described in terms of the energy density $\psi(\mathfrak{C})$

$$\frac{\mathrm{d}}{\mathrm{d}t} E(\dot{\mathfrak{C}}; \mathfrak{C}) = \frac{\mathrm{d}}{\mathrm{d}t} \int_{\mathcal{B}} \psi(\mathfrak{C})\, \mathrm{d}V, \tag{6.15}$$

which, by application of the chain rule yields

$$\frac{\mathrm{d}}{\mathrm{d}t} E(\dot{\mathfrak{C}}; \mathfrak{C}) = \int_{\mathcal{B}} (\partial_{\boldsymbol{\varepsilon}} \psi : \dot{\boldsymbol{\varepsilon}} - \partial_m \psi \operatorname{div} \dot{\mathbb{h}} + \partial_d \psi\ \dot{d} + \partial_{\boldsymbol{\varepsilon}^p} \psi : \dot{\boldsymbol{\varepsilon}}^p + \partial_\alpha \psi\ \dot{\alpha} + \partial_{m^p} \psi\ \dot{m}^p)\, \mathrm{d}V. \tag{6.16}$$

In the latter equation, we made use of the fluid mass balance $(6.6)_2$. Similarly to the rate of energy, the dissipation potential can be expressed in terms of a dissipation potential density $\phi(\dot{\mathfrak{C}})$

$$D(\dot{\mathfrak{C}}) = \int_{\mathcal{B}} \phi(\dot{\mathfrak{C}})\, \mathrm{d}V. \tag{6.17}$$

Combing the right-hand sides of equations (6.16) and (6.17) yields the internal rate-potential density per unit volume

$$\pi(\dot{\mathfrak{C}};\mathfrak{C}) = \partial_{\boldsymbol{\varepsilon}}\psi : \dot{\boldsymbol{\varepsilon}} - \partial_m\psi \operatorname{div}\mathbb{h} + \partial_d\psi\ \dot{d} + \partial_{\boldsymbol{\varepsilon}^p}\psi : \dot{\boldsymbol{\varepsilon}}^p + \partial_{m^p}\psi\ \dot{m}^p + \partial_\alpha\psi\ \dot{\alpha} + \phi(\dot{\mathfrak{C}}). \quad (6.18)$$

so that

$$\Pi(\dot{\mathfrak{U}};\mathfrak{U}) := \int_{\mathcal{B}} \pi(\dot{\mathfrak{C}};\mathfrak{C})\ \mathrm{d}V - P_{\text{ext}}(\dot{\mathfrak{U}}). \quad (6.19)$$

The particular forms of the energy density $\psi(\mathfrak{C})$, the dissipation-potential density $\phi(\dot{\mathfrak{C}})$ and the potential of the external loading $P_{\text{ext}}(\dot{\mathfrak{U}})$ will be discussed in the following sections.

Constitutive energy density. The energy density has two contributions, one from the solid ψ_{solid} and one from the fluid ψ_{fluid}

$$\psi(\mathfrak{C}) = \psi_{\text{solid}}(\boldsymbol{\varepsilon} - \boldsymbol{\varepsilon}^p, \alpha, d) + \psi_{\text{fluid}}(\boldsymbol{\varepsilon} - \boldsymbol{\varepsilon}^p, m - m^p). \quad (6.20)$$

Energy density of the solid phase. The energy density of the solid phase ψ_{solid} can be decomposed into an effective elastic and a plastic part

$$\psi_{\text{solid}}(\boldsymbol{\varepsilon}^e, \alpha, d) = \psi_{\text{eff}}(\boldsymbol{\varepsilon}^e, d) + \psi_{\text{plast}}(\alpha, d). \quad (6.21)$$

Both parts depend on the fracture phase field d by means of a degradation function $g(d)$. The degraded effective elastic energy reads

$$\psi_{\text{eff}}(\boldsymbol{\varepsilon}^e, d) = [g(d) + k]\psi^{0+}_{\text{eff}}(\boldsymbol{\varepsilon}^e) + \psi^{0-}_{\text{eff}}(\boldsymbol{\varepsilon}^e), \quad (6.22)$$

where the superscript "0" indicates the energy density of the undamaged solid matrix. In the latter equation, we have decomposed the undamaged energy into tensile and compressive parts (indicated by the superscripts "+" and "-", respectively), from which only the tensile part is assumed to contribute to fracture propagation. The parameter $k \ll 1$ ensures the well posedness of the problem. In what follows, we assume that $g(d) = (1-d)^2$.

The undamaged effective energies $\psi^{0\pm}_{\text{eff}}$ represent the behavior of the elastic matrix and take the simple quadratic forms

$$\psi^{0\pm}_{\text{eff}}(\boldsymbol{\varepsilon}^e) = \tfrac{\lambda}{2}\big\langle \operatorname{tr}(\boldsymbol{\varepsilon}^e)\big\rangle^2_{\pm} + G\ \boldsymbol{\varepsilon}^e_{\pm} : \boldsymbol{\varepsilon}^e_{\pm} \quad \text{with} \quad \boldsymbol{\varepsilon}^e_{\pm} = \textstyle\sum_{i=1,3}\langle\lambda^e_i\rangle_{\pm}\boldsymbol{n}_i \otimes \boldsymbol{n}_i \quad (6.23)$$

in terms of the elastic strain $\boldsymbol{\varepsilon}^e$ and the Lamé constants $\lambda \geq -\frac{2}{3}G$ and $G \geq 0$. The tensile and compressive strains $\boldsymbol{\varepsilon}^e_{\pm}$ are given in terms of the eigenvalues of the strain tensor λ^e_i and the ramp function $\langle x\rangle_{\pm} = (x \pm |x|)/2$.

The plastic energy density considers isotropic saturation-type hardening and takes the form

$$\psi_{\text{plast}}(\alpha, d) = [g(d)+k]\psi^0_{\text{plast}}(\alpha) \quad \text{with} \quad \psi^0_{\text{plast}}(\alpha) = \tfrac{h}{2}\alpha^2 + \sigma_y\big[\alpha + \tfrac{1}{\omega}\exp(-\omega\alpha) - \tfrac{1}{\omega}\big]. \quad (6.24)$$

Here, $h \geq 0$ is the hardening modulus, σ_y is the saturated yield shift and ω is a saturation parameter, see Kienle et al. 2019. The resulting hardening function $\beta(\alpha, d) = \partial_\alpha\psi_{\text{plast}}(\alpha, d)$ is shown in Figure 6.4.

Energy density of the fluid phase. Based on Biot's theory of consolidation Biot 1941 the fluid energy density is chosen as

$$\psi_{\text{fluid}}(\boldsymbol{\varepsilon}^e, m^e) = \tfrac{M}{2}\big[b\,\text{tr}(\boldsymbol{\varepsilon}^e) - \tfrac{m^e}{\rho_f}\big]^2, \tag{6.25}$$

where M is Biot's modulus, b is Biot's coefficient and ρ_f is the fluid density. It satisfies the following conditions in terms of the fluid pressure p

$$p := -\tfrac{1}{b}\partial_{\text{tr}\,\boldsymbol{\varepsilon}}\psi_{\text{fluid}} = \rho_f \partial_m \psi_{\text{fluid}}. \tag{6.26}$$

We refer to Miehe et al. 2015b for a more detailed discussion on the construction of ψ_{fluid}. Note that according to (6.25) and (6.26) the fluid pressure depends only on the elastic quantities $\boldsymbol{\varepsilon}^e$ and m^e.

Dissipation-potential density. Similar to the energy density the dissipation potential density can be additively decomposed into individual contributions, here associated with dissipative effects arising from fluid flow, fracture evolution and plastic deformations. The dissipation potential density is formally given by

$$\phi(\dot{\mathfrak{C}}) = \phi_{\text{fluid}}(\mathbb{h}) + \phi_{\text{frac}}(\dot{d}, \dot{\nabla d}) + \phi_{\text{plast}}(\dot{\boldsymbol{\varepsilon}}^p, \dot{\alpha}, \dot{m}^p). \tag{6.27}$$

Dissipation-potential density for fluid flow. We follow Miehe et al. 2015b and employ a dissipation-potential density in terms of the fluid flux $\mathbb{h}$ given by

$$\phi_{\text{fluid}}(\mathbb{h}) = \tfrac{1}{2}\boldsymbol{K}^{-1} : (\mathbb{h} \otimes \mathbb{h}) \tag{6.28}$$

The permeability tensor $\boldsymbol{K}$ at a given state $\{\boldsymbol{\varepsilon}, d, \nabla d\}$ is defined as*

$$\boldsymbol{K}(\boldsymbol{\varepsilon}, d, \nabla d) = \begin{cases} [1 - f(d)]\boldsymbol{K}_0 + f(d)\boldsymbol{K}_{\text{frac}}(\boldsymbol{\varepsilon}, \nabla d) & \text{for } d \geq 0.8 \\ \boldsymbol{K}_0 & \text{otherwise,} \end{cases} \tag{6.29}$$

where $\boldsymbol{K}_0$ is the permeability tensor of the undamaged bulk and $\boldsymbol{K}_{\text{frac}}$ is the permeability tensor within a crack. Clearly, the function $f(d)$ acts as an interpolation function between intact and fully damaged states of the material. In what follows, we select $f(d) = d^\epsilon$, where ϵ is an interpolation parameter.

While the permeability tensor of the undamaged bulk can be formulated in an isotropic manner based on the spatial permeability K as $\boldsymbol{K}_0 = \rho_f^2 K \boldsymbol{1}$, the permeability tensor within a crack can be expressed in terms of the fracture-opening function $w(\boldsymbol{\varepsilon}, \nabla d)$

$$\boldsymbol{K}_{\text{frac}}(\boldsymbol{\varepsilon}, \nabla d) = \rho_f^2 \tfrac{w^2(\boldsymbol{\varepsilon}, \nabla d)}{12\eta_f}\big(\boldsymbol{1} - \boldsymbol{n} \otimes \boldsymbol{n}\big) \quad \text{with} \quad \boldsymbol{n} := \tfrac{\nabla d}{|\nabla d|}, \tag{6.30}$$

which is anisotropic in nature. In the above definition, η_f is the fluid's dynamic viscosity. Note that the representation of the permeability in (6.30) is derived based on the lubrication theory and relates to Poiseuille-type flow within the fractures. A schematic representation of the interpolation between Darcy's flow and the Poiseuille-type flow can be seen in Figure 6.2.

*We note that other approaches for the delineation of cracks from the bulk have been proposed. Here, we would like to refer, e.g., to Lee et al. 2017 for an approach using level-set functions, to Santillán et al. 2017, who introduce cracks as lower-dimensional entities whenever a certain damage threshold is met, and to Chukwudozie et al. 2019 for an approach using line integrals along the streamlines of phase-field gradients across fractured cells.

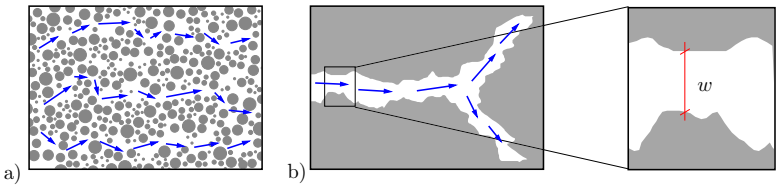

Figure 6.2: Schematic representation of a) fluid flow in porous medium according to Dracy's law and b) within developing fractures according to Poiseuille–type law with fracture opening w.

In the context of (6.30), the fracture-opening function is given as

$$w(\boldsymbol{\varepsilon}, \nabla d) = (\boldsymbol{n} \cdot \boldsymbol{\varepsilon} \cdot \boldsymbol{n}) L_{\perp}, \tag{6.31}$$

where $L_{\perp}$ is the length of a line element that is perpendicular to the crack. In a finite-element representation this can be identified as the element size h^e. Note that the approximation of the fracture opening (6.31) with $L_{\perp} = h^e$ is associated with a uniform rectangular finite-element mesh, where the crack is aligned with the element edges. Deviations of the resulting fracture width might occur in case of regular finite-element meshes with element edges that are inclined to the crack, see Appendix B.

We further note that according to (6.30) the crack normal $\boldsymbol{n}$ in (6.31) is defined in terms of the gradient of the phase field d. In the numerical setting the gradient is recovered by a lumped L_2 projection. Such a procedure allows the definition of the crack normal in fully broken finite-element cells ($d = 1$). The effect of the lumped L_2 projection is show schematically in Figure 6.3.

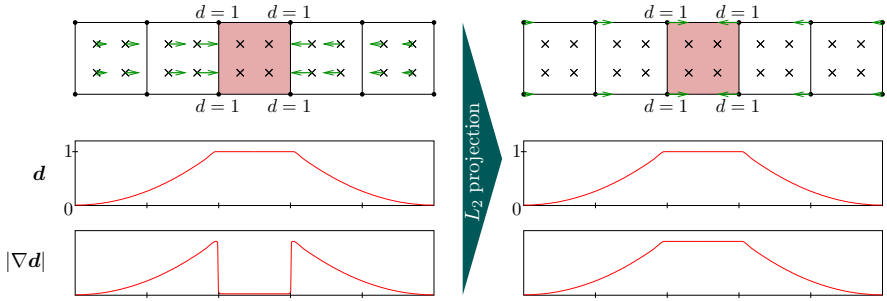

Figure 6.3: Projection and smoothing of the phase-field gradient ∇d shown schematically. A representation of fine elements is shown on the top. A fully broken cell in the center is colored in red. The green arrows indicate the gradient of the phase field at the quadrature points (top left) and at the nodes (top right). In the middle the distribution of the phase field is shown along a horizontal cut. The distribution of the gradient of the phase-field is shown at the bottom.

Dissipation-potential density for fracture evolution. The dissipation-potential density associated with fracturing accounts for the dissipation of an evolving crack surface. It preserves thermodynamical consistency by ensuring a local irreversibility condition of the

fracture phase field $\dot{d} \geq 0$, which can be achieved by introducing the indicator function $I(\dot{d})$.

For general Griffith-type fracturing the dissipation-potential density reads

$$\phi_{\text{frac}}^{g_c}(\dot{d}, \dot{\nabla d}) := \frac{\mathrm{d}}{\mathrm{d}t}\Big\{ g_c \gamma(d, \nabla d) \Big\} + I(\dot{d}), \tag{6.32}$$

where g_c is Griffith's critical energy-release rate. The indicator function $I(\dot{d})$ is given as

$$I(\dot{d}) := \begin{cases} 0 & \text{for } \dot{d} \geq 0, \\ \infty & \text{otherwise.} \end{cases} \tag{6.33}$$

Note that the fracture evolution described by (6.32) does not include any threshold value for the fracture evolution. In that case, damage occurs already at very small load levels. Hence, to clearly separate the material response during loading in elastic and plastic behavior as well as subsequent fracturing, the following dissipation-potential density will be used

$$\phi_{\text{frac}}(\dot{d}, \dot{\nabla d}) := \frac{\mathrm{d}}{\mathrm{d}t}\Big\{ [1 - g(d)]\psi_c + 2\psi_c l \gamma(d, \nabla d) \Big\} + I(\dot{d}), \tag{6.34}$$

where ψ_c is a threshold value.

Dissipation-potential density for plastic response. The dissipation-potential density accounting for plastic behavior can be derived based on the principle of maximum dissipation. For that, the thermodynamical driving forces for the plastic strain, the hardening and the change of plastic fluid content need to be specified. Using the second law of thermodynamics (Clausius–Planck inequality) yields the driving forces as thermodynamical duals of $\boldsymbol{\varepsilon}^p$, α and m^p as

$$\begin{aligned} \boldsymbol{\sigma} &:= -\partial_{\boldsymbol{\varepsilon}^p}\psi = -\partial_{\boldsymbol{\varepsilon}^p}\psi_{\text{eff}} - \partial_{\boldsymbol{\varepsilon}^p}\psi_{\text{fluid}} = \boldsymbol{\sigma}_{\text{eff}} - b\rho_f \mu \boldsymbol{1} \\ \beta &:= -\partial_{\alpha}\psi = -\partial_{\alpha}\psi_{\text{plast}} \\ \mu &:= -\partial_{m^p}\psi = -\partial_{m^p}\psi_{\text{fluid}}. \end{aligned} \tag{6.35}$$

We denote the set of diving forces as $\mathfrak{F} = \{\boldsymbol{\sigma}, \beta, \mu\}$, wherein $\boldsymbol{\sigma}$ is the Cauchy stress, β is the hardening function and μ is the fluid potential. Based on that, we construct the dissipation-potential density ϕ_{plast}, which is formulated in terms of the constrained optimization problem

$$\phi_{\text{plast}}(\dot{\boldsymbol{\varepsilon}}^p, \dot{\alpha}, \dot{m}^p) := \sup_{\mathfrak{F} \in \mathbb{E}} [\boldsymbol{\sigma} : \dot{\boldsymbol{\varepsilon}}^p + \beta\dot{\alpha} + \mu\dot{m}^p] \ . \tag{6.36}$$

In the above definition, the plastic driving forces are constrained to lie within the elastic domain $\mathbb{E} := \{\mathfrak{F} | f^p(\mathfrak{F}) \leq 0\}$, which is characterized by the yield function f^p. The latter will be specified at a later stage. By introducing the Lagrange multiplier λ^p the constrained optimization in (6.36) can be rewritten as

$$\phi_{\text{plast}}(\dot{\boldsymbol{\varepsilon}}^p, \dot{\alpha}, \dot{m}^p) := \sup_{\mathfrak{F}} \inf_{\lambda^p \geq 0} \big[\boldsymbol{\sigma} : \dot{\boldsymbol{\varepsilon}}^p + \beta\dot{\alpha} + \mu\dot{m}^p - \lambda^p f^p(\mathfrak{F})\big], \tag{6.37}$$

The latter representations are related to the rate-independent elastic-plastic material response, which leads to non-smooth evolution of plastic deformations. The non-smoothness

can be relaxed by introducing viscous regularization, which yields the modified dissipation-potential density

$$\phi_{\text{plast}}(\dot{\boldsymbol{\varepsilon}}^p, \dot{\alpha}, \dot{m}^p) := \sup_{\mathfrak{F}} \big[\underbrace{\boldsymbol{\sigma} : \dot{\boldsymbol{\varepsilon}}^p + \beta\dot{\alpha} + \mu\dot{m}^p - \tfrac{1}{2\eta_p}\langle f^p(\mathfrak{F})\rangle_+^2}_{\mathfrak{D}_{\text{plast}}} \big]. \tag{6.38}$$

From a mathematical point of view this density is obtained from an optimization procedure with side condition, the latter of which is enforced by a quadratic penalty term. The penalty parameter is given by the plastic viscosity η_p.

In the present work it is assumed that the yield function f^p_{solid} describes the plastic response of the drained solid matrix. It is thus expressed in terms of the effective stresses $\boldsymbol{\sigma}_{\text{eff}}$ and the hardening function β. It should be equal to the yield function f^p of the undrained bulk, which can be expressed in terms of the total stress $\boldsymbol{\sigma}$, the hardening function β and the fluid potential μ

$$f^p_{\text{solid}}(\boldsymbol{\sigma}_{\text{eff}}, \beta) = f^p(\boldsymbol{\sigma}, \beta, \mu). \tag{6.39}$$

A similar assumption has been made in Armero 1999. The starting point for the derivation of an appropriate yield function for the presented model is given by the yield function for frictional materials presented in Kienle et al. 2019, see also Vermeer and de Borst 1984 and Lambrecht and Miehe 2001. Making use of equations $(6.35)_1$ and (6.39) yields

$$f^p(\boldsymbol{\sigma}, \beta, \mu) = \sqrt{\tfrac{3}{2}}\sqrt{|\operatorname{dev}[\boldsymbol{\sigma}]|^2 + M_\phi^2 q_1^2} - M_\phi(s_{\max} - \tfrac{1}{3}\operatorname{tr}\boldsymbol{\sigma} - b\rho_f\mu) + \beta M_h(\boldsymbol{\sigma}, \mu), \tag{6.40}$$

where M_ϕ is related to the friction angle, q_1 is a parameter related to the regularization of the tip of the yield surface and $s_{\max}$ is related to the cohesion of the material. The hardening response is limited to friction hardening by choosing the material function $M_h(\boldsymbol{\sigma}, \mu)$ as

$$M_h(\boldsymbol{\sigma}, \mu) = 1 - \sqrt{\tfrac{3}{2}} q_1 \exp\big[\tfrac{1}{3}\operatorname{tr}\boldsymbol{\sigma} + b\rho_f\mu - s_{max}\big]. \tag{6.41}$$

By inserting equation $(6.35)_1$ in equation (6.40) the yield function $f^p_{\text{solid}}(\boldsymbol{\sigma}_{\text{eff}}, \beta)$ can be recovered. The yield function in terms of the effective stress $\boldsymbol{\sigma}_{\text{eff}}$ is visualized in Figure 6.4.

Potential of external loading. The external loading in form of mechanical tractions and fluid potential is formulated as

$$P_{\text{ext}}(\dot{\mathfrak{U}}) = \int_{\partial\mathcal{B}_{\boldsymbol{t}}} \bar{\boldsymbol{t}} \cdot \dot{\boldsymbol{u}} \, \mathrm{d}A - \int_{\partial\mathcal{B}_\mu} \bar{\mu}\mathbb{h} \cdot \boldsymbol{n} \, \mathrm{d}A, \tag{6.42}$$

where $\bar{\boldsymbol{t}}$ is the mechanical traction vector applied on the traction boundary $\partial\mathcal{B}_{\boldsymbol{t}}$ of the domain $\mathcal{B}$. The fluid contribution is due to the fluid transport over the boundary $\partial\mathcal{B}_\mu$ of the domain $\mathcal{B}$, where the fluid potential $\bar{\mu}$ is applied.

6.3.2. Minimization principle and mixed variational principle

Based on the above introduced functions we can introduce a rate-type minimization principle that governs the boundary-value problems of porous-elastic-plastic solids at fracture

$$\boxed{\dot{\mathfrak{U}}^* = \arg\ \big\{ \inf_{\dot{\mathfrak{U}} \in \mathfrak{V}}\ \Pi(\dot{\mathfrak{U}}; \mathfrak{U}) \big\}} \tag{6.43}$$

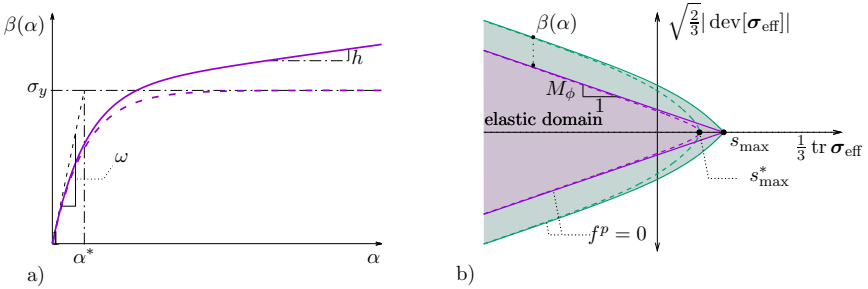

Figure 6.4: Hardening function $\beta(\alpha; d = 0)$ with linear hardening $h \neq 0$ (solid line) and without linear hardening $h = 0$ (dashed line), where $\alpha^* = (\frac{h}{\sigma_y} + \omega)^{-1}$ in a). In b) the yield function in two-dimensional hydrostatic-deviatoric plane with and without regularization (dashed/solid lines) where $s^*_{\max} = s_{\max} - \sqrt{\frac{2}{3}}q_1$. In green with hardening and no hardening in purple.

where $\mathfrak{W} = \{\mathcal{W}_{\dot{\boldsymbol{u}}}, \mathcal{W}_{\mathbb{h}}, \mathcal{W}_{\dot{d}}, \mathcal{W}_{\dot{\boldsymbol{\varepsilon}}^p}, \mathcal{W}_{\dot{\alpha}}, \mathcal{W}_{\dot{m}^p}\}$ is the set of admissible spaces corresponding to the set of the rate of unknowns $\dot{\mathfrak{U}}$. The admissible spaces are given as

$$\begin{aligned} \mathcal{W}_{\dot{\boldsymbol{u}}} &:= \{\dot{\boldsymbol{u}} \in H^1(\mathcal{B}) | \dot{\boldsymbol{u}} = \dot{\bar{\boldsymbol{u}}} \text{ on } \partial\mathcal{B}_{\boldsymbol{u}}\}, & \mathcal{W}_{\mathbb{h}} &:= \{\mathbb{h} \in H(\operatorname{div}, \mathcal{B}) | \mathbb{h} \cdot \boldsymbol{n} = \bar{h} \text{ on } \partial\mathcal{B}_{\mathbb{h}}\} \\ \mathcal{W}_{\dot{d}} &:= \{\dot{d} \in H^1(\mathcal{B})\}, & \mathcal{W}_{\dot{\boldsymbol{\varepsilon}}^p} &:= \{\boldsymbol{\varepsilon}^p \in L^2\} \\ \mathcal{W}_{\dot{\alpha}} &:= \{\dot{\alpha} \in L^2\}, & \mathcal{W}_{\dot{m}^p} &:= \{\dot{m}^p \in L^2\}. \end{aligned} \tag{6.44}$$

Combining the global minimization principle (6.43) with the local maximization principle in (6.38) yields the mixed variational principle

$$\boxed{\{\dot{\mathfrak{U}}^*, \mathfrak{F}^*\} = \arg \left\{ \inf_{\dot{\mathfrak{U}} \in \mathfrak{W}} \sup_{\mathfrak{F} \in L^2} \int_{\mathcal{B}} \pi^\star(\dot{\mathfrak{C}}, \mathfrak{F}; \mathfrak{C}) \, \mathrm{d}V - P_{\text{ext}}(\dot{\mathfrak{U}}) \right\}} \tag{6.45}$$

where $\pi^\star(\dot{\mathfrak{C}}, \mathfrak{F}; \mathfrak{C})$ is the mixed potential density. It reads

$$\pi^\star(\dot{\mathfrak{C}}, \mathfrak{F}; \mathfrak{C}) = \tfrac{\mathrm{d}}{\mathrm{d}t}\psi(\mathfrak{C}) + \mathfrak{D}_{\text{plast}}(\dot{\boldsymbol{\varepsilon}}^p, \dot{\alpha}, \dot{m}^p, \mathfrak{F}) + \phi_{\text{fluid}}(\mathbb{h}) + \phi_{\text{frac}}(\dot{d}, \dot{\nabla} d). \tag{6.46}$$

Performing the variation of (6.46) at a fixed state $\mathfrak{C}$, we obtain the Euler equations of the mixed variational principle (6.45) for the global unknowns as

$$\boxed{\begin{aligned} \operatorname{div}[\partial_{\boldsymbol{\varepsilon}}\psi] &= \boldsymbol{0} && \text{in} && \mathcal{B} \\ \nabla[\partial_m\psi] + \partial_{\mathbb{h}}\phi &= \boldsymbol{0} && \text{in} && \mathcal{B} \\ \partial_d\psi + \partial_{\dot{d}}\phi - \operatorname{div}[\partial_{\dot{\nabla} d}\phi] &\ni 0 && \text{in} && \mathcal{B} \\ -\partial_m\psi + \bar{\mu} &= 0 && \text{on} && \partial\mathcal{B}_\mu \\ \partial_{\boldsymbol{\varepsilon}}\psi \cdot \boldsymbol{n} - \bar{\boldsymbol{t}} &= \boldsymbol{0} && \text{on} && \partial\mathcal{B}_{\boldsymbol{t}} \\ \partial_{\dot{\nabla} d}\phi \cdot \boldsymbol{n} &= 0 && \text{on} && \partial\mathcal{B}_{\mathbb{t}} \end{aligned}} \tag{6.47}$$

and the local unknowns with the corresponding thermodynamic duals as

$$\boxed{\begin{aligned} \partial_{\boldsymbol{\varepsilon}^p}\psi + \boldsymbol{\sigma} &= \boldsymbol{0} && \text{in} \quad \mathcal{B} \\ \partial_{\alpha}\psi + \beta &= 0 && \text{in} \quad \mathcal{B} \\ \partial_{m^p}\psi + \mu &= 0 && \text{in} \quad \mathcal{B} \\ \dot{\boldsymbol{\varepsilon}}^p - \lambda_v^p\, \partial_{\boldsymbol{\sigma}} f^p &= \boldsymbol{0} && \text{in} \quad \mathcal{B} \\ \dot{\alpha} - \lambda_v^p\, \partial_{\beta} f^p &= 0 && \text{in} \quad \mathcal{B} \\ \dot{m}^p - \lambda_v^p\, \partial_{\mu} f^p &= 0 && \text{in} \quad \mathcal{B} \end{aligned}} \tag{6.48}$$

The equations in (6.47) represent the global balance laws and the corresponding Neumann boundary conditions. In (6.48) the definition of the thermodynamic duals of the local fields as well as their evolution equations are given. In the latter, we introduced the visco-plastic multiplier $\lambda_v^p := \frac{1}{\eta_p}\langle f^p \rangle_+$.

Condensation of local variables. The set of the rate of the primary fields can be split into a local and global part. The former is given as $\dot{\mathfrak{U}}_{\mathrm{l}} = \{\dot{\boldsymbol{\varepsilon}}^p, \dot{\alpha}, \dot{m}^p\}$ and the latter arises as $\dot{\mathfrak{U}}_{\mathrm{g}} = \dot{\mathfrak{U}} \setminus \dot{\mathfrak{U}}_{\mathrm{l}} = \{\dot{\boldsymbol{u}}, \dot{d}, \mathbb{h}\}$. The set of the rate of the local fields $\dot{\mathfrak{U}}_{\mathrm{l}}$ is governed by the mixed variational principle

$$\boxed{\{\dot{\mathfrak{U}}_{\mathrm{l}}^*, \dot{\mathfrak{F}}^*\} = \arg\big\{ \inf_{\dot{\mathfrak{U}}_{\mathrm{l}}} \sup_{\dot{\mathfrak{F}}} \pi^\star(\dot{\mathfrak{C}}, \dot{\mathfrak{F}}; \mathfrak{C})\big\}} \tag{6.49}$$

In order to obtain a solution for $\dot{\mathfrak{U}}_{\mathrm{g}}$ the reduced potential density is introduced as

$$\pi^\star_{\mathrm{red}}(\dot{\mathfrak{C}}_{\mathrm{red}}; \mathfrak{C}_{\mathrm{red}}) = \inf_{\dot{\mathfrak{U}}_{\mathrm{l}}} \sup_{\dot{\mathfrak{F}}} \pi^\star(\dot{\mathfrak{C}}, \dot{\mathfrak{F}}; \mathfrak{C}), \tag{6.50}$$

where the reduced constitutive state $\mathfrak{C}_{\mathrm{red}} = \{\boldsymbol{\varepsilon}, m, d, \nabla d\}$ and its evolution $\dot{\mathfrak{C}}_{\mathrm{red}} = \{\dot{\boldsymbol{\varepsilon}}, \mathbb{h}, \operatorname{div}\mathbb{h}, \dot{d}, \dot{\nabla} d\}$ are introduced. The set of the rate of the global fields is given by the following minimization principle

$$\boxed{\dot{\mathfrak{U}}_{\mathrm{g}}^* = \{\dot{\boldsymbol{u}}^*, \dot{d}^*, \mathbb{h}^*\} = \arg\Big\{ \inf_{\dot{\boldsymbol{u}}\in\mathcal{W}_{\dot{\boldsymbol{u}}}} \inf_{\dot{d}\in\mathcal{W}_{\dot{d}}} \inf_{\mathbb{h}\in\mathcal{W}_{\mathbb{h}}} \int_{\mathcal{B}} \pi^\star_{\mathrm{red}}(\dot{\mathfrak{C}}_{\mathrm{red}}; \mathfrak{C}_{\mathrm{red}})\, \mathrm{d}V - P_{\mathrm{ext}}(\dot{\mathfrak{U}}) \Big\}} \tag{6.51}$$

6.3.3. Modification of the fracture driving force

In this section a closer look at equation $(6.47)_3$ is taken. Inserting the definitions of the energy density and the dissipation potential density yields

$$-2(1-d)[\psi_{\mathrm{eff}}^{0+} + \psi_{\mathrm{plast}}^0 - \psi_c] + 2\psi_c(d - l^2\Delta d) + \partial_{\dot{d}} I \ni 0. \tag{6.52}$$

By introducing the crack driving history field $\mathcal{H}$ this is modified to

$$-2(1-d)\mathcal{H} + 2\psi_c(d - l^2\Delta d) = 0 \quad \text{with} \quad \mathcal{H} := \max_{s\in[0,t]} \langle \psi_{\mathrm{eff}}^{0+} + \psi_{\mathrm{plast}}^0 - \psi_c \rangle_+. \tag{6.53}$$

This follows the notation for brittle fracture in Miehe et al. 2010a and for ductile fracture in Miehe et al. 2016a, 2015a.

For plasticity models with a yield limit that is independent of the stress state it is possible to formulate a plastic energy density $\widetilde{\psi}^0_{\text{plast}}(\alpha)$, which contains not only the work of the hardening for the solid matrix but also the work of the ideal plastic deformation of the solid matrix. One such example is given by von-Mises plasticity, for which we can write

$$\widetilde{\psi}^0_{\text{plast}}(\alpha) \overset{\text{von Mises}}{=} w_{\text{plast}} \quad \text{with} \quad w_{\text{plast}} \overset{(6.49)}{=} \int \boldsymbol{\sigma}^0_{\text{eff}} : \dot{\boldsymbol{\varepsilon}}^p \, \mathrm{d}t \tag{6.54}$$

Note that the undamaged effective stress $\boldsymbol{\sigma}^0_{\text{eff}}$ acting on the solid matrix is used here. The plastic work w_{plast} can alternatively be expressed in terms of the undamaged total stress $\boldsymbol{\sigma}^0$ and the fluid potential μ as

$$w_{\text{plast}} = \int \boldsymbol{\sigma}^0_{\text{eff}} : \dot{\boldsymbol{\varepsilon}}^p \, \mathrm{d}t = \int \boldsymbol{\sigma}^0 : \dot{\boldsymbol{\varepsilon}}^p + \mu \dot{m}^p \, \mathrm{d}t. \tag{6.55}$$

Since the construction of an energy density $\widetilde{\psi}^0_{\text{plast}}$ like $(6.54)_1$ is not possible for more complicated plasticity models such as the Drucker–Prager model, the crack driving history field in $(6.53)_2$ is modified to

$$\mathcal{H} = \max_{s\in[0,t]} \langle \psi^{0+}_{\text{eff}} + w_{\text{plast}} - \psi_c \rangle_+. \tag{6.56}$$

With the representation of the crack driving history field in (6.56) it is possible to model ductile fracture evolution that is driven by the elastic and the ideal plastic deformation as well as the hardening. With the representation in $(6.53)_2$ and the definition of the plastic energy in $(6.24)_2$ it is only possible to model a ductile fracture evolution which is driven by the elastic deformation and the hardening.

A visualization of the different energy contributions to the crack driving history is shown in Figure 6.5.

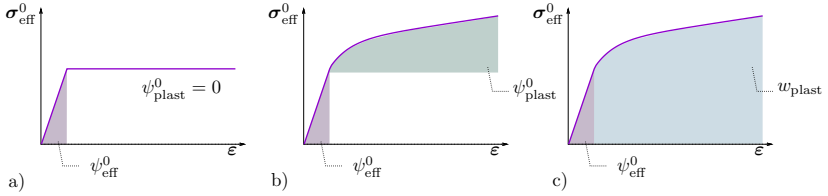

Figure 6.5: Visualization of the different energy contributions to the crack driving history field $\mathcal{H}$. For the representation of $\mathcal{H}$ in $(6.53)_2$ only the elastic energy and the energy arising from the hardening, as show in a) and b), will drive the crack. For ideal plasticity the plastic energy vanishes ($\psi^0_{\text{plast}} = 0$) leading to pure brittle fracture, see a). By using (6.56) the crack is driven by the elastic energy and the full plastic work, see c).

Relation between plastic strain and change of fluid content. Based on the construction of the yield function, see (6.39), the evolution of the plastic strain $(6.48)_4$ can be reformulated as

$$\dot{\boldsymbol{\varepsilon}}^p = \lambda^p_v \, \partial_{\boldsymbol{\sigma}} f^p = \lambda^p_v \, \partial_{\boldsymbol{\sigma}_{\text{eff}}} f^p_{\text{solid}}. \tag{6.57}$$

Furthermore, reformulation of the evolution of the change of plastic fluid content $(6.48)_6$ yields

$$\dot{m}^p = \lambda_v^p \, \partial_\mu f^p = \lambda_v^p \, \rho_f b \;\; \mathrm{tr}(\partial_{\boldsymbol{\sigma}_{\mathrm{eff}}} f^p_{\mathrm{solid}}). \tag{6.58}$$

Combining the above two equations gives a relation between the evolution of the plastic strain and the evolution of the change of the plastic fluid content

$$\dot{m}^p = \rho_f b \, \mathrm{tr} \, \dot{\boldsymbol{\varepsilon}}^p. \tag{6.59}$$

We observe that the change of the plastic fluid content depends exclusively on volumetric plastic deformation.

6.4. Numerical Treatment

6.4.1. Incremental variational formulation

The incremental version of the rate-type potential introduced in Section 6.3 is obtained by algorithmic time integration over a given time step $\tau = [t_n, t_{n+1})$. For a pure Dirichlet problem ($P_{\mathrm{ext}} = 0$) we arrive at

$$\Pi^\tau(\mathfrak{U}, \mathfrak{F}) = \mathrm{Algo}\Big\{ \int_{t_n}^{t_{n+1}} \Pi(\dot{\mathfrak{U}}, \mathfrak{F}; \mathfrak{C}) \; \mathrm{d}t \Big\} = \int_{\mathcal{B}} \pi^{\star\tau}(\mathfrak{C}, \mathfrak{F}; \mathfrak{C}_n) \; \mathrm{d}V, \tag{6.60}$$

where $\pi^{\star\tau}(\mathfrak{C}, \mathfrak{F}; \mathfrak{C}_n)$ is the incremental potential density. It is given in terms of the energy density ψ, the incremental fluid and fracture dissipation-potential density $\phi^\tau_{\mathrm{fluid}}$ and $\phi^\tau_{\mathrm{frac}}$, respectively, as well as the incremental dissipation density related to the visco-plastic behavior $\mathfrak{D}^\tau_{\mathrm{plast}}$ as

$$\pi^{\star\tau}(\mathfrak{C}, \mathfrak{F}; \mathfrak{C}_n) = \psi(\mathfrak{C}) + \mathfrak{D}^\tau_{\mathrm{plast}}(\boldsymbol{\varepsilon}^p, \alpha, m^p, \mathfrak{F}; \boldsymbol{\varepsilon}^p_n, \alpha_n, m^p_n) + \phi^\tau_{\mathrm{fluid}}(\mathbb{h}) + \phi^\tau_{\mathrm{frac}}(d, \nabla d, d_n). \tag{6.61}$$

The individual dissipative contributions read

$$\begin{aligned} \phi^\tau_{\mathrm{fluid}} &= \tau \phi_{\mathrm{fluid}}(\mathbb{h}) \\ \phi^\tau_{\mathrm{frac}} &= [1 - g(d)]\psi_c + 2\psi_c l \gamma(d, \nabla d) + I^\tau(d, d_n) \\ \mathfrak{D}^\tau_{\mathrm{plast}} &= \boldsymbol{\sigma} : (\boldsymbol{\varepsilon}^p - \boldsymbol{\varepsilon}^p_n) + \beta(\alpha - \alpha_n) + \mu(m^p - m^p_n) + \tfrac{\tau}{2\eta_p} \langle f^p(\mathfrak{F}) \rangle^2_+. \end{aligned} \tag{6.62}$$

Furthermore the fluid mass balance $(6.6)_2$ is satisfied by the implicit update

$$m = m_n - \tau \, \mathrm{div} \, \mathbb{h}. \tag{6.63}$$

Condensation of local variables.. Similar as in the continuous problem, the set of primary fields can be decomposed into a local and global part. Again, the local fields are identified as $\mathfrak{U}_{\mathrm{l}} = \{\boldsymbol{\varepsilon}^p, \alpha, m^p\}$ and the global fields as $\mathfrak{U}_{\mathrm{g}} = \mathfrak{U} \setminus \mathfrak{U}_{\mathrm{l}} = \{\boldsymbol{u}, d, \mathbb{h}\}$. The local fields are governed by the mixed variational principle

$$\boxed{\mathfrak{U}^*_{\mathrm{l}} = \mathrm{arg}\{ \inf_{\mathfrak{U}_{\mathrm{l}}} \sup_{\mathfrak{F}} \pi^{\star\tau}(\mathfrak{C}, \mathfrak{F}; \mathfrak{C}_n)\}} \tag{6.64}$$

Using the representation (6.38) the mixed variational principle (6.64) leads to the following condition

$$\partial_{\mathfrak{U}_l,\mathfrak{F}}\pi^\star = \begin{bmatrix} \partial_{\boldsymbol{\varepsilon}^p}\psi + \boldsymbol{\sigma} \\ \partial_\alpha\psi + \beta \\ \partial_{m^p}\psi + \mu \\ \boldsymbol{\varepsilon}^p - \boldsymbol{\varepsilon}_n^p - \gamma_v^p\,\partial_{\boldsymbol{\sigma}} f^p \\ \alpha - \alpha_n - \gamma_v^p\,\partial_\beta f^p \\ m^p - m_n^p - \gamma_v^p\,\partial_\mu f^p \end{bmatrix} = \boldsymbol{0}. \tag{6.65}$$

Here, $\gamma_v^p := \tau\lambda_v^p = \frac{\tau}{\eta_p}\langle f^p\rangle_+$ is the incremental visco-plastic multiplier. The local system of equations in (6.65) is solved via a general return mapping scheme summarized in Box 6.1.

Reduced global problem.. In order to obtain a solution for $\mathfrak{U}_g$ the reduced potential density is introduced

$$\pi_{\text{red}}^{\star\tau}(\mathfrak{C}_{\text{red}}) = \inf_{\mathfrak{U}_l}\ \sup_{\mathfrak{F}}\ \pi^{\star\tau}(\mathfrak{C},\mathfrak{F};\mathfrak{C}_n), \tag{6.67}$$

where the reduced constitutive state $\mathfrak{C}_{\text{red}} = \{\boldsymbol{\varepsilon}, \mathbb{h}, \operatorname{div}\mathbb{h}, d, \nabla d\}$ is introduced. The global fields are then given by the minimization principle

$$\boxed{\mathfrak{U}_g^* = \{\boldsymbol{u}^*, d^*, \mathbb{h}^*\} = \arg\left\{\inf_{\boldsymbol{u}\in\mathcal{W}_{\boldsymbol{u}}}\ \inf_{d\in\mathcal{W}_d}\ \inf_{\mathbb{h}\in\mathcal{W}_{\mathbb{h}}} \int_{\mathcal{B}} \pi_{\text{red}}^{\star\tau}(\mathfrak{C}_{\text{red}})\ \mathrm{d}V\right\},} \tag{6.68}$$

with the admissible spaces

$$\mathcal{W}_{\boldsymbol{u}} := \{\boldsymbol{u}\in H^1(\mathcal{B}) | \boldsymbol{u} = \bar{\boldsymbol{u}} \text{ on } \partial\mathcal{B}_{\boldsymbol{u}}\},\quad \mathcal{W}_{\mathbb{h}} := \{\mathbb{h}\in H(\operatorname{div},\mathcal{B}) | \mathbb{h}\cdot\boldsymbol{n} = \bar{h} \text{ on } \partial\mathcal{B}_{\mathbb{h}}\},$$
$$\mathcal{W}_d := \{d\in H^1(\mathcal{B})\}. \tag{6.69}$$

6.4.2. Space-time-discrete finite-element formulation

Considering a finite-element discretization $\mathcal{T}^h(\mathcal{B})$, the discrete state vector $\mathbf{d}$ containing the discrete values of $\{\boldsymbol{u}, \mathbb{h}, d\}$ and the interpolation of the constitutive state $\mathfrak{C}_{\text{red}}^h = \mathbf{B}\mathbf{d}$ the global minimization principle (6.68) can be written as

$$\mathbf{d}^* = \arg\{\inf_{\mathbf{d}}\ \Pi^{\tau h}(\mathbf{d})\} \quad \text{with} \quad \Pi^{\tau h}(\mathbf{d}) = \int_{\mathcal{B}} \pi_{\text{red}}^{\star\tau h}(\mathbf{B}\mathbf{d})\ \mathrm{d}V. \tag{6.70}$$

Here, we employ the shape functions from Raviart and Thomas 1977 for the interpolation of the fluid flux, see also Teichtmeister et al. 2019. The nodal displacement is interpolated by the shape functions of the enhanced-assumed-strain formulation, see Simo and Rifai 1990. The interpolation of the nodal phase-field values is done by the standard Q_1-type shape functions.

The global algebraic minimization principle (6.70) leads to the following condition

$$\mathbf{R} := \Pi_{,\mathbf{d}}^{\tau h} = \int_{\mathcal{B}} \mathbf{B}^T\mathbf{S}\ \mathrm{d}V = \boldsymbol{0} \tag{6.71}$$

0. Get trial values $[\boldsymbol{\varepsilon}^{e,\mathrm{tr}};\ m^{e,\mathrm{tr}};\ \alpha^{\mathrm{tr}}]^T = [(\boldsymbol{\varepsilon} - \boldsymbol{\varepsilon}^p_n);\ (m - m^p_n);\ \alpha_n]^T$

1. Set initial values $[\boldsymbol{\varepsilon}^e;\ m^e;\ \alpha]^T = [\boldsymbol{\varepsilon}^{e,\mathrm{tr}};\ m^{e,\mathrm{tr}};\ \alpha^{\mathrm{tr}}]$ and $\gamma^p_v = 0$.

2. Compute derivatives of energy density and yield function

$$\psi(\boldsymbol{\varepsilon}^e, m^e, \alpha; d) \qquad \boldsymbol{s} = \begin{bmatrix} \psi_{,\boldsymbol{\varepsilon}^e} \\ \psi_{,m^e} \\ \psi_{,\alpha} \end{bmatrix} \quad \mathbb{E} = \begin{bmatrix} \psi_{,\boldsymbol{\varepsilon}^e\boldsymbol{\varepsilon}^e} & \psi_{,\boldsymbol{\varepsilon}^e m^e} & \psi_{,\boldsymbol{\varepsilon}^e\alpha} \\ \psi_{,m^e\boldsymbol{\varepsilon}^e} & \psi_{,m^e m^e} & \psi_{,m^e\alpha} \\ \psi_{,\alpha\boldsymbol{\varepsilon}^e} & \psi_{,\alpha m^e} & \psi_{,\alpha\alpha} \end{bmatrix}$$

$$f^p(\boldsymbol{\sigma}, \mu, \beta) \qquad \boldsymbol{n} = \begin{bmatrix} f^p{}_{,\boldsymbol{\sigma}} \\ f^p{}_{,\mu} \\ f^p{}_{,\beta} \end{bmatrix} \quad \mathbb{F} = \begin{bmatrix} f^p{}_{,\boldsymbol{\sigma}\boldsymbol{\sigma}} & f^p{}_{,\boldsymbol{\sigma}\mu} & f^p{}_{,\boldsymbol{\sigma}\beta} \\ f^p{}_{,\mu\boldsymbol{\sigma}} & f^p{}_{,\mu\mu} & f^p{}_{,\mu\beta} \\ f^p{}_{,\beta\boldsymbol{\sigma}} & f^p{}_{,\beta\mu} & f^p{}_{,\beta\beta} \end{bmatrix}$$

3. Check for yielding. If yielding do a local Newton iteration

if $f^p < 0$ **then** `// elastic step`

- set $[\boldsymbol{\sigma};\ \psi_{,m}]^T = [\psi_{,\boldsymbol{\varepsilon}^e};\ \psi_{,m^e}]^T$ and $\mathbb{E}^{\mathrm{ep}} = \mathbb{E}$
- **return**

else `// plastic step`

- **compute** residual vector
  - $\boldsymbol{r} := [(\boldsymbol{\varepsilon}^p_n - \boldsymbol{\varepsilon}^p);\ (m^p_n - m^p);\ (\alpha_n - \alpha)]^T + \gamma^p_v\,\boldsymbol{n}$
- **check** if local Newton is converged
  - if $[\ \sqrt{\boldsymbol{r}^T\boldsymbol{r} + [\ f^p - \frac{\eta_p}{\tau}\gamma^p_v\ ]^2} < tol\ ]$ go to **4.**
- **compute** incremental plastic parameter
  - $\Delta\gamma^p_v = \frac{1}{C}[\ f^p - \boldsymbol{n}^T\mathbb{X}\,\boldsymbol{r}\ ]$ with $C := \boldsymbol{n}^T\mathbb{X}\,\boldsymbol{n} + \frac{\eta^p}{\tau}$ and $\mathbb{X} := [\ \mathbb{E}^{-1} + \gamma^p_v\mathbb{F}\ ]^{-1}$
- **compute** incremental strains, plastic fluid content and hardening variable
  - $[\Delta\boldsymbol{\varepsilon}^p;\ \Delta m^p;\ \Delta\alpha]^T = -\mathbb{E}^{-1}\mathbb{X}\,[\ \boldsymbol{r} + \Delta\gamma^p_v\,\boldsymbol{n}\ ]$
- **update** plastic quantities
  - $[\boldsymbol{\varepsilon}^p;\ m^p\ ;\alpha;\ \gamma^p_v]^T \Leftarrow [\boldsymbol{\varepsilon}^p;\ m^p;\ \alpha;\ \gamma^p_v]^T + [\Delta\boldsymbol{\varepsilon}^p;\ \Delta m^p;\ \Delta\alpha;\ \Delta\gamma^p_v]^T$
- **update** elastic quantities
  - $[\boldsymbol{\varepsilon}^e;\ m^e]^T = [(\boldsymbol{\varepsilon} - \boldsymbol{\varepsilon}^p);\ (m - m^p)]^T$
- go to **2**.

4. For plastic step: Obtain stresses and consistent moduli

$$[\boldsymbol{\sigma};\ \psi_{,m}]^T = [\psi_{,\boldsymbol{\varepsilon}^e};\ \psi_{,m^e}]^T \quad \text{and} \quad \mathbb{E}^{\mathrm{ep}} = \mathbb{X} - \frac{1}{C}\,[\,\mathbb{X}\cdot\boldsymbol{n}\,]\otimes[\,\boldsymbol{n}\cdot\mathbb{X}\,] \tag{6.66}$$

Box 6.1: Return mapping and tangent moduli for poro-elasto-plasticity. It is based on the algorithm for elasto-plasticity in Miehe 1998.

where the generalized array $\mathbf{S}$ is introduced. This array is defined as follows

$$\mathbf{S} := \left[\begin{array}{c} \psi_{,\boldsymbol{\varepsilon}^h} \\ -\tau\psi_{,m^h} \\ \tau\phi_{,\mathbb{h}^h} \\ \hline -2(1-d)\mathcal{H} + \phi^{\tau\prime}_{,d^h} \\ \phi^{\tau}_{,\nabla d^h} \end{array}\right] \tag{6.72}$$

Note that this array is not obtained by straightforward differentiation of $(6.70)_2$, i.e. we have in general $\mathbf{S} \neq \partial_{\boldsymbol{\mathfrak{e}}^h_{\text{red}}} \pi^{\star\tau h}_{\text{red}}$. This is due to the consideration of the history field $\mathcal{H}$ in (6.53). Above, we have introduced the $\phi^{\tau\prime} = \phi^{\tau} - I^{\tau}(d, d_n)$, where $I^{\tau}(d, d_n)$ is the time discrete version of the indicator function (6.33). The system of equations (6.71) is solved by a Newton–Raphson-type iteration yielding

$$\mathbf{d} \leftarrow \mathbf{d} - \mathbf{K}^{-1}\mathbf{R} \quad \text{with} \quad \mathbf{K} := \Pi^{\tau h}_{,\mathbf{dd}} = \int_{\mathcal{B}} \mathbf{B}^T \mathbf{C} \boldsymbol{B} \, \mathrm{d}V. \tag{6.73}$$

The generalized tangent array $\mathbf{C}$ is given as

$$\mathbf{C} := \partial_{\boldsymbol{\mathfrak{e}}^h_{\text{red}}} \mathbf{S} = \left[\begin{array}{ccccc} \boxed{\mathbb{E}^{\text{ep}}_{\boldsymbol{\varepsilon}\boldsymbol{\varepsilon}} & -\tau\mathbb{E}^{\text{ep}}_{\boldsymbol{\varepsilon}m} & 0} & \cdot & \cdot \\ -\tau\mathbb{E}^{\text{ep}}_{m\boldsymbol{\varepsilon}} & \tau^2\mathbb{E}^{\text{ep}}_{mm} & 0 & \cdot & \cdot \\ 0 & 0 & \tau\phi_{,\mathbb{h}^h\mathbb{h}^h} & 0 & 0 \\ \cdot & \cdot & 0 & \boxed{2\mathcal{H} + \phi^{\tau\prime}_{,d^h d^h}} & 0 \\ \cdot & \cdot & 0 & 0 & \boxed{\phi^{\tau}_{,\nabla d^h \nabla d^h}} \end{array}\right]. \tag{6.74}$$

Here "0" indicates that the corresponding derivative does not exists. The derivatives at the slots labeled with "." indeed exist but are not needed due to the modification of the fracture driving force (6.53) as consequence of an operator split. The latter leads to a decoupling of the related fields so that the two boxed sub-blocks in (6.74) can be treated in separate solution steps. The so called one-pass solution strategy is utilized here Miehe et al. 2015a, 2010a. This means that the displacement and flux is updated first and then the fracture phase-field is updated. This might underestimate the speed of the fracture evolution but can be controlled by the choice of an appropriated time step size τ Kienle et al. 2019.

6.5. Numerical Examples

In the following we present a sequence of numerical examples that demonstrate the capabilities of the model formulation. The examples start with a test of a porous-elastic-plastic medium that is surcharged with a rigid footing leading to the creation of shear bands. Furthermore, we analyze the effect of different driving forces on porous-elastic-plastic fracture evolution. The latter analysis is extended to the comparison of porous-elastic and porous-elastic-plastic materials response leading to the evolution of Hydraulically induced fractures.

Lamé parameter	$\lambda = 180.0$	GN/m^2	slope yield function	$M_\phi = 0.6$	–
Lamé parameter	$G = 31.0$	GN/m^2	position of peak	$s_{\max} = 4.0$	MN/m^2
hardening modulus	$h = 0.035$	MN/m^2	Biot's modulus	$M = 25.0$	GN/m^2
saturated yield shift	$\sigma_y = 0.1$	MN/m^2	Biot's coefficient	$b = 0.5$	–
saturation parameter	$\omega = 2.0$	–	fluids dyn. viscosity	$\eta_f = 1.0 \cdot 10^{-3}$	Ns/m^2
plastic viscosity	$\eta_p = 5.0 \cdot 10^{-6}$	s	permeability	$K = 9.8 \cdot 10^{-12}$	m^{3}s/kg
perturbation parameter	$q_1 = 0.04$	MN/m^2	fluid density	$\rho_f = 1000.0$	kg/m^3

Table 6.2: Material parameters for rigid footing test.

6.5.1. Rigid-footing test on porous-elastic-plastic medium

In the first example we consider a rigid footing test without fracture evolution. Our goal is to analyze the effect of plasticity as well as fluid flux and storage on the system's response. We thus take into account three different material types:

i) drained elastic-plastic material,
ii) undrained porous-elastic material,
iii) undrained porous-elastic-plastic material with different permeabilities.

The drained elastic-plastic material is recovered by setting Biot's modulus and coefficient to zero ($M = 0$, $b = 0$). In order to model the undrained porous-elastic material, the yield limit is increased to a very high value by setting $s_{\max} = 1 \cdot 10^4$ MN/m^2. For the undrained porous-elastic-plastic material all contributions of the model are active, hence no artificial choice of any material parameter is necessary. In order to analyze the effect of the permeability on the overall model response, we consider different magnitudes of permeabilities given by an original value K as well as a reduced and an increased permeability ($K/5$ and $5K$, respectively). The chosen material parameters are listed in Table 6.2.

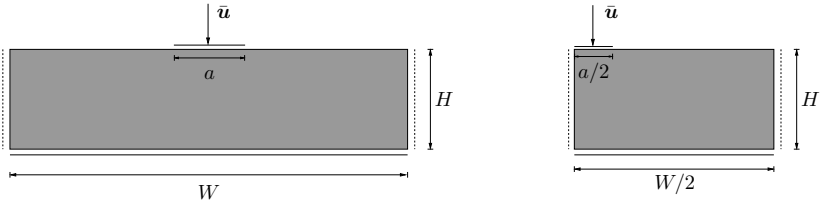

Figure 6.6: Rigid footing test: Geometry and boundary conditions. Bottom is mechanically fixed, left and right edge is mechanically fixed in horizontal direction. Bottom, left and right is impermeable.

The geometry and boundary conditions are shown in Figure 6.6. Due to the symmetry of loading and geometry only one half of the specimen is discretized by $2,376$ quadrilateral Raviart–Thomas-type enhanced-assumed-strain elements. The dimensions are $H = 4.758$ m, $W = 23.088$ m and $a = 4.587$ m. The loading increment is $\triangle\bar{\boldsymbol{u}} = 5 \cdot 10^{-6}$ m. The loading is linearly increased until a total displacement of $\bar{\boldsymbol{u}} = 0.0023$ m is reached.

In Figure 6.7 the distribution of the hardening variable α for the drained elastic-plastic material and undrained porous-elastic-plastic material is shown. It can be seen that the

plastic deformation is more pronounced in the case of the drained material. This leads to the conclusion that the fluid within the material leads to an additional hardening effect. The load-displacement curve in Figure 6.8 also shows this behaviour. Furthermore, a lower permeability leads to more pronounced hardening. This can be explained by the fact that the transport of the fluid is hindered and thus requires more work, see Figure 6.8.

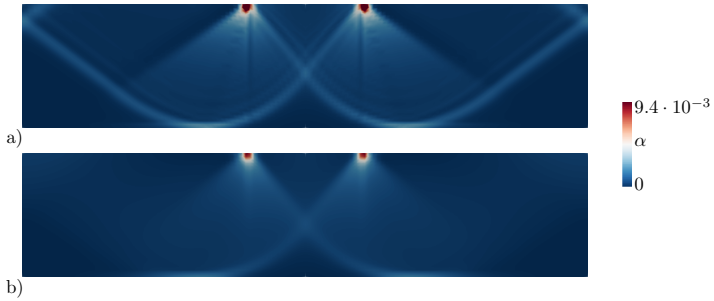

Figure 6.7: Rigid footing test: Distribution of the hardening variable α in drained elastic-plastic material in a) and undrained porous-elastic-plastic material in b).

Next, the distribution of the change of elastic fluid content m^e in the domain for the undrained porous-elastic material is compared with one of the undrained porous-elastic-plastic material, see Figure 6.9.

Note that for the elastic material the fluid is squeezed out right underneath the area where the loading is applied (see the negative change of the elastic fluid content at the boundary of the applied footing depicted in Figure 6.9a). Opposed to that, in the case of the elastic-plastic material, the highest (negative) change of elastic fluid content occurs in a more diffuse region that also extends to the bulk (see Figure 6.9b). This is precisely the area where most of the plastic deformation is happening, as can be observed in Figure 6.7 b). This phenomenon can be explained by the fact that the plastic deformation leads to a positive change of the plastic fluid content. Due to the additive decomposition of the change of the fluid content and the fact that no fluid is injected, the change of the elastic

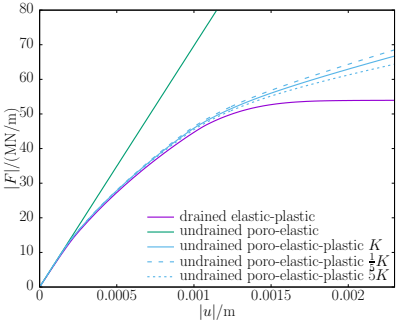

Figure 6.8: Rigid footing: Load displacement curve for the different tested material types. The load and displacement is taken from the area were the displacement is prescribed, see Figure 6.6.

fluid content becomes negative in the plastifying areas.

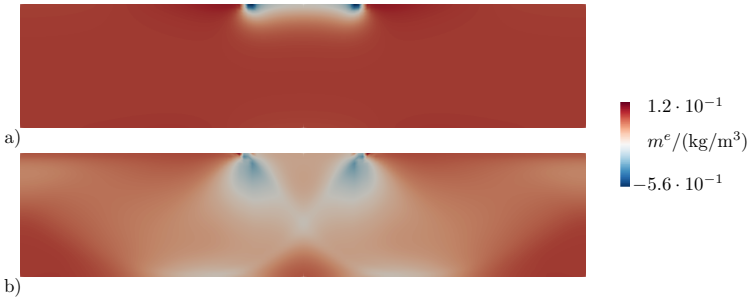

Figure 6.9: Rigid footing test. Change of the elastic fluid content m^e for undrained porous-elastic material in a) and in b) for undrained porous-elastic-plastic material.

We depict the distribution of the change of the elastic m^e, the plastic m^p and total fluid content m for the undrained porous-elastic-plastic material in Figure 6.10. One can observe that the change of the total fluid content m is strongly dominated by the change of the plastic fluid content m^p.

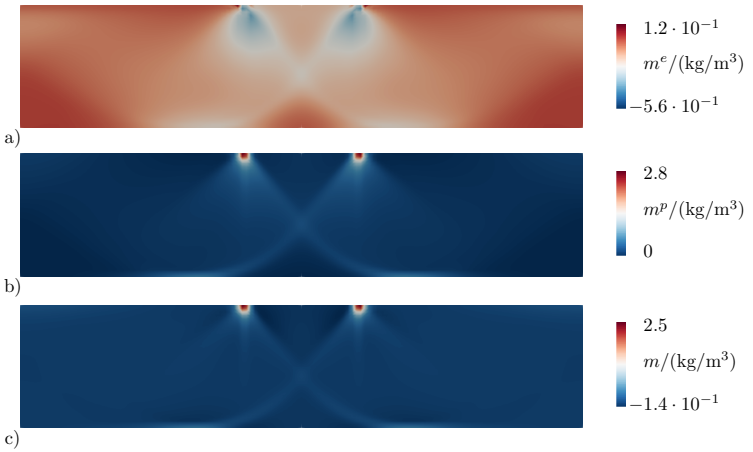

Figure 6.10: Rigid footing test: Change of fluid content for undrained porous-elastic-plastic material. Change of elastic fluid content m^e in a), change of plastic fluid content m^p in b) and change of total fluid content m in c).

6.5.2. Comparison of different fracture driving forces for porous-elastic-plastic fracturing

In the present example, we investigate the influence of the presented fracture driving forces defined in (6.53) and (6.56). For that purpose, a squared domain with the dimensions of

Lamé parameter	$\lambda = 180.0$	GN/m^2	Biot's modulus	$M = 25.0$	GN/m^2
Lamé parameter	$G = 31.0$	GN/m^2	Biot's coefficient	$b = 0.5$	–
hardening modulus	$h = 5.0$	MN/m^2	fluids dyn. viscosity	$\eta_f = 1.0 \cdot 10^{-3}$	Ns/m^2
saturated yield shift	$\sigma_y = 0.1$	MN/m^2	permeability	$K = 9.8 \cdot 10^{-12}$	m^{3}s/kg
saturation	$\omega = 2.0$	–	fluid density	$\rho_f = 1000.0$	kg/m^3
plastic viscosity	$\eta_p = 5.0 \cdot 10^{-6}$	s	crit. fracture energy	$\psi_c = 5.0 \cdot 10^{-8}$	MN/m^2
perturbation parameter	$q_1 = 2.0 \cdot 10^{-5}$	MN/m^2	length scale	$l = 0.5$	m
slope yield function	$M_\phi = 1.8$	–	residual stiffness	$k = 1 \cdot 10^{-5}$	–
position of peak	$s_{\max} = 2 \cdot 10^{-3}$	MN/m^2	interpolation parameter	$\epsilon = 50$	–

Table 6.3: Material parameters for hydraulically induced fracture.

80 m × 80 m and a notch of the length $a = 8$ m in its center is considered, see Figure 6.11. The fracture evolution is triggered by fluid injection into the notch.

Due to the symmetry of loading and geometry only one half of the domain is discretized with 12,060 quadrilateral Raviart–Thomas-type enhanced-assumed-strain elements. The mesh is uniform and the elment edged are aligned with the crack. The elements in the area surrounding the anticipated crack are refined yielding an element size of $h^e = 0.25$ m in that region ($[0\text{ m}, 40\text{ m}] \times [31.875\text{ m}, 48.125\text{ m}]$ around the notch).

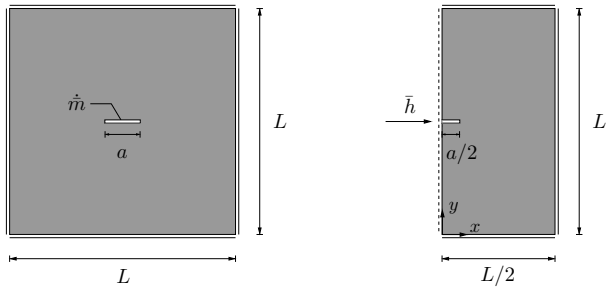

Figure 6.11: Comparison of different fracture driving forces: Geometry and boundary conditions. Due to the symmetry of both only one half of the specimen is discretized. Here the prescribed flux is $\bar{h} = \dot{\bar{m}} = 0.01$ kg/s. All edges are mechanically fixed and permeable.

The fluid injection is modeled by a prescribed fluid flux of $\bar{h} = 0.01\ \frac{\text{kg}^3}{\text{s}}$. The time step is set to $\tau = 1 \cdot 10^{-3}$ s and the material parameters are listed in Table 6.3.

The test was performed for the following two undrained settings with different choices of fracture driving forces:

i) porous-elastic-plastic material with $\mathcal{H} = f(\psi^0_{\text{eff}}, \psi^0_{\text{plast}})$ according to (6.53)
ii) porous-elastic-plastic material with $\mathcal{H} = f(\psi^0_{\text{eff}}, w_{\text{plast}})$ according to (6.56)

We now compare the hydraulically induced fracture lengths for the two porous-elastic-plastic settings. As can be observed in Figure 6.12, both driving forces lead to the evolution of cracks. The fracture evolution in consideration of the fracture driving force $\mathcal{H} = f(\psi^0_{\text{eff}}, \psi^0_{\text{plast}})$ is however less prominent. Note that in that setting, only the elastic and hardening energies contribute to the fracture driving force. Thus, we would not obtain

ductile fracture evolution in case of ideal plasticity with ($h = 0$, $\sigma_y = 0$; not investigated here). In particular the latter observation justifies the presented modification of the fracture driving force in (6.56).

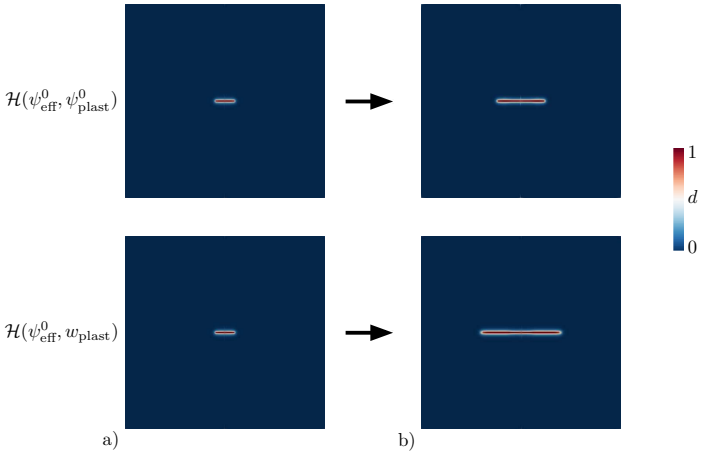

Figure 6.12: Comparison of different fracture driving forces: Distribution of the fracture phase-field for a porous-elastic-plastic with $\mathcal{H} = f(\psi^0_{\text{eff}}, \psi^0_{\text{plast}})$ and a porous-elastic-plastic material with $\mathcal{H} = f(\psi^0_{\text{eff}}, w_{\text{plast}})$ at two time steps: a) $t = 0$ s and b) $t = 90$ s.

6.5.3. Detailed analysis of hydraulically induced porous-elastic-plastic fracture

Finally, we investigate the ductile fracture evolution driven by an injected fluid, where we also analyze the influence of the fluid-injection rate. The setup of the geometry and boundary conditions as well as the material parameters are taken from the previous example (please refer to Figure 6.11 and Table 6.3).

The test was performed for two kinds of undrained materials:

i) porous-elastic material
ii) porous-elastic-plastic material with $\mathcal{H} = f(\psi^0_{\text{eff}}, w_{\text{plast}})$.

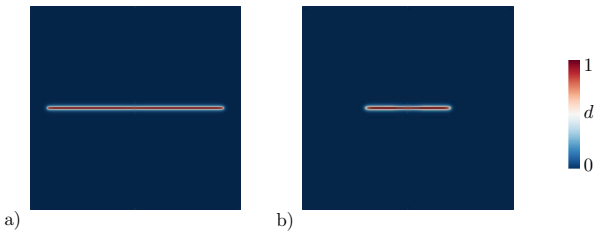

Figure 6.13: Hydraulically induced ductile fracture: Distribution of the fracture phase-field in a) porous-elastic material in b) porous-elastic-plastic material at $t = 90$ s.

As can be seen in Figure 6.13, the length of the finally induced crack for the porous-elastic material is much more pronounced that in case of the porous-elastic-plastic material. This goes along with the observation of a higher fluid pressure inside the crack, see Figure 6.14. We conclude that in case of an elastic-plastic material more fluid needs to be injected into the crack to drive fracturing.

For the elastic material we can observe a characteristic drop of the pressure within the fracture at the onset of fracture propagation (injected fluid volume $V \approx 4 \cdot 10^{-5}$ m^3). In the elastic-plastic material this drop cannot be observed (Figure 6.14). Furthermore, it can be observed that the fluid pressure is not constant over the fracture length. Since the fluid pressure is influenced by the fluid injection rate, we conclude that the fracture propagates under a viscosity dominated regime in this study. This means that the fracture propagation is characterized more by the fluids dynamic viscosity than by the critical fracture energy. For the porous-elastic-plastic material this effect becomes less pronounced. However, for the porous-elastic material the critical pressure (injected fluid volume $V \approx 4 \cdot 10^{-5}$ m^3) at the fracture tip at $x = 4.0$ m, $y = 39.875$ m is almost identical for the different injection rates, see Figure 6.14b.

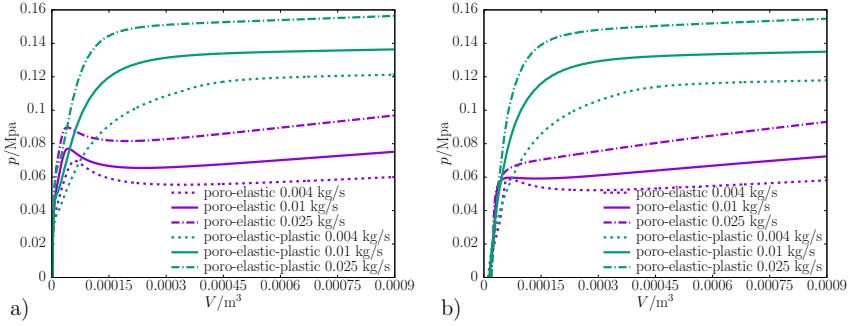

Figure 6.14: Hydraulically induced fracture: Fluid pressure within fractures over injected volume for porous-elastic and porous-elastic-plastic material. The pressure value is detected at $x = 1.0$ m, $y = 39.875$ m in a) and $x = 4.0$ m, $y = 39.875$ m in b), the latter being associated with the crack tip. The solid lines refer to an injection rate of 0.01 kg/s, the dashed lines to an injection rate of 0.004 kg/s and the dashed-dotted lines refer to an injection rate of 0.025 kg/s.

We note that there exists a closed-form solution for the critical pressure p_c and the crack opening width w for a boundary value problem similar to the one considered above (Sneddon and Lowengrub 1969). Here, the critical pressure is defined as the magnitude of pressure that is needed to propagate the crack. The closed-form solution is valid for a porous-elastic material with a static crack under spatially constant pressure loading and without leak-off to the surrounding bulk. Please refer to the Appendix A, in which we provide a comparison of the numerical solution with the closed-form solution for the porous-elastic case.

In Figure 6.15 the distribution of the change of the elastic fluid content is shown for the final equilibrium state. The individual lengths of the cracks are clearly visible. Due to the short crack length in the elastic-plastic case, the injected fluid is distributed over a smaller region. This then gives rise to a higher change of the elastic fluid content, in particular

close to the fracture center. Note carefully that the change of the elastic fluid content in front of the fracture tips is negative for the elastic-plastic material. This phenomenon is investigated in a more detailed way in Figure 6.16, where the contributions of the change of the fluid content in the elastic-plastic material are shown.

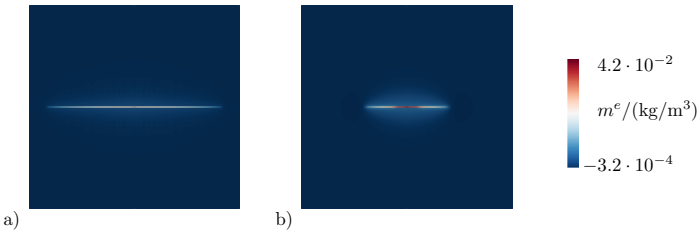

Figure 6.15: Hydraulically induced ductile fracture: Change of elastic fluid content m^e for porous-elastic material in a) and porous-elastic-plastic material in b).

By taking a look at Figure 6.16c, it can be seen that most of the volumetric plastic deformation occurs at the fracture tips ($\dot{m}^p = \rho_f b \operatorname{tr} \dot{\boldsymbol{\varepsilon}}^p$). This leads to a positive change of the plastic fluid content. Since the permeability in the bulk is comparably low, very little amount of fluid diffuses from the fracture into the bulk. In other words, the change of the fluid content at the fracture tips is almost zero. Due to the definition $m = m^e + m^p$ the positive change of the plastic fluid content leads to a negative change of elastic fluid content. Hence the fluid in the fully saturated medium, which is initially stored elastically, is now stored plastically due to the plastic deformation of the solid matrix.

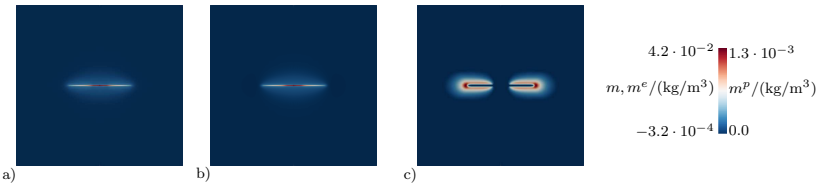

Figure 6.16: Hydraulically induced ductile fracture: Change of total fluid content m in a), change of elastic fluid content m^e in b) and change of plastic fluid content m^p in c) for porous-elastic-plastic material.

In Figure 6.17 we show the distribution of the change of fluid content as well as the pressure and the fracture-opening width along x at $y = 40$ m. These distributions refer to the final equilibrium state for both the porous-elastic and the porous-elastic-plastic material. The difference in the crack length for the two different materials and the positive change of the plastic fluid content as well as the negative change of the elastic fluid content in front of the fracture tip in the elastic-plastic material can again be observed.

Finally, we depict a sequence of three snapshots in the course of the fracture evolution of the porous-elastic-plastic material in Figure 6.18. To be specific, we show the fracture phase field across the whole domain together with the change of fluid content, the pressure and the fracture-opening width at three different time steps along x at $y = 40$ m. The first time step is at $t = 0$ s, the second time step is at $t = 45$ s and the third time step is at the

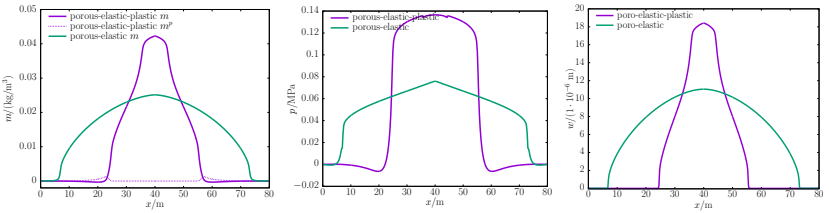

Figure 6.17: Hydraulically induced ductile fracture: Change of fluid content m and m^p, fluid pressure p and fracture opening w for porous-elastic and porous-elastic-plastic material over x at $y = 40$ m.

final state ($t = 90$ s). As can be seen, all considered quantities are mainly concentrated in the center of the fracture. Such a concentration is less prominent in case of an elastic material, see Figure 6.17.

6.6. Conclusion

A model for hydraulically induced fracturing in porous-elastic-plastic solids was developed in the present work. It incorporates a phase-field approach to fracture that is combined with a Drucker–Prager-type plasticity formulation and a Darcy–Biot-type fluid model. The model exploits a variational structure leading to a global minimization formulation. For this variational formulation it is crucial to introduce a plastic fluid content as an additional unknown yielding a constitutive fluid pressure in terms of only the elastic quantities. The global minimization structure demands the use of an $H(\mathrm{div})$-conforming finite-element formulation, which has been implemented by means of Raviart–Thomas-type shape functions. The locking phenomenon of the plasticity formulation is overcome by using an enhanced-assumed-strain formulation for the deformation.

In the first numerical example a comparison of an undrained porous-elastic, an undrained porous-elastic-plastic and a drained elastic-plastic formulation was performed. Here, the different physical effects were investigated. It could be shown that the permeability of porous media can be considered an additional hardening parameter. The second example shows the effect of the proposed modification of the fracture driving force. In the third example, a hydraulically induced crack in a porous-elastic and a porous-elastic-plastic medium was investigated. There it could be shown that neglecting the plastic effects underestimates the pressure inside the fracture and overestimates the fracture length.

Acknowledgments. This work was funded by the Deutsche Forschungsgemeinschaft (DFG, German Research Foundation) – Project Number 327154368 – SFB 1313. This funding is gratefully acknowledged.

Appendix A: Comparison of porous-elastic material with closed form solution.

In what follows, we compare numerical results obtained with the model of the present contribution with the closed-form solution of Sneddon and Lowengrub 1969. The latter constitutes an analytical solution for the critical pressure p_c and of the crack-opening

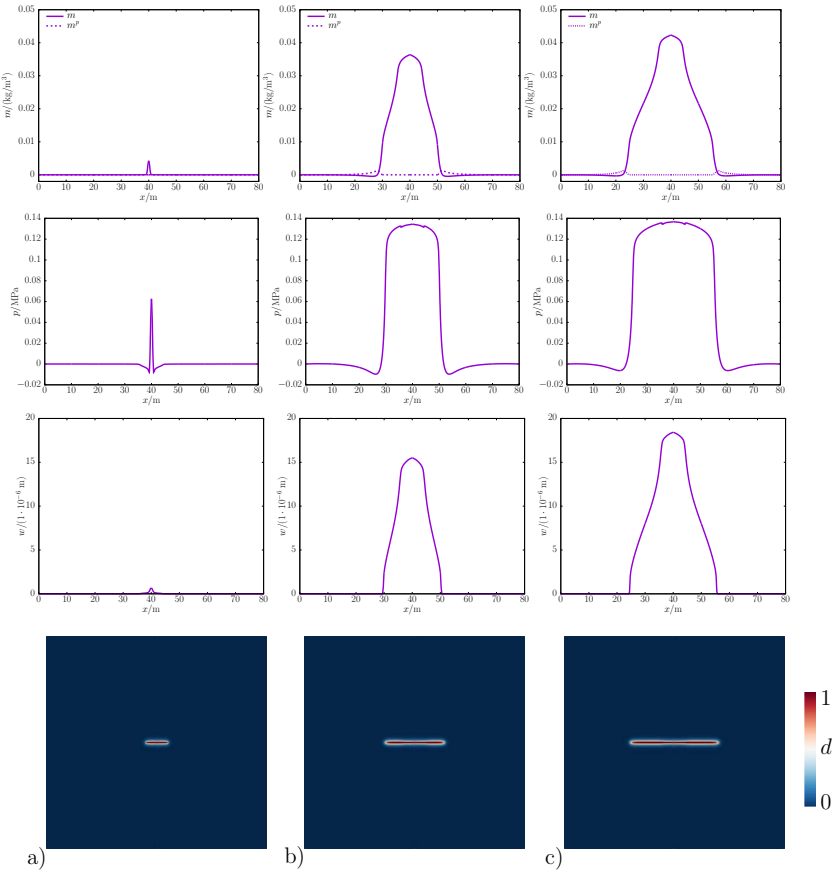

Figure 6.18: Hydraulically induced ductile fracture: Distribution of the fracture phase field and change of fluid content m and m^p, fluid pressure p and fracture opening w over x at $y = 40$ m for three different time steps: a) $t = 0$ s, b) $t = 45$ s and c) $t = 90$ s.

width w. The analytical solution is valid for porous-elastic materials with static cracks, the latter of which have a spatially constant pressure distribution and do not allow leak off to the surrounding medium.

The critical pressure p_c can be expressed as

$$p_c = \sqrt{\frac{2Eg_c}{(1-\nu^2)\pi a}}\,, \tag{6.75}$$

see Wilson and Landis 2016. Here $E = G(3\lambda + 2G)/(\lambda + G)$ is Young's modulus, $\nu = \lambda/[2(\lambda+G)]$ is Poisson's ratio and $g_c = 8\sqrt{2}l\psi_c/3$ is Griffith's critical energy-release. The latter has been obtained from the critical fracture energy ψ_c by considering an optimal damage profile, see Pham et al. 2011a. The analytical solution for the profile of the crack-opening width w is given by (Sneddon and Lowengrub 1969)

$$w(x) = \frac{pa(1-\nu^2)}{E}\sqrt{1-\frac{x^2}{l^2}}. \tag{6.76}$$

Based on the above solutions, we obtain for the given parameters (Table 6.3) the critical pressure $p_c^{\text{closed}} \approx 0.028$ MPa and the profile of the crack-opening width as shown in Figure 6.19. In that figure, we have also plotted the numerical solutions of the critical pressure and the crack profile for a porous-elastic material in consideration of different injection rates of the fluid (cf. Section 4.5.3).

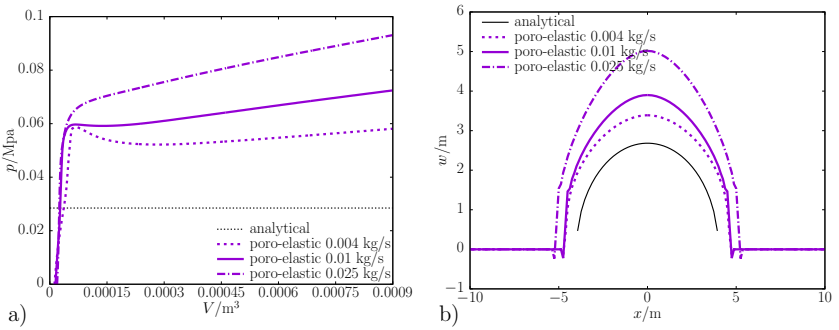

Figure 6.19: Comparison of porous-elastic material with closed form solution: Fluid pressure within the fracture at $x = 4.0$ m, $y = 39.875$ m over inject volume for porous-elastic material in a). The solid lines are for the injection rate 0.01 kg/s, the dashed lines are for the injection rate 0.004 kg/s and the dash-dotted are for the injection rate 0.025 kg/s. Crack opening w over x at $y = 39.875$ m at fracture initiation in b).

We observe a mismatch between the analytical and numerical solutions for both the critical pressure and the crack-width profile. The reasons for this mismatch could be related to the different assumptions of the closed-form and the numerial model (static vs. transient crack; constant vs. non-constant pressure; leak off vs. no leak off). This conclusion is substantiated by the comparison performed by Mauthe 2017, who has taken into account the porous-elastic model proposed by Mauthe and Miehe 2017 and boundary consitions in accordance with the ones considered by Sneddon and Lowengrub 1969.

Mauthe 2017 could show that the numerical solution for such a model is able to perfectly reproduce the analytical solution. For an in-depth discussion of related effects we further refer to Wilson and Landis 2016.

Appendix B: Mesh-dependence of hydraulically induced crack propagation

As shown by Wilson and Landis 2016, the hydro-mechanically induced crack evolution associated with models of the type (6.31) shows mesh-dependent response. We demonstate this effect by repeating the finite-element simulations documented in Section 6.5.3 with a rotated finite-element mesh, see Fig. 6.20. In that figure, the first row of pictures shows crack patterns for a mesh whose element edges are aligned with the direction of the resulting crack (cf. Section 6.5.3); the second row shows results for a mesh that is rotated by an angle of 45° w.r.t. the aligned mesh. In both cases, the left column relates to a porous-elastic material and the right column to porous-elastic-plastic material. The injection rate of the fluid is in both the cases set to 0.01 kg/s.

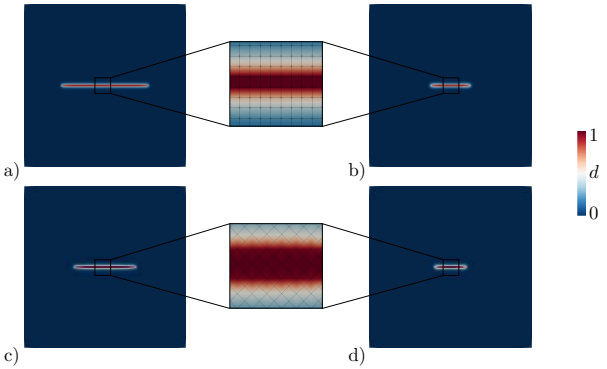

Figure 6.20: Hydraulically induced ductile fracture: Distribution of the fracture phase-field at $t = 35$ s. Porous-elastic material in a) with aligned mesh and in b) with rotated mesh. Porous-elastic-plastic material in c) with aligned mesh and in d) with rotated mesh.

The plots shown in Fig. 6.20 clearly demonstrate the mesh-dependence of the presented formulation. In case of the rotated mesh, the crack is generally shorter and wider than in case of the unrotated mesh. This observation is in line with the findings of Wilson and Landis 2016 and shall be taken into account in numerical simulations involving models of the type (6.31). Such investigations are however beyond the scope of the present contribution and serve as motivation for future work.

The fluid pressure within the crack for both meshes and both cases is shown in Fig. 6.21. In that figure it can be seen that the pressure within the crack is higher in case of the rotated mesh. This observation goes along with the above observations of the crack length and width.

We summarize that both the fluid pressure and the crack geometry are mesh dependent, which confirms the observations of Wilson and Landis 2016. While this provides important pointers for future research, associated improvements are beyond the scope of the present work.

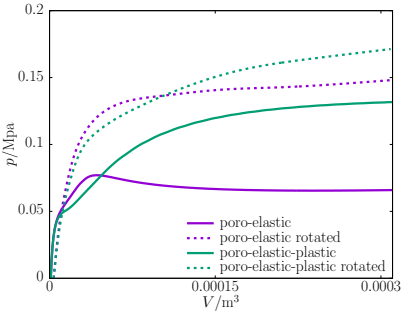

Figure 6.21: Hydraulically induced ductile fracture: Fluid pressure within the fracture over injected volume for porous-elastic and porous-elastic-plastic material at $x = 1.0$ m, $y = 39.875$ m. The solid lines refer to the case where the mesh and the crack are aligned, the dashed lines refer to a rotated mesh by 45°.

Bibliography

Adachi, J., E. Siebrits, A. Peirce, and J. Desroches (2007). "Computer simulation of hydraulic fractures". In: *International Journal of Rock Mechanics & Mining Sciences* 44, pp. 739–757.

Aldakheel, F., N. Noii, T. Wick, and P. Wriggers (2020). "A global-local approach for hydraulic phase-field fracture in poroelastic media". In: *arXiv preprint arXiv:2001.06055*.

Alessi, R., J.-J. Marigo, C. Maurini, and S. Vidoli (2018a). "Coupling damage and plasticity for a phase-field regularisation of brittle, cohesive and ductile fracture: One-dimensional examples". In: *International Journal of Mechanical Sciences* 149, pp. 559–576.

Alessi, R., S. Vidoli, and L. de Lorenzis (2018b). "A phenomenological approach to fatigue with a variational phase-field model: The one-dimensional case". In: *Engineering fracture mechanics* 190, pp. 53–73.

Ambati, M., T. Gerasimov, and L. de Lorenzis (2015). "Phase-field modeling of ductile fracture". In: *Computational Mechanics* 55, pp. 1017–1040.

Amor, H., J.-J. Marigo, and C. Maurini (2009). "Regularized formulation of the variational brittle fracture with unilateral contact: Numerical experiments". In: *Journal of the Mechanics and Physics of Solids* 57, pp. 1209–1229.

Armero, F. (1999). "Formulation and finite element implementation of a multiplicative model of coupled poro-plasticity at finite strains under fully saturated conditions". In: *Computer Methods in Applied Mechanics and Engineering* 171.34, pp. 205–241. ISSN: 0045-7825.

Bear, J. (1972). *Dynamics of Fluids in Porous Media*. Dover Publications, New York.

Biot, M. A. (1941). "General theory of three-dimensional consolidation". In: *Journal of Applied Physics* 12, pp. 155–164.

Biot, M. A. (1984). "New variational-Lagrangian irreversible thermodynamics with application to viscous flow, reaction-diffusion, and solid mechanics". In: *Advances in Applied Mechanics*. Ed. by J. Hutchinson and T. Wu. Vol. 24. Elsevier, pp. 1–91.

Bluhm, J. and R. de Boer (1997). "The volume fraction concept in the porous media theory". In: *ZAMM-Journal of Applied Mathematics and Mechanics/Zeitschrift für Angewandte Mathematik und Mechanik* 77.8, pp. 563–577.

Borden, M. J., T. J. R. Hughes, C. M. Landis, A. Anvari, and I. J. Lee (2016). "A phase-field formulation for fracture in ductile materials: Finite deformation balance law derivation, plastic degradation, and stress triaxiality effects". In: *Computer Methods in Applied Mechanics and Engineering* 312, pp. 130–166.

Bourdin, B., G. A. Francfort, and J.-J. Marigo (2000). "Numerical experiments in revisited brittle fracture". In: *Journal of the Mechanics and Physics of Solids* 48, pp. 797–826.

Bourdin, B., G. A. Francfort, and J.-J. Marigo (2008). *The Variational Approach to Fracture*. Springer.

Bourdin, B., C. P. Chukwudozie, and K. Yoshioka (2012). "A variational approach to the numerical simulation of hydraulic fracturing". In: *SPE Annual Technical Conference and Exhibition*. Society of Petroleum Engineers.

Cajuhi, T., L. Sanavia, and L. de Lorenzis (2018). "Phase-field modeling of fracture in variably saturated porous media". In: *Computational Mechanics* 61.3, pp. 299–318.

Carrara, P., M. Ambati, R. Alessi, and L. de Lorenzis (2020). "A framework to model the fatigue behavior of brittle materials based on a variational phase-field approach". In: *Computer Methods in Applied Mechanics and Engineering* 361, p. 112731.

Castonguay, S. T., M. E. Mear, R. H. Dean, and J. H. Schmidt (2013). "Predictions of the growth of multiple interacting hydraulic fractures in three dimensions". In: *SPE annual technical conference and exhibition*. Society of Petroleum Engineers.

Chukwudozie, C., B. Bourdin, and K. Yoshioka (2019). "A variational phase-field model for hydraulic fracturing in porous media". In: *Computer Methods in Applied Mechanics and Engineering* 347, pp. 957–982.

Dahi-Taleghani, A. and J. E. Olson (2011). "Numerical modeling of multistranded-hydraulic-fracture propagation: accounting for the interaction between induced and natural fractures". In: *SPE journal* 16.03, pp. 575–581.

Damjanac, B., I. Gil, M. Pierce, M. Sanchez, A. Van As, and J. McLennan (2010). "A new approach to hydraulic fracturing modeling in naturally fractured reservoirs". In: *44th US Rock Mechanics Symposium and 5th US-Canada Rock Mechanics Symposium*. American Rock Mechanics Association.

Darcy, H. (1856). *Les fountaines publiques de la ville de Dijon*. Victor Dalmont, Paris.

de Boer, R. (2000). *Theory of Porous Media*. Springer, Berlin.

Detournay, E. and A. H.-D. Cheng (1993). "Fundamentals of poroelasticity". In: *Comprehensive Rock Engineering: Principles, Practice and Projects, Vol. II, Analysis and Design Method*. Ed. by C. Fairhurst. Pergamon Press. Chap. 5, pp. 113–171.

Drucker, D. C. and W. Prager (1952). "Soil mechanics and plastic analysis or limit design". In: *Quarterly of applied mathematics* 10.2, pp. 157–165.

Ehlers, W. (2002). "Foundations of multiphasic and porous materials". In: *Porous Media: Theory, Experiments and Numerical Applications*. Ed. by W. Ehlers and J. Bluhm. Springer-Verlag, Berlin, pp. 3–86.

Ehlers, W. and C. Luo (2017). "A phase-field approach embedded in the Theory of Porous Media for the description of dynamic hydraulic fracturing". In: *Computer Methods in Applied Mechanics and Engineering* 315, pp. 348–368.

Ehlers, W. and C. Luo (2018). "A phase-field approach embedded in the Theory of Porous Media for the description of dynamic hydraulic fracturing, Part II: The crack-opening indicator". In: *Computer Methods in Applied Mechanics and Engineering* 341, pp. 429–442.

Francfort, G. A. and J.-J. Marigo (1998). "Revisiting brittle fracture as an energy minimization problem". In: *Journal of the Mechanics and Physics of Solids* 46, pp. 1319–1342.

Gordeliy, E. and A. Peirce (2013a). "Coupling schemes for modeling hydraulic fracture propagation using the XFEM". In: *Computer Methods in Applied Mechanics and Engineering* 253, pp. 305–322.

Gordeliy, E. and A. Peirce (2013b). "Implicit level set schemes for modeling hydraulic fractures using the XFEM". In: *Computer Methods in Applied Mechanics and Engineering* 266, pp. 125–143.

Griffith, A. A. (1921). "The phenomena of rupture and flow in solids". In: *Philosophical transactions of the royal society of london. Series A, containing papers of a mathematical or physical character*, pp. 163–198.

Gupta, P. and C. A. Duarte (2014). "Simulation of non-planar three-dimensional hydraulic fracture propagation". In: *International Journal for numerical and analytical methods in geomechanics* 38, pp. 1397–1430.

Heider, Y. and B. Markert (2017). "A phase-field modeling approach of hydraulic fracture in saturated porous media". In: *Mechanics Research Communications* 80, pp. 38–46.

Irwin, G. R. (1958). "Fracture". In: *Encyclopedia of Physics*. Ed. by S. Flügge. Vol. 6, Elasticity and Plasticity. Springer, pp. 551–590.

Johnson, E. and M. P. Cleary (1991). "Implications of recent laboratory experimental results for hydraulic fractures". In: *Low permeability reservoirs symposium*. Society of Petroleum Engineers.

Kienle, D., F. Aldakheel, and M.-A. Keip (2019). "A finite-strain phase-field approach to ductile failure of frictional materials". In: *International Journal of Solids and Structures* 172, pp. 147–162.

Kuhn, C. and R. Müller (2010). "A continuum phase field model for fracture". In: *Engineering Fracture Machanics* 77, pp. 3625–3634.

Lambrecht, M. and C. Miehe (2001). "A note on formulas for localized failure of frictional materials in compression and biaxial loading modes". In: *International Journal for Numerical and Analytical Methods in Geomechanics* 25, pp. 955–971.

Lee, S., M. F. Wheeler, and T. Wick (2017). "Iterative coupling of flow, geomechanics and adaptive phase-field fracture including level-set crack width approaches". In: *Journal of Computational and Applied Mathematics* 314, pp. 40–60.

Li, B., C. Peco, D. Millán, I. Arias, and M. Arroyo (2015). "Phase-field modeling and simulation of fracture in brittle materials with strongly anisotropic surface energy". In: *International Journal for Numerical Methods in Engineering* 102.3-4, pp. 711–727.

Lo, Y.-S., M. J. Borden, K. Ravi-Chandar, and C. M. Landis (2019). "A phase-field model for fatigue crack growth". In: *Journal of the Mechanics and Physics of Solids* 132, p. 103684.

Mauthe, S. (2017). *Variational multiphysics modeling of diffusion in elastic solids and hydraulic fracturing in porous media*. Institut für Mechanik (Bauwesen), Lehrstuhl für Kontinuumsmechanik, Universität Stuttgart.

Mauthe, S. and C. Miehe (2017). "Hydraulic fracture in poro-hydro-elastic media". In: *Mechanics Research Communications* 80, pp. 69–83.

Miehe, C. (1998). "A formulation of finite elastoplasticity based on dual co- and contravariant eigenvector triads normalized with respect to a plastic metric". In: *Computer Methods in Applied Mechanics and Engineering* 159, pp. 223–260.

Miehe, C., F. Aldakheel, and A. Raina (2016a). "Phase Field Modeling of Ductile Fracture at Finite Strains. A Variational Gradient-Extended Plasticity-Damage Theory". In: *International Journal of Plasticity* in press.

Miehe, C., M. Hofacker, L.-M. Schänzel, and F. Aldakheel (2015a). "Phase Field Modeling of Fracture in Multi-Physics Problems. Part II. Brittle-to-Ductile Failure Mode

Transition and Crack Propagation in Thermo-Elastic-Plastic Solids". In: *Computer Methods in Applied Mechanics and Engineering* 294, pp. 486–522.

Miehe, C., M. Hofacker, and F. Welschinger (2010a). "A phase field model for rate-independent crack propagation: Robust algorithmic implementation based on operator splits". In: *Computer Methods in Applied Mechanics and Engineering* 199, pp. 2765–2778.

Miehe, C., D. Kienle, F. Aldakheel, and S. Teichtmeister (2016b). "Phase field modeling of fracture in porous plasticity: A variational gradient-extended Eulerian framework for the macroscopic analysis of ductile failure". In: *Computer Methods in Applied Mechanics and Engineering* 312, pp. 3–50.

Miehe, C., S. Mauthe, and S. Teichtmeister (2015b). "Minimization principles for the coupled problem of Darcy-Biot-type fluid transport in porous media linked to phase field modeling of fracture". In: *Journal of the Mechanics and Physics of Solids* 82, pp. 186–217.

Miehe, C., S. Teichtmeister, and F. Aldakheel (2016c). "Phase-Field Modeling of Ductile Fracture: A Variational Gradient-Extended Plasticity-Damage Theory and its Micromorphic Regularization". In: *Philisophical Transactions of the Royal Society A* 374.

Miehe, C., F. Welschinger, and M. Hofacker (2010b). "Thermodynamically consistent phase-field models of fracture: Variational principles and multi-field FE implementations". In: *International Journal for Numerical Methods in Engineering* 83, pp. 1273–1311.

Mikelić, A., M. F. Wheeler, and T. Wick (2019). "Phase-field modeling through iterative splitting of hydraulic fractures in a poroelastic medium". In: *GEM-International Journal on Geomathematics* 10.1, p. 2.

Mikelić, A., M. F. Wheeler, and T. Wick (2015a). "A Phase-Field Method for Propagating Fluid-Filled Fractures Coupled to a Surrounding Porous Medium". In: *SIAM Multiscale Modeling Simulation* 13.1, pp. 367–398.

Mikelić, A., M. F. Wheeler, and T. Wick (2015b). "Phase-field modeling of a fluid-driven fracture in a poroelastic medium". In: *Computational Geosciences*.

Mikelić, A., M. F. Wheeler, and T. Wick (2015c). "A phase-field method for propagating fluid-filled fractures coupled to a surrounding porous medium". In: *Multiscale Modeling & Simulation* 13.1, pp. 367–398.

Pham, K., H. Amor, J.-J. Marigo, and C. Maurini (2011a). "Gradient damage models and their use to approximate brittle fracture". In: *International Journal of Damage Mechanics* 20.4, pp. 618–652.

Pham, K., H. Amor, J.-J. Marigo, and C. Maurini (2011b). "Gradient damage models and their use to approximate brittle fracture". In: *International Journal of Damage Mechanics* 20.4, pp. 618–652.

Pise, M., J. Bluhm, and J. Schröder (2019). "Elasto-plastic phase-field model of hydraulic fracture in saturated binary porous media". In: *International Journal for Multiscale Computational Engineering* 17.2.

Raviart, P. A. and J. M. Thomas (1977). "Primal hybrid finite element methods for 2nd order elliptic equations". In: *Mathematics of computation* 31.138, pp. 391–413.

Santillán, D., R. Juanes, and L. Cueto-Felgueroso (2017). "Phase field model of fluid-driven fracture in elastic media: Immersed-fracture formulation and validation with analytical solutions". In: *Journal of Geophysical Research: Solid Earth* 122.4, pp. 2565–2589.

Schreiber, C., C. Kuhn, R. Müller, and T. Zohdi (2020). "A phase field modeling approach of cyclic fatigue crack growth". In: *International Journal of Fracture*, pp. 1–12.

Shauer, N. and C. A. Duarte (2019). "Improved algorithms for generalized finite element simulations of three-dimensional hydraulic fracture propagation". In: *International Journal for Numerical and Analytical Methods in Geomechanics* 43.18, pp. 2707–2742.

Simo, J. C. and M. S. Rifai (1990). "A class of mixed assumed strain methods and the method of incompatible modes". In: *International Journal for Numerical Methods in Engineering* 29, pp. 1595–1638.

Sneddon, I. N. and M. Lowengrub (1969). *Crack problems in the classical theory of elasticity*. John Wiley & Sons, Inc., New York.

Steinke, C., I. Zreid, and M. Kaliske (2020). "Modelling of Ductile Fracture of Strain-hardening Cement-based Composites-Novel Approaches Based on Microplane and Phase-field Method". In: *Plasticity, Damage and Fracture in Advanced Materials*. Springer, pp. 175–199.

Storm, J., D. Supriatna, and M. Kaliske (2020). "The concept of representative crack elements for phase-field fracture: Anisotropic elasticity and thermo-elasticity". In: *International Journal for Numerical Methods in Engineering* 121.5, pp. 779–805.

Teichtmeister, S., S. Mauthe, and C. Miehe (2019). "Aspects of finite element formulations for the coupled problem of poroelasticity based on a canonical minimization principle". In: *Computational Mechanics* 64.3, pp. 685–716.

Teichtmeister, S., D. Kienle, F. Aldakheel, and M.-A. Keip (2017). "Phase field modeling of fracture in anisotropic brittle solids". In: *International Journal of Non-Linear Mechanics* 97, pp. 1–21.

Terzaghi, K. (1925). *Erdbaumechanik auf bodenphysikalischer Grundlage*. F. Deuticke.

Vermeer, P. and R. de Borst (1984). "Non-associated plasticity for soils, concrete and rock". In: *Heron* 29.3, pp. 1–64.

Wheeler, M. F., T. Wick, and S. Lee (2020). "IPACS: Integrated Phase-Field Advanced Crack Propagation Simulator. An adaptive, parallel, physics-based-discretization phase-field framework for fracture propagation in porous media". In: *Computer Methods in Applied Mechanics and Engineering* 367, p. 113124.

Wick, T. (2020). *Multiphysics Phase-Field Fracture: Modeling, Adaptive Discretizations, and Solvers*. Vol. 28. Walter de Gruyter GmbH & Co KG.

Wilson, Z. A. and C. M. Landis (2016). "Phase-Field Modeling of Hydraulic Fracture". In: *ICES Report* 16-10.

Wu, T. and L. de Lorenzis (2016). "A phase-field approach to fracture coupled with diffusion". In: *Computer Methods in Applied Mechanics and Engineering* 312, pp. 196–223.

Yin, B. and M. Kaliske (2020). "A ductile phase-field model based on degrading the fracture toughness: Theory and implementation at small strain". In: *Computer Methods in Applied Mechanics and Engineering* 366, p. 113068.

Institute of Applied Mechanics (IAM)
Chair for Continuum Mechanics

The modeling of fracture, i.e. fracture initiation and fracture growth, has been the subject of intensive research in the field of continuum mechanics over the last decades. The overall goal is to use simulations to make the production or development process of new parts, materials or techniques cheaper and faster. These simulations are based on material models which are derived using fundamental concepts of continuum mechanics and thermodynamics. This includes the mathematical description of the motion and deformation of a body as well as the definition of mechanical stresses, heat and mass flows.

In the present work, the above process of model conceptualization and numerical implementation is applied to ductile fracture in porous metals, fracture in ductile frictional materials, and ductile frictional materials at hydraulic fracture. With these three models, it is possible to treat ductile failure problems such as cup-cone failure surfaces, ductile fractures in soil materials, and hydraulically induced fractures in ductile soil materials. The latter aims at describing the ongoing processes in hydraulic fracturing. The models are mathematically derived and implemented based on an appropriate finite element description.

ISBN 978-3-937399-59-1